

**Politecnico  
di Torino**

Arnaud Gillioz

# **ROCK FRACTURING DUE TO CO<sub>2</sub> INJECTION**

**Master of Science in Petroleum Engineering**

Supervisors Prof. Francesca Verga  
Prof. Chiara Deangeli

Candidate Arnaud Gillioz

**2023**



# Abstract

One of the challenges posed by the growing consumption of energy is to limit CO<sub>2</sub> emissions to the atmosphere. To that end, CO<sub>2</sub> geological storage, where supercritical CO<sub>2</sub> is injected into underground porous formations, has been proposed as a potential solution. In particular, deep saline aquifers can potentially store many decades worth of CO<sub>2</sub> emissions. However, before an underground formation can be considered for geological storage, its ability to trap the injected fluid over thousands of years must be proven. When injecting into deep saline aquifers, a potential problem is fracturing of the caprock that may result from excessive overpressures. In this context, this work proposes an investigation of caprock tensile failure behavior. Using a model built in CMG GEM, 23 parameters have been selected and varied in order to determine their influence on caprock failure. The work concludes by summarizing all investigated parameters in a tornado plot. Within the range of considered values, parameters such as reservoir matrix permeability, caprock Young modulus, and the number of injection wells have been found to have the strongest impact on the CO<sub>2</sub> mass that can be injected before the caprock undergoes tensile failure.

# Contents

<b>Abstract</b>	<b>II</b>
<b>List of Figures</b>	<b>VI</b>
<b>List of Tables</b>	<b>X</b>
<b>1 Introduction</b>	<b>1</b>
1.1 CO <sub>2</sub> emissions and global warming . . . . .	1
1.2 Carbon capture and storage . . . . .	1
1.3 Numerical modelling of CO <sub>2</sub> storage . . . . .	3
1.4 Scope of the work . . . . .	4
<b>2 CO<sub>2</sub> injection in deep saline aquifers</b>	<b>5</b>
2.1 Suitable storage formations . . . . .	5
2.2 Assessment of storage integrity . . . . .	8
2.3 Injection depth . . . . .	9
2.4 Injection strategy . . . . .	10
2.5 Trapping mechanisms . . . . .	10
2.5.1 Stratigraphic and structural trapping . . . . .	11
2.5.2 Hydrodynamic trapping . . . . .	11
2.5.3 Residual trapping . . . . .	12
2.5.4 Solution trapping . . . . .	14
2.5.5 Mineral trapping . . . . .	15
2.5.6 Other types of fixation . . . . .	15
2.6 Suitable caprock systems . . . . .	15
2.7 Stress response to CO <sub>2</sub> injection . . . . .	17
2.7.1 Pore pressure . . . . .	17
2.7.2 Stresses and strains . . . . .	18
2.7.3 Fault reactivation . . . . .	19
2.8 CO <sub>2</sub> leakage mechanisms . . . . .	21
2.8.1 Caprock breaching . . . . .	22
2.8.2 Caprock fracturing . . . . .	23
2.8.3 Leakage through wells . . . . .	24
2.9 Tensile opening of fractures . . . . .	24
2.10 Monitoring of geomechanical effects . . . . .	25
2.11 Geomechanical characterization of potential storage sites . . . . .	26
<b>3 Barton-Bandis model of fracture closure</b>	<b>28</b>
3.1 Generalities . . . . .	28

3.2	Normal fracture closure behavior . . . . .	28
3.3	Joint roughness coefficient . . . . .	30
3.3.1	Generalities . . . . .	30
3.3.2	JRC determination . . . . .	30
3.4	Joint compressive strength . . . . .	34
3.5	Scale-dependence . . . . .	34
3.6	Hydraulic fracture aperture . . . . .	34
3.7	Mobilization of roughness during shear . . . . .	35
3.8	Fracture permeability . . . . .	36
3.9	Model range of validity . . . . .	36
<b>4</b>	<b>CMG GEM reservoir simulator</b>	<b>38</b>
4.1	Generalities . . . . .	38
4.2	Constitutive models for rock behavior . . . . .	38
4.3	Basic equations . . . . .	39
4.3.1	Fluid-flow . . . . .	39
4.3.2	Deformable porous medium . . . . .	41
4.3.3	Phase equilibrium . . . . .	43
4.3.4	Injector well model . . . . .	43
4.3.5	Time coupling . . . . .	44
4.3.6	Coupling functions . . . . .	47
4.3.7	Spatial coupling . . . . .	51
4.4	Modified Barton-Bandis stress-permeability model . . . . .	52
4.4.1	Generalities . . . . .	52
4.4.2	Initial state of fractures . . . . .	52
4.4.3	Tensile opening of fractures . . . . .	53
4.4.4	Fracture closure . . . . .	53
4.4.5	Basic equations for fracture closure . . . . .	53
4.5	Shear failure of fractures . . . . .	54
4.5.1	Generalities . . . . .	54
<b>5</b>	<b>CMG GEM reservoir model</b>	<b>56</b>
5.1	Base model . . . . .	56
5.2	Base case results . . . . .	61
<b>6</b>	<b>Sensitivity analysis</b>	<b>68</b>
6.1	Reservoir properties . . . . .	69
6.1.1	Matrix permeability . . . . .	69
6.1.2	Matrix permeability anisotropy . . . . .	72
6.1.3	Porosity . . . . .	74
6.1.4	Young modulus . . . . .	77
6.1.5	Poisson ratio . . . . .	80
6.1.6	Dip angle . . . . .	83
6.1.7	Salinity . . . . .	85
6.1.8	Reference pore pressure . . . . .	88
6.2	Caprock properties . . . . .	91
6.2.1	Matrix permeability . . . . .	91

## Contents

6.2.2	Fracture permeability . . . . .	93
6.2.3	Young modulus . . . . .	95
6.2.4	Poisson ratio . . . . .	97
6.2.5	Thickness . . . . .	97
6.2.6	Fracture spacing . . . . .	99
6.2.7	Fracture opening stress . . . . .	99
6.2.8	Residual fracture permeability . . . . .	101
6.3	Simulation options . . . . .	102
6.3.1	Porosity coupling function . . . . .	102
6.3.2	Shear failure . . . . .	104
6.3.3	Equation of state . . . . .	105
6.4	Injection parameters . . . . .	109
6.4.1	Injection rate . . . . .	109
6.4.2	Number of wells . . . . .	113
6.4.3	Well profile . . . . .	116
6.4.4	Perforated interval . . . . .	118
6.5	Summary and discussion . . . . .	120
<b>7</b>	<b>Conclusions</b>	<b>123</b>
	<b>Bibliography</b>	<b>125</b>

# List of Figures

1.1	Possible CO <sub>2</sub> capture methods: (a) fossil fuel-based power generation without capture, (b) post-combustion capture, (c) pre-combustion capture, (d) oxyfuel combustion. [8]	2
1.2	Representation of the two types of aquifers: unconfined (left) and confined (right). [11]	3
2.1	Simplified diagram of the Sleipner CO <sub>2</sub> storage project. [8]	8
2.2	Temperature, pressure and CO <sub>2</sub> density with depth in the Swedish sector of the Baltic Sea basin. [34]	9
2.3	Illustration of the main trapping mechanisms and their respective timescales. [8]	11
2.4	CO <sub>2</sub> plume updip migration in the post-injection phase. [44]	13
2.5	Caprock integrity factor (IF) for different lithologies based on strength, ductility, compressibility and sonic velocity, with halite being the ideal caprock system (IF close to 1). [57]	16
2.6	Horizontal stress response to fluid injection. [57]	19
2.7	Possible causes of induced seismicity related to CO <sub>2</sub> geological storage. [66]	21
2.8	Possible CO <sub>2</sub> leakage mechanisms and remedial measures. [8]	22
2.9	Mechanism of gas breakthrough across the caprock. [73]	23
2.10	Possible mechanisms of crack onset in a block subjected to loads. [35]	24
2.11	Possible monitoring techniques for CO <sub>2</sub> geological storage. [13]	26
3.1	Typical joint roughness profiles with corresponding JRC ranges. [98]	31
3.2	Amplitude-over-length method abacus for JRC correlation. [99]	32
3.3	Representation of a tilt test on faulted core. [98]	33
4.1	Representative element volume. [111]	39
4.2	Flow chart for dual-grid iterative coupling in GEM. [117]	46
4.3	Example of compaction-dilation curves. [111]	50
4.4	Relationship between effective normal stress and fracture permeability in the modified Barton-Bandis stress-permeability model. [108]	52
4.5	Evolution of Mohr circles with increasing pore pressure in a normal-faulting stress regime, and effect of coupling model. [125]	55
5.1	Model scheme.	58
5.2	Relative permeability curves.	60
5.3	IK section of the model showing grid thickness.	60
5.4	Fracture effective normal stress and fracture vertical permeability at the bottom center of the caprock.	61
5.5	Gas saturation at the end of the injection period.	62

*List of Figures*

5.6	Well BHP and fracture vertical permeability at two adjacent blocks at the top of the caprock. . . . .	63
5.7	Average pressure inside the aquifer and vertical displacement at the center top of the caprock. . . . .	64
5.8	Horizontal stresses along the wellbore after 4 months of injection (pre-failure). . . . .	65
5.9	Relative effective horizontal stress decrease after 9 months of injection (pre-breakthrough). . . . .	66
5.10	Relative pressure increase after 9 months of injection. . . . .	66
5.11	Vertical displacement profile along the overburden top and caprock top after 4 months of injection (pre-failure). . . . .	67
5.12	Effective horizontal normal stress above the caprock ( $\{51,1,10\}$ ). . . . .	67
6.1	Well BHP (solid) and fracture vertical permeability (dashed) at the bottom of the caprock with time. . . . .	69
6.2	Gas flux along the wellbore after 3 months of injection. . . . .	70
6.3	Gas mass density (solid) and well BHP (dashed) at the uppermost perforation. . . . .	71
6.4	Vertical displacement profile along the caprock bottom after 8 months of injection (pre-breakthrough). . . . .	71
6.5	Current porosity profile along the caprock bottom after 8 months of injection (pre-breakthrough). . . . .	72
6.6	Gas flux along the wellbore after 3 months of injection. . . . .	73
6.7	Peak vertical displacement at the bottom center of the caprock over time. . . . .	74
6.8	Well BHP with time. . . . .	75
6.9	Gas flux along the wellbore after 3 months of injection. . . . .	76
6.10	Gas saturation after one year of injection: from left to right, $\phi = 0.13$ , $\phi = 0.27$ , and $\phi = 0.41$ . . . . .	76
6.11	Vertical fracture permeability at the bottom center of the caprock. . . . .	77
6.12	Vertical displacement profile along the bottom of the caprock after 6 months of injection (pre-failure). . . . .	78
6.13	Well BHP with time. . . . .	78
6.14	Horizontal stresses along the wellbore after 4 months of injection (pre-failure). . . . .	79
6.15	Cumulative injected mass at first crack as a function of Young modulus. . . . .	80
6.16	Horizontal stresses along the wellbore after 4 months of injection (pre-failure). . . . .	81
6.17	Peak vertical displacement (solid) and fracture permeability (dashed) over time at the top center of the caprock. . . . .	82
6.18	Fracture normal effective stress (solid) and fracture permeability (dashed) over time at the bottom center of the caprock. . . . .	82
6.19	Gas saturation after one year of injection: from left to right, $\alpha = 0^\circ$ , $\alpha = 10^\circ$ , and $\alpha = 20^\circ$ ; maps are untilted for readability. . . . .	83
6.20	Gas saturation with time in below the caprock. . . . .	84
6.21	Fracture normal effective stress (solid) and fracture permeability (dashed) over time at the top center of the caprock. . . . .	84
6.22	Vertical displacement profile along the caprock bottom after 8 months of injection (pre-breakthrough). . . . .	85
6.23	Gas flux along the wellbore after 3 months of injection. . . . .	86
6.24	Vertical displacement profile along the caprock bottom after 3 months of injection (pre-breakthrough). . . . .	87

*List of Figures*

6.25	Vertical fracture permeability at the bottom center of the caprock with time. . . . .	87
6.26	Gas mass density (solid) and well BHP (dashed) at the uppermost perforation. . . . .	88
6.27	Gas flux along the wellbore after 8 months of injection. . . . .	89
6.28	Peak vertical displacement at the bottom center of the caprock over time. . . . .	89
6.29	Horizontal stresses along the wellbore after 5 months of injection (pre-failure). . . . .	90
6.30	Fracture normal effective stress (solid) and fracture permeability (dashed) over time at the bottom center of the caprock. . . . .	91
6.31	Well BHP with time. . . . .	92
6.32	Cumulative injected mass at first crack (solid) and gas breakthrough (dashed) as a function of caprock matrix permeability. . . . .	92
6.33	Well BHP with time. . . . .	93
6.34	Vertical displacement profile along the caprock top after 4 months of injection (pre-failure). . . . .	94
6.35	Cumulative injected mass at first crack (solid) and gas breakthrough (dashed) as a function of caprock fracture and matrix permeability. . . . .	94
6.36	Peak vertical displacement (solid) and fracture permeability (dashed) over time at the top center of the caprock. . . . .	95
6.37	Horizontal stresses along the wellbore after 2 months of injection (pre-failure). . . . .	96
6.38	Cumulative injected mass at first crack (solid) and gas breakthrough (dashed) as a function of caprock Young modulus. . . . .	96
6.39	Time to first crack (solid) and gas breakthrough (dashed) as a function of caprock Poisson ratio. . . . .	97
6.40	Fracture normal effective stress (solid) and fracture permeability (dashed) over time at the bottom center of the caprock. . . . .	98
6.41	Peak vertical displacement at the top center of the caprock over time. . . . .	98
6.42	Cumulative injected mass at first crack (solid) and gas breakthrough (dashed) as a function of fracture spacing. . . . .	99
6.43	Well BHP with time. . . . .	100
6.44	Time to first crack appearance as a function of fracture opening stress. . . . .	100
6.45	Cumulative injected mass at first crack appearance as a function of fracture opening stress. . . . .	101
6.46	Fracture permeability (solid) and fracture normal effective stress (green, common for all runs) over time at the bottom center of the caprock. . . . .	101
6.47	Evolution of porosity (solid) and pressure (dashed) in the gridblock containing the uppermost perforation. . . . .	102
6.48	Current porosity as a function of pressure in the gridblock containing the bottommost perforation. . . . .	103
6.49	Fracture permeability (dashed) and peak vertical displacement (solid) over time at the top center of the caprock. . . . .	103
6.50	Fracture normal effective stress (solid) and fracture permeability (dashed) over time at the bottom center of the caprock. . . . .	104
6.51	Vertical displacement profile along the caprock bottom after 5 months of injection (pre-failure). . . . .	105
6.52	Gas flux along the wellbore after 3 months of injection. . . . .	106
6.53	Horizontal stresses along the wellbore after 4 months of injection (pre-failure). . . . .	107
6.54	Peak vertical displacement (solid) and fracture permeability (dashed) over time at the top center of the caprock. . . . .	108

*List of Figures*

6.55	Well BHP with time. . . . .	109
6.56	Horizontal stresses along the wellbore after 4 months of injection (pre-failure). . . . .	110
6.57	Vertical fracture permeability at the top center of the caprock as a function of cumulative injected volume (RC). . . . .	111
6.58	Cumulative injected volume at CO <sub>2</sub> breakthrough as a function of injection rate. . . . .	111
6.59	Time to CO <sub>2</sub> breakthrough across the caprock as a function of injection rate. . . . .	112
6.60	Vertical displacement (absolute values) in gridblock {51,1,11} at CO <sub>2</sub> breakthrough as a function of injection rate. . . . .	112
6.61	Fracture normal effective stress (solid) and fracture permeability (dashed) over time at the bottom center of the caprock. . . . .	113
6.62	Normal fracture effective stress with time at the bottom of the caprock. . . . .	114
6.63	Pressure profile along the bottom of the caprock after 8 months of injection (pre-breakthrough). . . . .	115
6.64	Vertical displacement profile along the bottom of the caprock after 8 months of injection (pre-breakthrough). . . . .	115
6.65	Fracture normal effective stress (solid) and fracture permeability (dashed) over time at the top center of the caprock. . . . .	116
6.66	Gas saturation after one year of injection: from left to right, vertical well, short horizontal well, and long horizontal well. . . . .	117
6.67	Vertical displacement profile along the caprock bottom after 8 months of injection (pre-breakthrough). . . . .	117
6.68	Pressure profile along the perforated wellbore length after 12 months of injection (long horizontal well). . . . .	118
6.69	Gas mass density (solid) and well BHP (dashed) at the uppermost perforation. . . . .	119
6.70	Gas flux along the wellbore after 3 months of injection. . . . .	119
6.71	Fracture normal effective stress (solid) and fracture permeability (dashed) over time at the bottom center of the caprock. . . . .	120
6.72	Effect of investigated parameters on the injected CO <sub>2</sub> mass at the time of first fracture (on the underside of the caprock), relative to base case. . . . .	122

# List of Tables

1.1	Potential storage capacity for CO <sub>2</sub> in the U.S. and Canada. [16]	2
2.1	Formation characteristics affecting injection costs. [26]	7
5.1	Rock properties.	57
5.2	Reference effective stresses.	57
5.3	Hydraulic parameters.	58
5.4	CO <sub>2</sub> component properties.	59
5.5	Barton-Bandis parameters.	59
6.1	Parameters and values considered in the sensitivity analysis.	68

# 1 Introduction

## 1.1 CO<sub>2</sub> emissions and global warming

CO<sub>2</sub> is a greenhouse gas naturally present in the atmosphere, as well as emitted by anthropogenic activities. While the global warming potential of CO<sub>2</sub> is less than that of other gases such as methane, the quantity in which it is emitted makes it a major cause of global warming and ocean acidification, among other effects.

The burning of fossil fuels makes up a large part of worldwide GHG emissions; in fact, fossil fuels have been cited as being responsible for more than 25 % of the total amount of CO<sub>2</sub> emitted to the atmosphere by humans. [1]–[5]

The demand in primary energy sources is forecasted to keep growing in the coming decades. Despite the commitments made by countries around the world to develop renewable energies, fossil fuels will cover the larger part of this increase in energy demand, contributing to CO<sub>2</sub> emissions. [1]

It then becomes a necessity to reduce global CO<sub>2</sub> emissions. To achieve this goal, a combination of solutions will be needed, such as (1) improvements in energy efficiency, (2) increasing reliance on renewable energy sources, and (3) use of carbon capture and storage (CCS) technologies.

## 1.2 Carbon capture and storage

CCS technologies involve first the separation of the emitted CO<sub>2</sub> from the other exhaust gases. The gas can be captured from the smokestacks of thermal plants, cement plants, refineries, steel mills, ceramic plants, or factories dedicated to heavy industry. Several processes exist for separating CO<sub>2</sub> from flue gas (fig. 1.1). Once captured, CO<sub>2</sub> is transported to the location of final storage, before being injected in a suitable geological formation in order to isolate it from the atmosphere in the long term (*i.e.* thousands of years). [1], [2], [6], [7]

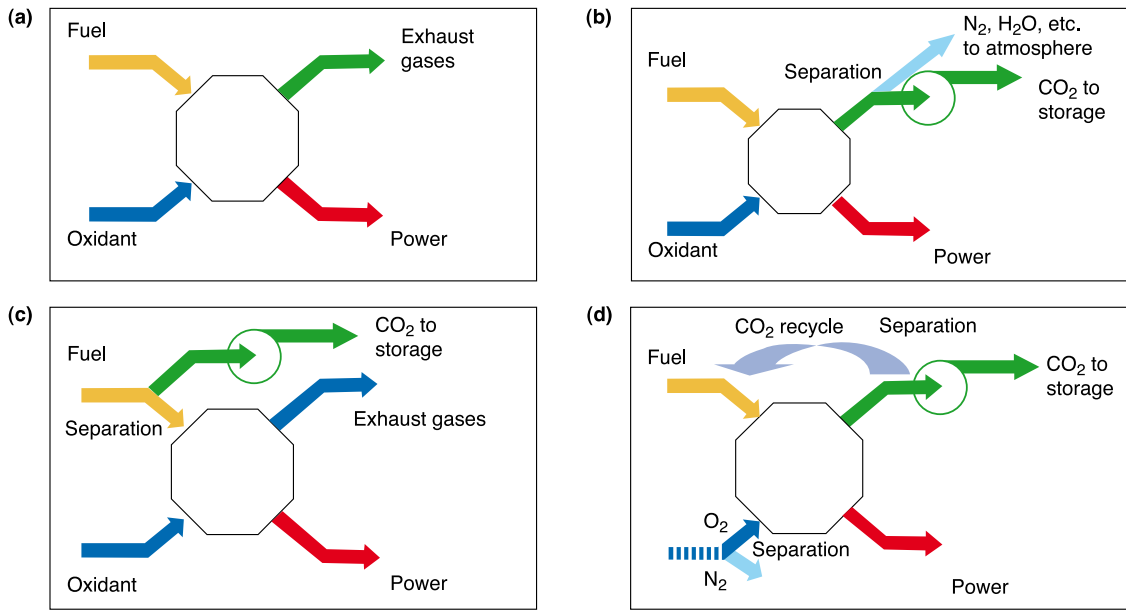


**Figure 1.1** – Possible CO<sub>2</sub> capture methods: (a) fossil fuel-based power generation without capture, (b) post-combustion capture, (c) pre-combustion capture, (d) oxyfuel combustion. [8]

The geological formations usually considered for the storage of CO<sub>2</sub> are either porous media such as (1) deep saline aquifers, (2) depleted oil and gas reservoirs and (3) unmineable coal seams, or non-porous media such as (4) dissolved salt caverns. [1], [2], [6], [9] Alternatively, CO<sub>2</sub> can be stored as part of EOR processes, where CO<sub>2</sub> is injected for the purpose of increasing the oil recovery factor (in the order of 7 to 23 %). Injection is done with the aim of sequestering the displacing fluid (CO<sub>2</sub>) once production is stopped and the field is abandoned. An example of this type of geological storage is the Weyburn project in Saskatchewan, Canada. [8]

Deep saline aquifers are porous and permeable reservoirs filled with formation water not suitable for consumption or use due to its high salinity (usually greater than 33,000 ppm). Of all the possible formations for CO<sub>2</sub> storage, saline aquifers present by far the largest storage capacity (table 1.1), as well as being a very common formation type globally. In consequence, saline aquifers are the only type of formation which permit large-scale (*i.e.* decades of emissions) CO<sub>2</sub> storage. In Europe alone, the storage capacity in deep saline aquifers has been estimated to be around 325 Gt. [1], [3], [6], [10]–[15]

**Table 1.1** – Potential storage capacity for CO<sub>2</sub> in the U.S. and Canada. [16]

Formation type	Storage capacity (10 <sup>9</sup> metric tons)	Percentage
Saline aquifers	3297–12,618	91.8–97.5
Unmineable coal seams	157–178	4.4–1.4
Mature oil & gas reservoirs	138	3.8–1.1
<i>Total capacity</i>	<i>3592–12,934</i>	<i>100</i>

Saline aquifers can be found in two types: confined and unconfined (open boundary conditions). Confined aquifers are similar to oil and gas reservoirs in that the fluid is trapped by structural

(*e.g.* anticlines) or stratigraphic (*e.g.* pinch-outs) geological features. These types of aquifers offer both vertical and lateral confinement, but have lower storage capacities than unconfined aquifers, in which the injected fluid is allowed to move laterally in an unrestricted way (fig. 1.2).

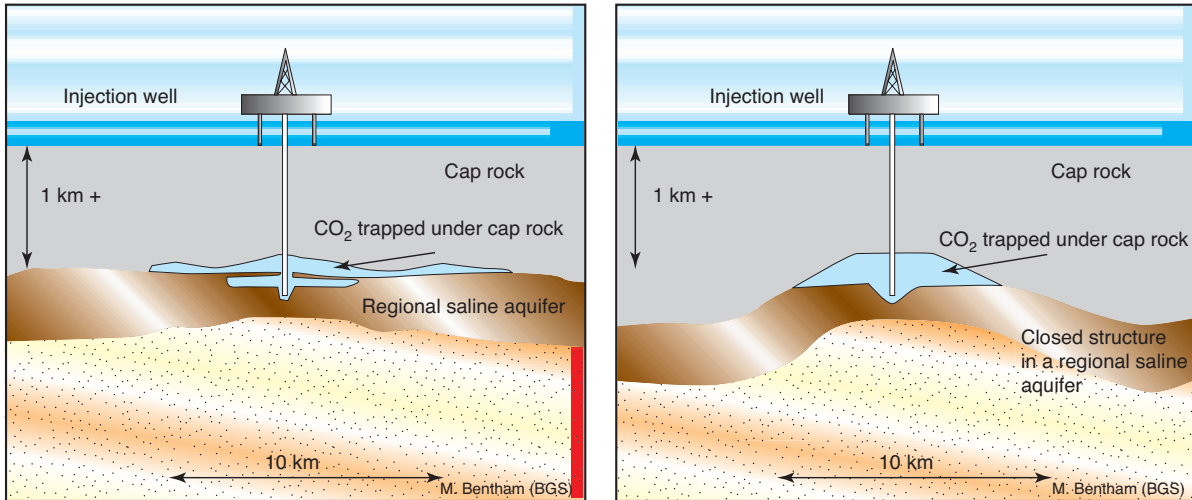


**Figure 1.2** – Representation of the two types of aquifers: unconfined (left) and confined (right). [11]

In unconfined aquifers, the main trapping mechanisms are CO<sub>2</sub> dissolution in water and residual trapping, but a portion of the injected fluid is structurally trapped in small domes naturally present in the underside of the caprock. With this type of aquifer, extensive investigation is needed to demonstrate storage integrity due to the very large distances over which the CO<sub>2</sub> plume migrates. [11], [12], [17]

### 1.3 Numerical modelling of CO<sub>2</sub> storage

When injecting CO<sub>2</sub> into underground formations, the geomechanical effects resulting from changes in the state of stress may result in damage to the caprock or well casings, compromising storage security. Furthermore, fluid-flow properties such as porosity and permeability can be affected by the expansion of the reservoir. Consequently, the geomechanical response of the storage formation to injection must be investigated.

Non-coupled fluid-flow simulators can approximate certain geomechanical effects such as subsidence and compaction through the use of empirical formulas and without computing the actual geomechanical response of the porous medium. In simple problems (*e.g.* linear-elastic rock materials), a non-coupled simulator may give a similar estimation of compaction as that which would be obtained from a coupled geomechanical simulator. Nevertheless, when faced with non-linear material behavior, as for most reservoir rocks, a coupled simulator is needed in order to accurately predict geomechanical effects. [18], [19]

In the particular context of CO<sub>2</sub> storage, modelling is used to assess a number of fluid-flow, geomechanical and geochemical behaviors, namely

- the CO<sub>2</sub> plume migration in time and space,

- the effect of geochemical reactions on porosity, permeability and CO<sub>2</sub> trapping,
- the integrity of the caprock and well completion,
- the impact of temperature variations inside the reservoir,
- the possible leakage pathways for free-phase CO<sub>2</sub>,
- the importance of secondary caprocks if present,
- the effects of unplanned hydraulic fracturing of the reservoir rock,
- the extent of CO<sub>2</sub> migration,
- the impact of CO<sub>2</sub> on cement, and
- the consequences of well failure. [20]

### 1.4 Scope of the work

The general objective of this thesis is to investigate fracturing induced by CO<sub>2</sub> injection using CMG GEM's geomechanical solver. Firstly, the theoretical principles concerning CO<sub>2</sub> geological storage are reviewed in chapter 2. In particular, fundamental concepts related to geomechanics are explained. Chapter 3 then presents the original Barton-Bandis empirical fracture permeability model; a modified version of this model is used in CMG GEM to simulate tensile fracture opening. Next, the characteristics and fundamental equations of GEM's fluid-flow and reservoir simulators are listed in chapter 4.

In order to understand the behavior of GEM's geomechanical simulator, a base model is built and simulated, and the results of this first simulation are then analysed (chapter 5). Then, a sensitivity analysis is performed, where 23 different parameters are varied and compared to the original model; chapter 6 presents and discusses the results of the analysis. Finally, the main takeaways of the work are summarized in chapter 7.

## 2 CO<sub>2</sub> injection in deep saline aquifers

### 2.1 Suitable storage formations

In order to be considered for CO<sub>2</sub> geological storage, an aquifer or underground formation must possess:

- (1) high capacity, *i.e.* high porosity ( $\phi > 20\%$ , depending on thickness), sufficient closure and lateral extent, to accommodate the intended injection volume;
- (2) high injectivity (*i.e.* high  $kh$ , with  $k$  in excess of 500 mD), to accept CO<sub>2</sub> at the supplied rate and provide adequate flow mobility;
- (3) sufficient confinement (a confining structure, sealing faults or an impermeable layer) to prevent buoyancy-driven CO<sub>2</sub> migration to the upper layers and the surface;
- (4) tectonic stability, to avoid compromising the integrity of the sealing structure. [3], [6], [8], [11], [15], [21]–[24]

Sedimentary rocks (sandstones) are often the only rocks providing sufficient storage capacity thanks to their high porosity, as well as the necessary permeability for good injectivity. In particular, poorly cemented sands have both ductile behavior, which delays fracture onset, and relatively high compressibility, which allows the formation to absorb some of the excess pore pressure through expansion of the pore space. [21], [25]

In confined aquifers, where the principal constraint is caprock stability with respect to pressure increase, the storage capacity can be estimated as

$$M_{\text{CO}_2}^{\text{eff}} = A \cdot h \cdot \text{NTG} \cdot \phi \cdot \rho_{\text{CO}_2} \cdot \Delta p \cdot (c_r + c_f), \quad (2.1)$$

where  $M_{\text{CO}_2}$  is the effective storage capacity in units of mass,  $A$  is the areal extent of the aquifer,  $h$  is the average thickness, NTG is the average net-to-gross ratio,  $\phi$  is the average porosity,  $\rho_{\text{CO}_2}$  is the average CO<sub>2</sub> density at reservoir conditions,  $\Delta p$  is the allowable pressure increase relative to the initial pressure,  $c_r$  and  $c_f$  are the average rock and fluid compressibility. [20], [24]

Conversely, the storage capacity of unconfined aquifers is calculated as

$$M_{\text{CO}_2}^{\text{eff}} = A \cdot h \cdot \text{NTG} \cdot \phi \cdot \rho_{\text{CO}_2} \cdot \zeta_{\text{eff}}, \quad (2.2)$$

where  $\zeta_{\text{eff}}$  is the storage efficiency factor ( $< 1$ ), which is a measure of the fraction of useful pore volume. [24] A possible estimation of  $\zeta_{\text{eff}}$  has been proposed as

$$\zeta_{\text{eff}} = C_g C_h C_i, \quad (2.3)$$

where  $C_g$  and  $C_h$  are geometric capacity coefficients, and  $C_i$  is the intrinsic capacity coefficient, or

$$C_i = S_g + (1 - S_g)\chi_b^g \frac{\rho_b}{\rho_{CO_2}}, \quad (2.4)$$

with  $S_g$  the average  $CO_2$  saturation within the plume,  $\rho_b$  the average brine density, and  $\chi_b^g$  the average  $CO_2$  mass fraction dissolved in the brine. [5]

Wellbore injectivity is defined as the ability of a particular formation to accept the injection of a given fluid, and it is limited by the allowable bottomhole pressure. For an injector, the injectivity index  $II$  is written

$$II = \frac{q_{sc}}{p_{wf} - p_s}, \quad (2.5)$$

where  $q_{sc}$  is the injection rate at standard conditions,  $p_{wf}$  is the flowing BHP, and  $p_s$  is the static reservoir pressure.

Considering the solution to the diffusivity equation in transient flow conditions,  $II$  can be rewritten

$$II = \frac{4\pi kh}{B_g \mu \ln(2.25t_D + 2S)}, \quad (2.6)$$

where  $t_D$  is the dimensionless time,

$$t_D = \frac{kt}{\mu c_t \phi r_w^2}. \quad (2.7)$$

BHP, and hence injectivity, depends on many factors such as permeability (absolute and relative), formation thickness, completion type and stimulation, viscosity and compressibility of the injected fluid (table 2.1). The maximum allowable BHP is limited by many regulators to 90 % of the reservoir fracture pressure, in order to avoid uncontrolled fracturing of the reservoir rock in the vicinity of the injector. [26] Consequently, the number of wells must be carefully chosen with respect to injectivity to allow for the desired total injection rate while avoiding hydraulic fracturing. Finally, note that continued  $CO_2$  injection may lead to precipitation of salts by vaporization of water in the near-wellbore zone, decreasing permeability and thus injectivity. [20]

**Table 2.1** – Formation characteristics affecting injection costs. [26]

<b>Factor</b>	<b>Effect on injection costs</b>
Permeability	As permeability increases, injectivity increases, requiring fewer wells and reducing costs.
Fracture gradient	An increase in fracture gradient will increase the maximum injection pressure, reducing the number of wells needed and reducing costs.
Formation thickness	An increase in thickness increases injectivity, reducing the number of wells and reducing costs.
Formation depth	A 1 km deep well is sensitive to permeability decreases, requiring more wells and higher costs. A 2 to 3 km deep well is less sensitive to permeability decreases, therefore having a lesser effect on costs.
Well deviation	Horizontal wells maximize surface area contact with the target formation, increasing injectivity, and reducing the number of wells needed and costs.
Degree of hydraulic fracturing	Hydraulic fracturing creates higher permeability of the formation in the near-wellbore area and increases injectivity. It has been shown that in low permeability situations (around 1 mD), hydraulic fracturing of the reservoir reduces costs as the increase in injectivity offsets the extra costs involved in the fracturing operation.

Note that there exists a limit up to which a reservoir may accept the injection of a fluid, regardless of the number of injectors. If the injected fluid is not able to displace the resident brine fast enough, the resulting high pressure zone may prevent further fluid injection as the pressure difference between the wellbore and the formation is reduced. This effect can be the result of interference from multiple wells, creating a high pressure zone. In this case, injection is restricted without effect on the injectivity index, as this is a reservoir rather than wellbore effect. [27]

CO<sub>2</sub> is usually stored at depths greater than 1000 m to maximize storage capacity thanks to its higher density at higher pressures and temperatures. Note however that porosity (and hence pore volume) is reduced at depth due to the increased degree of cementation and compaction. [8], [28]

Low permeability or faulted reservoirs (with low transmissibility faults) are not suited to geological storage as injection would cause an excessive pressure increase at the perforations, since the flow of the injected fluid is impeded. As a result, injection rate is limited and the risk exists of fracturing the reservoir rock and/or caprock from overpressure. Similarly, overpressured formations (either through compaction or generation of hydrocarbons) are unsuitable for safety reasons. This makes large, unfaulted, underpressured, high permeability reservoirs located in geologically stable areas (low tectonic activity) the ideal storage sites for CO<sub>2</sub>. [8], [11]

A final consideration for the selection of potential storage sites is the presence of hydrocarbons, and the maturity of the producing fields. Indeed, in hydrocarbon-bearing basins, a good knowledge of the subsurface has already been acquired through seismic surveying, well logs and



## 2.3 Injection depth

In order to maximize storage capacity, CO<sub>2</sub> density at injection depth should be as high as possible. CO<sub>2</sub> is ideally stored in formations in which temperature and pressure exceed the critical point ( $T_c = 31.1\text{ °C}$  and  $p_c = 7.38\text{ MPa}$ ), as supercritical CO<sub>2</sub> has a liquid-like density between 200 and 800 kg/m<sup>3</sup> (fig. 2.2). Furthermore, as a supercritical fluid, CO<sub>2</sub> behaves as a gas and shows gas-like compressibility and viscosity (in the order of 0.04 to 0.07 cP). [1]–[3], [6], [12], [15], [31], [32] Note that CO<sub>2</sub> is compressed before injection so that the fluid to be injected is in a supercritical state at the wellhead. This avoids problems caused by phase transitions and biphasic flow inside the tubing, like the formation of hydrates. [14], [33]

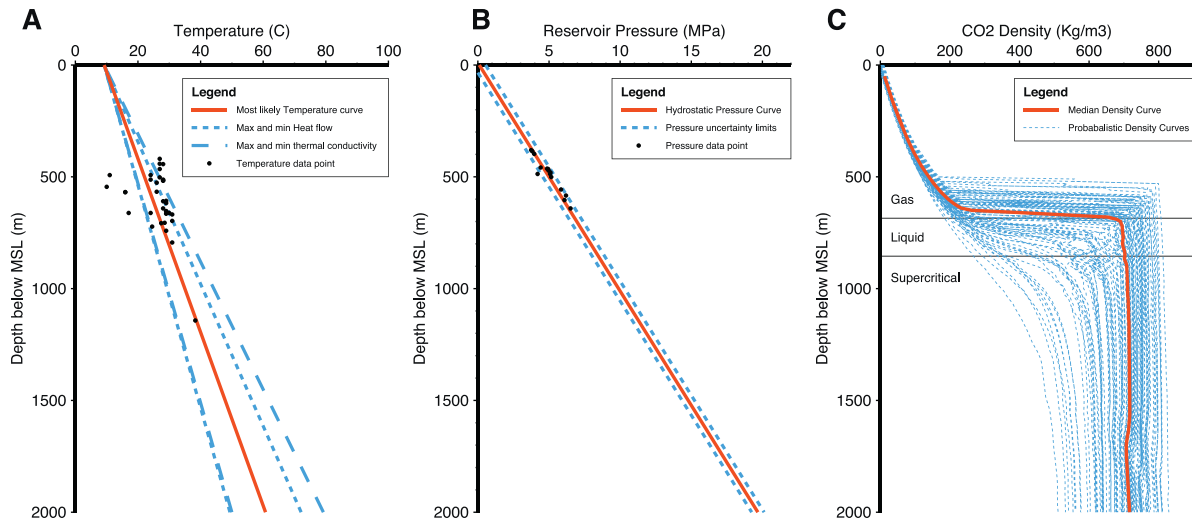


**Figure 2.2** – Temperature, pressure and CO<sub>2</sub> density with depth in the Swedish sector of the Baltic Sea basin. [34]

Under average pressure and temperature gradients (10 MPa/km and 25 °C/km respectively), supercriticality is reached at around 800 m, which means that aquifers shallower than 800 m are not candidates for CO<sub>2</sub> storage. Above depths of 500 to 600 m, CO<sub>2</sub> is in gaseous state, and between 600 and 800 m it exists in liquid phase. As fluid density does not vary appreciably beyond 1000 m, there is no further increase in storage capacity below this depth. [1], [6], [11]

It should be noted that supercritical conditions may be reached at much shallower depths depending on surface temperatures. In some tropical and subtropical basins, such as in Texas, Venezuela, Colombia, Ecuador or Africa and the Middle East, the 31.1 °C isotherm can lie at depths as shallow as 150 to 500 m. Nevertheless, colder basins (low temperature gradient) are theoretically preferable due to the increased density of CO<sub>2</sub> at low temperatures and decreased buoyant forces. In practice, this advantage is somewhat offset by the increased cost of drilling for deep targets. [2], [8], [17]

While CO<sub>2</sub> density at injection depth is liquid-like, it is still significantly lighter (by 30 to 40 %) than the formation fluid, as brine density at reservoir conditions may exceed 1200 kg/m<sup>3</sup>. This density difference generates a proportional buoyancy force, which drives the injected fluid vertically until it reaches the caprock and starts migrating laterally. [3], [12], [14], [32] Note

that supercritical CO<sub>2</sub> also has a much higher mobility than the resident brine thanks to its gas-like viscosity. [9]

## 2.4 Injection strategy

The most common injection strategy is to bring the CO<sub>2</sub> to supercritical conditions prior to injection using a staged compressor train with intercoolers. The supercritical fluid is then injected as-is. [26]

Several other strategies have been proposed with the aim to improve storage security. Surface dissolution is a process in which CO<sub>2</sub> is dissolved into brine prior to injection. Using this process, since the injected fluid is slightly denser than the pore fluid, there is no buoyancy force and thus no risk of buoyancy-driven leakage, reducing the need for monitoring. [26], [35], [36]

Another potential strategy is the co-injection of water and CO<sub>2</sub> in the form of water-alternating-gas (WAG) or simultaneous water-alternating-gas (SWAG). In a WAG process, the injection of both fluids is done sequentially through the same injector, while in SWAG processes different injectors are used. [36] Using these processes, residual and solution trapping of CO<sub>2</sub> can be enhanced. If water is injected above the CO<sub>2</sub> plume, an imbibition process takes place as water flows down while CO<sub>2</sub> flows up, enhancing residual trapping; the reduction of the quantity of mobile (free-phase) CO<sub>2</sub> leads to an increase in storage safety. However, water producers may have to be drilled in order to counteract the large pressure increases caused by water injection. [26], [29], [32], [37]

Finally, Javadpour and Nicot (2011) proposed to add depleted uranium nanoparticles to the injected CO<sub>2</sub> in order to increase convective mixing and decrease buoyancy flow of the plume. [38], [39]

## 2.5 Trapping mechanisms

The trapping of the injected fluid inside the storage formation is achieved by a number of different mechanisms, which vary with the geological configuration of the formation, injection parameters (rate, duration and perforated interval), as well as time. [32] Trapping mechanisms can be either physical or geochemical. Physical trapping mechanisms are most important shortly after injection, but provide poor storage security; geochemical processes are more secure and permanent forms of trapping, but take place over much longer timescales. [40]

The most important physical storage mechanisms are (1) structural and stratigraphic trapping, (2) hydrodynamic trapping, and (3) residual or capillary trapping. Geochemical processes are (4) solution or solubility trapping, and (5) mineral trapping (fig. 2.3).

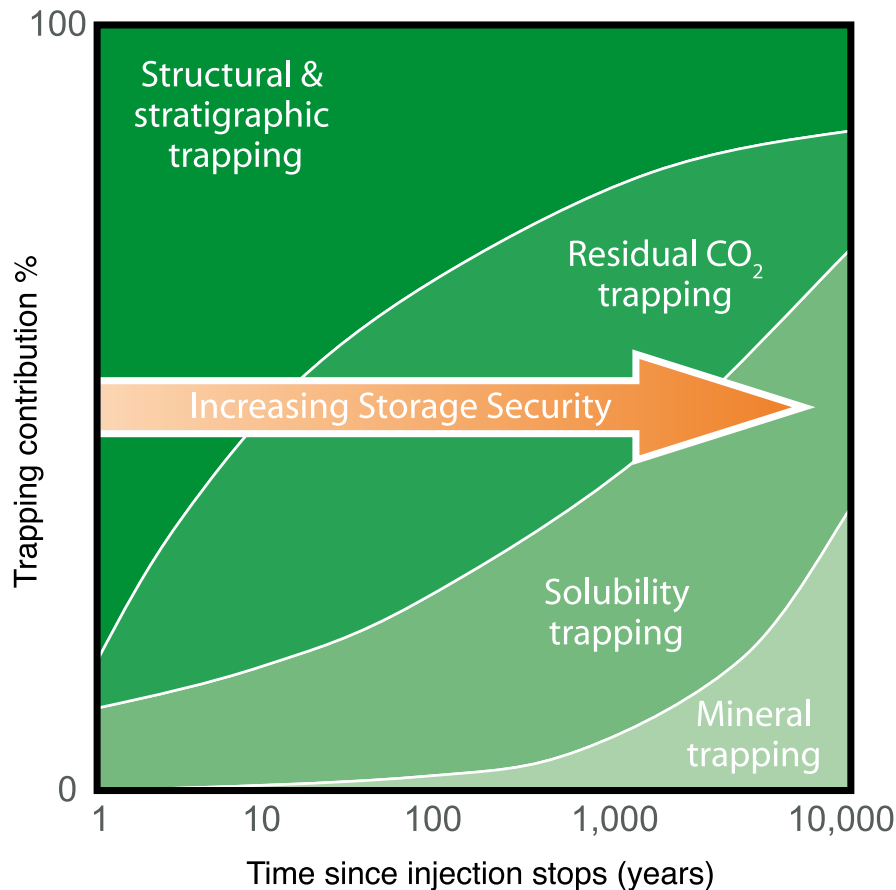


**Figure 2.3** – Illustration of the main trapping mechanisms and their respective timescales. [8]

### 2.5.1 Stratigraphic and structural trapping

If the storage formation possesses structural or stratigraphic features that provide both a top and lateral seal (*e.g.* anticline), the injected fluid will initially remain physically trapped between the top of the structure and the spill point. This mechanism of trapping is one of the least secure, as the CO<sub>2</sub> is stored as a free fluid and may leak to the surface if allowable overpressure is exceeded and seal integrity is compromised. [8], [23], [35]

### 2.5.2 Hydrodynamic trapping

In formations that do not present a structural or stratigraphic trap, such as open saline aquifers, the stored CO<sub>2</sub> is initially trapped hydrodynamically. The injected fluid remains as a separate phase in the form of a plume, and migrates vertically due to buoyancy effects until it reaches the top seal. Since there is no lateral seal, the plume slowly migrates laterally at a rate of 1 to 10 cm/y, driven both by buoyancy forces and the natural hydrodynamic flow of groundwater. Like in the case of structural and stratigraphic trapping, the risk of CO<sub>2</sub> escaping to the surface is large as it remains in a mobile phase. In practice, only sites with low groundwater velocity are considered for injection. [8], [9], [32]

In open formations, hydrodynamic trapping predominates until the free phase gradually becomes trapped as residual saturation, in local structural and stratigraphic traps, or dissolved into the formation fluid. [8]

### 2.5.3 Residual trapping

When injecting into reservoirs with no organic material content, the rock is water-wet and CO<sub>2</sub> is the non-wetting phase. As supercritical CO<sub>2</sub> is only slightly soluble in water, the injected fluid initially remains a separate phase. In the near-wellbore region, CO<sub>2</sub> flow is dominated by viscous forces, which cause it to spread radially in a two-phase immiscible-flow system. Further from the well, the free-phase plume is driven upwards by buoyancy forces before pooling underneath the caprock. If the impermeable layer is not perfectly horizontal, the plume will start to slowly migrate updip. As CO<sub>2</sub> dissolves into the formation water, which becomes increasingly saturated with CO<sub>2</sub>, it sinks to the bottom of the reservoir as brine saturated with CO<sub>2</sub> is about 1% denser than pure saline water. [3], [11], [12], [29], [33], [40], [41] As a consequence of the migration of the CO<sub>2</sub> plume, three distinct zones can be observed: (1) a zone swept by anhydrous CO<sub>2</sub> in the vicinity of the wellbore, (2) a zone fully saturated with formation water away from the plume, and (3) a Buckley-Leverett zone (mixing zone) in between. [41], [42]

During the injection phase, a drainage process occurs where the non-wetting CO<sub>2</sub> displaces the aqueous phase. Post-injection, as the plume migrates away from the injection point, the displaced brine slowly reoccupies the pore space at the trailing edge of the plume in an imbibition process (B in fig. 2.4). Several competing pore-scale mechanisms occur during imbibition, such as snap-off and piston-like displacement. In particular, snap-off phenomena leave behind a residual CO<sub>2</sub> saturation in the form of droplets tens to hundreds of micrometers in size, trapped by capillary forces (C). In sandstones,  $S_{gr}$  has been measured between 10 and 33%, making residual trapping a very important storage mechanism. [5], [43] On the other hand, some chemical interactions such as the dissolution of CO<sub>2</sub> into the formation brine may influence the wettability of the rock matrix to brine, making it neutrally or even CO<sub>2</sub>-wet. In this scenario, the displacing brine tends to advance with piston-like behavior during the imbibition process, and little to no residual saturation is left behind. [44]

Capillary trapping mobilizes large volumes of CO<sub>2</sub> from the free-phase plume, shrinking it and limiting the extent of its migration. The residual gas saturation left behind by imbibition is effectively trapped forever, making residual trapping a permanent and safe storage mechanism. Furthermore, the capillary trapped fraction is not subject to buoyant forces, reducing buoyant stress on the caprock. [44]

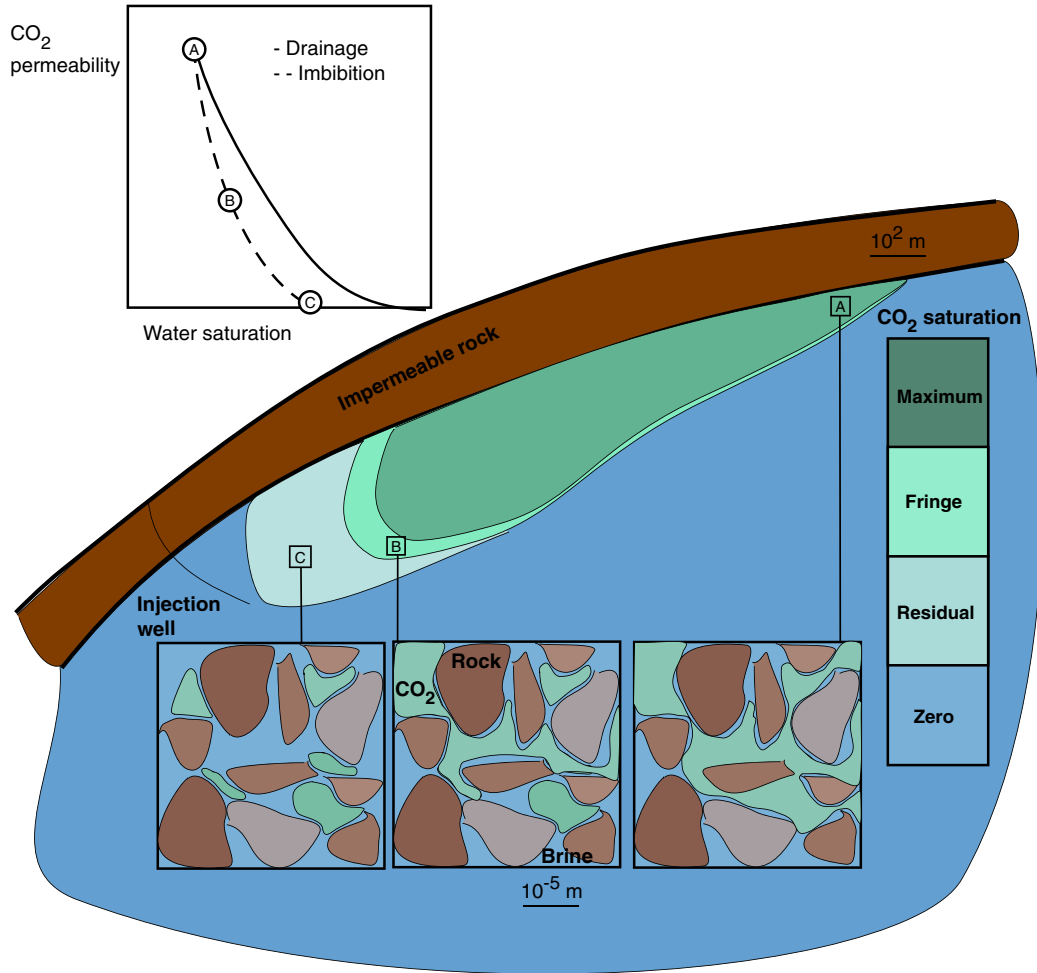


**Figure 2.4** – CO<sub>2</sub> plume updip migration in the post-injection phase. [44]

At the pore scale, the amount of residual trapping is governed by

- (1) the wettability (or contact angle), where a preferentially water-wet media favours snap-off, leading to more trapping,
- (2) the balance between viscous forces and capillary forces, quantified by the capillary number  $N_c$ ,
- (3) the ratio between pore and throat size, where large pores and narrow throats enhance trapping, and
- (4) the connectivity between pores, where better connected pores decrease residual trapping. [5], [44]

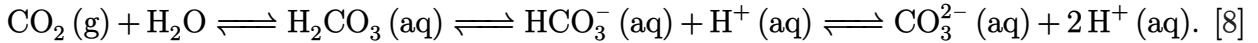
At the field scale, residual trapping is determined by the amount of brine contacted by free-phase CO<sub>2</sub>, which itself depends on the shape of the plume. The plume shape is a function of the balance between viscous and gravity forces, which is expressed as the gravity number  $N_g$ :

$$N_g = \frac{k_v \Delta \rho g \cos \alpha}{\mu v}, \quad (2.8)$$

where  $k_v$  is the vertical permeability,  $\Delta\rho$  is the density difference between brine and CO<sub>2</sub> at reservoir conditions,  $g$  is the gravitational acceleration,  $\alpha$  is the dip angle,  $\mu$  is the CO<sub>2</sub> viscosity, and  $v$  is the sandface Darcy velocity. Large values of  $N_g$  correspond to a plume movement dominated by gravity forces. [45]

#### 2.5.4 Solution trapping

Solution trapping consists of the dissolution of CO<sub>2</sub> in the aqueous phase, which proceeds according to the following chemical reactions:



The decomposition of CO<sub>2</sub> into H<sup>+</sup> and HCO<sub>3</sub><sup>-</sup> ions upon dissolution into water leads to a reduction in pH of the brine from 7.0 to around 3.5–5.0; this decrease in pH lowers the solubility of CO<sub>2</sub> in water. Like in the case of residual trapping, the degree of dissolution depends on the contact area between the CO<sub>2</sub> and the brine, which increases as the plume migrates away from the injection point. Consequently, both residual and solution trapping are most important in the post-injection phase, and before CO<sub>2</sub> becomes mobilized in mineral trapping. [8], [46]

Solubility of CO<sub>2</sub> into brine is a function of pressure, temperature and salinity. The relationship between pressure and solubility is governed by Henry's law, in which the concentration of dissolved gas at equilibrium conditions is proportional to the partial pressure of the gas. On the other hand, an increase of temperature has a negative effect on solubility; indeed, the added thermal energy works to overcome the attractive forces between the solvent and the gas molecules. However, the effect of temperature on solubility is relatively small compared to that of pressure. Finally, in presence of salts, water molecules are attracted to the salt ions, which reduces the number of H<sup>+</sup> and O<sub>2</sub><sup>-</sup> ions available to dissociate gas molecules. Hence, salinity has a negative effect on CO<sub>2</sub> solubility. [40]

The combination of pure CO<sub>2</sub> rising upwards due to buoyancy and saturated brine sinking due to its higher density creates convection currents, which promote mixing and increase CO<sub>2</sub> dissolution. [14] In reservoirs with a high vertical-to-horizontal permeability ratio  $k_v/k_h$ , the CO<sub>2</sub> plume will have a larger vertical flow component compared to horizontal, which will be detrimental to CO<sub>2</sub> dissolution into brine. In a similar way, injection into dipping formations promotes lateral displacement of the plume, increasing the amount of dissolution occurring. [47]

The proportion of injected CO<sub>2</sub> that eventually dissolves into water is in the range of 20 to 60 kg/m<sup>3</sup> of brine depending on depth and salinity. [3], [8], [40]

Since dissolved CO<sub>2</sub> no longer exists as a separate phase, it is not subject to buoyancy-driven flow. Consequently, solution trapping is considered a safe storage mechanism. Nevertheless, there is a risk that the dissolved CO<sub>2</sub> comes out of solution in the event of a significant change in pressure or temperature, for example if the caprock is breached. [8], [23], [32], [35]

### 2.5.5 Mineral trapping

The injection of  $CO_2$  triggers various other chemical reactions between the porous medium, brine and injected fluid, such as salt precipitation from the stripping of water molecules by anhydrous  $CO_2$  in the vicinity of the injector, or dissolution of minerals in carbonate reservoirs. These reactions affect both porosity and permeability near the injector. [3], [6], [7], [21], [41], [48]–[50]

Furthermore, once  $CO_2$  has dissolved into water and dissociated, bicarbonate ions may react with the surrounding rock to form solid precipitates in the form of carbonate minerals like calcite, dolomite or siderite. This form of trapping is the most permanent and safest form of storage. The time for the precipitation reaction to proceed depends on the minerals that react with  $CO_2$ ; it may be in the order of days for some carbonate minerals, and up to thousands of years for silicate minerals. [23], [32], [35], [51]

All these reactions have an impact on hydraulic properties such as porosity and permeability, which in turn affect geomechanical properties such as stiffness and strength. [6], [52] In particular, mineral dissolution can lead to wormholes and fingering, subsidence, increased compaction creep, and increased porosity and permeability; conversely, mineral precipitation leads to a decrease in porosity and permeability. [21], [53] Nonetheless, the effect of chemical reactions on hydraulic and geomechanical properties appears limited even over large time scales, especially in shales and mudstones. [21], [47]

### 2.5.6 Other types of fixation

Other types of trapping may exist, such as  $CO_2$  adsorption onto coal or organic-rich shales, or the formation of  $CO_2$  hydrates in cold regions. [8]

In aquifers exhibiting local variations of capillary entry pressure,  $CO_2$  may become trapped under local heterogeneities of high capillary entry pressure while migrating upwards due to buoyancy. This is a highly secure storage mechanism, which persists even after buoyancy-driven flow has stopped. The fluid trapped by this mechanism is not susceptible to leaking in case of caprock integrity loss. This type of local trapping, termed local capillary trapping (LCT), is very beneficial as the  $CO_2$  saturation in these zones is much higher than residual gas saturation, meaning that a large amount of  $CO_2$  can be safely stored through this process. [54]

## 2.6 Suitable caprock systems

The injected fluid displaces the resident fluid (*i.e.* brine) and forms a plume which propagates, driven by the pressure differential between the injection point and the aquifer boundary. Additionally,  $CO_2$  rises vertically due to buoyancy, as  $CO_2$  is lighter than the brine initially present in the aquifer. As a result, candidate aquifers should be capped by an impermeable layer with geomechanical properties such that it can provide containment for the rising fluid, as well as sustain the pressure buildup caused by injection over the considered time scale and for the considered injection strategy. [7], [11], [48], [55], [56] The sealing layer must have

a sufficient lateral extent to prevent undesired CO<sub>2</sub> migration to the surface; in the case of unconfined aquifers, the areal extent of the caprock might have to be as large as sub-regional or regional. [6]

The main consideration in determining the suitability of a particular aquifer for geological storage is seal integrity, which is related to the caprock's propensity to develop structural permeability, or its susceptibility to hydraulic fracture propagation. [56], [57] Whereas the properties of the top seal in depleted reservoirs are already studied, the sealing capability of aquifer caprocks is initially unknown. [21] As a result, caprock lithology, thickness and fracture density must be evaluated in order to assess its sealing properties. [56]

In ductile lithologies such as halites, mudrocks and organic shales, fractures are less likely to be permeable to flow thanks to the self-sealing properties of the medium (fault smearing). Consequently, caprocks that are able to deform plastically are the least likely to suffer loss of integrity (fig. 2.5), despite having low shear strength compared to stiff and brittle lithologies. [11], [21], [57]

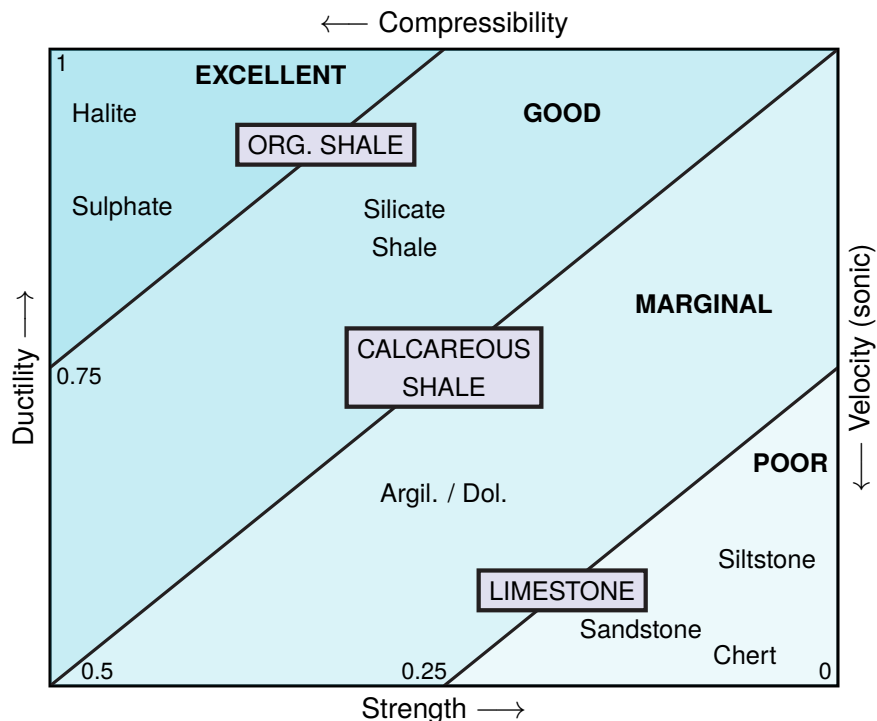


**Figure 2.5** – Caprock integrity factor (IF) for different lithologies based on strength, ductility, compressibility and sonic velocity, with halite being the ideal caprock system (IF close to 1). [57]

In order to preserve seal integrity and prevent Darcy-type flow to the upper aquifers and the surface, caprock permeability should be low, while capillary entry pressure should be high. More specifically, the caprock's capillary entry pressure should be higher than the expected overpressure resulting from the CO<sub>2</sub> injection, or the maximum predicted buoyant force of the CO<sub>2</sub> column. [15], [21], [27] Capillary entry pressures for CO<sub>2</sub> in CO<sub>2</sub>-brine systems may be as low as 0.1 MPa and up to 10 MPa, meaning that leakage may happen even with very small overpressures depending on conditions. [21] Caprock capillary entry pressure is a function of

CO<sub>2</sub>-water interfacial tension, pore throat size and wettability of CO<sub>2</sub> to rock, and is negatively affected by the presence of discontinuities that have a higher permeability than the rock matrix. [56], [57]

Finally, while homogeneous caprocks will fail directly above the injection point, failure of heterogeneous caprocks occurs in zones of high Young modulus and Poisson ratio (stiff zones), as these are not able to absorb the applied stress by deforming elastically. Accordingly, the more petrophysically heterogeneous is the caprock, the greater is the risk of CO<sub>2</sub> leakage. [58]

Consequently, thick, homogeneous and unfaulted clays, claystones, mudstones and evaporites (such as anhydrites and halites) compose most of the suitable caprock systems for CO<sub>2</sub> storage. [6], [11], [21]

## 2.7 Stress response to CO<sub>2</sub> injection

### 2.7.1 Pore pressure

The injection of cold CO<sub>2</sub> causes the aquifer to respond locally due to an increase in pore pressure and a change of temperature. The extent of the pore pressure increase varies widely depending on the geometry of the storage formation. In depleted reservoirs, pore pressure at the start of injection is usually lower than when the reservoir was first produced. On the other hand, when injecting into saline aquifers, pore pressure will increase beyond initial values, meaning that caprock integrity at the expected value of overpressure needs to be demonstrated. Note that many sedimentary basins have an initial state close to limit equilibrium, meaning that the window of acceptable overpressure is relatively narrow. [25]

The increase in pore pressure is lower in unconfined aquifers compared to confined and semi-confined ones, as the displaced fluid can travel radially unimpeded. Moreover, when the pressure disturbance reaches the outer boundary of a confined aquifer, the reflection of the pressure front causes an additional overpressure. [48]

Aquifers overlain by a relatively permeable caprock ( $k > 0.01$  mD) experience a lower pressure buildup as formation fluid can leak through the seal. [48] Similarly, the presence of fractures in brittle reservoir rocks decreases the pressure build-up above the injector by favouring lateral migration of the plume. [59] Rock compressibility also has an effect on pressure build-up; as formations with a high compressibility can undergo more expansion, the excess pore pressure is partially absorbed by the increased pore volume. [25]

Note that reaching overpressure may also be desirable in depleted reservoirs, where it would yield an increased storage capacity. In fact, if water injection has been used to increase recovery during production, pore pressure at reservoir end-of-life (and beginning of geological storage) may be the same as initial (pre-production) reservoir pressure, as was the case in the Weyburn CO<sub>2</sub> storage project in Saskatchewan, Canada.

At the Weyburn oil field, unsupported production reduced pore pressure from 15 MPa to 6 MPa. Pressure then returned to its initial value because of water injection, and rose to 20 MPa

after starting CO<sub>2</sub> injection. There, CO<sub>2</sub> is injected both for long-term storage and enhanced recovery, which means that production and injection are occurring simultaneously. [13]

In the Sleipner project, while the injection well is not equipped with downhole pressure gauges, the pore pressure increase between 1998 and 2007 has been estimated using seismic travel time shifts to be at most 0.2 MPa. Abnormal pressures have been recorded during the first months of injection and between 2001 and 2003 due to sand accumulation in the perforated liners and problems with the thermostatic temperature controls. [13]

The total pore volume of the Utsira sandstone is estimated to be around  $6 \times 10^{11} \text{ m}^3$ , while the injected CO<sub>2</sub> volume is roughly  $18 \times 10^6 \text{ m}^3_{\text{rc}}$ , or 0.003 % of the total pore volume. Additionally, the Utsira sand possesses high permeability at 1 to 3 D, and no evidence of compartmentalization (sealing faults) has been found. As a result of the excellent flow properties and large extent of the storage formation (the aquifer covers some 26,000 km<sup>2</sup>), the magnitude of the pore pressure increase, and hence the geomechanical effects, has been kept very low. [13], [60]–[62]

### 2.7.2 Stresses and strains

The original state of stress in the subsurface is a function of depth, pore pressure and active geological processes. However, in-situ stresses are affected by the pressure and temperature changes that occur during CO<sub>2</sub> injection. [63]

The increased pore pressure results in the volumetric expansion of the reservoir through a decrease in effective stresses. Because the ground surface is unconstrained, total vertical stress remains relatively insensitive to pressure variations. On the other hand, the lateral confinement of the reservoir opposes its horizontal expansion, leading to an increase of total horizontal stresses. However, in order for the reservoir-caprock system to remain in equilibrium, the increased  $\sigma_h$  in the reservoir must be counteracted by a decreased  $\sigma_h$  above and below the reservoir (fig. 2.6). This decrease may be sufficient to open tensile cracks within the caprock. Finally, in the post-injection stage, the reservoir contracts as the built-up pressure subsides, and faults that were stabilized by reservoir expansion are now at risk of reactivating. Once pressure has decayed to its new static value however, the reservoir is no longer at risk of geomechanical failure due to internal forces. [20], [63]–[65]

Injection of a cold fluid also induces thermal contraction of the reservoir rock in the near-wellbore region, where the resulting horizontal total stress reduction may result in shear failure. While the opening of fractures in the near-wellbore zone is beneficial to injectivity as it increases permeability, there is concern that thermal contraction may destabilize fractures in the caprock, jeopardizing seal integrity. As discussed by Vilarrasa (2016), the reduction in horizontal stress resulting from injection of a cold fluid benefits caprock stability in normal-faulting stress regimes (by decreasing the propensity of shear failure), while it decreases caprock stability in strike-slip and reverse faulting stress regimes. [66] The magnitude of the horizontal total stress reduction depends on the thermal expansion coefficient of the rock, where a higher coefficient leads to an earlier failure. [67]

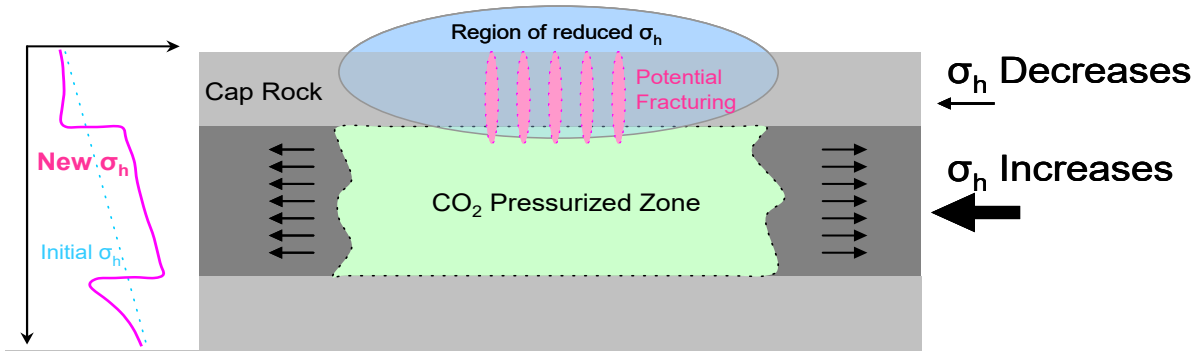


**Figure 2.6** – Horizontal stress response to fluid injection. [57]

If the reservoir is assumed to react elastically to the change in pore pressure, the variation of total horizontal stress under uniaxial conditions can be written as per the theory of poroelasticity:

$$\Delta\sigma_h = \frac{\nu}{1-\nu}\Delta\sigma_v + \left(1 - \frac{\nu}{1-\nu}\right)\alpha\Delta p, \quad (2.9)$$

where  $\nu$  is Poisson's ratio,  $\Delta\sigma_v$  is the change in total vertical stress,  $\alpha$  is Biot's coefficient, and  $\Delta p$  is the pore pressure variation. [63]

Note that  $\Delta\sigma_v$  is equal to zero if the overburden is relatively compliant, and/or if the reservoir's lateral extent is much greater than its thickness. If injection has caused reactivation of faults, the total vertical stress may vary slightly.

The volumetric expansion of the aquifer may be measured as heave on the surface or seafloor, as well as bending of the caprock above the injector. [13], [21], [22], [28], [58], [68]–[70] Heave phenomena are amplified at higher injection rates. [70] If the fluid pressure rises to a high enough level, for example when injecting at high rates, irreversible geomechanical effects could be triggered, such as the creation of hydraulic fractures or reactivation of critically-stressed faults due to shear and fault slippage. As faults often have strongly heterogeneous geomechanical properties, the exact overpressure that will cause the fault to slip may be difficult to estimate. [21], [28], [67]–[69], [71] The changes in the state of stress also affects multiphase flow properties of the porous medium, as some petrophysical properties such as permeability are sensitive to pressure. [13]

Finally, note that the stress-strain relationship of a particular formation depends on many factors such as lithology, degree of cementation and cementing material, fluid saturation, rock and fluid compressibilities, reservoir pressure and temperature, porosity and permeability. As a result, a given overpressure will result in different geomechanical effects depending on the considered reservoir and caprock system. [41]

### 2.7.3 Fault reactivation

The increase in total horizontal stresses induced by injection may either stabilize or destabilize faults, depending on their orientation. CO<sub>2</sub> injection has a destabilizing effect on reverse faults, favouring slippage, and a stabilizing effect on normal faults; consequently, extensional

stress regimes are more conducive to  $CO_2$  injection. [72] However, in the case where  $CO_2$  has migrated into the fault spaces, the resulting decrease of normal fracture effective stress may cause either type of fault to slip. For a given fault orientation, fault slippage happens if

$$\tau/\sigma_n > \mu, \quad (2.10)$$

with  $\tau$  and  $\sigma_n$  being respectively

$$\tau = \frac{\sigma_v - \sigma_h}{2} \sin(2\theta), \quad (2.11)$$

$$\sigma_n = \frac{\sigma_v + \sigma_h}{2} + \frac{\sigma_v - \sigma_h}{2} \cos(2\theta), \quad (2.12)$$

where  $\sigma_v$  is the vertical stress,  $\sigma_h$  is the minimum principal stress, and  $\theta$  is the fault dip angle. [22], [25]

Note that the effect of the pressure increase can be seen far beyond the extent of the  $CO_2$  plume, as the pressure disturbance travels further than the plume. [7], [42] Furthermore, geomechanical effects themselves can happen beyond the extent of the pressure disturbance. [21] As a result, if the pressure disturbance encounters dormant tectonic faults, it poses the risk of reactivating them even at great distances from the injector.

Slippage of geological layers along pre-existing faults may cause felt seismic events (fig. 2.7). While most events occur in the domain of microseismicity, between  $M_w - 3$  and 0 (moment magnitude scale), fault slippage has the potential to trigger events of magnitude greater than  $M_w 3$ , which might compromise the long-term seal integrity of the storage site. [13], [21], [22], [28], [71] Depending on the orientation of existing faults, even a small increase of the pore pressure could trigger seismic events. [55] Since faults are activated upon being reached by the pressure front, and this front is travelling ahead of the plume, seismic events will be recorded before leakage happens. In consequence, stopping injection once seismicity is recorded may suffice to prevent leakage.

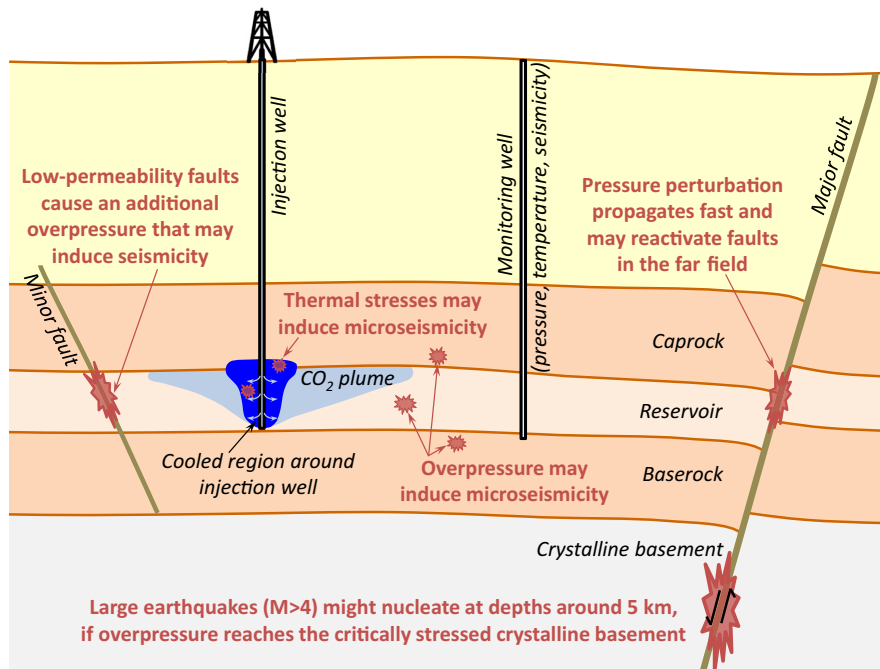


**Figure 2.7** – Possible causes of induced seismicity related to CO<sub>2</sub> geological storage. [66]

## 2.8 CO<sub>2</sub> leakage mechanisms

In general, CO<sub>2</sub> leakage potential is linked to the total fraction of mobile CO<sub>2</sub> in the aquifer. [35] There are several ways through which storage integrity may be compromised (fig. 2.8), among which:

- diffusive loss through the caprock;
- leakage through pores after the capillary entry pressure is overcome (breaching);
- leakage through pre-existing but initially closed faults and fractures;
- caprock fracturing due to tensile cracks formation;
- leakage through degraded or inappropriately abandoned wells. [11], [21], [59]

## 2 CO<sub>2</sub> injection in deep saline aquifers

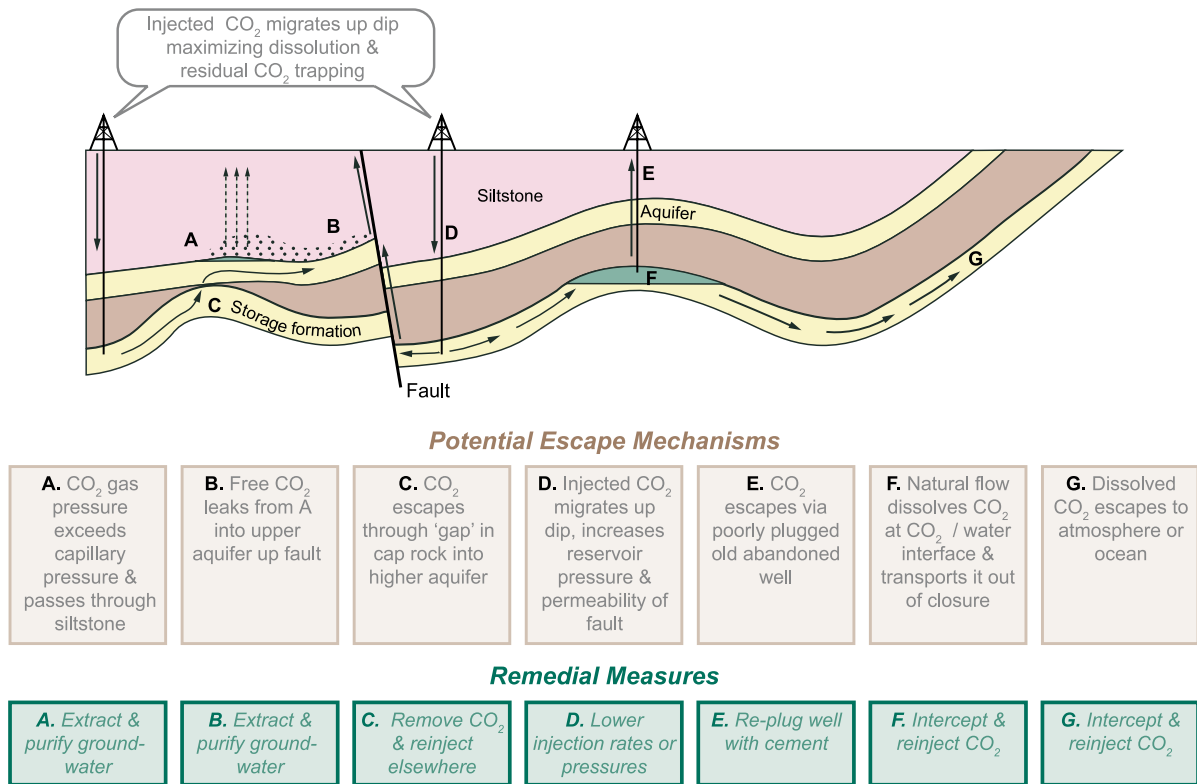


**Figure 2.8** – Possible CO<sub>2</sub> leakage mechanisms and remedial measures. [8]

### 2.8.1 Caprock breaching

Originally, the caprock is able to sustain a certain pressure discontinuity at the CO<sub>2</sub>-brine interface. Once buoyancy pressure overcomes the capillary entry pressure, CO<sub>2</sub> invades the caprock (fig. 2.9). If there are conductive paths through the caprock, CO<sub>2</sub> will leak into the upper aquifers; otherwise, a pressure gradient is maintained across the seal. [21]

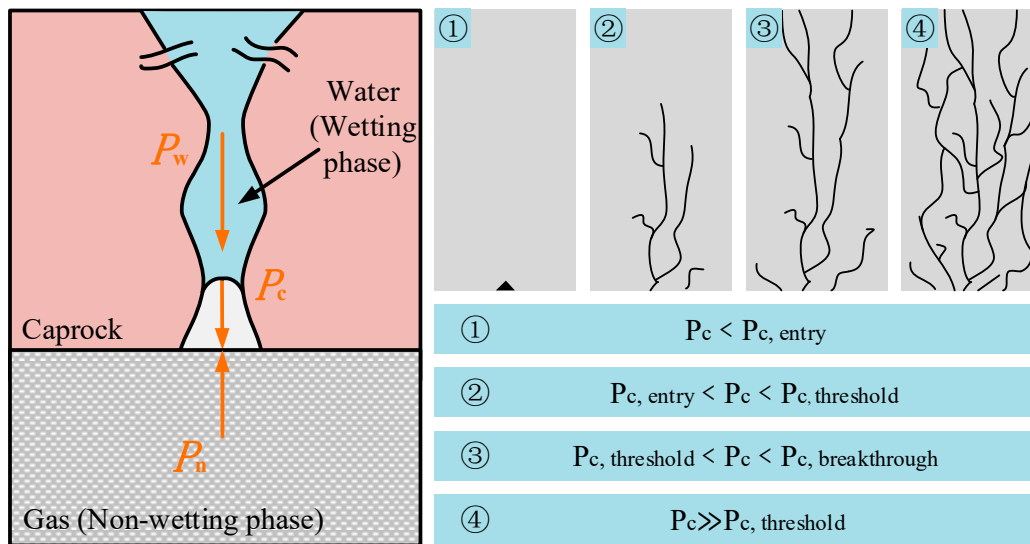


**Figure 2.9** – Mechanism of gas breakthrough across the caprock. [73]

### 2.8.2 Caprock fracturing

Fault opening and reactivation is one of the greatest risks posed to storage integrity. [13], [59] Fractures can open due to tensional forces if the fluid pressure exceeds the fracture pressure, creating pathways that allow free-phase CO<sub>2</sub> to flow through the caprock, driven by buoyancy. [21], [37], [56], [59] Alternatively, if the applied shear stress overcomes the resistant force of the fracture asperities, shear opening of fractures can occur. [7]

To avoid fracturing of the caprock, the pore pressure gradient should never be allowed to exceed the caprock fracture gradient, which may be evaluated from leak-off tests performed above the intended injection point. [21] There are several possible scenarios which may induce a fracture (fig. 2.10):

- in case (a), a crack is formed when the tensile stress exceeds the tensile strength of the material;
- in case (b), the fracture occurs due to a compressional load and is parallel to the loading direction;
- in case (c), the crack initiates at the top of the block (which is under tensional load) and propagates to the bottom (which is under compressional load);
- case (d) represents a general scenario, where the block is subject to loads from all sides and fails mainly due to shear. [35]

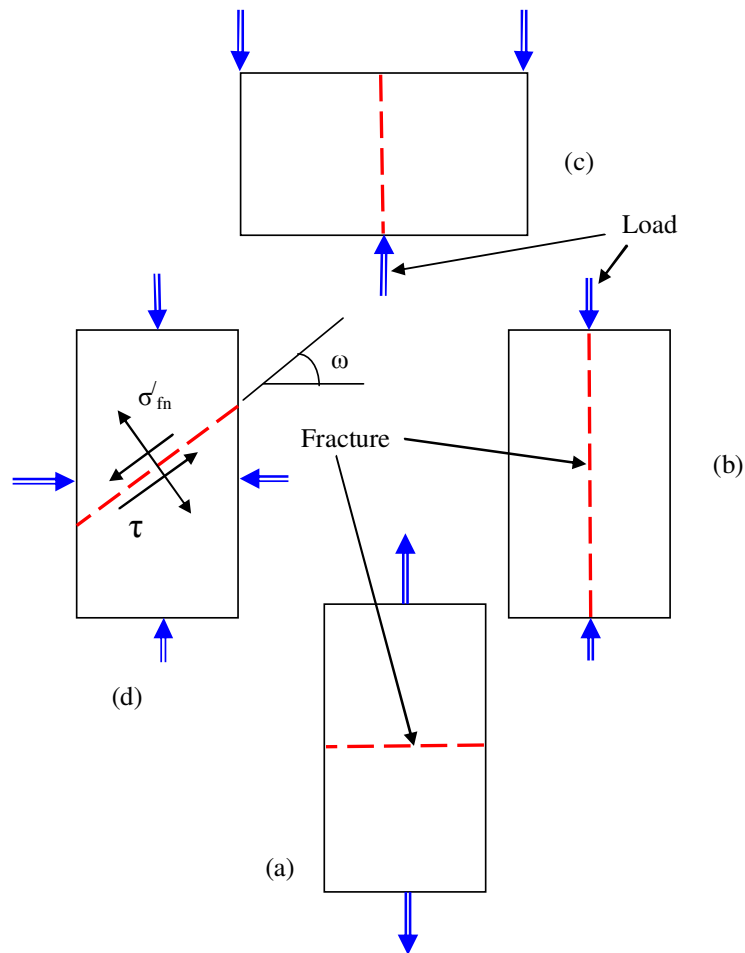


**Figure 2.10** – Possible mechanisms of crack onset in a block subjected to loads. [35]

Note that when investigating caprock failure, horizontal fractures are hardly relevant as they do not affect vertical transmissibility; the critical fractures are those that are vertical (subject to tensile opening) or subvertical (subject to shear opening). [35]

### 2.8.3 Leakage through wells

Due to the corrosive properties of CO<sub>2</sub> on cement and the intended life of injection wells, the materials used to line wells must have extremely strict specifications in order to avoid leakage because of cement degradation. [21] The expansion of the reservoir against the overburden may also induce shear stresses in the wellbore, potentially triggering casing failure. [13]

## 2.9 Tensile opening of fractures

The stress acting on a volume of rock due to the weight of the overburden is partially sustained by the fluid present inside its pores. For materials with incompressible grains, *i.e.* soils, this

relationship can be described using Terzaghi's law:

$$\sigma_{ij} = \sigma'_{ij} + p\delta_{ij}, \quad (2.13)$$

where  $\sigma_{ij}$  is the total stress or overburden stress tensor,  $\sigma'_{ij}$  is the effective stress tensor, *i.e.* the stress sustained by the rock grains acting on each other,  $p$  is the pore pressure, *i.e.* the pressure exerted by the fluid on the rock grains, and  $\delta_{ij}$  is the Kronecker delta or identity matrix  $\mathbf{I}$ . [58], [70], [74], [75]

Furthermore, a generalization of Terzaghi's law applicable to rocks can be written as

$$\sigma_{ij} = \sigma'_{ij} + \alpha p\delta_{ij}, \quad (2.14)$$

where  $\alpha$  is the Biot-Willis coefficient, which is a dimensionless scaling factor representing the interaction between pore pressure and effective stress. Real rocks may have a Biot coefficient ranging between 0.7 and 1.0, with lower values at higher depths. [74], [76], [77] Biot's coefficient is defined as

$$\alpha = 1 - \frac{K'}{K_s}, \quad (2.15)$$

where  $K'$  is the drained bulk modulus of the rock skeleton, and  $K_s$  the bulk modulus of the solid grains.

Tensile failure (or hydraulic fracturing) is assumed to occur when the pore pressure exceeds the least principal effective stress by an amount larger than the tensile strength of the rock, or

$$p \geq \sigma'_3 + T_0, \quad (2.16)$$

where  $\sigma'_3$  is the least principal effective stress, and  $T_0$  is the tensile strength. The tensile strength of sedimentary rocks is of a few MPa at most, and is often assumed to be zero. [58], [74]

Once the failure criterion is reached, tensile failure occurs and the fracture propagates perpendicularly to the direction of the least principal effective stress  $\sigma'_3$ . [58] If the pore pressure is reduced such that the tensile failure criterion is no longer satisfied, the fracture will begin to close but may remain partially open if the fracture walls have experienced shear displacement and are no longer interlocking. [78]

## 2.10 Monitoring of geomechanical effects

A number of methods are available to quantify the geomechanical changes resulting from  $CO_2$  injection (fig. 2.11). Compaction or expansion of the reservoir and overburden can be correlated from seismic data through travel time shifts. Changes in seismic anisotropy (indicated by shear wave splitting) can also indicate rotation of the stress tensors during deformation. Alternatively, subsidence or heave can be measured at the surface using satellite imaging techniques such as InSAR (interferometric synthetic aperture radar) or GPS surveying. For subsea storage sites, where satellite imaging is not possible, tiltmeters can be placed either in the borehole or at the surface to measure the change in inclination resulting from uplift. [13], [61], [79], [80]

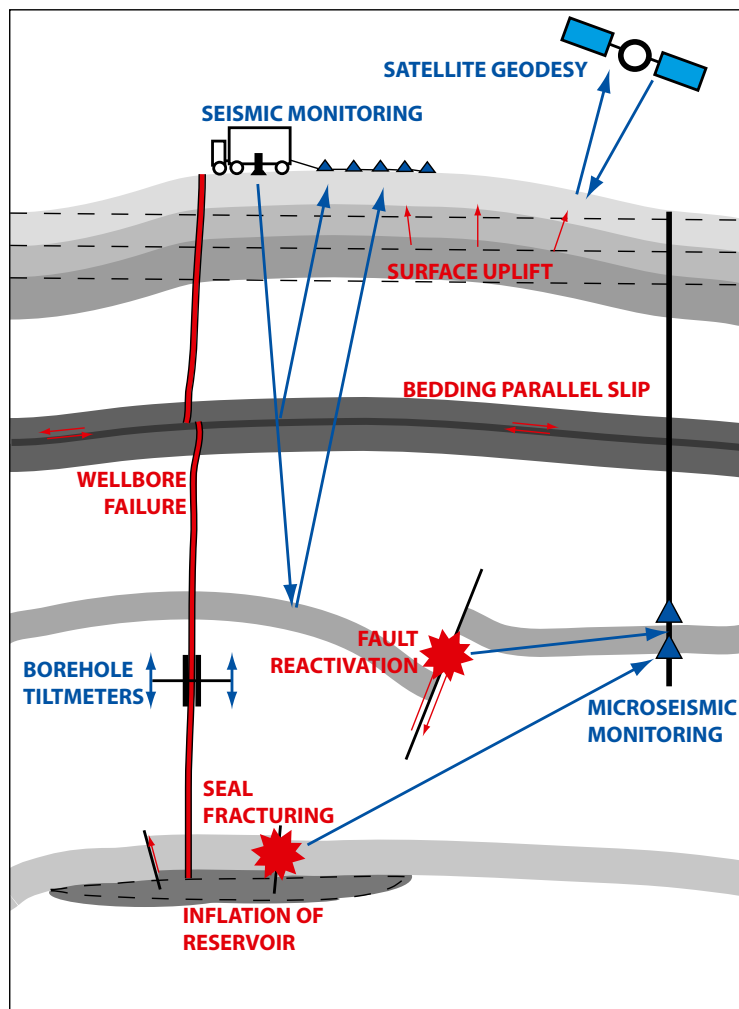


**Figure 2.11** – Possible monitoring techniques for CO<sub>2</sub> geological storage. [13]

Additionally, when hydrogen-deficient CO<sub>2</sub> displaces hydrogen-rich water or hydrocarbons, the change in saturation can be observed in neutron-porosity logs as an increase in hydrogen index. [81]

Finally, if significant overpressures are expected, *i.e.* for small reservoirs with low permeability, induced microseismicity may be recorded using geophones placed either in monitoring wells or at the surface. [13], [61]

## 2.11 Geomechanical characterization of potential storage sites

In order to properly assess the geomechanical behavior of a particular storage formation, a wide range of data must be collected, namely:

- in-situ stresses;
- rock strength (compressive shear strength and tensile strength);

- rock deformation properties (elastic constants);
- rock thermal properties (thermal expansion coefficient);
- presence, location, extent, orientation and strength of discontinuities;
- initial pore pressure and temperature distributions;
- expected pore pressure and temperature changes during operation. [27]

In tectonically-stable depositional environments, and where strata can be considered as mostly flat (“layer-cake” stratigraphy), the overburden stress can reasonably be assumed to be a principal stress. Consequently, the in-situ state of stress can be fully characterized by knowing  $\sigma_v$ ,  $\sigma_H$ ,  $\sigma_h$  and the azimuth of either one of the horizontal stresses, being the two horizontal stresses orthogonal. Knowing the in-situ state of stress and elastic properties of the storage formation is necessary to estimate the reservoir fracture pressure, and thus the maximum allowable injection pressure. [20], [27]

Regarding seal integrity evaluation, additional data is needed from the caprock, typically obtained from core samples:

- permeability and capillary entry pressure;
- mineralogical composition, to assess the potential for geochemical reactions with CO<sub>2</sub>;
- pore water analyses, to determine the origin of the pore fluid;
- reactivity of the caprock to CO<sub>2</sub> and brine;
- presence of faults and facies changes within and above the caprock, determined from seismic sections;
- properties of discontinuities within and above the caprock, to evaluate tightness and leakage potential. [20]

## 3 Barton-Bandis model of fracture closure

### 3.1 Generalities

Joints that have not been healed and mineralized are particularly affected by changes in the state of stress as they have lower stiffness and shear strength than the rock matrix. Additionally, unfilled joints have very low or null tensile strength and cohesion. As a result, most of the elastic deformation in a rock is the result of joint slippage and closure, in particular that of pre-existing fractures since their mechanical properties are lower than those of the intact rock. [65], [82]–[85]

Several empirical models are available to model changes in matrix and fracture permeability due to geomechanical effects. The Barton-Bandis hyperbolic fracture closure model is one of the most widely used models to represent tensile and shear failure of fractures, for example in hydraulic fracturing. [68], [86] This empirical model is based on extensive loading and unloading tests of fractures from many different outcropping rock lithologies (64 joint samples of 5 different rock types, *i.e.* slate, dolerite, limestone, siltstone and sandstone). [78], [84], [87]–[90]

According to the Barton-Bandis model, the parameters needed to fully characterize joint behavior both in shear and in compression are as follows:

- (1) JRC, joint roughness coefficient (dimensionless);
- (2) JCS, joint compressive strength (kPa);
- (3)  $\sigma_c$ , unconfined compression strength of the rock adjacent to the joint wall (kPa);
- (4)  $\phi_r$ , residual friction angle (deg);
- (5)  $E$ , mechanical fracture aperture (m);
- (6)  $e$ , conducting or hydraulic fracture aperture (m). [90]

### 3.2 Normal fracture closure behavior

The Barton-Bandis model considers that fracture walls are irregular with a given roughness. Fractures are naturally present in rock due to tensional, shear or mixed brittle failure. When an open fracture is subjected to a normal stress that causes it to close, and if the fracture was subjected to a shear stress that resulted in shear displacement during its past history, a residual aperture can be observed due to the fact that the fracture irregularities no longer interlock, and full joint closure can no longer be reached. Bandis *et al.* (1983) proposed a

hyperbolic function to model fracture closure using a few simple measurements from index tests. [78], [82], [83], [87], [91], [92]

Closure of a fracture due to normal stress causes the asperities on the fracture walls to come into contact. The contact area increases as the fracture closes and asperities deform, which leads to an increased normal stiffness and a decreased permeability. [87], [93] As  $\sigma_n$  increases, joint closure becomes almost exclusively dependent on the deformability of the asperities. [82] This behavior is independent of the rock and joint type. Bandis *et al.* (1983) found that the relationship between normal stress and fracture closure is strongly non-linear, and they fitted their empirical findings with

$$\sigma'_n = \frac{k_{ni} \cdot V_j}{1 - V_j/V_m} \text{ or } V_j = \frac{\sigma'_n}{k_{ni} + \sigma'_n/V_m}, \quad (3.1)$$

where  $\sigma'_n$  is the effective normal stress (positive in compression),  $k_{ni}$  is the initial normal fracture stiffness, *i.e.* the rate of change of the normal stress with respect to the normal displacement,  $V_j$  is the joint normal closure at a given state of normal stress (positive in closure), and  $V_m$  is the maximum normal closure, *i.e.* the difference between the maximum opening and the smallest aperture. [82], [87]–[89]

The normal, stress-dependent mechanical fracture aperture is related to fracture closure according to

$$E_n = E_0 - V_j, \quad (3.2)$$

where  $E_0$  is the initial mechanical joint aperture, or

$$E_0 = \frac{\text{JRC}}{5} \left( 0.2 \frac{\sigma_c}{\text{JCS}} - 0.1 \right), \quad (3.3)$$

with the relative alteration  $\sigma_c/\text{JCS}$  being a dimensionless number. [82], [85], [89]–[92], [94] Mechanical aperture usually varies from 0.05 to 1 mm. [95]

For unaltered or unweathered joint surfaces, the JCS is equal to  $\sigma_c$  and the mechanical aperture becomes a function of surface roughness only, or

$$E_0 = \frac{\text{JRC}}{50}. \quad [85], [90]–[92] \quad (3.4)$$

Maximum fracture closure  $V_m$  and initial normal fracture stiffness  $k_{ni}$  are a function of initial aperture  $E_0$ , joint compressive strength JCS and joint roughness coefficient JRC, which are experimental parameters proposed by Barton and Choubey (1977) to characterize joint walls.  $V_m$  and  $k_{ni}$  can be estimated from laboratory experiments as

$$V_m = -A_v - B_v \cdot \text{JRC} - C_v \left( \frac{\text{JCS}}{E_0} \right)^{-D_v}, \quad (3.5)$$

$$k_{ni} = -A_k - B_k \cdot \text{JRC} - C_k \left( \frac{\text{JCS}}{E_0} \right), \quad (3.6)$$

where  $A \sim D$  are empirical constants obtained from regression on laboratory experiments.

The factors influencing the behavior of joint normal stiffness with fracture closure are the initial contact area, joint wall roughness, strength and deformability of the asperities, and properties of the infilling material if present. [82]

### 3.3 Joint roughness coefficient

#### 3.3.1 Generalities

The JRC is a measure of the slip angle of a jointed rock sample, and is defined for unweathered joints as

$$\text{JRC} = \frac{\tan^{-1}(\tau/\sigma_n) - \phi_b}{\log(\sigma_c/\sigma_n)}, \quad (3.7)$$

where  $\tau$  is the peak shear strength under a normal stress  $\sigma_n$ , and  $\phi_b$  is the basic friction angle of the slip surface. [91], [96]

For weathered joints,  $\sigma_c$  is replaced by the JCS such that

$$\text{JRC} = \frac{\tan^{-1}(\tau/\sigma_n) - \phi_b}{\log(\text{JCS}/\sigma_n)}. \quad (3.8)$$

Most commonly, the JRC is either estimated from profile matching or measured with the amplitude-over-length (a/L) method. [91] It typically takes values between 0 and 20, with 0 being a smooth and planar surface and 20 a very rough and undulating surface. [7], [94], [95], [97]

#### 3.3.2 JRC determination

##### Profile matching

Profile matching was proposed by Barton and Choubey (1977) and is the simplest empirical method of evaluating the JRC. [94] The considered joint is physically compared with a set of ten roughness profiles, each corresponding to a certain range of JRC values (fig. 3.1).



An abacus can also be used to obtain the corresponding JRC value from the amplitude measurement (fig. 3.2).

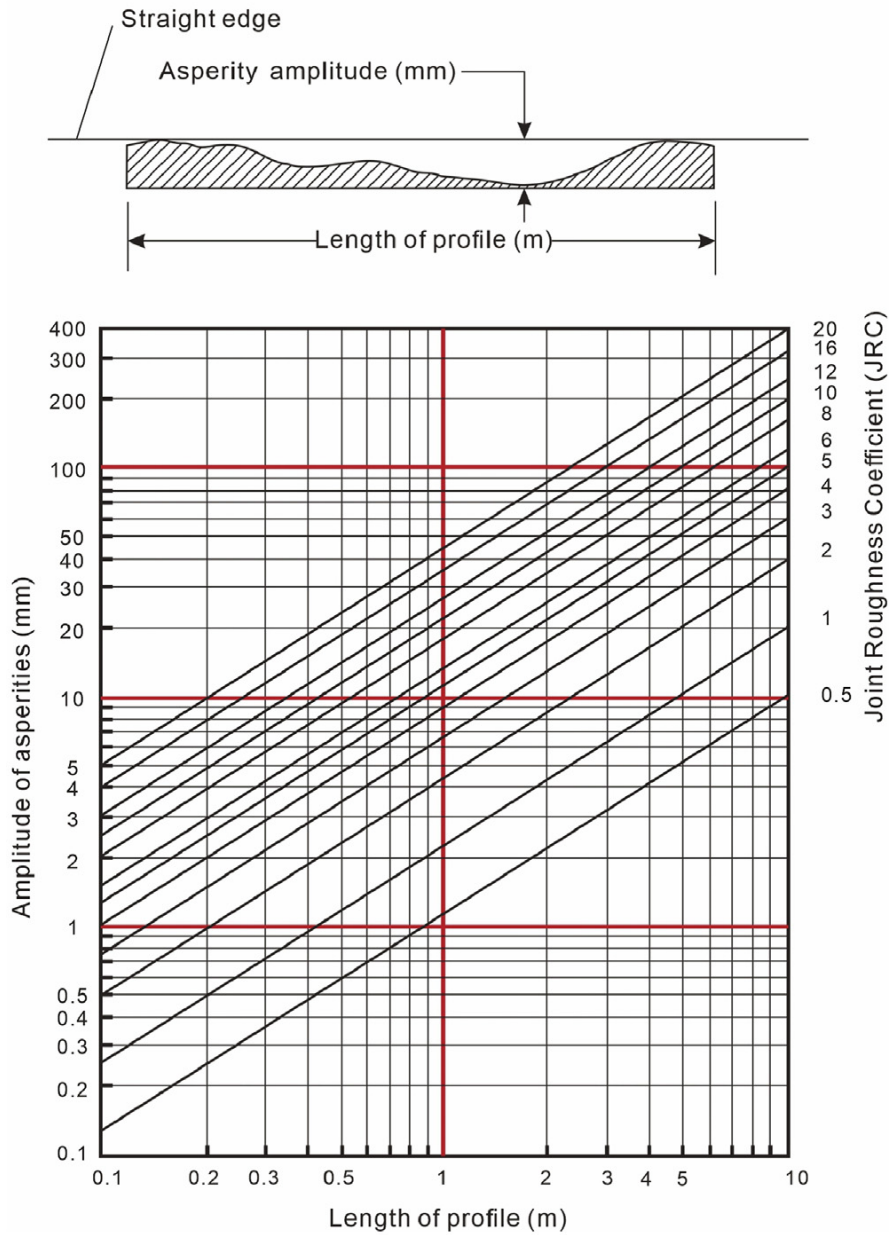


**Figure 3.2** – Amplitude-over-length method abacus for JRC correlation. [99]

An alternative  $a/L$  method has also been proposed to address the problem of excessive JRC values when using small-scale samples:

$$JRC = 49 \exp(29L_0/450L) \arctan\left(\frac{8a}{L}\right), \quad (3.10)$$

where  $L_0$  is the sample length of the joint at laboratory scale (100 mm). [99]

**Tilt tests**

Performing tilt tests on jointed cores (fig. 3.3) is a more reliable method of indirectly obtaining the JRC, which is calculated according to

$$JRC = \frac{\alpha - \phi_r}{\log(JCS/\sigma'_{n0})}, \quad (3.11)$$

where  $\alpha$  is the tilt angle at which sliding occurs,  $\sigma'_{n0}$  is the effective normal stress acting across the joint when sliding occurs (*i.e.* the weight of the upper portion of the sample, corrected for the sliding angle, divided by the joint area), and  $\phi_r$  is the residual friction angle. [85], [90], [98], [100] It should be noted that for residual non-dilatant joint surfaces, where the JRC is equal to zero,  $\alpha$  is equal to  $\phi_r$ . [90]

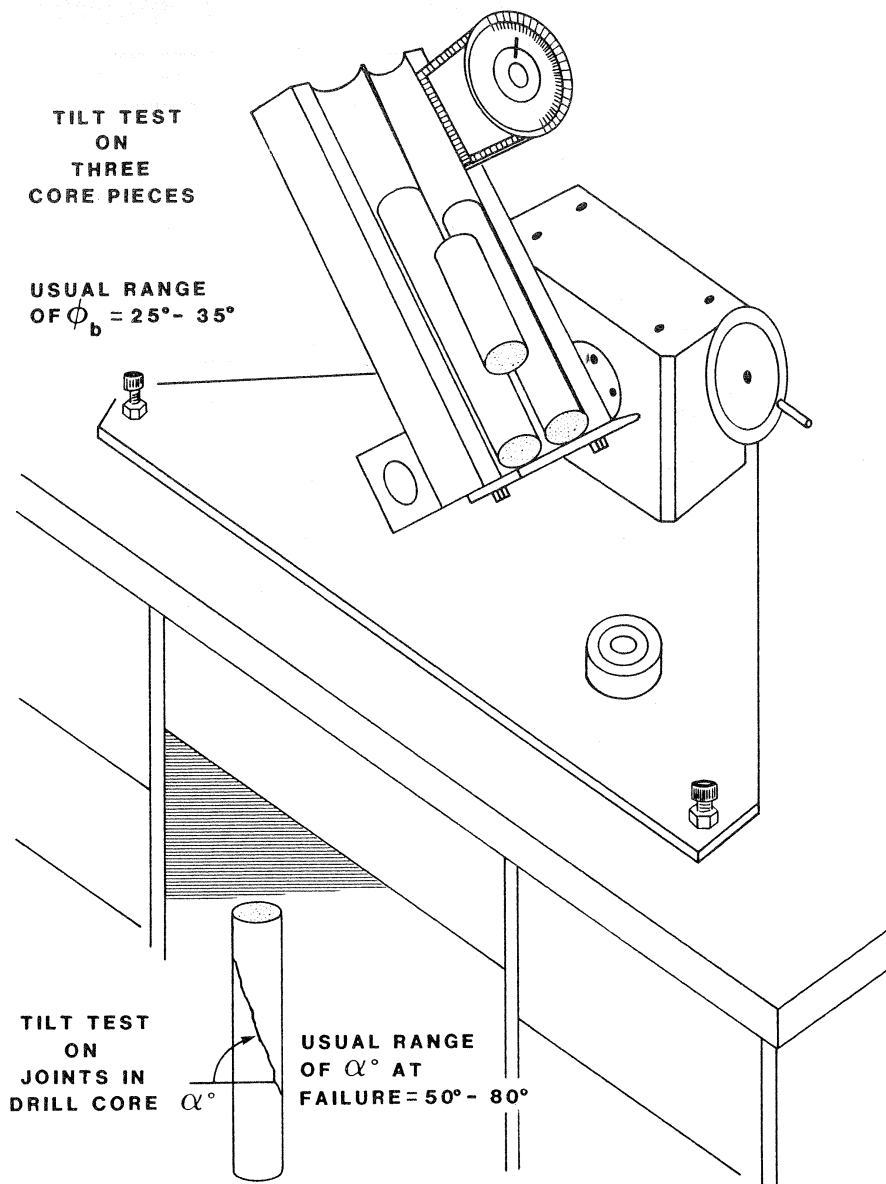


**Figure 3.3** – Representation of a tilt test on faulted core. [98]

Being the residual friction angle  $\phi_r$  very difficult to determine experimentally, an empirical approach has been proposed, in which

$$\phi_r = (\phi_b - 20) + 20 \frac{r}{R}, \quad (3.12)$$

where  $\phi_b$  is the minimum friction angle of flat, unweathered rock surfaces (such as those resulting from a saw cut) obtained from tilt tests,  $r$  is the mean Schmidt rebound number on saturated and weathered joint surfaces, and  $R$  is the mean Schmidt rebound number on dry, unweathered rock surfaces. [90], [98]

Usual values for  $\phi_r$  are 20 to 35° (respectively strongly weathered and unweathered), while the basic angle of internal friction  $\phi_b$  typically ranges between 25 and 35°. [95], [96], [98]

### 3.4 Joint compressive strength

The most widely used technique to estimate the JCS is by employing the Schmidt hammer, with

$$\log \text{JCS} = 0.0008 \cdot \gamma \cdot R + 1.01, \quad (3.13)$$

where  $\gamma$  is the mean unit weight of joint wall material, and  $R$  is the mean rebound number from the L-type Schmidt hammer on dry joint surfaces. [82], [85]

Other methods have been proposed by Barton (1978). [101]

### 3.5 Scale-dependence

Both the JRC and the JCS are scale-dependent. Consequently, measurements obtained from small-scale laboratory samples must be extrapolated to in-situ block sizes. This is done using two empirical correlations proposed by Barton (1982):

$$\text{JRC}_n = \text{JRC}_0 \left( \frac{L_n}{L_0} \right)^{-0.02\text{JRC}_0}, \quad (3.14)$$

$$\text{JCS}_n = \text{JCS}_0 \left( \frac{L_n}{L_0} \right)^{-0.03\text{JRC}_0}, \quad (3.15)$$

where the  $n$  subscript refers to in-situ block sizes, and the 0 subscript refers to 100 mm core samples. [85], [98], [102]

### 3.6 Hydraulic fracture aperture

When computing fracture permeability, the relevant section is that which is open to flow, *i.e.* the hydraulic or conducting fracture aperture  $e$ . It is defined as the aperture of a smooth conduit with the same permeability as the real fracture. [93] The hydraulic aperture is smaller

than the mechanical aperture  $E$  because the asperities of the joint walls can block or impede fluid motion. [85], [88]

Note that the larger the fracture opening, the closer is  $e$  to  $E$ . The exact ratio between  $e$  and  $E$  depends on the amount of shear displacement experienced by the joint (shear-induced dilation). [78], [92] In some cases, shear-induced dilation or tensile opening can open the fracture enough that both values become equal. [102] Usual values for  $e$  are 0.005 to 1 mm. [95]

Hydraulic aperture is defined through an empirical relation, and depends on whether the fracture is critically stressed:

$$e = \begin{cases} \frac{E_n^2}{\text{JRC}^{2.5}}, & u_s/u_{\text{peak}} \leq 0.75 \text{ (i.e. normal closure);} \\ E_n^{0.5} \text{JRC}_{\text{mob}}, & u_s/u_{\text{peak}} \geq 1 \text{ (i.e. shear closure);} \end{cases} \quad (3.16)$$

where  $\text{JRC}_{\text{mob}}$  is the mobilized JRC (dimensionless),  $u_{\text{peak}}$  is the peak shear displacement and  $u_s$  the actual shear displacement, with the ratio  $u_s/u_{\text{peak}}$  being dimensionless. In the case where  $0.75 \leq u_s/u_{\text{peak}} \leq 1$ ,  $e$  is interpolated linearly, and the first case is only valid for  $E/e \geq 1$ . [85], [92], [94], [97], [98], [102]

Note that the findings of Lavrov (2016) and Chen *et al.* (2000) are inconsistent with Barton's formulas for hydraulic aperture. [93], [103]

The term  $u_s/u_{\text{peak}}$  is a measure of the shear displacement experienced by the joint and indicates whether the fracture is critically stressed. Critically stressed fractures are defined as fractures where the actual shear displacement is larger than peak shear displacement, *i.e.*  $u_s/u_{\text{peak}} \geq 1$ . This ratio depends mainly on the block size, where fractures with a larger block size are more likely to be critically stressed. [91], [92], [104]

Generally, the hydraulic aperture  $e$  is roughly equal to to the mechanical aperture  $E$  for critically stressed fractures, and close to zero for non critically stressed fractures. In this second case, the slight mismatch between the asperities of the fracture walls may result in a small contribution to flow, *i.e.* a low value of  $e$ . [91]

Actual shear displacement  $u_s$  is obtained from numerical modelling, while peak shear displacement  $u_{\text{peak}}$  can be estimated as

$$u_{\text{peak}} = \frac{B_n}{500} \left( \frac{\text{JRC}_n}{B_n} \right)^{0.33}, \quad (3.17)$$

where  $B_n$  is the block size (*i.e.* the spacing of the fracture set that intersects the fracture of interest), and  $\text{JRC}_n$  is the JRC corresponding to block size  $B_n$ . [91]

### 3.7 Mobilization of roughness during shear

The JRC values considered previously have been peak values. The mobilized JRC ( $\text{JRC}_{\text{mob}}$ ) is a measure of the roughness which is actually mobilized during shear displacement (pre-peak),

or the roughness which is destroyed post-peak. [90], [100], [102] The ratio  $JRC_{\text{mob}}/JRC_{\text{peak}}$  can be calculated from the following empirical relationship:

$$\frac{JRC_{\text{mob}}}{JRC_{\text{peak}}} = -\frac{\phi_r}{i}, \text{ and } i = JRC_{\text{peak}} \cdot \log \frac{JCS}{\sigma'_n}, \quad (3.18)$$

where  $\phi_r$  is the residual friction angle,  $\sigma'_n$  is the normal stress acting across the joint, and the ratio  $JCS/\sigma'_n$  is dimensionless. [90], [98]

### 3.8 Fracture permeability

The fracture permeability of each segment is computed as

$$k_f = \frac{e^2}{12} \cdot [65], [105] \quad (3.19)$$

Fracture permeability usually presents hysteresis in loading-unloading cycles, in which  $k_f$  after unloading is higher than it was at the same stress level during loading. [93] The contribution of fracture flow to total flow depends on the ratio between fracture and matrix permeability, where a higher matrix permeability equals a lower contribution of fracture flow. [91]

Equation (3.19) can be used to directly measure hydraulic fracture aperture  $e$  from borehole pumping tests. Packers are set to isolate individual joints, and the pumping test is interpreted as

$$e = \sqrt{12k_f} \cdot [90] \quad (3.20)$$

### 3.9 Model range of validity

The Barton-Bandis model is a proven method of characterizing rock joint behavior, and has been extensively used in the field. The necessary parameters can be estimated from several possible methods involving simple index tests, and have an actual physical meaning. [84] The model is able to describe the behavior both of stiff fractures (where stiffness is initially high and slowly increases with normal stress) and of compliant fractures (which are highly compressible at low values of stress, and become very stiff as closure approaches  $V_m$ ). [87]

In theory, the Barton-Bandis model is not applicable to cases where fractures of different dimensions are present, due to the scale-dependence of parameters such as the JRC and JCS. Even in this case, it often provides a better empirical fit compared to other models. [88] However, the model is only valid for positive values of effective normal stress, and is not applicable at high values of normal stress, where negative apertures might be predicted. Since the Barton-Bandis model does not consider the impact of diagenesis, it is theoretically not applicable to carbonates and other chemically reactive rocks, as chemical reactions may modify fracture aperture and roughness. [83], [92] In addition, the original model is based on fracture apertures ranging between 0.1 and 0.6 mm, while some studies have found rocks with fracture apertures as low as 0.002 mm. [83]

Finally, note that when a field is first developed, information regarding joint roughness and aperture is rarely available, as acoustic or electric logs do not possess the necessary resolution to provide reliable data. As a result, this data is often gathered from outcrop samples, which may not represent properties at depth. [93]

## 4 CMG GEM reservoir simulator

### 4.1 Generalities

CMG GEM is a compositional reservoir simulator based on the finite volume method (FVM) and equipped with a geomechanical solver. It uses either the Peng-Robinson (PR) or the Soave-Redlich-Kwong (SRK) cubic equations of state to model fluid properties (component composition, fugacity in the gas phase, gas density and compressibility of each phase). Material balance equations are solved at each block face using the finite difference method (FDM). [4], [12], [37], [60], [79], [85], [106]–[109]

Fugacities of the components in the gas phase are calculated from the EoS, and fugacities in the water phase are modelled with Henry's law. Harvey's correlations are used to calculate Henry's constants when temperature and salinity vary throughout the aquifer. [37], [60], [65], [79], [108]

Gas viscosity is determined from the component viscosities using mixing rules, while aqueous phase viscosity is calculated from the Kestin *et al.* (1981) correlation. For gas viscosity predictions, the Pedersen correlation can be used if experimental data is available, or, alternatively, the HZYT or Jossi, Stiel and Thodos (JST) models can be applied. Note that at high pressures, the Pedersen correlation shows better results than the JST model. Finally, GEM uses Pénéoux's volume shift to improve molar volume predictions of both PR and SRK EoS. Aqueous phase density is calculated from the Rowe and Chou (1970) correlation. [37], [60], [79]

Purely hydraulic simulators assume non-deformable reservoirs, where the pore volume is variable but the bulk volume is constant, *i.e.* the gridblocks maintain a constant shape. These simulators usually incorporate correlations based on rock compressibility in order to replicate some geomechanical effects. True geomechanical modelling supposes that the reservoir is deformable, and both bulk volume and pore volume are variable. [70] This is necessary for investigating effects such as wellbore stability, sand production and hydraulic fractures at the well scale, and fault activation, seal integrity, flow effects, subsidence and heave at the field scale.

### 4.2 Constitutive models for rock behavior

GEM's geomechanics module provides a number of constitutive models, which can be classified into (1) non-linear elastic models, (2) elastoplastic models, (3) elasto-viscoplastic models, and (4) strain hardening and softening models.

For materials that exhibit non-linear elasticity, the rock can obey either a hypoelastic or hyperelastic constitutive model. In the hypoelastic model, the bulk modulus  $K$  and the shear modulus  $G$  vary with mean effective stress, while Poisson's ratio remains constant. This model distinguishes between loading, neutral loading and unloading cases, which happen when the amount of work done  $dW$  is respectively positive, equal to zero, and negative. In the hyperelastic model, both Young's modulus and Poisson's ratio vary with minimum principal stresses. The loading cases are separated depending on the value of shear stress: if current shear stress is higher than the reference shear stress, loading occurs and *vice versa*.

For elastoplastic materials, the possible yield criteria are (1) Mohr-Coulomb, (2) Drucker-Prager, (3) Von Mises, and (4) Tresca. The Mohr-Coulomb and Drucker-Prager criteria are the most widely used for frictional porous materials, *i.e.* soils and rocks, while the Von Mises and Tresca criteria are mainly used for metal plasticity. [37], [108] The Mohr-Coulomb criterion has a larger elastic region than the Drucker-Prager criterion due to the larger friction angle value. When plotted in effective stress space ( $\sigma'_1$ ,  $\sigma'_2$  and  $\sigma'_3$ ), the Mohr-Coulomb criterion has the shape of a hexagon while the Drucker-Prager model takes the shape of a circle, making the latter computationally faster. [37]

Elasto-viscoplastic models are used for materials which exhibit creep behavior. There are two possible creep models, one of which is based on the Drucker-Prager yield surface and the other on the Von Mises surface. Finally, the modified Cam-clay model can be used to model strain hardening or softening.

## 4.3 Basic equations

### 4.3.1 Fluid-flow

The basic equations defining reservoir flow in homogeneous and isotropic porous media are the mass and energy conservation equations, Darcy's fluid-flow law, and cubic equations of state for fluid properties. These equations are developed for a single-phase, single-component flow system and following a continuum approach at the macroscopic scale, where average porosity is constant. The analysis is done on a representative element volume (REV, fig. 4.1). [18], [19], [77], [110], [111]

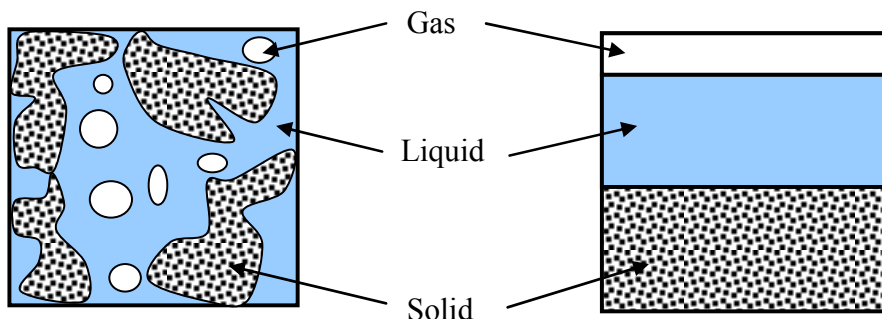


Figure 4.1 – Representative element volume. [111]

In conventional fluid-flow simulators, the bulk volume of reservoir blocks is assumed constant and, as a result,  $\epsilon_v = 0$ . When using a coupled geomechanical simulator, the pore volume calculated by the geomechanical solver is used by the flow simulator to model flow properties; however, this pore volume is not constant in time. In order to account for the change in pore volume in the fluid-flow simulator, true porosity is replaced by a new variable called reservoir porosity  $\phi^*$ , to be used in flow modelling:

$$\phi^* = \frac{V_p}{V_b^0}, \quad (4.1)$$

with  $V_p$  the current pore volume and  $V_b^0$  the initial bulk volume.

The value of porosity calculated by the geomechanical solver (true porosity) is

$$\phi = \frac{V_p}{V_b}, \quad (4.2)$$

where  $V_b$  is the current bulk volume.

From eqs. (4.1) and (4.2), we obtain

$$\phi^* = (1 - \epsilon_v)\phi, \quad (4.3)$$

where  $\epsilon_v$  is the volumetric strain, defined positive in compression. Note that  $\phi^*$  is a function of volumetric strain, which is itself a function of total mean stress, pressure and temperature through the constitutive law for the porous medium. As a result,  $\phi^* = f(p, T, \sigma_m)$ .

Then, the mass conservation equation is defined as

$$\frac{\partial}{\partial t} [\phi \rho_f (1 - \epsilon_v)] = -\nabla \cdot (\rho_f \mathbf{v}) + Q_f, \quad (4.4)$$

where  $\rho_f$  is the fluid density,  $Q_f$  is the mass flow rate of fluid per unit volume,  $\mathbf{v}$  is the fluid velocity tensor, and  $\phi$  is the true porosity.

Equation (4.3) can now be substituted into (4.4) to obtain the mass conservation equation,

$$\frac{\partial}{\partial t} (\phi^* \rho_f) = -\nabla \cdot (\rho_f \mathbf{v}) + Q_f. \quad (4.5)$$

The flow velocity tensor  $\mathbf{v}$  is defined by Darcy's law as

$$\mathbf{v} = -\frac{\mathbf{k}}{\mu} (\nabla p - \rho_f \mathbf{g}), \quad (4.6)$$

where  $\mathbf{k}$  is the absolute permeability tensor,  $\mathbf{g}$  is the gravitational acceleration,  $\mu$  is the fluid viscosity, and  $p$  is the fluid pressure.

Substituting eq. (4.6) into (4.5), we can write the mass flow equation in porous media:

$$\frac{\partial}{\partial t} (\phi^* \rho_f) - \nabla \cdot \left[ \rho_f \frac{\mathbf{k}}{\mu} (\nabla p - \rho_f \mathbf{g}) \right] = Q_f. \quad (4.7)$$

This equation is now in a form such that it can be used by a conventional flow simulator, with geomechanical effects being included through the reservoir porosity variable.

Finally, note that if the reservoir temperature varies with time, the energy conservation equation is used instead of the mass flow equation:

$$\frac{\partial}{\partial t} [\phi^* \rho_f U_f + (1 - \phi^*) \rho_r U_r] + \nabla \cdot \left[ -\rho_f \frac{\mathbf{k}}{\mu} (\nabla p - \rho_f \mathbf{g}) H_f \right] - \nabla \cdot (\kappa \nabla T) = Q_h, \quad (4.8)$$

where  $U$  is the internal energy,  $H$  is enthalpy,  $\kappa$  is the bulk thermal conductivity, and  $T$  is temperature.

### 4.3.2 Deformable porous medium

The fundamental set of equations for solid deformation is based on Terzaghi's effective stress theory and Biot's 3D theory of consolidation. The equations considered in the model are valid in the small strain field, and the material for the geomechanics blocks is considered isotropic and homogeneous. Stresses and strains are defined positive in compression. [19], [111], [112]

As the stressed body is at rest, the sum of forces acting on it must be zero. This is represented by the force equilibrium equation,

$$\nabla \cdot \boldsymbol{\sigma} - \rho_r \mathbf{B} = 0, \quad (4.9)$$

where  $\boldsymbol{\sigma}$  is the total stress tensor,  $\rho_r$  is the solid grain density, and  $\mathbf{B}$  is the tensor of body forces acting through a unit volume. [28], [56], [70], [74], [77]

If  $\mathbf{u}$  is the displacement vector that defines the displacement experienced by a particle between the original and deformed configuration, the gradient of the displacement vector is defined as

$$\nabla \mathbf{u} = \frac{1}{2} [\nabla \mathbf{u} + (\nabla \mathbf{u})^T] + \frac{1}{2} [\nabla \mathbf{u} - (\nabla \mathbf{u})^T], \quad (4.10)$$

where the superscript T refers to the matrix transpose. [19]

The first term on the right-hand side of the equation is equal to the strain tensor  $\boldsymbol{\epsilon}$ , such that

$$\boldsymbol{\epsilon} = \frac{1}{2} [\nabla \mathbf{u} + (\nabla \mathbf{u})^T]. \quad (4.11)$$

Next, we consider Terzaghi's law of effective stress with Biot's coefficient,

$$\boldsymbol{\sigma} = \boldsymbol{\sigma}' + \alpha p \mathbf{I}, \quad (4.12)$$

where  $\boldsymbol{\sigma}'$  is the effective stress tensor, and  $\mathbf{I}$  is the unit tensor or identity matrix.

For a single dimension, the constitutive law between effective stress, strain and temperature, can be defined as

$$\sigma' = E (\epsilon - \beta_r \Delta T), \quad (4.13)$$

where  $E$  is Young's modulus,  $\beta_r$  is the linear thermal expansion coefficient of the solid rock, and  $\Delta T$  is the variation of temperature.

For multiple dimensions, the general constitutive law becomes

$$\boldsymbol{\sigma}' = \mathbf{C} : \boldsymbol{\epsilon} - \eta \Delta T \mathbf{I}, \quad (4.14)$$

where  $\mathbf{C}$  is the tangential stiffness tensor, which in 1D is equivalent to Young's modulus, and  $\eta$  is the thermo-elastic constant, defined as

$$\eta = \begin{cases} \frac{E\beta_r}{(1-2\nu)}, & \text{for 3D and plane strain;} \\ \frac{E\beta_r}{(1-\nu)}, & \text{for plane stress.} \end{cases} \quad (4.15)$$

One way to define the stiffness tensor  $\mathbf{C}$  is through the elastic constants  $E$  and  $\nu$ :

$$\mathbf{C} = \frac{E(1-\nu)}{(1+\nu)(1-2\nu)} \begin{bmatrix} 1 & \frac{\nu}{1-\nu} & \frac{\nu}{1-\nu} & 0 & 0 & 0 \\ \frac{\nu}{1-\nu} & 1 & \frac{\nu}{1-\nu} & 0 & 0 & 0 \\ \frac{\nu}{1-\nu} & \frac{\nu}{1-\nu} & 1 & 0 & 0 & 0 \\ 0 & 0 & 0 & \frac{1-2\nu}{2(1-\nu)} & 0 & 0 \\ 0 & 0 & 0 & 0 & \frac{1-2\nu}{2(1-\nu)} & 0 \\ 0 & 0 & 0 & 0 & 0 & \frac{1-2\nu}{2(1-\nu)} \end{bmatrix}. \quad (4.16)$$

The stress-strain relationship is computed by putting together Terzaghi's law with the rock constitutive law, giving

$$\boldsymbol{\sigma} = \mathbf{C} : \boldsymbol{\epsilon} + (\alpha p - \eta \Delta T) \mathbf{I}. \quad (4.17)$$

Upon substitution of eqs. (4.11) and (4.17) into (4.9), the displacement equation in isothermal conditions is obtained:

$$\nabla \cdot \left[ \mathbf{C} : \frac{1}{2} (\nabla \mathbf{u} + (\nabla \mathbf{u})^T) \right] = -\nabla \cdot [(\alpha p - \eta \Delta T) \mathbf{I}] + \rho_r \mathbf{B}. \quad (4.18)$$

Equations (4.7) and (4.18) are solved for the three primary variables  $\{\mathbf{u}, p, T\}$ .  $\phi^*$  and  $\mathbf{k}$  are intermediate unknowns. In a fully-coupled process, all three variables are solved simultaneously. In an iterative process, the procedure is as follows:

- (1) the geomechanical solver obtains the values of pressure and temperature from the reservoir simulator;
- (2) then, the displacement equation (4.18) is solved and displacements are obtained;
- (3) strains are computed through the strain-displacement relation (4.11);
- (4) the effective stress tensor is calculated through the stress-strain relation (4.17);
- (5) the reservoir simulator computes new values of pressure based the geomechanics data, and then displacements are recomputed;
- (6) the process is repeated until convergence is achieved.

### 4.3.3 Phase equilibrium

The solubility of CO<sub>2</sub> in brine is calculated by considering that the fugacities of CO<sub>2</sub> in the gas and aqueous phase are equal, or

$$f_{\text{CO}_2(\text{g})} = f_{\text{CO}_2(\text{aq})}, \quad (4.19)$$

where the gas fugacity  $f_{\text{CO}_2(\text{g})}$  is obtained from a cubic EoS, and  $f_{\text{CO}_2(\text{aq})}$  is calculated from Henry's law as follows:

$$f_{\text{CO}_2(\text{aq})} = H_{\text{CO}_2(\text{aq})} \cdot y_{\text{CO}_2(\text{aq})}, \quad (4.20)$$

with  $H_{\text{CO}_2(\text{aq})}$  the Henry constant for CO<sub>2</sub> solubility, and  $y_{\text{CO}_2(\text{aq})}$  the mole fraction of CO<sub>2</sub> in the brine. [16], [113]

### 4.3.4 Injector well model

Injectors can be governed by either bottomhole pressure or injection rate. We first define the well injectivity index WI as

$$\text{WI} = \frac{2\pi kh}{\ln(r_e/r_w) + S} \cdot \text{wfrac} \cdot \text{ff}, \quad (4.21)$$

where  $k$  is the effective permeability in the plane normal to the well axis,  $h$  is the gridblock thickness along the well axis,  $r_e$  is the effective radius and  $r_w$  the wellbore radius,  $S$  is the dimensionless skin factor,  $\text{wfrac}$  is the well fraction, and  $\text{ff}$  is the fraction of completion of the well in the gridblock. [108], [114], [115]

Well fraction takes into account the position of the well with respect to the gridblock and is measured as a fraction of a circle; it is defined as

$$\text{wfrac} = \begin{cases} 1, & \text{if the well is located in the center of a gridblock;} \\ 0.5, & \text{if the well is located along a gridblock edge;} \\ 0.25, & \text{if the well is located at a gridblock corner.} \end{cases} \quad (4.22)$$

The effective radius  $r_e$  is written

$$r_e = \text{CC} \sqrt{\frac{A_i}{\text{wfrac}}}, \quad (4.23)$$

where  $\text{CC}$  is a geometric factor and  $A_i$  is the area of gridblock  $i$ , measured perpendicularly to the well axis.

For a gridblock  $i$  containing a well perforation at layer  $m$ , the reservoir flow rate of phase  $\alpha$  (gas or water) can be expressed as the sum of the contributions of each perforated layer, or

$$Q_\alpha = \sum_m \text{WI}_{m,\alpha} (p_{\text{bh}} - p_i) \left( \frac{k_r}{\mu} \right)_{m,\alpha}, \quad (4.24)$$

where  $p_{\text{bh}}$  is the bottomhole pressure,  $p_i$  is the pressure of gridblock  $i$ ,  $k_r$  is the relative permeability, and  $\mu$  is the viscosity.  $Q_\alpha$  is the source term for the well.

In the case of multilayer completions, the gridblock pressure  $p_i$  is calculated from

$$p_i = p_{bh} - \int_z^{z_{bh}} \tilde{\rho} g dh, \quad (4.25)$$

where  $z$  is the depth, defined positive downwards, and  $\tilde{\rho}$  is the average density of the wellbore fluid within the considered interval.

### 4.3.5 Time coupling

#### Generalities

Numerical simulators use two sets of equations: one for fluid-flow in porous media, and one for stresses and strains. Fluid-flow equations, such as the law of conservation of mass and energy, provide solutions for pressure, temperature and saturation. In order to compute stresses and strains, the geomechanical module uses the values of pressure, temperature and saturation computed by the fluid-flow model. [65], [70], [77] The stresses and strains computed by the geomechanical simulator affect the values of porosity and permeability, which are in turn needed by the flow simulator. Coupling refers to the transfer of data between the two modules of the numerical simulator (fluid-flow and geomechanics). The frequency at which the geomechanical data is updated based on the fluid-flow solution is called implicitness. [111]

There are four possible types of coupling: (1) one-way or explicit coupling, (2) full or implicit coupling, (3) iterative coupling, and (4) pseudo-coupling. [111], [116]

#### One-way coupling

In one-way coupling schemes, pressure and temperature data are sent from the reservoir simulator to the geomechanical module, but no information is fed back to the flow simulator. The changes in stresses and strains do not impact the values of fluid pressure calculated by the reservoir simulator, since the two sets of equations are solved separately for each time period. One-way coupling functions in the same way as geomechanical post-processing, and can be used to assess the general effects and magnitude of stresses. However, this method of coupling is poorly accurate. [18], [37], [65], [70], [111], [116]

In order to understand the effect of deformation on petrophysical properties of the porous medium, a two-way coupling approach is required.

#### Full coupling

In fully coupled approaches, both the flow and stress equations are solved simultaneously in a large Jacobian matrix using the Newton-Raphson method. Full coupling is a robust approach that provides an accurate solution at the expense of high computation times. Furthermore, a common grid can be used for both flow and geomechanical modelling since the whole system is solved simultaneously. [7], [65], [69], [70], [76], [89], [116]

### Iterative coupling

Iterative coupling strategies involve solving the two sets of equations separately and sequentially, and data is then exchanged between the flow simulator and geomechanical model through coupling variables.

First, the flow equations are solved and sent to the geomechanical simulator to compute stresses, strains and displacements. This solution is then sent back to the flow simulator through coupling variables. The two variables which must be fed back to the flow simulator are porosity and permeability. As the mass conservation equation is mostly affected by pore volume and less by permeability, reservoir porosity  $\phi^*$  is considered the primary coupling variable, while  $\mathbf{k}$  is the secondary coupling variable. After the geomechanical solver feeds updated values of porosity and permeability to the flow simulator, a new pressure distribution can be computed, which is then fed to the geomechanical module for the next Newton iteration. The Newton iteration process is continued until reaching convergence, after which the next time step is taken (fig. 4.2). [7], [28], [37], [59], [70], [77], [89], [108], [111], [116]

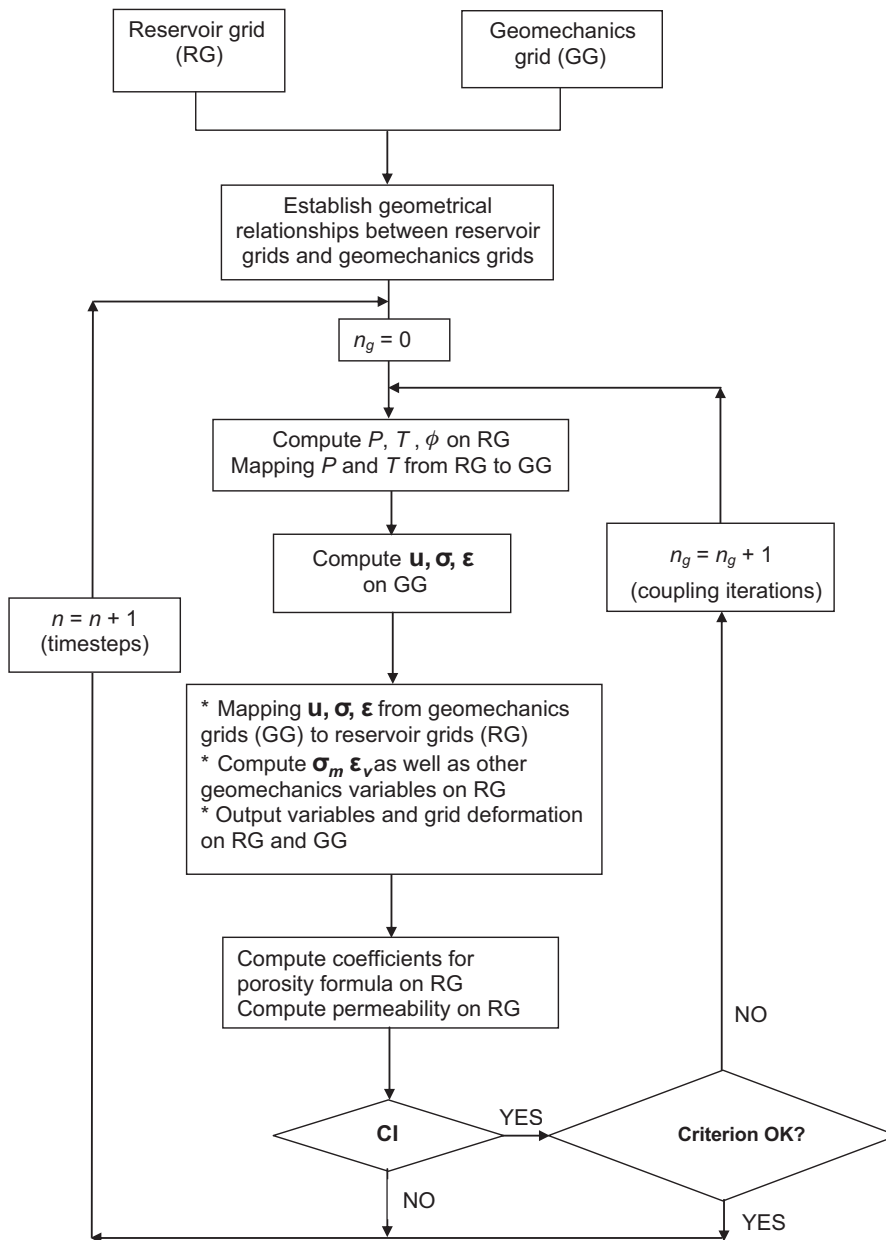


Figure 4.2 – Flow chart for dual-grid iterative coupling in GEM. [117]

Note that in GEM, a single Newton iteration is often sufficient to attain convergence within usual tolerance limits (user-specified). Only some specific behaviors such as stress arching or Mandel’s effects (increase in fluid pressure at early times of compaction) may require more than one Newton cycle per timestep. [108]

In the particular case of caprock failure modelling, fracture permeability must also be considered as an additional coupling variable. Fracture permeability is calculated from the fracture aperture given by the geomechanical solver, before iterating. [59], [89]

If the solution is iterated to full convergence, iterative coupling methods yield comparable accuracy to fully-coupled methods while reducing computation time. Additionally, this method offers increased flexibility as the coupling frequency (*i.e.* at which time intervals coupling is

performed) can be selected based on the rate of change of stresses and strains. Geomechanical properties can often be computed with sufficient accuracy using timesteps in the order of months, while fluid-flow calculations should be more frequent, on the order of days. Iterative coupling also allows the use of different grids for the geomechanical solver and the flow simulator. For example, if subsidence is to be evaluated, the flow simulation can be run on the reservoir grid, while geomechanical calculations would be performed on a larger grid which includes the overburden, allowing for reduced computational load. As a result, iterative coupling is the most commonly used method in numerical simulators. Nonetheless, it should be noted that for complex problems, the higher number of iterations needed to attain convergence compared to fully-coupled methods may offset the advantage of lighter computational workload. Furthermore, iterative coupling approaches require laboratory experiments to determine the porosity and permeability coupling laws which accurately represent the system under study. [7], [37], [59], [65], [69], [76], [89], [118]

### Pseudo-coupling

In pseudo-coupled methods, the fluid-flow solver uses empirical relations to link porosity with displacements and stresses. This allows the estimation of certain geomechanical effects without the use of a dedicated geomechanical solver. Porosity and absolute permeability are treated as a function of pressure, and are computed based on multiplier tables entered into the solver. [18], [111]

## 4.3.6 Coupling functions

### Porosity coupling

Recalling section 4.3.1, reservoir porosity is a function of pressure, temperature and mean total stress through the rock constitutive law:  $\phi^* = f(p, T, \sigma_m)$ .

In a one-way coupling system,  $\sigma_m$  is assumed constant and, as such,  $\phi^*$  becomes a function of pressure and temperature only. In two-way coupling schemes, porosity is also a function of deformation. Several porosity functions have been developed for iterative coupling methods and must be chosen based on laboratory experiments. In GEM, the choice of the porosity function is defined by the GCOUPLING command. [18]

Note that the porosity function is only used to compute the matrix porosity. Since the fracture porosity is usually much lower, it is approximated from a linear relationship with respect to pressure and temperature. [35]

**GCOUPLING 0** This corresponds to one-way coupling. The pressures and temperatures computed by the reservoir simulator are used by the geomechanical solver to compute formation stresses and strains, but the information is not fed back and, as such, fluid-flow properties do not depend on deformation. The recommended approach is to run one-way coupling first as it is computationally faster, and run two-way coupling if the geomechanical effects are significant. [70], [108], [110]

Here, while Young's modulus increases with effective stress, updated values of  $\sigma'$  are not available to the flow simulator. [108], [118], [119] Consequently,  $E$  is approximated from rock compressibility:

$$E = \frac{(1 - 2\nu)(1 + \nu)}{\phi_0 c_r (1 - \nu)}, \quad (4.26)$$

where  $\nu$  is Poisson's ratio,  $\phi_0$  is the initial porosity, and  $c_r$  is the compressibility of the rock.

**GCOUPLING 1** This is a two-way iterative method, where the reservoir porosity is defined as a function of pressure, temperature and volumetric strain:

$$\phi_{n+1}^* = \phi_0^* \left[ \frac{V_p^{n-1}}{V_p^0} + \frac{(V_p^n - V_p^{n-1})}{V_p^0 (p^n - p^{n-1})} (p - p^n) \right] - \beta_r (T - T_0), \quad (4.27)$$

where  $\phi_{n+1}^*$  is the reservoir porosity at timestep  $t_{n+1}$ ,  $V_p$  is the pore volume,  $p$  is the pressure,  $\beta_r$  is the volumetric thermal expansion coefficient of the formation, and  $T$  is the temperature.

**GCOUPLING 2** Here, the coupling mode is again iterative, but the porosity is dependent on pressure, temperature and total mean stress:

$$\phi_{n+1}^* = \phi_n^* + (c_0 + c_2 a_1)(p - p^n) + (c_1 + c_2 a_2)(T - T^n), \quad (4.28)$$

where

$$\begin{aligned} c_0 &= \frac{1}{V_b^0} \left( \frac{dV_p}{dp} + V_b \alpha c_b \frac{d\sigma_m}{dp} - V_p \beta_r \frac{dT}{dp} \right), \\ c_1 &= \frac{V_p}{V_b^0} \beta_r, \\ c_2 &= -\frac{V_b}{V_b^0} \alpha c_b, \\ a_1 &= \Gamma \left\{ \frac{2}{9} \frac{E}{(1 - \nu)} (c_b - c_r) \right\}, \\ a_2 &= \Gamma \left\{ \frac{2}{9} \frac{E}{(1 - \nu)} \beta_r \right\}, \end{aligned}$$

and  $V_b$  is the bulk volume,  $\alpha$  is Biot's coefficient,  $c_b$  is the bulk compressibility,  $\sigma_m$  is the mean total stress,  $\nu$  is Poisson's ratio, and  $\Gamma$  is a factor that takes into account the boundary conditions:

$$\Gamma = \begin{cases} 1, & \text{if the reservoir is constrained laterally and unconstrained vertically;} \\ \frac{3}{2} \left( \frac{1 - \nu}{1 - 2\nu} \right), & \text{if the reservoir is totally constrained in 3 directions;} \\ 0, & \text{if the reservoir is not constrained in any directions.} \end{cases} \quad (4.29)$$

This is a constant slope solution, with a linear relationship between  $\phi^*$  and pressure. Note that in the case of long time intervals or substantial pressure changes, the linear approximation may not be sufficiently accurate. [119]

**GCOUPLING 3** The porosity function is analogous to the previous one, and  $\phi^*$  is again a function of pressure, temperature and total mean stress:

$$\phi_{n+1}^* = \phi_n^* + c_0(p - p^n) + c_1(T - T^n) + c_2(\sigma_m - \sigma_m^n), \quad (4.30)$$

where  $c_0$ ,  $c_1$  and  $c_2$  are the same as for the previous case.

Finally, note that higher order (non-linear) solutions have also been proposed, for example by Tran *et al.* (2005), but they have not been implemented in GEM. [119]

### Matrix absolute permeability coupling

For reservoirs with simple geometries, a good estimation of compaction may be obtained without modelling the opening of fractures, and so without making use of a geomechanical solver (*i.e.* uncoupled system). The permeability increase resulting from the opening of fractures is modelled as an increase of matrix permeability. The use of an uncoupled model may decrease the computation time by as much as an order of magnitude. [112] There are three possible methods:

- (1) look-up tables;
- (2) compaction-dilation curves;
- (3) Li and Chalaturnyk's (2005) empirical equation.

In the case of look-up tables, the matrix permeability tensor  $\mathbf{k}$  may be expressed either as a function of reservoir porosity, volumetric strain, mean total stress or mean effective stress. Once the representative permeability function is identified from lab tests, it is entered into GEM in the form of permeability tables. [19], [108], [111] An example of a formula that relates permeability to reservoir porosity is

$$k = k_0 \cdot \exp \left[ k_{\text{mul}} \left( \frac{\phi^* - \phi_0}{1 - \phi_0} \right) \right], \quad (4.31)$$

where  $k_{\text{mul}}$  is a permeability multiplier, and  $\phi_0$  is the initial porosity.

For compaction-dilation curves, a table of porosity and permeability multipliers is entered as a function of pressure (fig. 4.3). This method is similar to the modified Barton-Bandis model, except that permeability is calculated from pressure (where an increase in pore pressure leads to an increase in permeability), whereas the Barton-Bandis model relates fracture permeability to effective stress. [75], [85], [108] Formation response to the increased pressure is represented by branched paths with different curves for loading and unloading (hysteresis effects). [108] Compaction-dilation curves do not model the creation of planar fractures, but simulate the creation of a stimulated reservoir volume (SRV). [75]

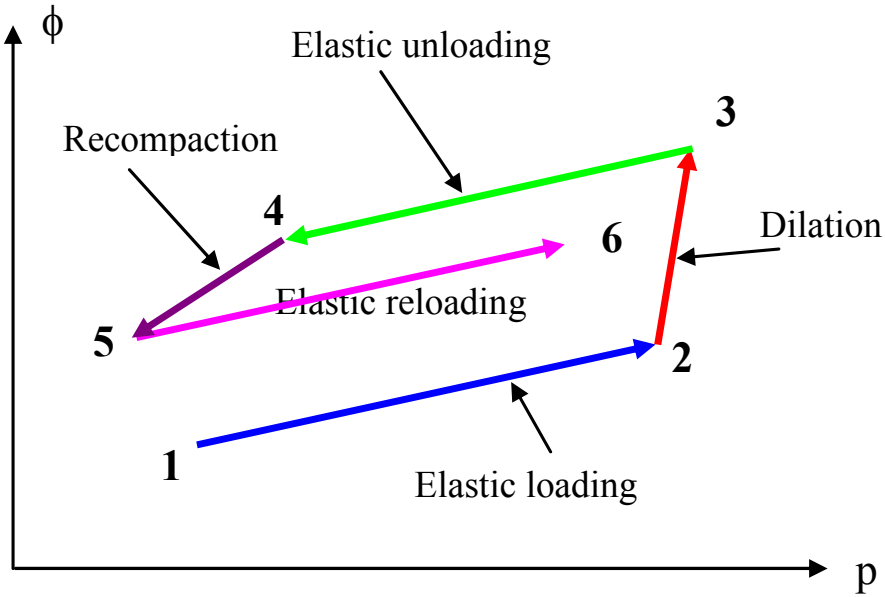


Figure 4.3 – Example of compaction-dilation curves. [111]

Alternatively, an empirical equation such as that proposed by Li and Chalaturnyk (2005) may be used. [120] This model is based on the work of Touhidi-Baghini (1998) and has been developed for oil sands. It relates the matrix permeability to the volumetric strain, and has been principally used to model steam-assisted gravity drainage (SAGD) processes. The application of this model requires laboratory experiments. [19], [70], [108], [120], [121] A multiplier is applied to the permeability of matrix blocks in all three directions:

$$\ln \left( \frac{k}{k_0} \right) = C_{n1} \cdot \epsilon_v, \quad (4.32)$$

where  $k$  and  $k_0$  are the current and initial permeabilities respectively,  $C_{n1}$  is an experimental parameter for the block's rock type, and  $\epsilon_v$  is the volumetric strain of the considered block. [108]

The empirical equation is less flexible than using tables, as the permeability multipliers cannot be set independently for each direction.

### Fracture absolute permeability coupling

If a more accurate representation of permeability changes due to the opening of fractures is needed, a dual-permeability (2K) or dual-porosity (2 $\phi$ ) model is used and fracture permeability  $k_f$  must be computed. A modified version of the Barton-Bandis fracture permeability model is used to compute  $k_f$ , and no matrix permeability multiplier is used. Before fracture failure, the value of  $k_m$  is used for modelling fluid-flow behavior. Once the stress acting on the fracture exceeds the material's strength,  $k_f$  is assigned to the gridblock and used in fluid-flow calculations. In 2K models, flow is permitted from fracture to fracture, matrix to matrix and matrix to fracture. [35], [70], [108], [122]

### 4.3.7 Spatial coupling

Both the geomechanical and fluid-flow models are discretized into grids, which may be colocated or not. As a consequence, some sort of coupling is required between the two grids. [111]

Because of the different requirements of the geomechanical and fluid-flow solvers, the grids may have different resolutions. Additionally, the overburden, sideburden and underburden are usually included solely into the geomechanical grid, as these formations do not require fluid-flow modelling. The grid coupling may be either a single-grid or a dual-grid system.

In a single-grid system, the fluid-flow and geomechanical grids are colocated at the start of the simulation. As the simulation progresses, the geomechanical grid is allowed to deform while the fluid-flow blocks maintain constant volume; however, a one-to-one correspondence between both grids is maintained at all times. Note that the fluid-flow solver uses a finite difference (FD) grid and the geomechanical solver a finite element (FE) grid. In the FD grid, flow parameters are computed at the center of the grid while in the FE grid, displacements are computed at each block corner and for each direction (24 calculations for each block). In a single-grid system, the number of geomechanics blocks is usually higher than it needs to be, drastically affecting computation time because of the large number of computations per block. [37], [70], [108], [111], [117]

In dual-grid models, the two grids are not colocated and may have different resolutions, the geomechanics grid usually being coarser. A complex mapping algorithm is required between the grids, and some sort of relation must exist between the two grids in order to set up this algorithm; this means that either grid must be a subset of the other. This system is used for mapping fractures, where the geomechanical calculations are only coupled to the matrix blocks, but the fracture behavior (linked to the secondary grid) is dependent upon the geomechanical effects calculated for the matrix blocks. [86], [111], [117] When using a dual-grid system with matrix and natural fractures, pressures are calculated for both grids. In order to compute stresses and strains, a single value of pressure must be used; the pressure considered for geomechanics calculations (geo-corrected pressure) is derived as

$$p_{\text{geo}} = \left( \frac{\phi_m}{\phi_m + \phi_f} \right) p_m + \left( 1 - \frac{\phi_m}{\phi_m + \phi_f} \right) p_f, \quad (4.33)$$

where the m and f subscripts correspond to matrix and fracture properties respectively. [108]

The possible grid types, both for the geomechanics grid or the reservoir grid, are (1) cartesian, (2) corner point, and (3) radial. When using cartesian or radial grids, pressure and temperature must be interpolated from each block center to the corresponding nodes of the geomechanical finite element. This can be done using one of four methods:

- (1) arithmetic average;
- (2) inverse distance weighted interpolation;
- (3) pore volume weighted interpolation;
- (4) bulk volume weighted interpolation. [70], [108]

## 4.4 Modified Barton-Bandis stress-permeability model

### 4.4.1 Generalities

The most widely used model to represent tensile opening of fractures in GEM is a modified version of the Barton-Bandis joint constitutive model. A dual-permeability or dual-porosity system with a dual-grid must be used, where stresses and strains are only coupled to the porous rock matrix blocks. The second grid consists of the fracture blocks, and can be colinear to the matrix grid or not. The opening and closing of the fractures is dependent upon the stresses computed in the matrix blocks. [22], [37], [108], [123], [124]

Such a configuration is used to represent a naturally fractured caprock, with fractures being initially closed due to the normal stress acting on them. A very low initial fracture permeability is assigned, so as to make the caprock essentially a no-flow boundary. [37], [70], [75] Stresses within the matrix are calculated to determine possible tensile failure of the fractures, which leads to a change in fracture permeability. Permeability changes happen only in the damaged zone as the Barton-Bandis model is applied only to failed fractures. Matrix permeability is not affected. [59], [65], [75]

### 4.4.2 Initial state of fractures

The fractures within the rock are initially dormant (point A in fig. 4.4). As CO<sub>2</sub> is injected, pore pressure  $p$  increases in the matrix grid (*cf.* section 2.7.1) while the overburden or total stress  $\sigma$  remains constant (path AB). As a result, according to Terzaghi's law, the effective stress  $\sigma'$  decreases:

$$\sigma'_{ij} = \sigma_{ij} - \alpha p \delta_{ij}. \quad (4.34)$$

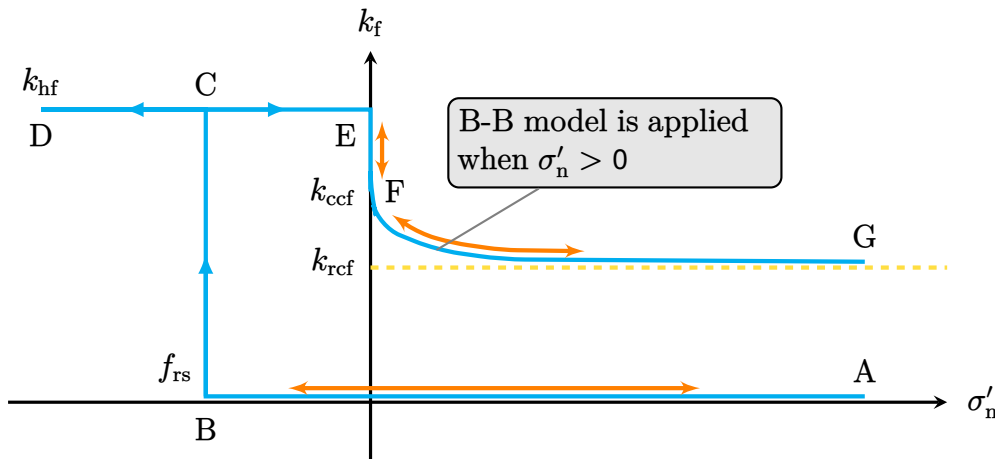


**Figure 4.4** – Relationship between effective normal stress and fracture permeability in the modified Barton-Bandis stress-permeability model. [108]

Along path AB, fracture permeability retains its very low value, making the caprock effectively a no-flow boundary, and behavior is reversible. As effective stress keeps decreasing due to

injection, it eventually reaches a point called critical fluid pressure or fracture opening stress ( $p_{fc}$  or  $f_{rs}$ , point B). The fracture opening stress is equal to the yield limit of the material, and higher values lead to shorter time until fracture reactivation. [22], [37], [58], [59], [65], [70], [74], [86], [124]

#### 4.4.3 Tensile opening of fractures

Once the Biot effective stress decreases such that it reaches the critical fluid pressure, and if the rock is sufficiently brittle, tensile failure occurs and the fracture instantaneously becomes transmissible to flow, corresponding to maximum fracture permeability  $k_{hf}$  (point C). [22], [37], [58], [59], [65], [70], [75] In the particular case of propped hydraulic fracturing, hydraulic fracture permeability  $k_{hf}$  is equal to the permeability of the proppant pack. [77]

When the fracture opens, the gridblock permeability switches to a fractured gridblock permeability. Fracture propagation length can be estimated by counting the number of activated blocks. Note that GEM's geomechanical simulator uses the Biot effective stress, which delays the fracture activation compared to using the Terzaghi effective stress, as the Biot coefficient  $\alpha$  is less than 1. [67]

#### 4.4.4 Fracture closure

When unloading (*i.e.* stopping injection or reducing rate), fractures remain fully open as long as effective normal stress is negative, *i.e.* the fracture is sollicitated in tension (path CE). When  $\sigma'_n$  becomes positive, fracture permeability decreases from  $k_{hf}$  to fracture closure permeability  $k_{ccf}$  (path EF). Fracture closure permeability represents the fracture permeability at zero effective stress, *i.e.* at the onset of fracture closure [37], [67], [124]

When  $\sigma'_n$  increases beyond zero, the Barton-Bandis equations are used to model fracture closure (path FG). Because of plastic deformation of the asperities which leads to increasing normal stiffness, the fracture cannot close completely even if the effective normal stress returns to initial (hysteresis effect, *i.e.* fracture permeability depends on the loading history). Fracture permeability reaches an asymptotic value called fracture closure permeability,  $k_{rcf}$ . Path GFED, like path AB, is fully reversible. [37], [65], [70], [77], [108], [123], [124]

#### 4.4.5 Basic equations for fracture closure

As mentioned before, only fracture closure, and not aperture, is modelled using the Barton-Bandis equations. The inputs needed by the model are:

- initial fracture aperture,  $E_0$ ;
- initial normal fracture stiffness,  $k_{ni}$ ;
- fracture opening stress,  $f_{rs}$ ;
- hydraulic fracture permeability,  $k_{hf}$ ;

- fracture closure permeability,  $k_{\text{ccf}}$ ;
- residual fracture permeability,  $k_{\text{rcf}}$ . [37], [75], [108]

Current fracture permeability is computed as a function of aperture, or

$$k_f = k_{\text{ccf}} \left( \frac{E_n}{E_0} \right)^4 \geq k_{\text{rcf}}, \quad (4.35)$$

which is the equation used to model fracture closure, *i.e.* path FG.

The current, stress-dependent fracture aperture  $E_n$  is calculated as

$$E_n = E_0 - V_j, \quad (4.36)$$

where  $V_j$  is the joint closure under a normal effective stress  $\sigma'_n$  (equal to the least principal effective stress), defined as

$$V_j = \frac{\sigma'_n}{k_{\text{ni}} + \sigma'_n/V_m}, \quad (4.37)$$

as per the Barton-Bandis theory.

The maximum closure  $V_m$ , corresponding to closure permeability, is

$$V_m = E_0 \left[ 1 - \left( \frac{k_{\text{rcf}}}{k_{\text{ccf}}} \right)^{\frac{1}{4}} \right]. \quad (4.38)$$

Maximum closure  $V_m$  is also equal to the difference between the maximum opening and the smallest aperture. [91]

## 4.5 Shear failure of fractures

### 4.5.1 Generalities

Another possible mode of fracture failure is shear fracturing. As effective stress decreases due to the increase in pore pressure, the Mohr circle moves to the left, approaching the failure envelope (fig. 4.5). During shear fracturing, the joint walls slide against each other, creating a mismatch (loss of interlocking) that may allow some fluid to flow. Fracture permeability from shear failure is much smaller than fracture permeability from tensile failure. [65], [75], [108] When both shear failure and tensile failure happen, the fracture permeability considered by GEM is the maximum value between the two failure modes, which is almost always the one from tensile failure. Nevertheless, modelling shear behavior may be important, as shear failure will weaken the rock and allow for easier tensile opening of the fractures. [75], [108] Fault orientation, the in-situ stress tensor, pore pressure and the ratio between principal stresses determine in which order tensile and shear failure happen. [65]

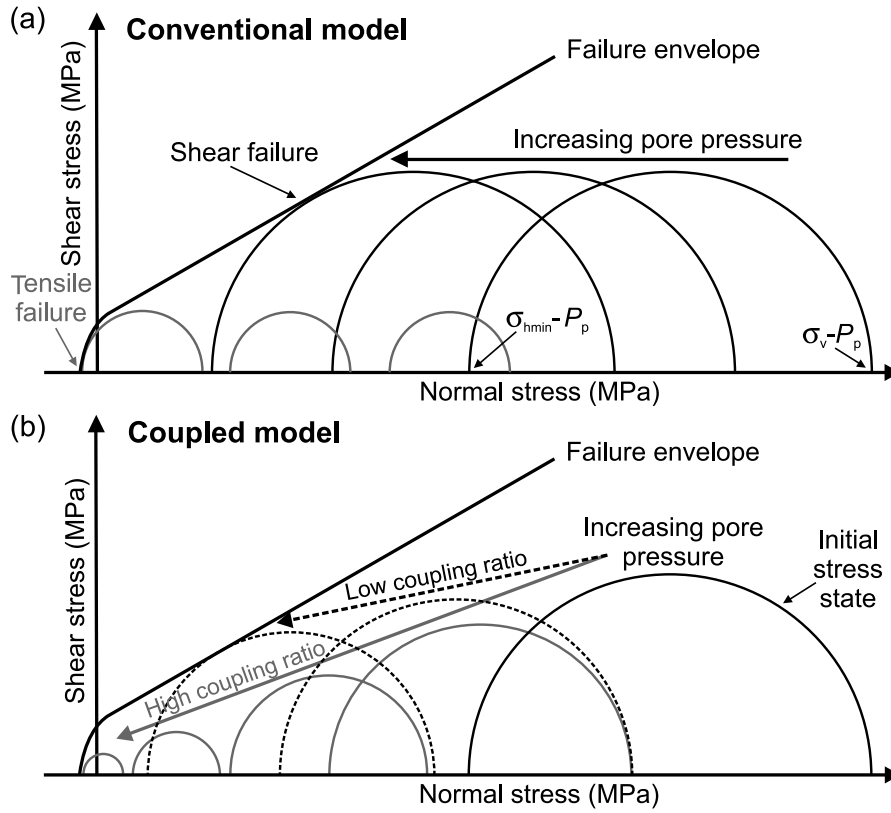


**Figure 4.5** – Evolution of Mohr circles with increasing pore pressure in a normal-faulting stress regime, and effect of coupling model. [125]

Note that changing rate during production will impact the minimum and maximum effective stresses and, as a consequence, the radius and the position of the Mohr circle will be modified. If the new Mohr circle touches the defined shear failure envelope, shear failure of the fractures will occur. [75] Shear fracturing occurs when the radius of the Mohr circle is greater than the shear failure criterion, or

$$\left[ \frac{\sigma'_1 - \sigma'_3}{2} \right] > \text{criterion}, \quad (4.39)$$

where  $\sigma'_1$  and  $\sigma'_3$  are respectively the maximum and minimum principal effective stresses. [108] If shear fracturing occurs, fracture permeability is computed as

$$k_f = k_{f0} \cdot \exp(-\gamma \cdot \Delta\sigma'_m), \quad (4.40)$$

where  $k_{f0}$  is the initial fracture permeability,  $\gamma$  is the permeability modulus, and  $\Delta\sigma'_m$  is the mean effective stress difference. [108]

## 5 CMG GEM reservoir model

### 5.1 Base model

The base model is built based on Tran *et al.* (2010), and consists of a cartesian grid comprising 101 blocks along I, 1 block along J and 33 blocks along K (vertically). The vertical extent of the model is 318 m, and the horizontal extent along I is 12,100 m. Blocks are  $100 \times 100$  m along the 2 horizontal directions, except towards the reservoir boundary where they increase to 500 m width in increments of 100 m. The model includes a storage formation overlain by a caprock and the corresponding overburden. The reservoir rock consists of 20 layers of thickness 7.6 m; the caprock, 3 layers of thickness 4.5 m; and the overburden, 10 layers of thickness 15.25 m. The overburden top is defined at 2263 m. The model is dual-permeability, where dual-permeability is only active in the caprock. The storage formation is penetrated by a vertical well perforated along the 4 bottommost layers, corresponding to a total perforated length of 22.8 m. The analysis is done in plane strain conditions ( $\epsilon_z = \gamma_{xz} = \gamma_{yz} = 0$ ).

Pressure is initialized from a reference pore pressure of 25,888 kPa at a depth of 2429 m (reservoir top). Horizontal displacement along J is not permitted. Along I, horizontal displacement is allowed except at model boundaries. Vertical displacement is permitted everywhere except at the bottom of the reservoir. Additionally, the reservoir is modelled as a closed aquifer, with no flow through boundaries. The fractures assigned to the caprock (layers 11 to 13) are orthogonal with a 10 m spacing along all directions, while the rest of the model is unfractured. The caprock and storage formation have the same rock properties except for compressibility, and they are modelled with the Mohr-Coulomb criterion, while the overburden obeys the Drucker-Prager criterion. The rock properties are defined by the Young modulus, Poisson ratio, cohesion and internal friction angle (table 5.1). The Barton-Bandis permeability model is applied to the caprock, and no matrix permeability multiplier is defined. The porosity function used is GCOUPLING 2 (*cf.* section 4.3.6). The reference effective stresses assigned to the geomechanics finite elements (table 5.2) are referred to gridblock  $\{1, 1, 1\}$  (top left block, K is positive downwards), and the actual initial effective stress distribution is calculated by summing the reference stress and the stress gradient for the considered block. A scheme of the model is shown in fig. 5.1.

**Table 5.1** – Rock properties.

Property	Overburden	Caprock	Storage formation	Unit
Rock constitutive law	D-P	M-C	M-C	–
Young's modulus, $E$	861,845	$5 \times 10^6$	$5 \times 10^6$	kPa
Poisson's ratio, $\nu$	0.3	0.25	0.25	–
Rock compressibility, $c_r$	$1.28 \times 10^{-6}$	$1.28 \times 10^{-5}$	$1.28 \times 10^{-6}$	$\text{kPa}^{-1}$
Cohesion, $c'$	689,476	689,476	689,476	kPa
Friction angle, $\phi'$	30	30	30	deg
Biot coefficient, $\alpha$	1	1	1	–

**Table 5.2** – Reference effective stresses.

Property	Direction	Value	Unit
Effective stress	I – J	3447.4	kPa
	K	6894.8	
Effective stress gradient	I – J	-10.5	kPa/m
	K	-20.9	

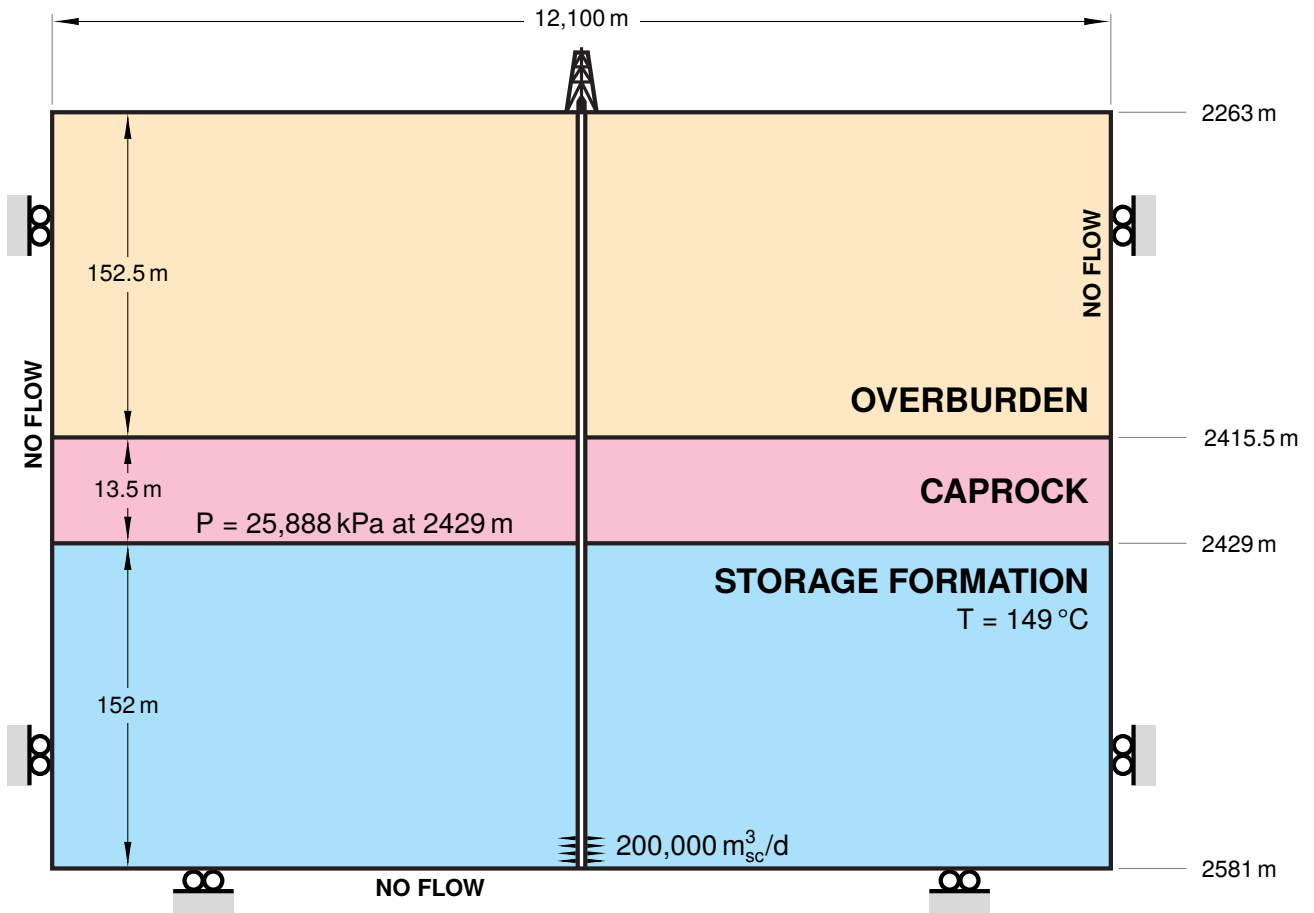


Figure 5.1 – Model scheme.

The caprock is defined as a brittle material (Young's modulus is high), so that cracks propagate quickly across it once the failure criterion is reached. Shear failure is not considered in the model and all the formations are assumed to be purely elastic (no plasticity). The initial fracture permeability is assumed very small (table 5.3) so that the transmissibility across the caprock is essentially null prior to fracture failure. Note that the permeability and porosity given in table 5.3 refer to zero stress values.

Table 5.3 – Hydraulic parameters.

Property	Overburden	Caprock	Storage formation	Unit
Matrix horizontal permeability, $k_{hm}$	20	$10^{-7}$	15	mD
Matrix porosity, $\phi_m$	0.13	0.13	0.13	–
Matrix anisotropy ratio, $k_{vm}/k_{hm}$	0.25	0.25	0.25	–
Fracture horizontal permeability, $k_{hf}$	–	$10^{-7}$	–	mD
Fracture porosity, $\phi_f$	–	0.13	–	–
Fracture anisotropy ratio, $k_{vf}/k_{hf}$	–	0.25	–	–

The reservoir temperature is constant at 149 °C, and the PR EoS is used to model PVT properties of the fluids. The volume shift is set to zero, and CO<sub>2</sub> viscosity is calculated from

the HZYT mixing rule. The aqueous viscosity is assumed constant, while the aqueous density is a linear function of pressure. Water compressibility is  $4.35 \times 10^{-7} \text{ kPa}^{-1}$ . As the simulation timescale is in the order of decades, chemical reactions are not considered, and water salinity is not included (0 ppm). The injection rate is constant and set to  $200,000 \text{ m}_{\text{sc}}^3/\text{d}$ , starting from 01-01-2030. The well is shut in after 5 years, and output values are generated every month. The injected fluid is 99.9 %  $\text{CO}_2$ , the remaining 0.1 % being  $\text{CH}_4$  added to facilitate the work of the numerical solver.  $\text{CO}_2$  component properties are given in table 5.4.

**Table 5.4** –  $\text{CO}_2$  component properties.

Property	Value	Unit
Critical pressure, $p_c$	72.8	atm
Critical temperature, $T_c$	304.2	K
Molecular weight, $M_w$	44.01	g/mol
Henry's constant, $H$	690,636	kPa

The Barton-Bandis parameters are shown in table 5.5, and the relative permeability curves are shown in fig. 5.2. The relative permeability curves are assumed the same in all formations. Capillary pressure is not considered in the model, irreducible water saturation  $S_{wi}$  is set to 16 %, and critical gas saturation  $S_{gc}$  is 0.5 %. All three formations (storage formation, caprock, overburden) are initially fully saturated with water, with formation water density set to  $1000.8 \text{ kg/m}^3$  at atmospheric pressure and reservoir temperature ( $149^\circ\text{C}$ ). A section of the model is shown in fig. 5.3. Finally, note that this model was set up with the aim to investigate caprock failure, and not to represent a real or potential reservoir-caprock system. As such, values have been chosen arbitrarily, and may not be compared to real-world situations.

**Table 5.5** – Barton-Bandis parameters.

Property	Value	Unit
Initial fracture aperture, $E_0$	$2 \times 10^{-5}$	m
Initial normal fracture stiffness, $k_{ni}$	$6.8 \times 10^7$	kPa/m
Fracture opening stress, $f_{rs}$	2000	kPa
Hydraulic fracture permeability, $k_{hf}$	233	mD
Fracture closure permeability, $k_{ccf}$	233	mD
Residual fracture permeability, $k_{rcf}$	233	mD

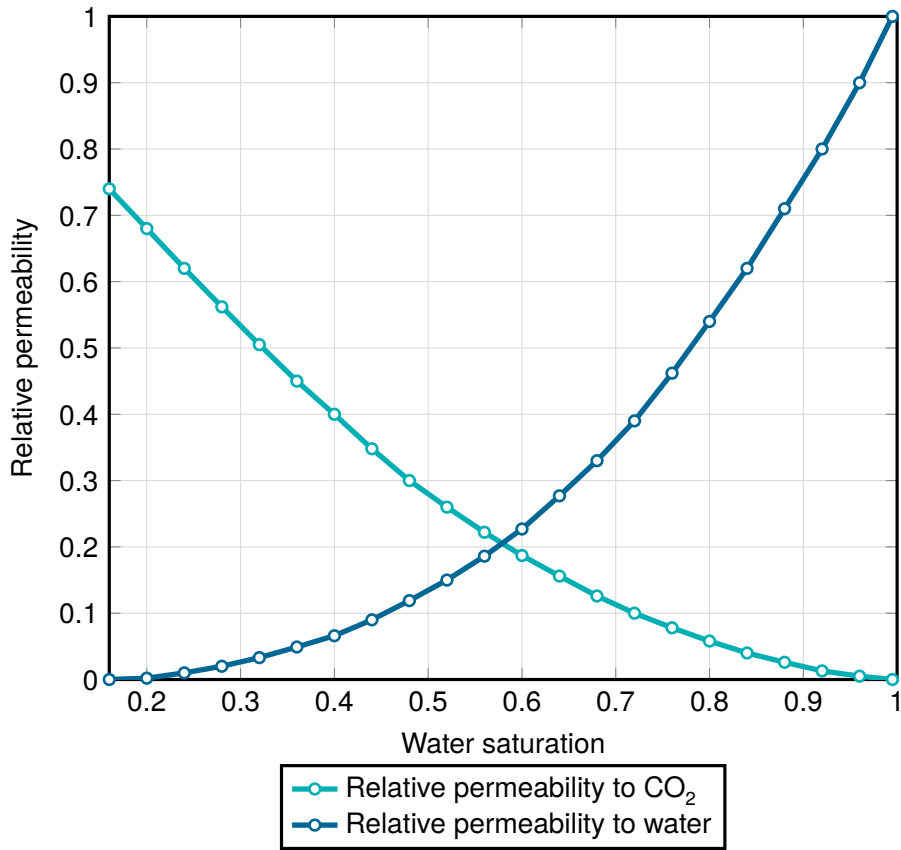


Figure 5.2 – Relative permeability curves.

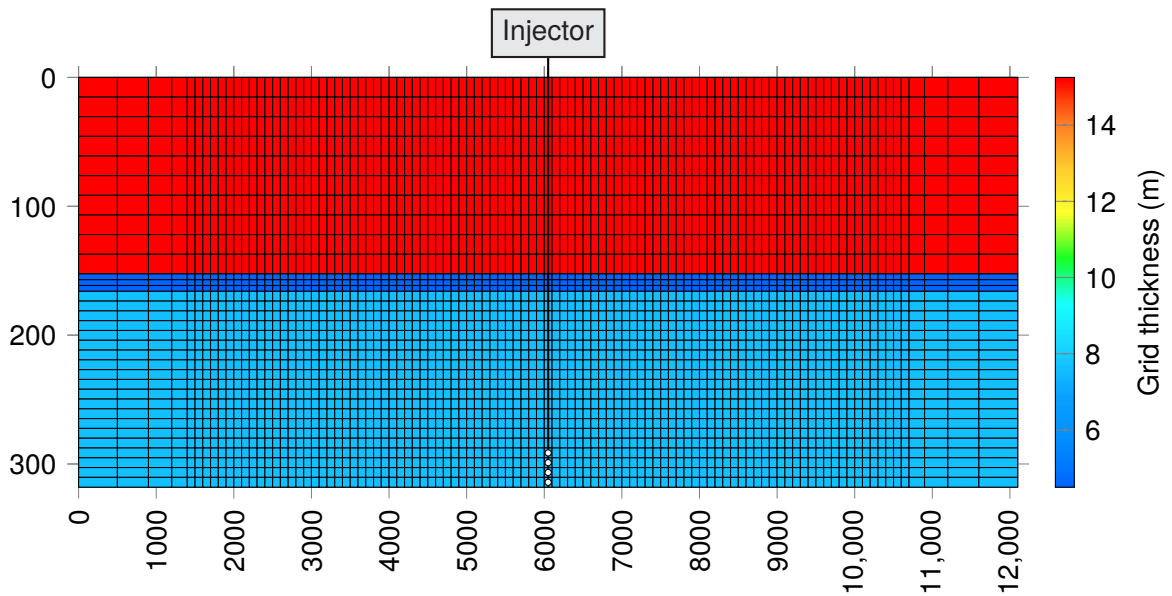
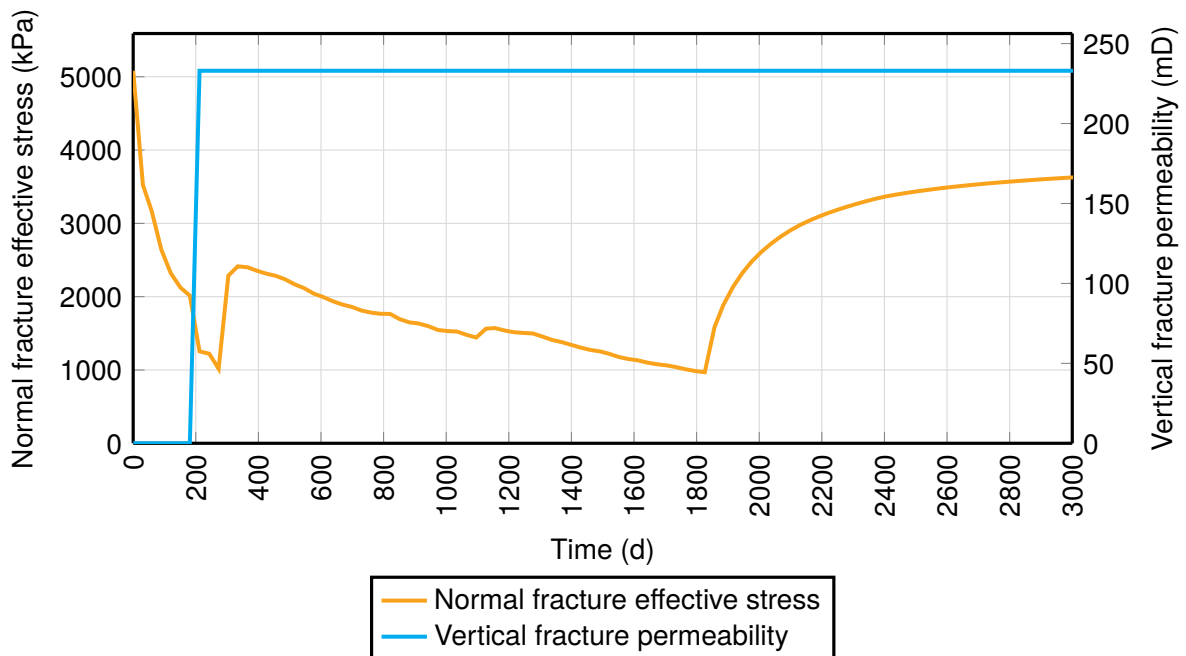


Figure 5.3 – IK section of the model showing grid thickness.

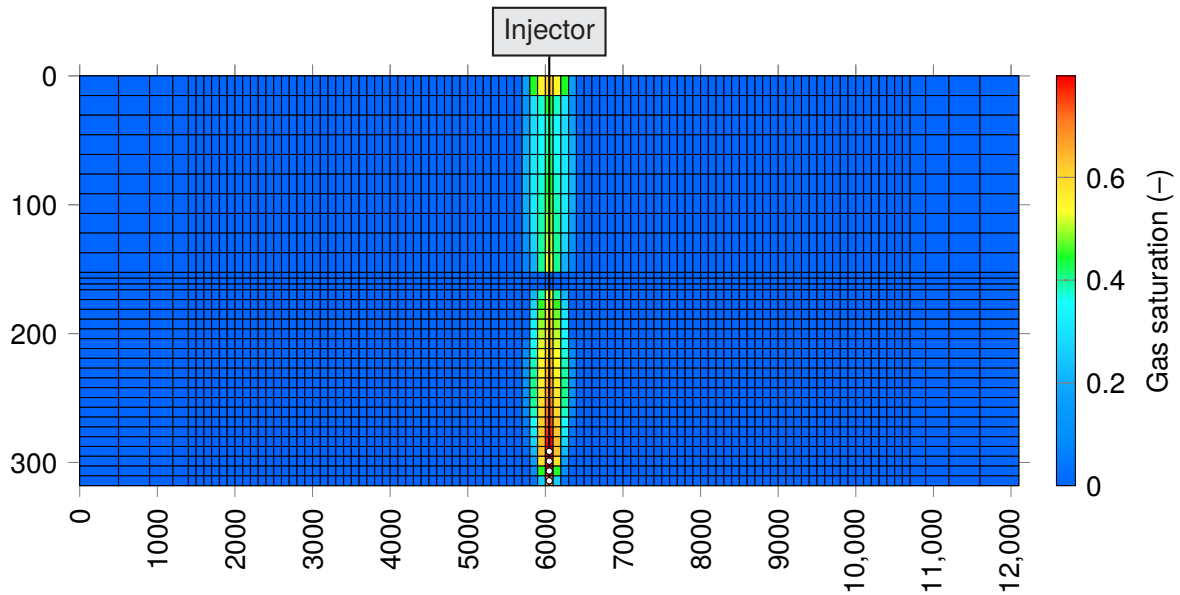
## 5.2 Base case results

As outlined previously, fracture failure in the model happens when fracture effective normal stress falls below the opening stress threshold  $f_{rs}$ , set to 2000 kPa. This behavior is apparent in fig. 5.4, where vertical fracture permeability in the caprock jumps from its initial value of  $2.5 \times 10^{-8}$  mD to 233 mD as fracture effective normal stress reaches the threshold. Failure happens first on the underside of the caprock, and the crack extends both horizontally and vertically until the caprock is broken through. In the base case, first crack happens at 181 d (6 months) and the caprock is fully breached after 273 d (9 months). Note that the fractures remain open even as normal fracture effective stress increases back beyond the threshold  $f_{rs}$ , as residual (closed) fracture permeability  $k_{rcf}$  is set to the same value as hydraulic (fully open) fracture permeability  $k_{hf}$  (233 mD).

After injection is stopped in 2035 (1826 d), normal effective stress increases as the overpressure inside the storage formation slowly drains away. It keeps increasing until a new static equilibrium is reached. The gas saturation at the end of the injection period is shown in fig. 5.5.

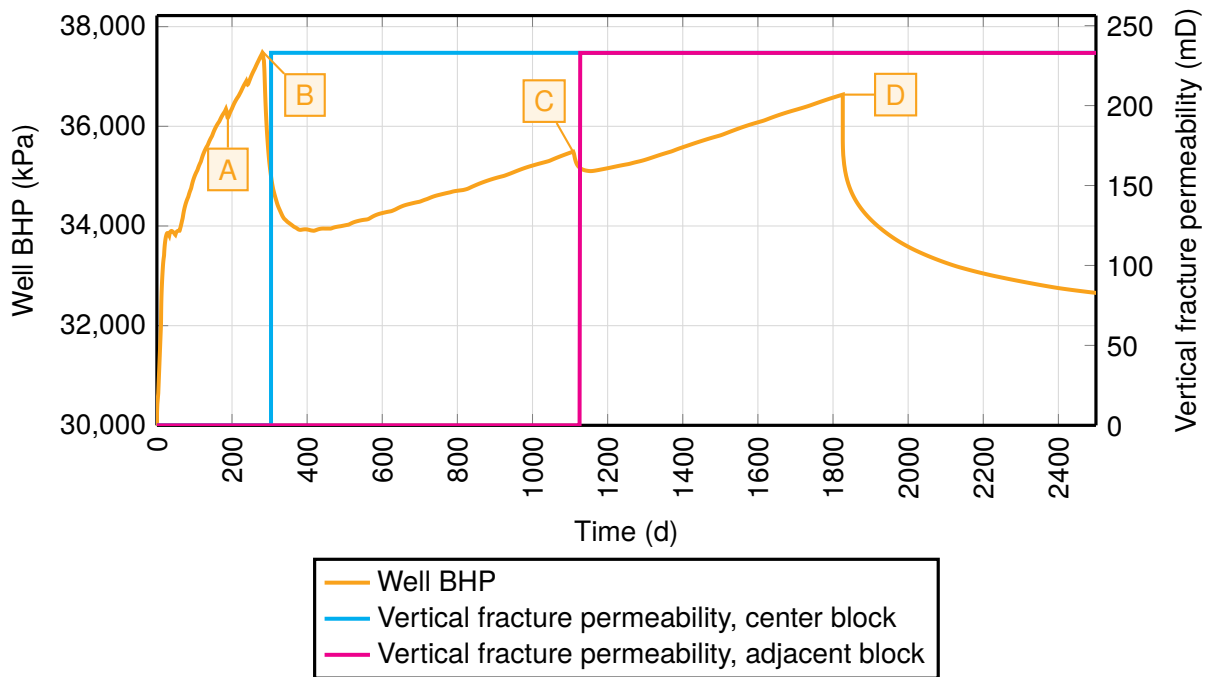


**Figure 5.4** – Fracture effective normal stress and fracture vertical permeability at the bottom center of the caprock.



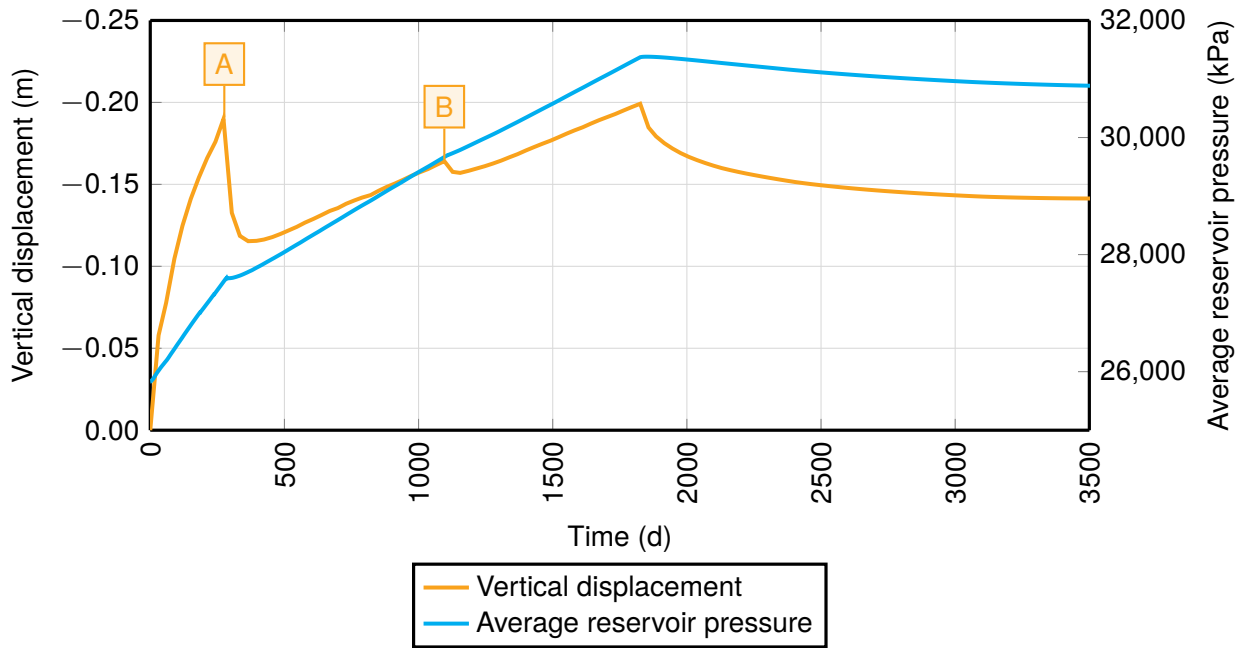
**Figure 5.5** – Gas saturation at the end of the injection period.

Figure 5.6 shows two successive fracture failures in adjacent blocks. Firstly, small drops are observed in the BHP curve as fractures open in the caprock, but before the caprock is fully breached (A). Once the fracture has propagated through the caprock and established communication with the layer above, well BHP drops sharply (B, 273 d). The caprock is breached first through the block situated vertically above the perforations ( $\{51,1,11\}$ ). A second drop in BHP is observed at 1096 d (C), which corresponds to the fracture propagating horizontally and failure of the adjacent block ( $\{52,1,11\}$ ). The final drop in BHP is due to shutting-in the well after 5 years of continued injection (D). Note that BHP increases at a slower pace once the caprock has been fractured, as the pressure increase is partly absorbed by the overburden.



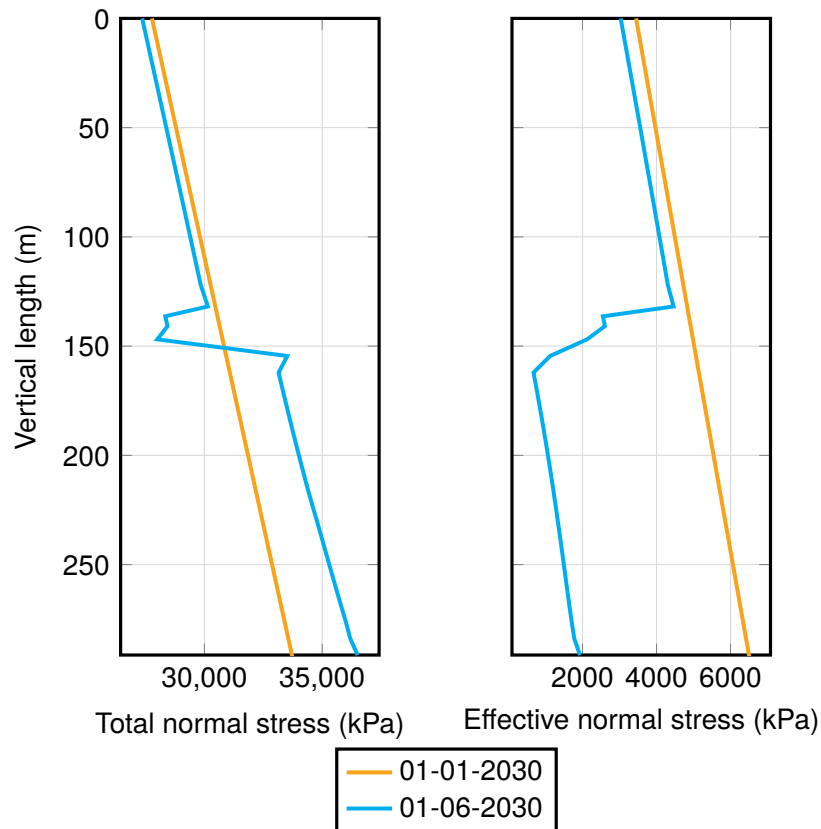
**Figure 5.6** – Well BHP and fracture vertical permeability at two adjacent blocks at the top of the caprock.

Figure 5.7 shows the average pressure in the aquifer, which increases at a slower pace after the caprock fractures and communication with the upper layer is established. At failure, the relative pressure increase is around 1.8 MPa. Post-injection, the pressure finds a new equilibrium for the two combined layers. The vertical displacement at the center of the caprock drops sharply after failure (A), as pressure is released. At 1096 d, the second caprock failure happens in the adjacent blocks and a much smaller drop can be observed (B). Post-injection, heave decreases with pressure. Note that the vertical displacement is negative, as  $K$  is defined positive downwards.



**Figure 5.7** – Average pressure inside the aquifer and vertical displacement at the center top of the caprock.

As shown in fig. 5.8, the increase in pore pressure within the aquifer leads to expansion of the reservoir and reduction of the horizontal effective stress compared to the pre-injection trend. Since the reservoir is laterally constrained, expansion along I is not permitted and the total horizontal stresses increase. In order for the system to remain consistent with the far-field stresses, an increase of  $\sigma_h$  in the aquifer must be counteracted by a decrease of  $\sigma_h$  in the caprock through a stress transfer process. [63]



**Figure 5.8** – Horizontal stresses along the wellbore after 4 months of injection (pre-failure).

Figure 5.9 shows how effective horizontal stress increases radially around the well, following the pressure trend (fig. 5.10). The magnitude of effective stress unloading is lower in the caprock compared to the reservoir, meaning that hydraulic fracturing is likely to happen before caprock fracturing.

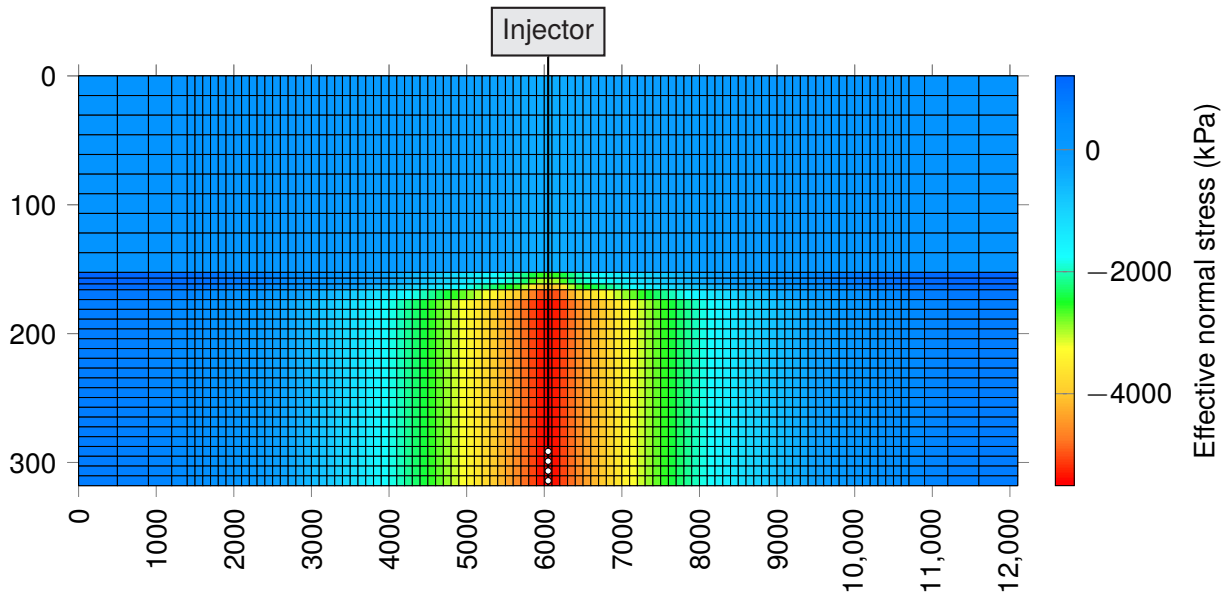


**Figure 5.9** – Relative effective horizontal stress decrease after 9 months of injection (pre-breakthrough).

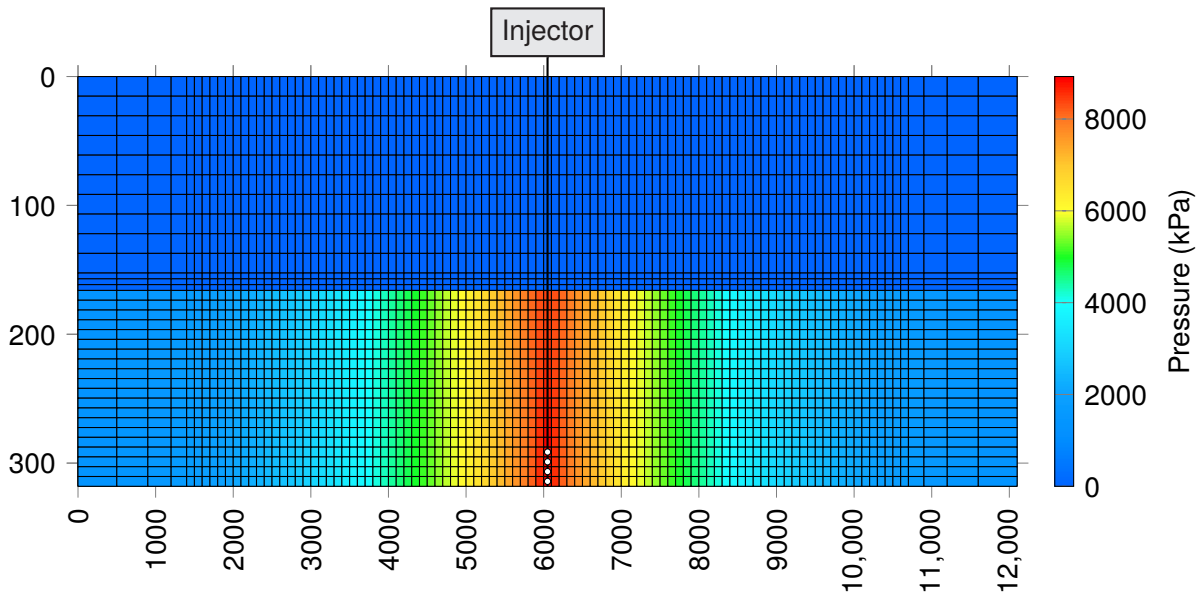


**Figure 5.10** – Relative pressure increase after 9 months of injection.

As expected, the local increase in pore pressure at the perforations leads to arching of the caprock (fig. 5.11). Peak displacement is higher at the top of the caprock compared to the overburden top; part of the displacement is absorbed by the overburden rock, which compacts due to its low stiffness (low  $E$ ). The arching of the caprock also causes a decrease in effective stress above the caprock, where the state of stress moves towards a tensional regime (fig. 5.12). However, the magnitude of the effective stress decrease is not nearly enough to cause tensile failure by itself, in which case a fracture would open first at the top of the caprock.

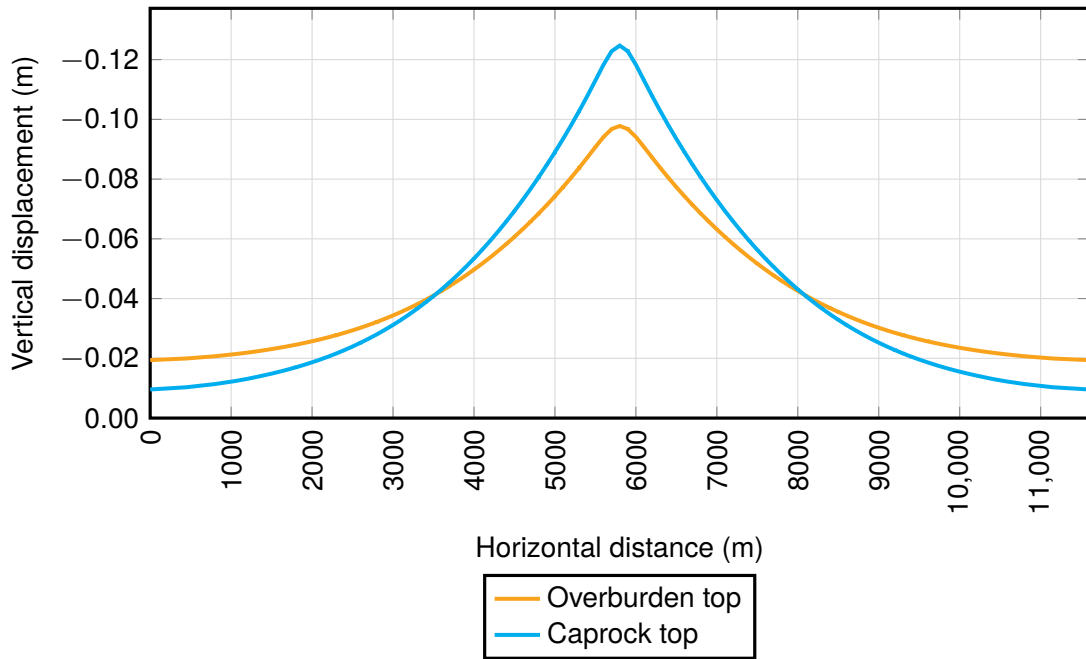


**Figure 5.11** – Vertical displacement profile along the overburden top and caprock top after 4 months of injection (pre-failure).

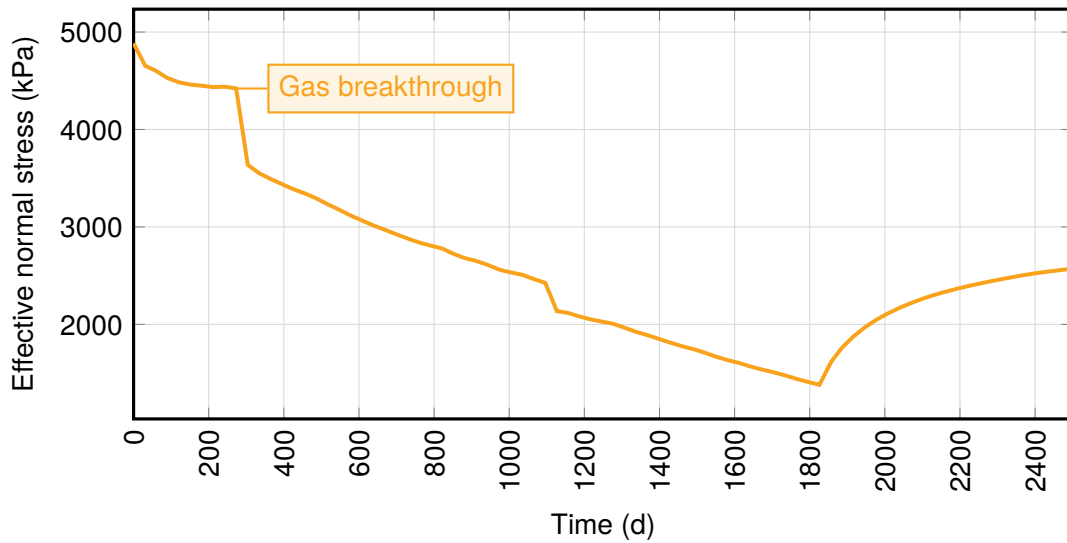


**Figure 5.12** – Effective horizontal normal stress above the caprock ({51,1,10}).

## 6 Sensitivity analysis

A sensitivity analysis is performed to evaluate the impact of different parameters on the simulation results. The base case is as described above, and the investigated parameters are given in table 6.1. In each simulation, only one parameter is varied in order to isolate its effect. The range of values of each parameters has been chosen with the aim to cause caprock failure within a reasonable simulation timeframe, and should not be taken as representative of a real situation.

**Table 6.1** – Parameters and values considered in the sensitivity analysis.

Parameter	Lower value	Upper value	Unit
<i>Reservoir properties</i>			
Matrix permeability	15	30	mD
Matrix permeability anisotropy	0.25	1	–
Porosity	0.13	0.41	–
Young modulus	5	30	GPa
Poisson ratio	0.2	0.35	–
Dip angle	0	20	deg
Salinity	0	200,000	ppm
Reference pore pressure	23,888	27,888	kPa
<i>Caprock properties</i>			
Matrix permeability	$10^{-7}$	$10^{-2}$	mD
Fracture permeability	$10^{-7}$	$10^{-2}$	mD
Young modulus	2.5	7.5	GPa
Poisson ratio	0.2	0.35	–
Thickness	6	21	m
Fracture spacing	0.01	100	m
Fracture opening stress	1600	2600	kPa
Residual fracture permeability	167	233	mD
<i>Simulation options</i>			
Porosity coupling function	0	3	–
Shear failure	No	Yes	–
Equation of state	PR	SRK	–
<i>Injection parameters</i>			
Injection rate	180,000	220,000	$m_{sc}^3/d$
Number of wells	1	3	–
Well profile	Vertical	Long horizontal	–
Perforated interval	30 to 33	20 to 23	–

## 6.1 Reservoir properties

### 6.1.1 Matrix permeability

Matrix permeability is increased from the original 15 mD to 22.5 mD and 30 mD. The permeability anisotropy ratio is kept at 0.25, meaning that vertical permeability is respectively 3.75 mD, 5.625 mD and 7.5 mD.

Figure 6.1 shows that for an increase in matrix permeability, there is a corresponding decrease in well BHP (before gas breakthrough). As the required BHP is lower, a higher permeability means a higher injectivity. In the 15 mD run, we can see a first crack appearing on the bottom of the caprock at 181 d (A, corresponding to the increase in fracture permeability), and a sudden drop in BHP at 282 d corresponding to the propagation of the crack through the caprock and release of built-up pressure (B). Finally, the smaller drop at 1108 d (C) is due to cracking of the adjacent blocks along the top of the caprock, and enlargement of the CO<sub>2</sub> escape path.

In the 22.5 mD scenario, the first crack occurs at 1155 d (D) in the gridblock situated directly above the well. Contrary to the previous case, the fracture does not propagate vertically and communication to the upper layers is never established. However, multiple small drops can be observed in the BHP curve (between 1212–1810 d). These correspond to the gradual horizontal propagation of the fracture. At the end of injection, the fractured zone extends some 2100 m along the underside of the caprock. In the 30 mD run, the horizontal propagation of the fracture is only 900 m on the same date.

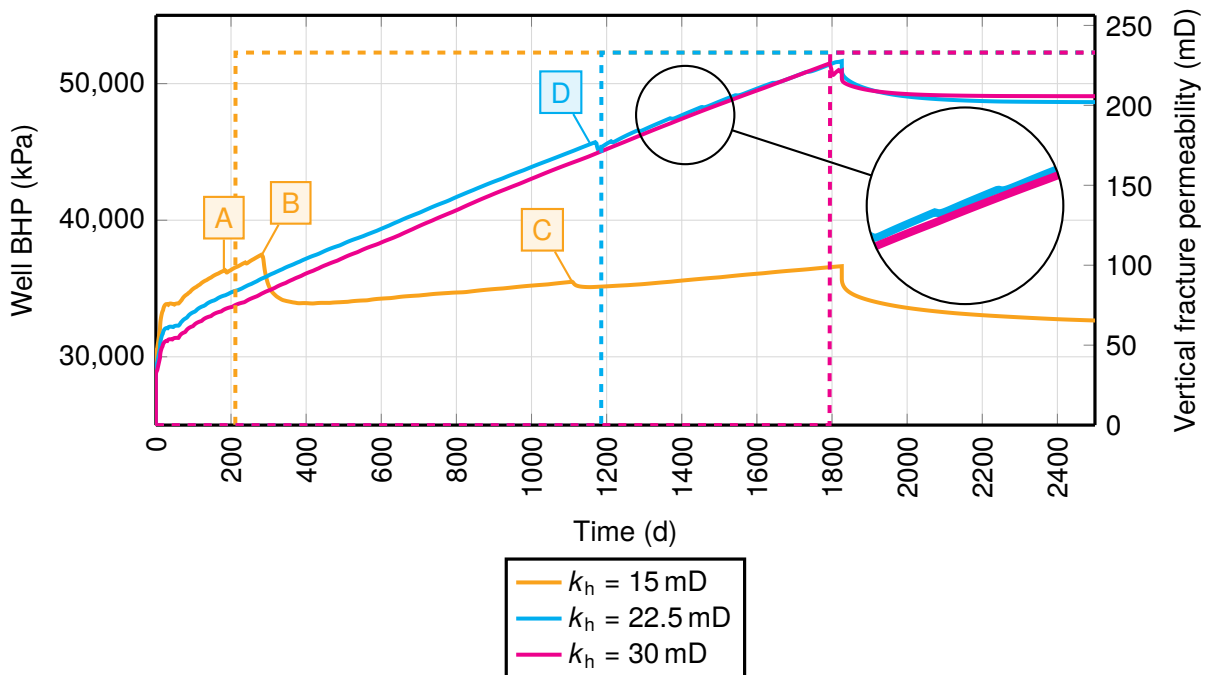


**Figure 6.1** – Well BHP (solid) and fracture vertical permeability (dashed) at the bottom of the caprock with time.

Increasing the matrix permeability initially increases both the vertical and horizontal flow components (fig. 6.2). Indeed, a higher permeability means a higher mobility, and hence less resistance to flow both horizontally and vertically. To compound this effect, the lower injection pressure resulting from higher permeability also reduces the supercritical CO<sub>2</sub> density, which implies greater buoyant forces and hence greater vertical flow (fig. 6.3). [51], [126] This could explain the greater magnitude of the increase in vertical flow component compared to the horizontal component, despite the fact that  $k_h$  is increased more than  $k_v$  (by a factor of 4). Note that free-phase CO<sub>2</sub> is considered as a gaseous component in GEM, even though it is in supercritical state.

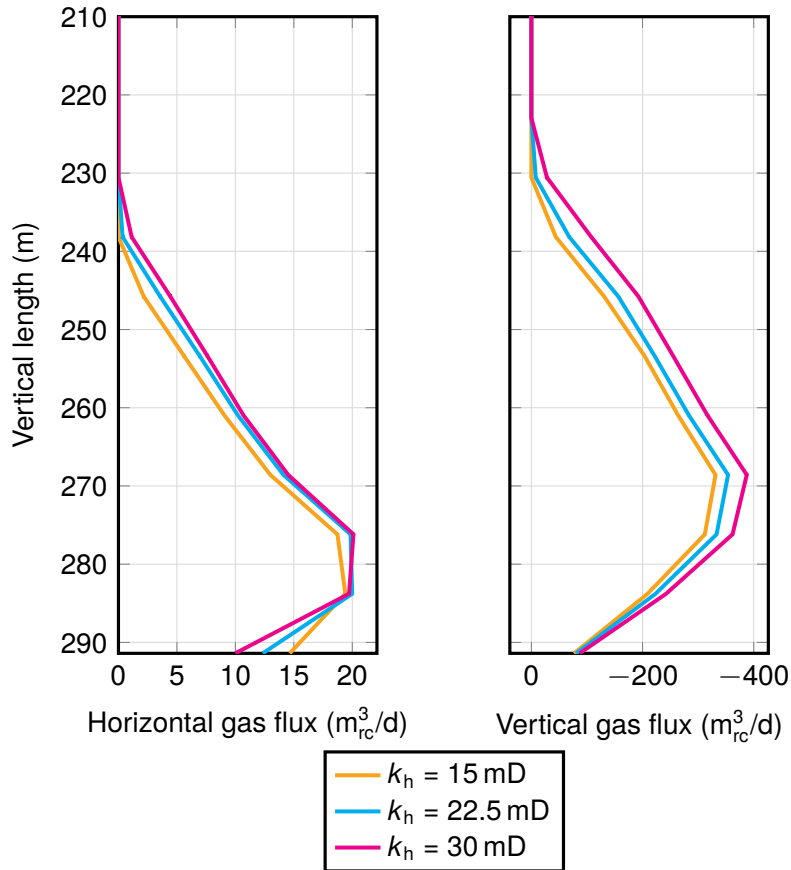


**Figure 6.2** – Gas flux along the wellbore after 3 months of injection.

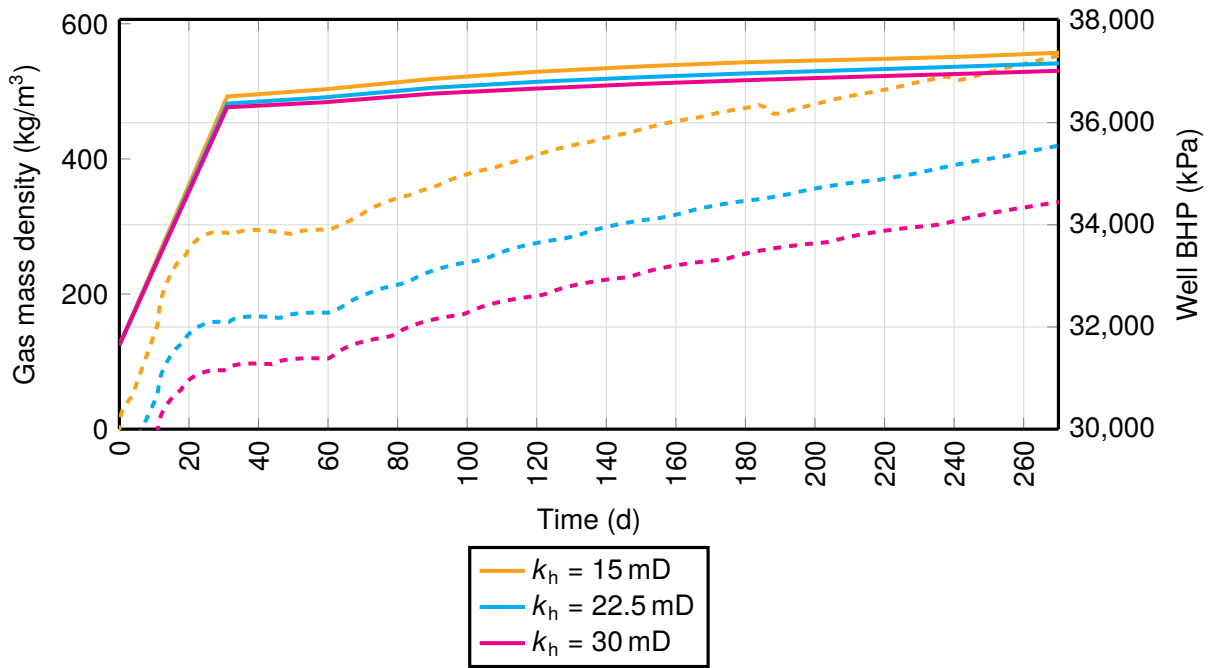


**Figure 6.3** – Gas mass density (solid) and well BHP (dashed) at the uppermost perforation.

Figure 6.4 shows a much flatter displacement profile for the higher permeability cases, corresponding to a greater horizontal dispersion of the plume. The porosity profile follows that of the vertical displacement (fig. 6.5). In the 15 mD run, the magnitude of the maximum porosity increase after 8 months is 1.15 % with respect to the original porosity of 0.13. Note that the higher the permeability, the larger is the area affected by porosity changes.

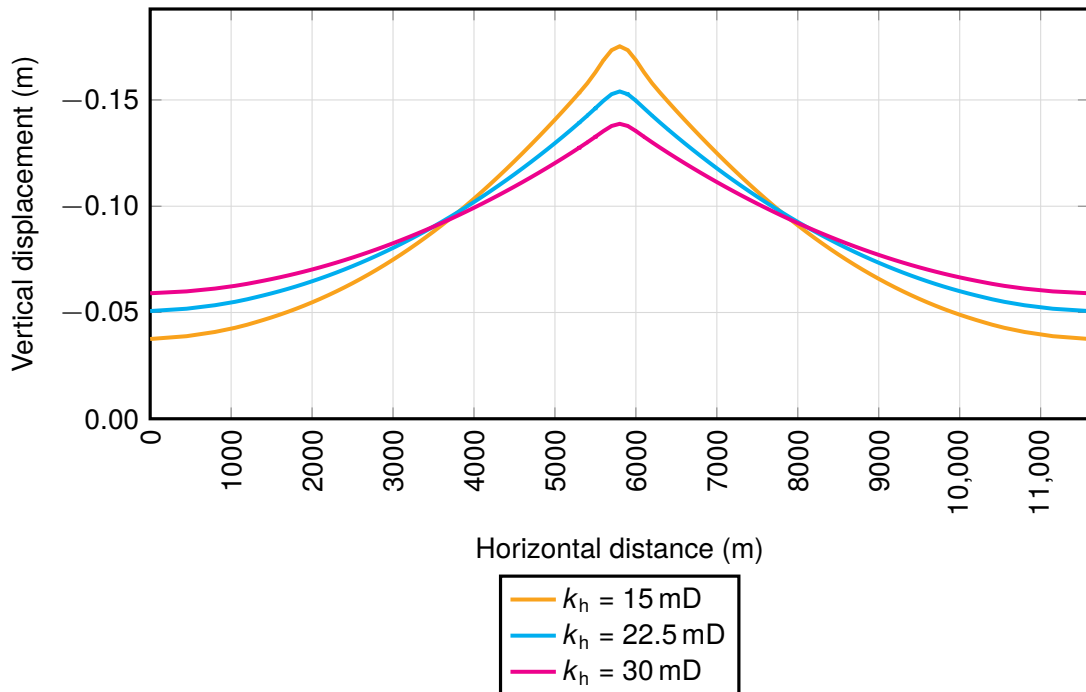


**Figure 6.4** – Vertical displacement profile along the caprock bottom after 8 months of injection (pre-breakthrough).

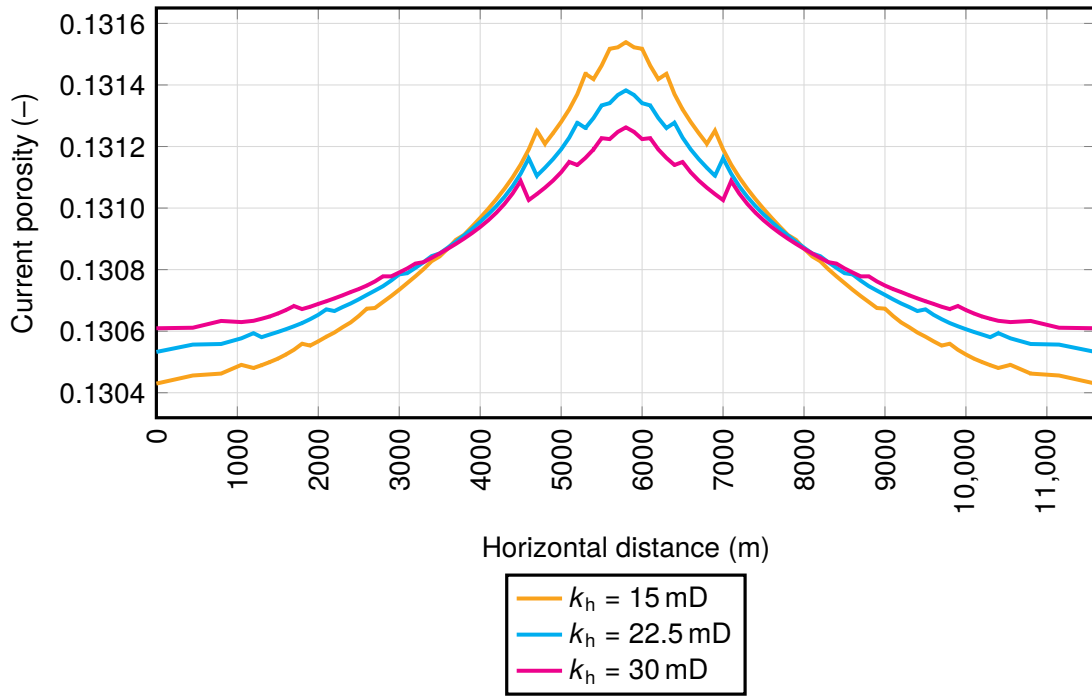


**Figure 6.5** – Current porosity profile along the caprock bottom after 8 months of injection (pre-breakthrough).

### 6.1.2 Matrix permeability anisotropy

The vertical-to-horizontal matrix permeability ratio is set to 0.25, 0.5, 0.75 and 1 respectively; horizontal matrix permeability remains unchanged at 15 mD.

The gravity number  $N_g$  is proportional to  $k_v$ , which increases with the anisotropy ratio. Consequently, at higher anisotropy ratios, the flow of the plume is dominated by gravity forces and the vertical flux component increases (fig. 6.6). Nevertheless, the increased buoyant force does not result in an earlier cracking of the underside of the caprock, as the first crack appears after 181 d in all four cases. In fact, it is apparent from fig. 6.7 that all runs share the same pre-breakthrough displacement curve. After the caprock has been breached however, a higher  $k_v/k_h$  results in a lower vertical displacement.

6 Sensitivity analysis

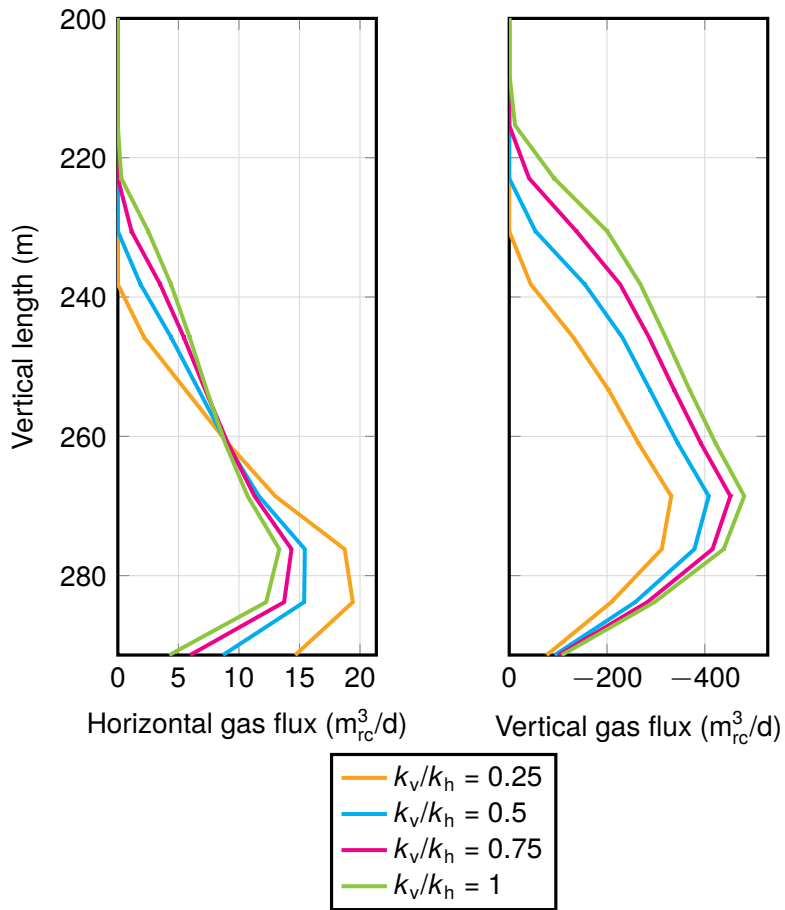
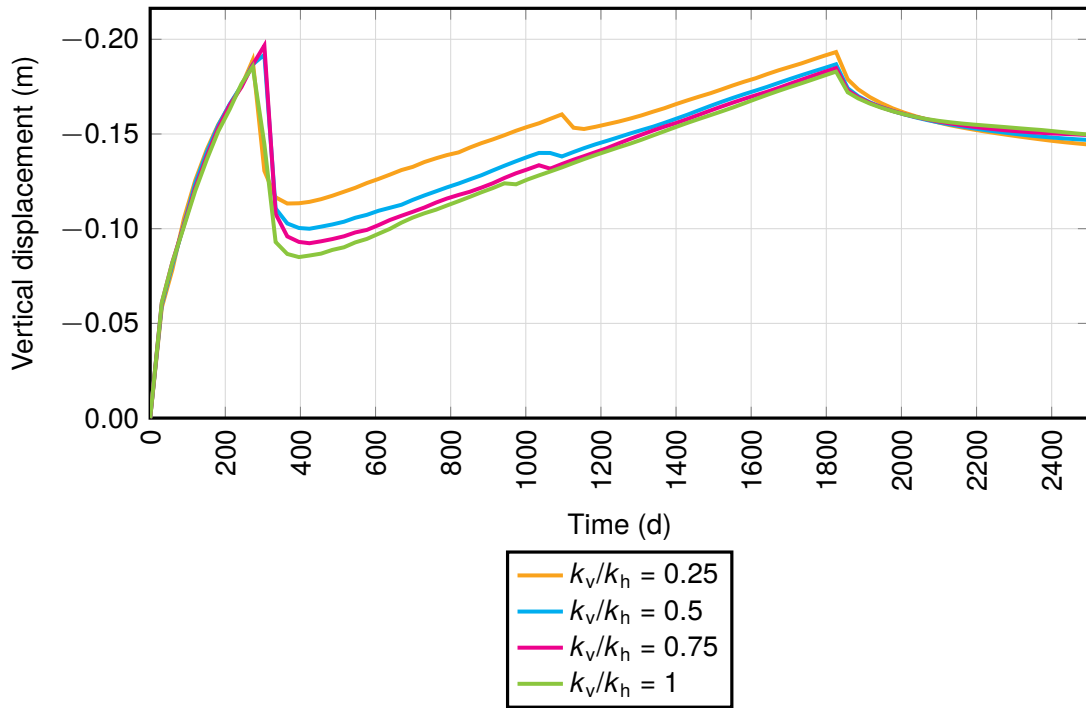


Figure 6.6 – Gas flux along the wellbore after 3 months of injection.



**Figure 6.7** – Peak vertical displacement at the bottom center of the caprock over time.

### 6.1.3 Porosity

In this run, the aquifer porosity is increased from 0.13 to 0.27 and 0.41 respectively.

Because the reservoir can accommodate more fluid at higher porosities, the required injection pressure is lower, hence the slope of the BHP curve pre-failure is less steep (fig. 6.8). This corresponds to the prediction from the analytical solution, where the flowing bottomhole pressure for an injector in transient flow can be written as

$$p_{wf} = p_i + \frac{q\mu}{2\pi kh} \ln \left( 2.25 \frac{kt}{\mu c_t \phi r_w^2} + 2S \right), \quad (6.1)$$

where it is apparent that an increase in  $\phi$  leads to a decrease in  $p_{wf}$ . Note that because of the logarithm, the influence of porosity variations on the BHP is greater when  $\phi$  is low than when it is high.

While the initial static pressure is the same in all runs (initialization values are unchanged), the new static pressure after the end of injection is lower in the high porosity case, as the injected fluid is contained inside a larger pore volume. The initial (lower) value of reservoir pore volume is roughly  $5 \times 10^7 \text{ m}^3$  with  $\phi = 0.13$ ,  $7.6 \times 10^7 \text{ m}^3$  with  $\phi = 0.21$ , and  $10^8 \text{ m}^3$  with  $\phi = 0.41$ . Pore volume increases slightly with time, as porosity increases with stress.

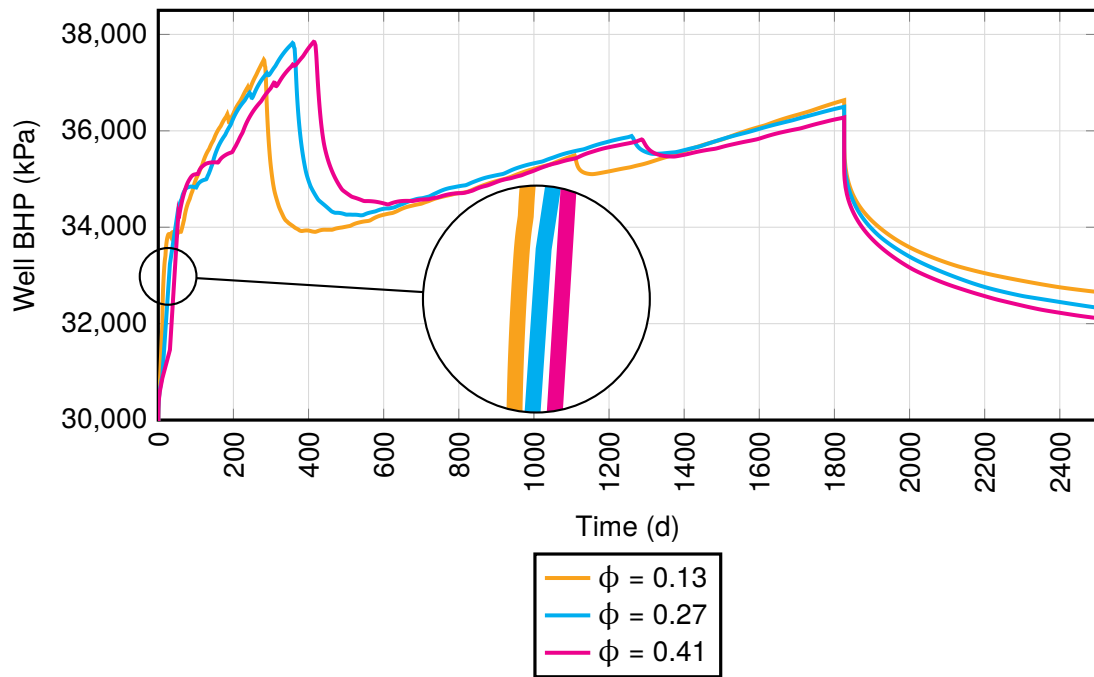


**Figure 6.8** – Well BHP with time.

Plume velocity is negatively affected by the higher porosity, both horizontally and vertically (fig. 6.9); because the pore volume is higher, more free-phase  $\text{CO}_2$  can be stored in each block, and the injected volume is concentrated into a smaller plume (fig. 6.10).

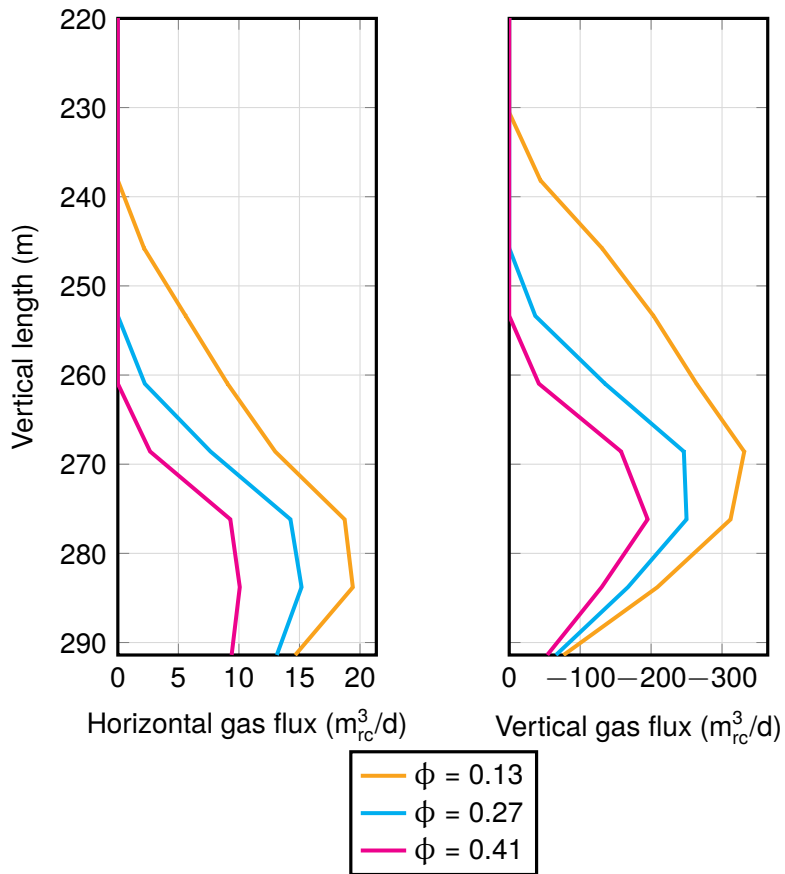


**Figure 6.9** – Gas flux along the wellbore after 3 months of injection.

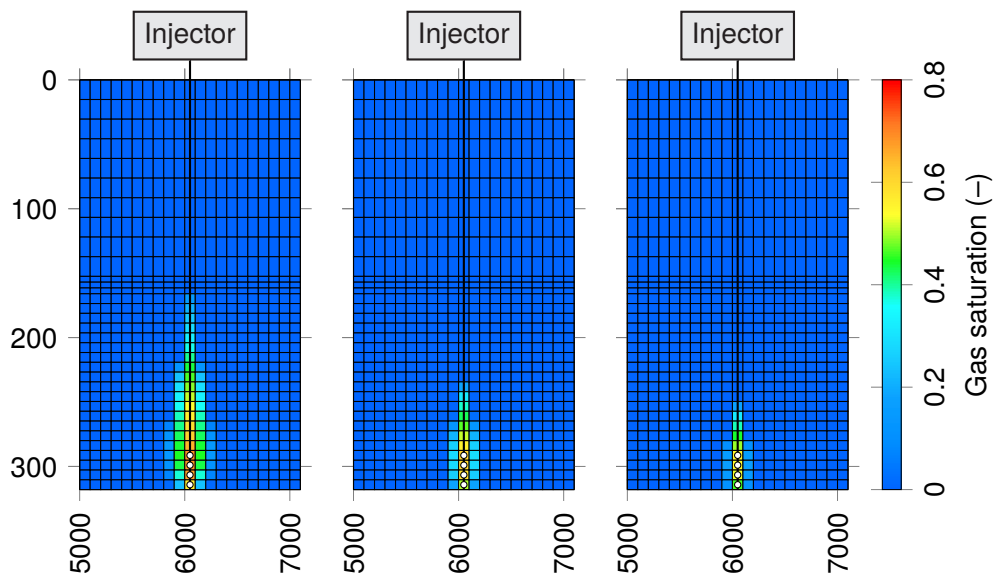


**Figure 6.10** – Gas saturation after one year of injection: from left to right,  $\phi = 0.13$ ,  $\phi = 0.27$ , and  $\phi = 0.41$ .

Because the interstitial velocity (in particular vertical) of the plume decreases, the buoyant

force becomes weaker and the opening of fractures in the caprock is delayed (fig. 6.11). By increasing  $\phi$  from 0.13 to 0.41, fracture opening is delayed by 4 months.

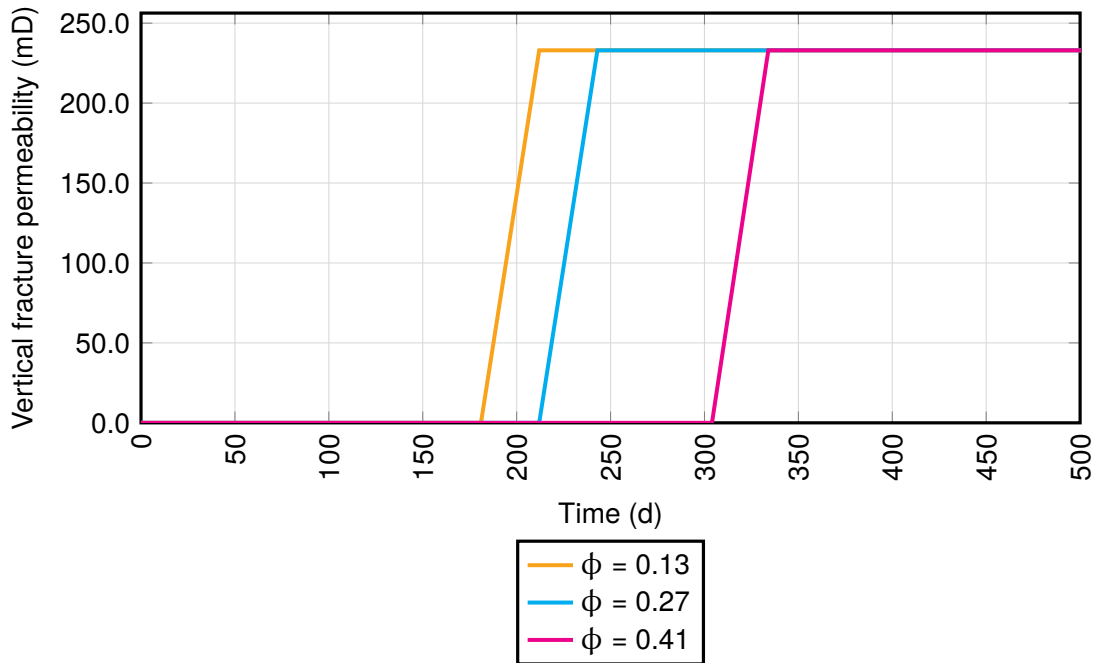


**Figure 6.11** – Vertical fracture permeability at the bottom center of the caprock.

#### 6.1.4 Young modulus

The Young modulus of the reservoir rock is increased from 5 to 30 GPa in increments of 5 GPa.

Rocks which have a high Young modulus are stiff and do not deform easily, as shown by the vertical displacement profile in fig. 6.12. In consequence, the reservoir cannot readily react to the pressure increase caused by injection, and the slope of the BHP curve is steeper (fig. 6.13).

However, despite the lower amount of deformation (both horizontal and vertical), total horizontal stress in the reservoir is increased at higher values of  $E$  (fig. 6.14) because of the higher pore pressure (*cf.* Terzaghi's law). On the other hand, the higher effective horizontal stresses in the caprock cause a delay in fracture opening as compared to the more ductile rock, as it takes a higher amount of unloading for fractures to open. Note that horizontal effective stress is the value that governs fracture opening, since the fractures relevant to caprock failure are vertical.

## 6 Sensitivity analysis

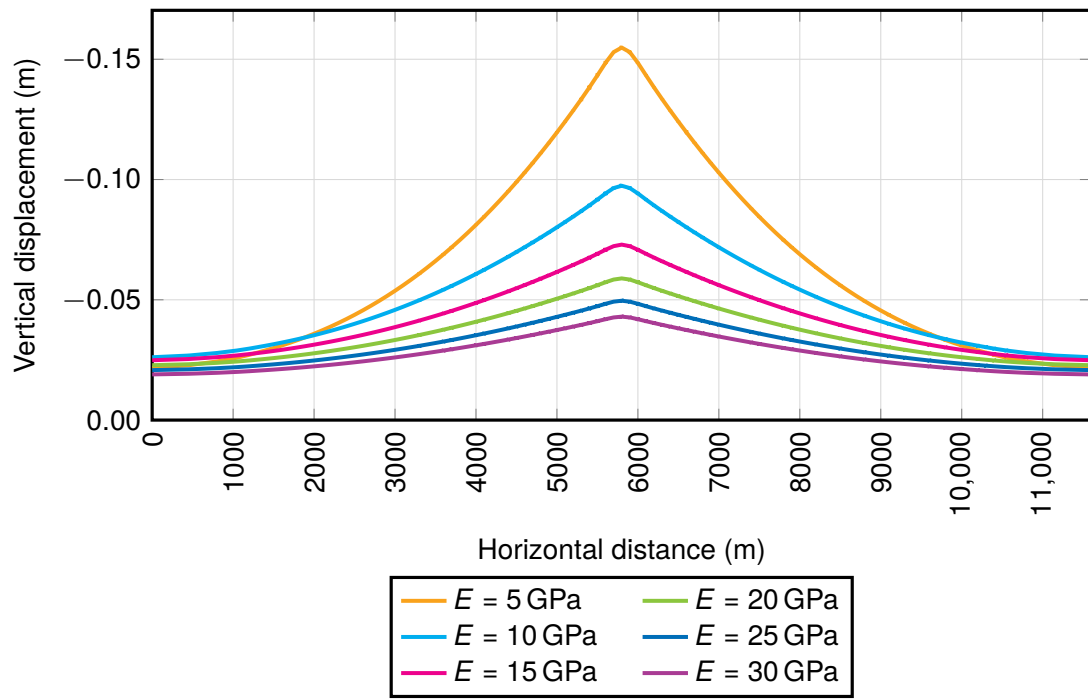


**Figure 6.12** – Vertical displacement profile along the bottom of the caprock after 6 months of injection (pre-failure).

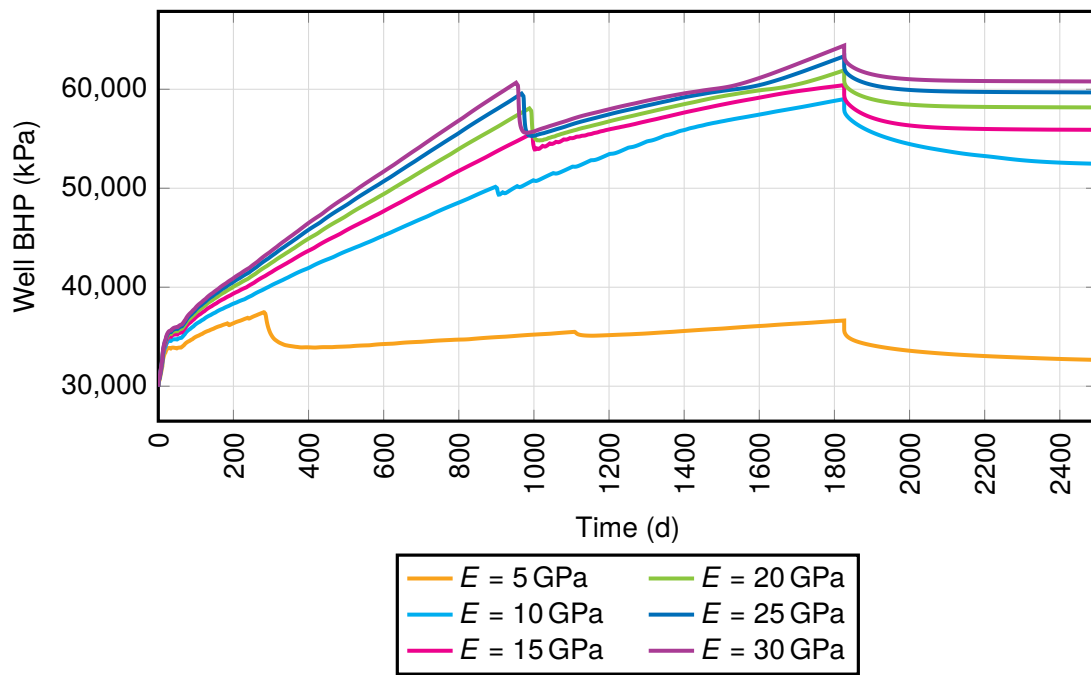


**Figure 6.13** – Well BHP with time.

## 6 Sensitivity analysis

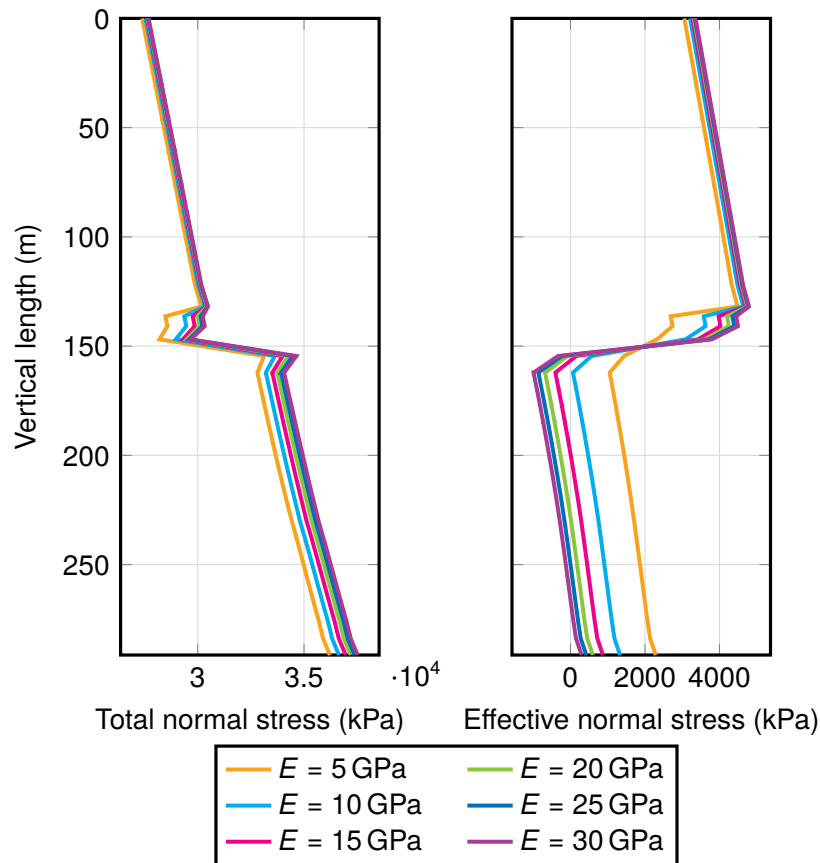


**Figure 6.14** – Horizontal stresses along the wellbore after 4 months of injection (pre-failure).

Finally, note the effect of the Young modulus on the cumulative injected mass at the onset of failure (fig. 6.15). Increasing the Young modulus initially has a markedly positive effect on the injected mass at failure, but the effect starts becoming slightly negative beyond 15 GPa. At 35 GPa and above, the reservoir rock becomes so stiff that vertical displacement is very low, and fractures in the caprock can only open slightly (not shown). In this last case, vertical fracture permeability remains in the nanodarcy range after failure.

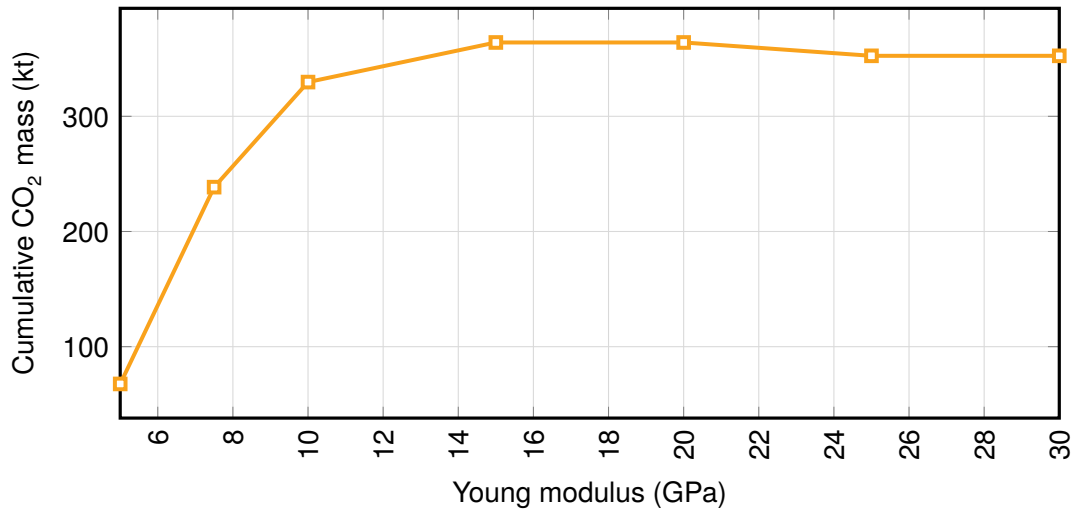


**Figure 6.15** – Cumulative injected mass at first crack as a function of Young modulus.

### 6.1.5 Poisson ratio

The Poisson ratio for the storage formation is changed from the original 0.25 to 0.2, 0.3 and 0.35.

By increasing the Poisson ratio, both effective and total horizontal normal stress are lower in the aquifer and higher in the caprock (fig. 6.16). As the reservoir has a greater propensity to deform laterally, there is a stronger process of unloading and the effective stress is lower. In order to compensate for the lower effective stress in the aquifer,  $\sigma'_h$  in the caprock must increase by a corresponding amount.

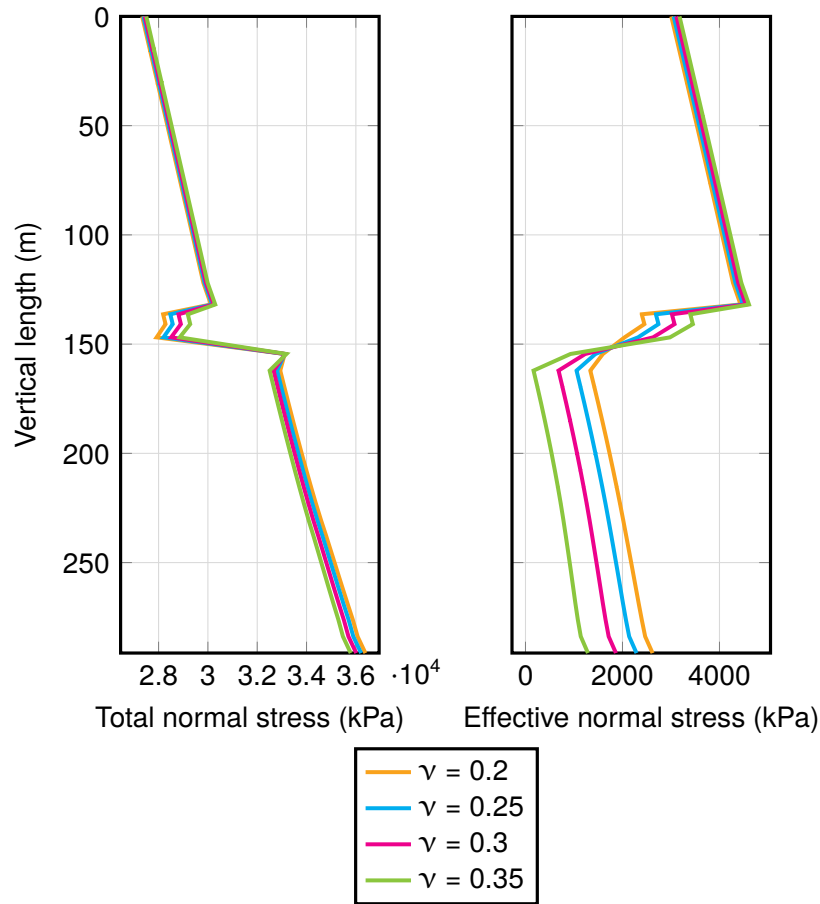


**Figure 6.16** – Horizontal stresses along the wellbore after 4 months of injection (pre-failure).

The higher is  $\nu$ , the more the reservoir will preferentially deform laterally, thus decreasing the slope of the peak vertical displacement curve (fig. 6.17). Furthermore, with higher effective horizontal stresses in the caprock (higher  $\nu$ ), vertical and subvertical fractures can sustain a higher degree of unloading before tensile opening (fig. 6.18). In fact, in the  $\nu = 0.35$  scenario, a fracture opens on the underside of the caprock but never propagates through the caprock; consequently, the built-up pressure is not released and vertical displacement does not show a sharp drop. Finally, note that in the  $\nu = 0.3$  run, the fracture permeability increase in gridblock {51,1,11} (center block) does not correspond to the drop in vertical displacement (A), as the caprock is first breached in the two adjacent blocks {50,1,11} and {52,1,11}.

6 Sensitivity analysis

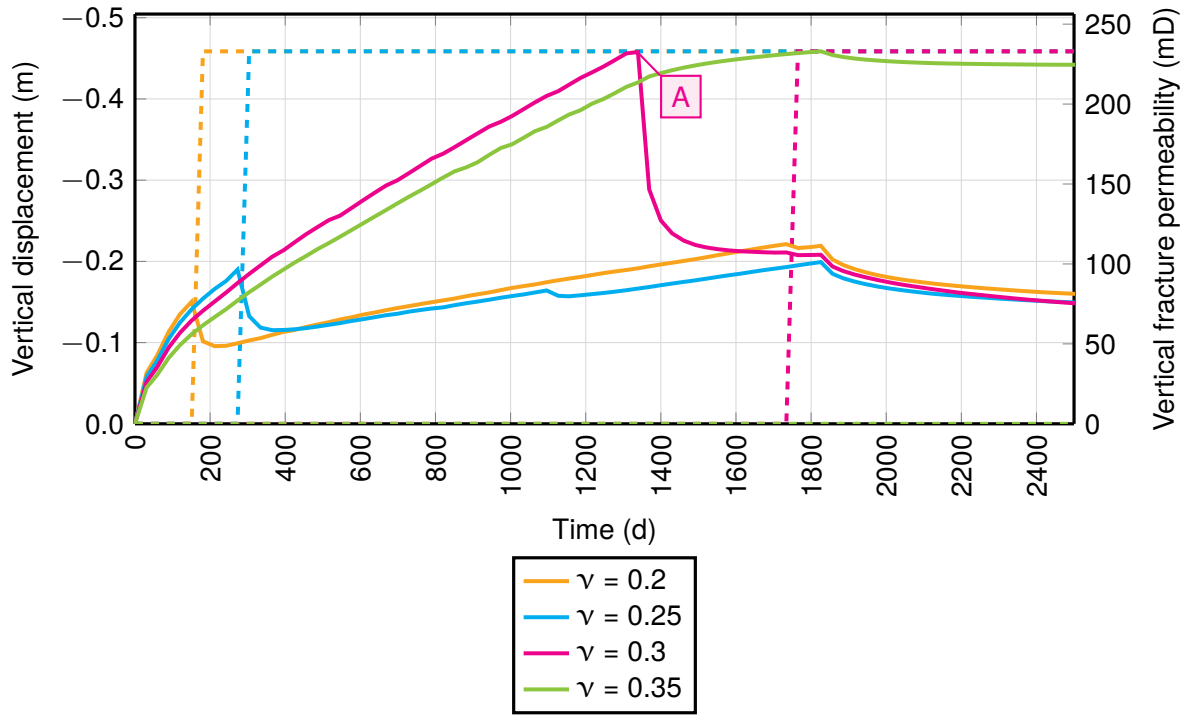


**Figure 6.17** – Peak vertical displacement (solid) and fracture permeability (dashed) over time at the top center of the caprock.

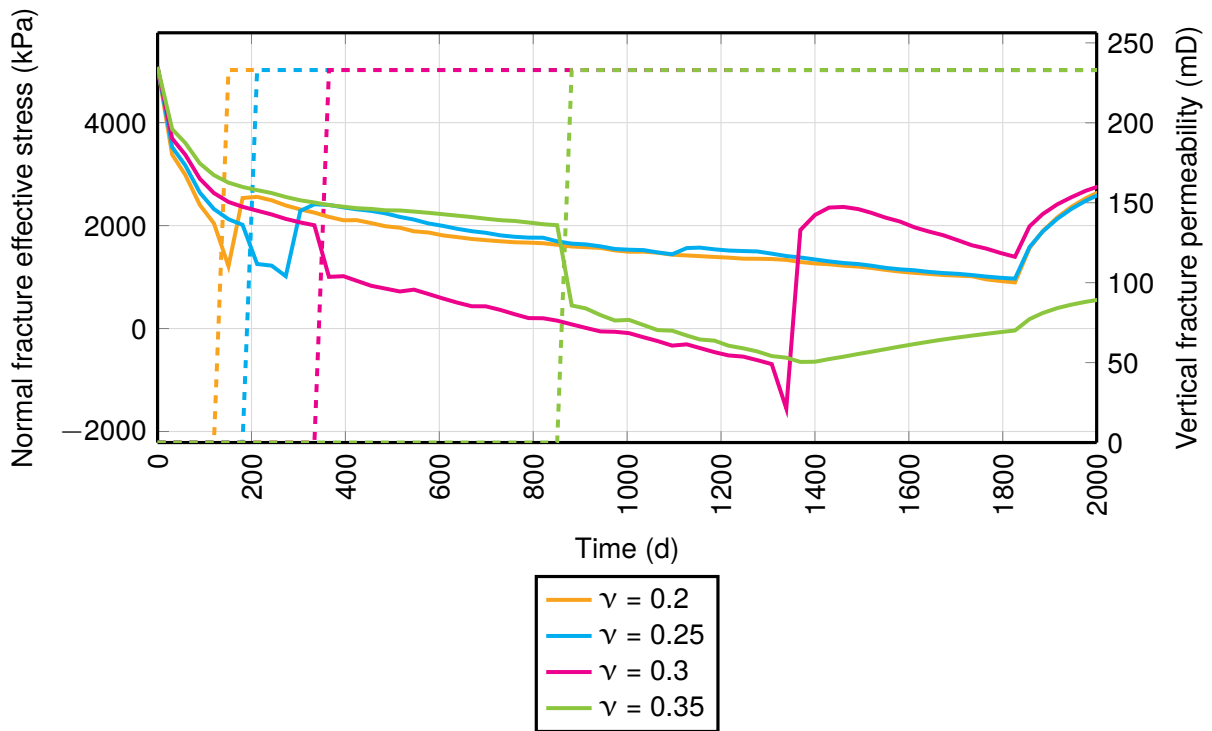


**Figure 6.18** – Fracture normal effective stress (solid) and fracture permeability (dashed) over time at the bottom center of the caprock.

### 6.1.6 Dip angle

In this section, the whole model is inclined by 10 and 20°. The original overburden top of 2263 m is kept the same directly above the well ( $\{51,1,1\}$ ), so as to maintain the same CO<sub>2</sub> density at the perforations.

Higher dip angles promote updip lateral movement of the plume (fig. 6.19). As a consequence, the time to reach top seal also increases with the dip angle (fig. 6.20), due to the larger vertical distance between the perforation and the point of contact of the plume below the caprock. The time to top seal is 334 d for no dip, 365 d at 10° and 455 d at 20°. Furthermore, the time to failure is also increased due to the larger horizontal dispersion of the plume (fig. 6.21), while the vertical displacement is decreased (fig. 6.22).

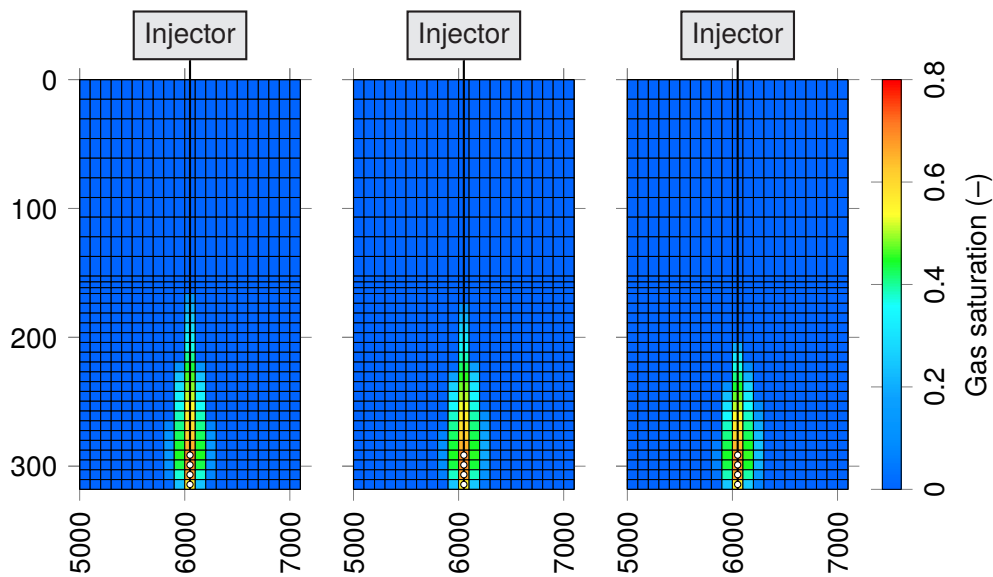


**Figure 6.19** – Gas saturation after one year of injection: from left to right,  $\alpha = 0^\circ$ ,  $\alpha = 10^\circ$ , and  $\alpha = 20^\circ$ ; maps are untilted for readability.

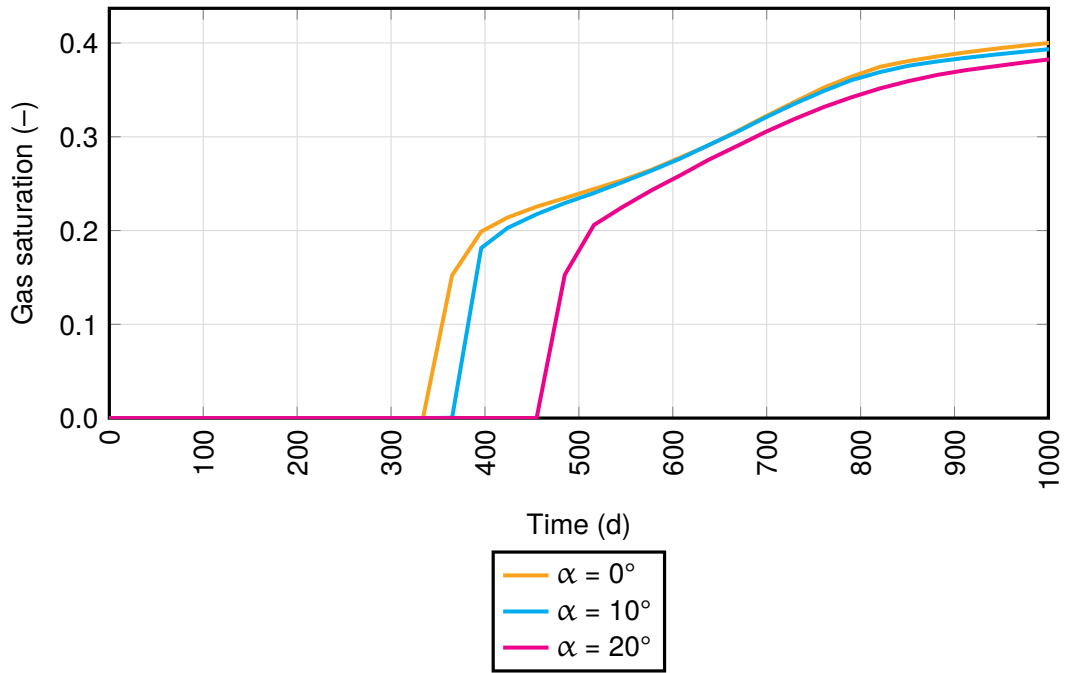


Figure 6.20 – Gas saturation with time in below the caprock.

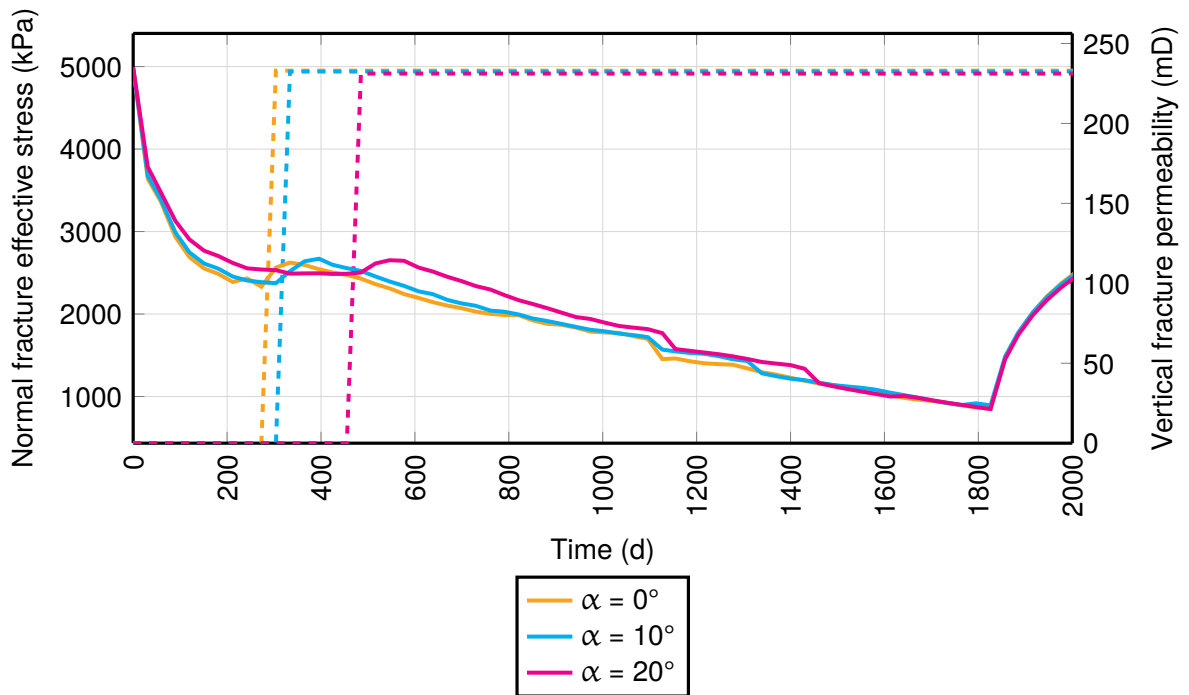
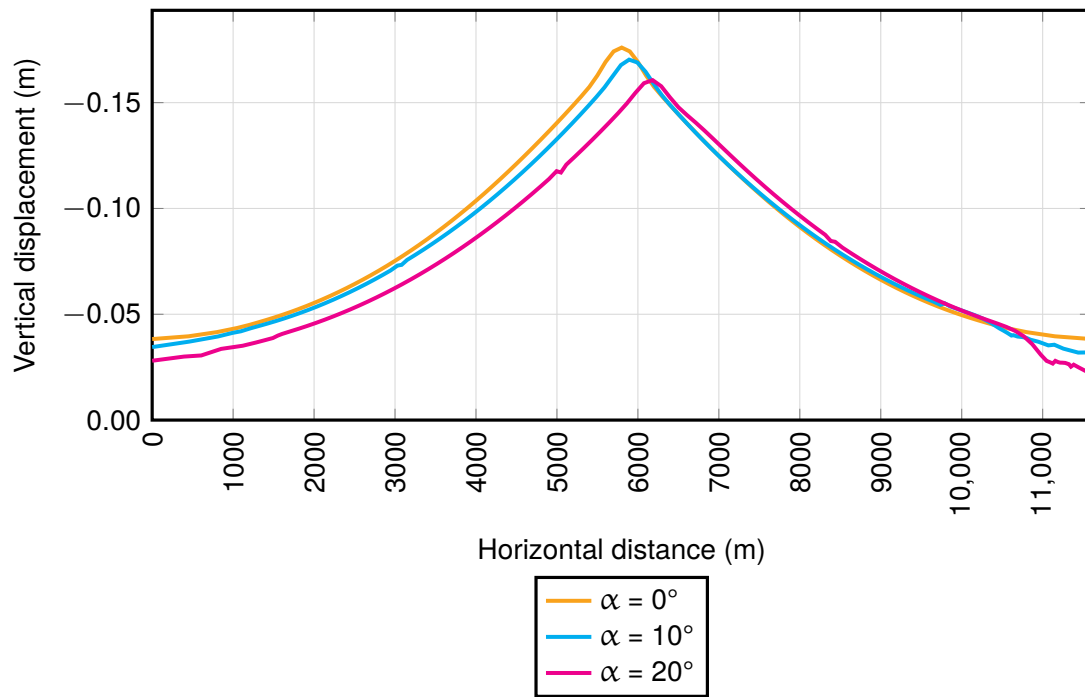


Figure 6.21 – Fracture normal effective stress (solid) and fracture permeability (dashed) over time at the top center of the caprock.



**Figure 6.22** – Vertical displacement profile along the caprock bottom after 8 months of injection (pre-breakthrough).

### 6.1.7 Salinity

The base case (0 ppm) is compared against two different brines of salinity 100,000 and 200,000 ppm. To isolate the effect of salinity, brine viscosity, compressibility and density are left unchanged.

Increasing salinity slightly increases horizontal plume mobility and has the opposite effect on vertical mobility (fig. 6.23). Between the base case and the 200,000 ppm run, the change in gas flux on 01-04-2030 is  $-16.1 \text{ m}^3/\text{d}$  vertically ( $-4.9\%$ ) and  $+0.7 \text{ m}^3/\text{d}$  horizontally ( $+3.7\%$ ). The time for the plume to reach the underside of the caprock decreases with increasing salinity, in accordance with the greater vertical mobility.

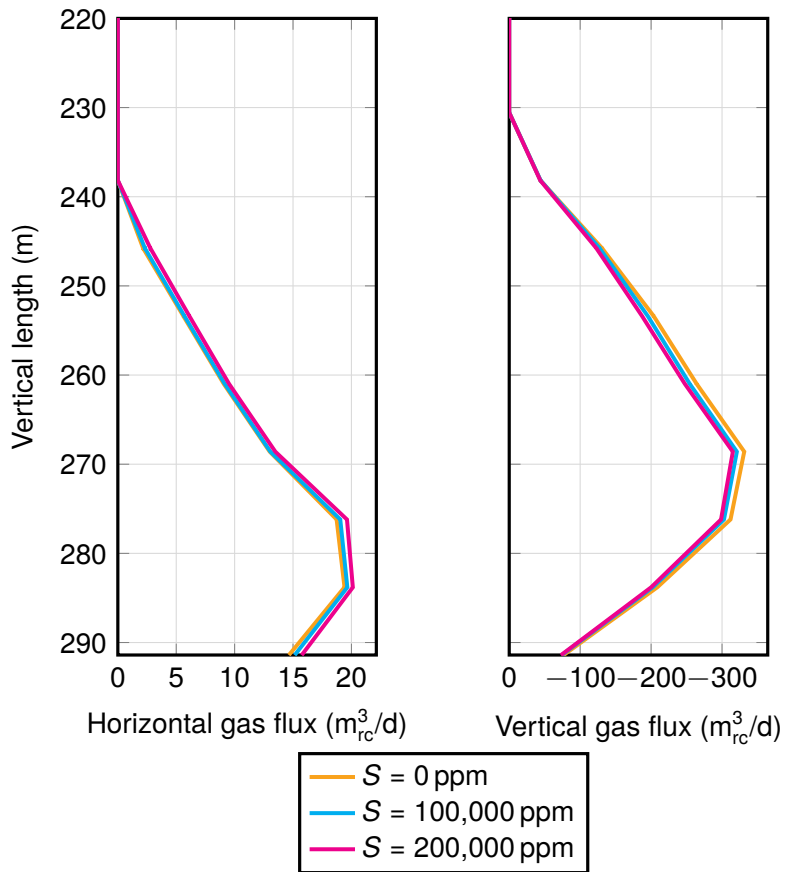


**Figure 6.23** – Gas flux along the wellbore after 3 months of injection.

The increased buoyancy force causes an amplification of caprock arching (fig. 6.24), as well as an earlier fracturing of the underside of the caprock (fig. 6.25); in the 200,000 ppm run, the first fracture appears 4 months earlier than in the base model.

6 Sensitivity analysis

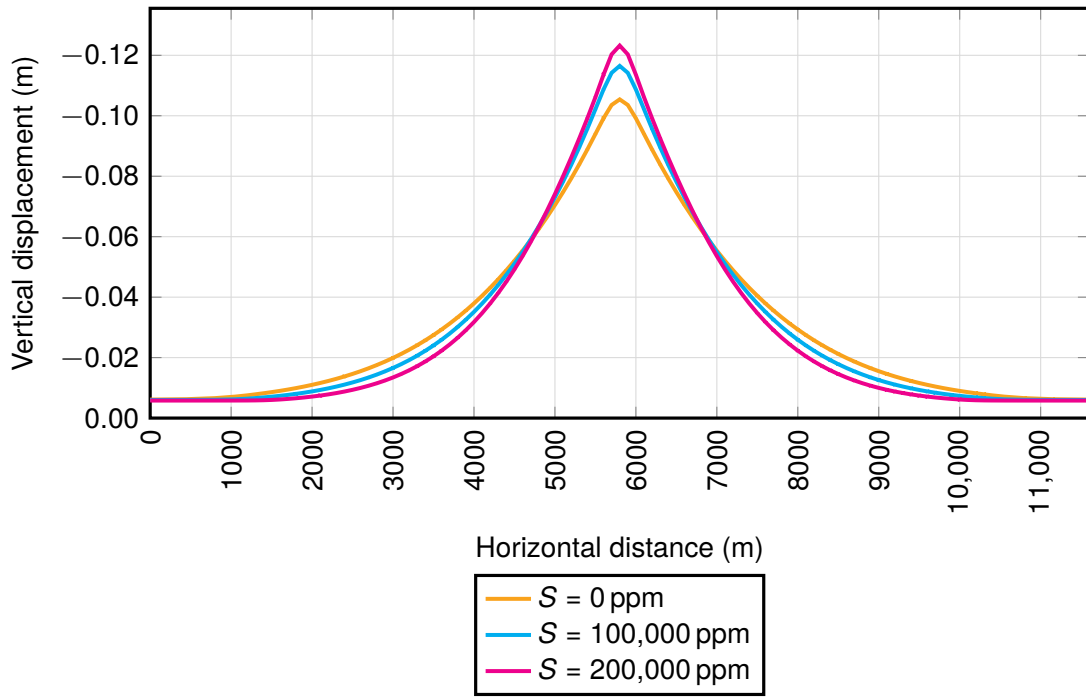


Figure 6.24 – Vertical displacement profile along the caprock bottom after 3 months of injection (pre-breakthrough).

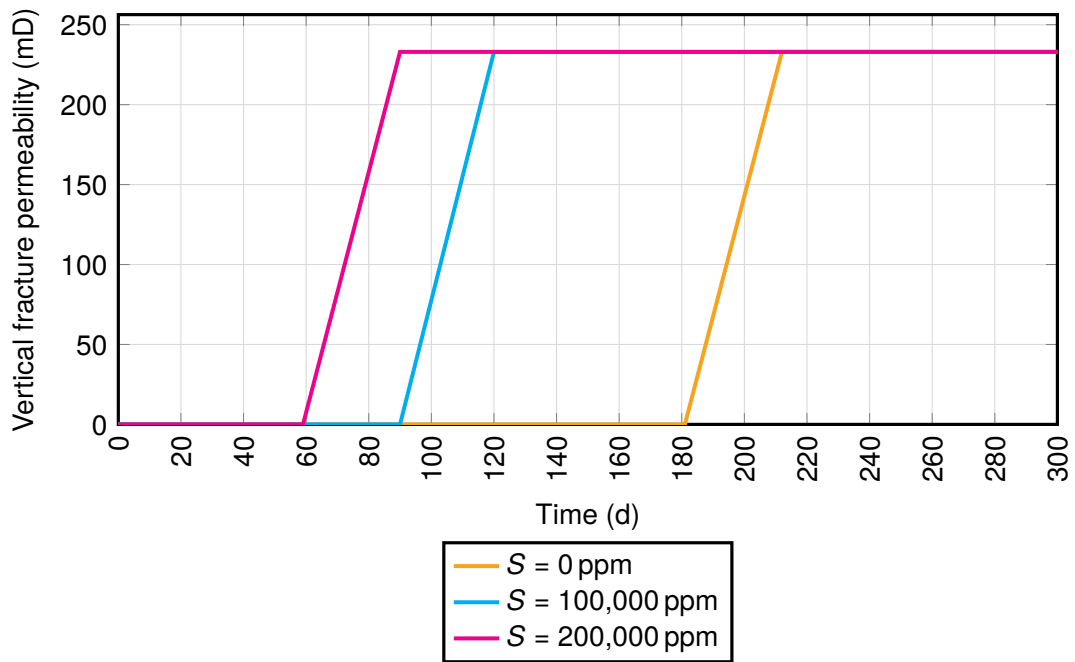
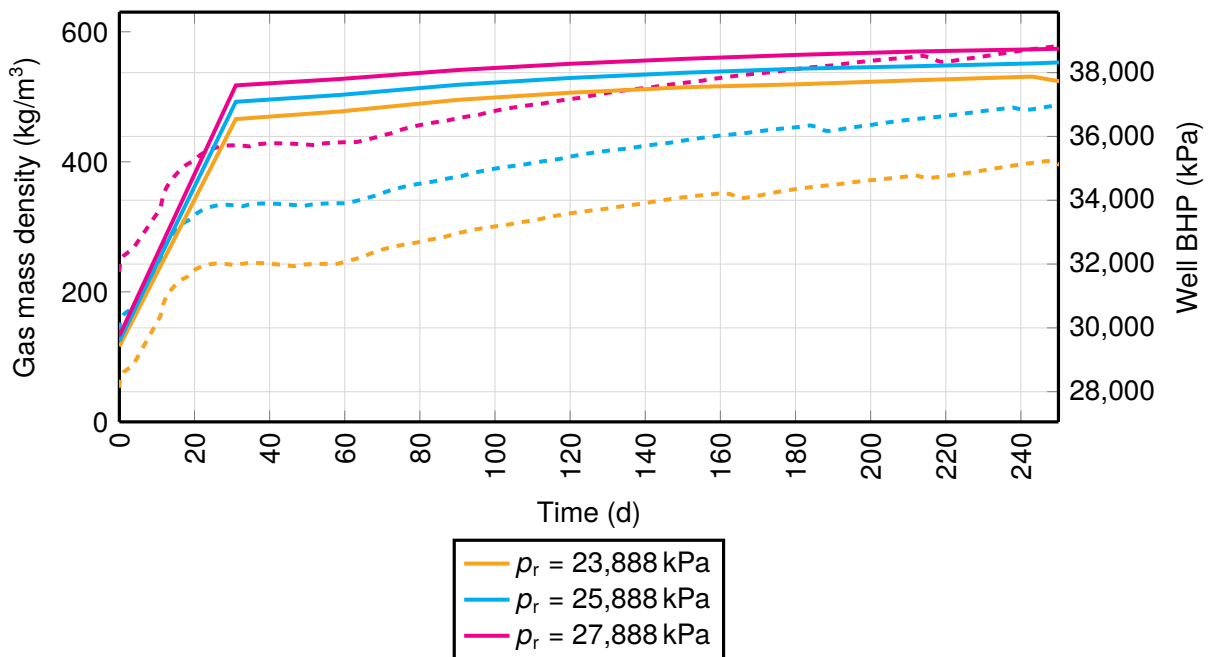


Figure 6.25 – Vertical fracture permeability at the bottom center of the caprock with time.

### 6.1.8 Reference pore pressure

In the base case, the initial pore pressure distribution is calculated based on a reference pressure of 25,888 kPa at 2429 m. The reference pressure is respectively increased and decreased by 2000 kPa to study the effect of initial pore pressure distribution on reservoir behavior. Note that changing the reference pressure has no effect on the initial effective stress distribution, which is initialized according to table 5.2 and independently from the pore pressure.

The variation of pore pressure corresponds to an equivalent variation of well BHP; at lower bottomhole pressures, the density of the injected fluid is also lower (fig. 6.26). The lower density of CO<sub>2</sub> translates as a stronger buoyant force (higher gravity number  $N_g$ ), and hence a larger vertical gas flux since the density difference between the formation fluid and the injected fluid is greater (fig. 6.27). Because of the higher magnitude of the buoyant force, the displacement curve pre-failure is slightly steeper (fig. 6.28).



**Figure 6.26** – Gas mass density (solid) and well BHP (dashed) at the uppermost perforation.

6 Sensitivity analysis

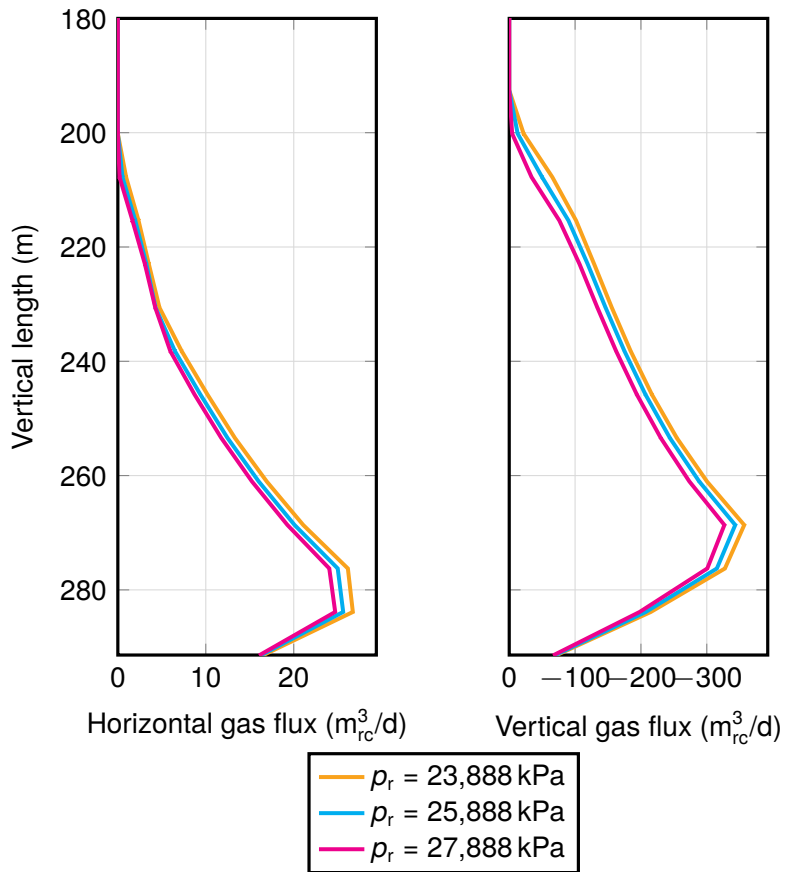


Figure 6.27 – Gas flux along the wellbore after 8 months of injection.

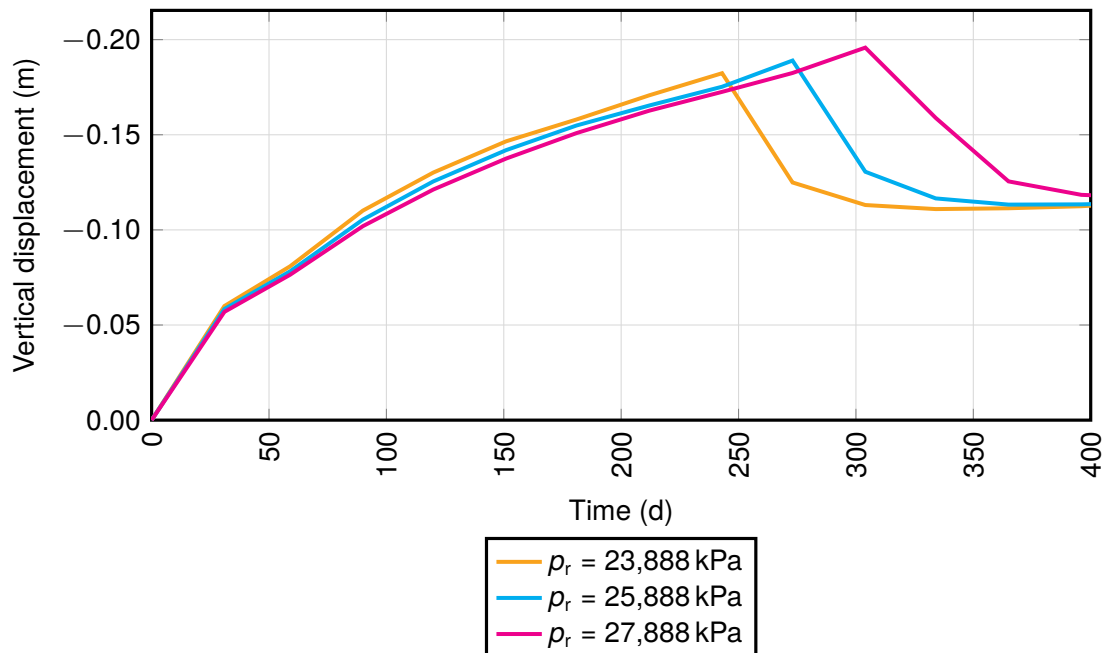
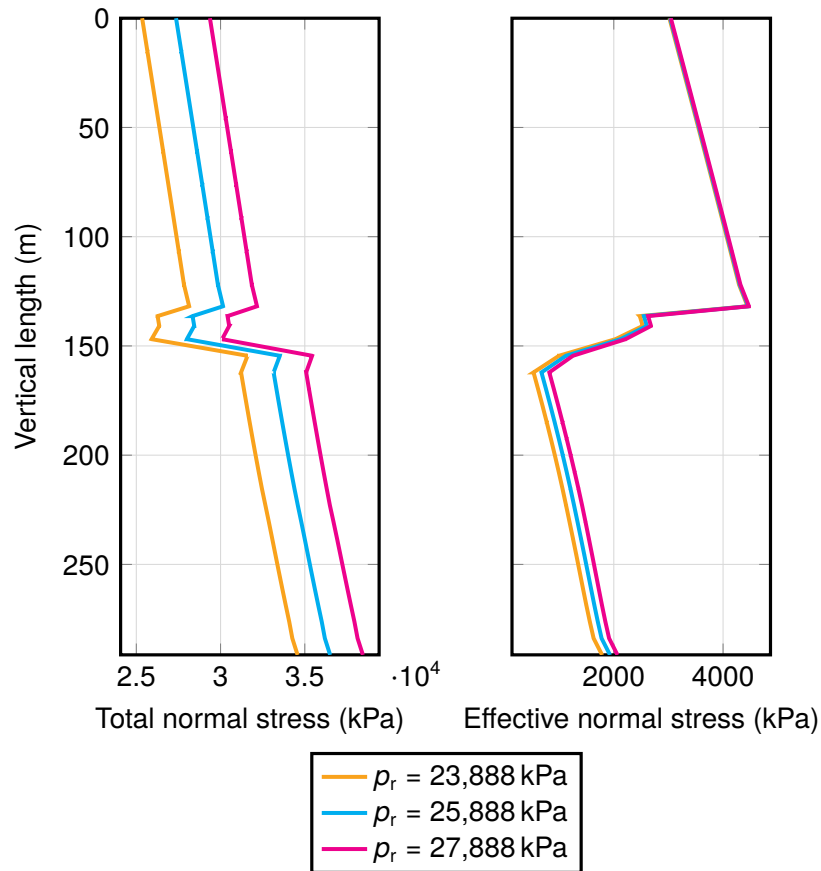


Figure 6.28 – Peak vertical displacement at the bottom center of the caprock over time.

## 6 Sensitivity analysis

The increased pore pressure translates as higher total and effective normal stresses, both in the reservoir and the caprock (fig. 6.29). Consequently, the state of stress in the caprock is brought further from failure conditions, delaying fracture onset by up to 2 months (fig. 6.30).



**Figure 6.29** – Horizontal stresses along the wellbore after 5 months of injection (pre-failure).

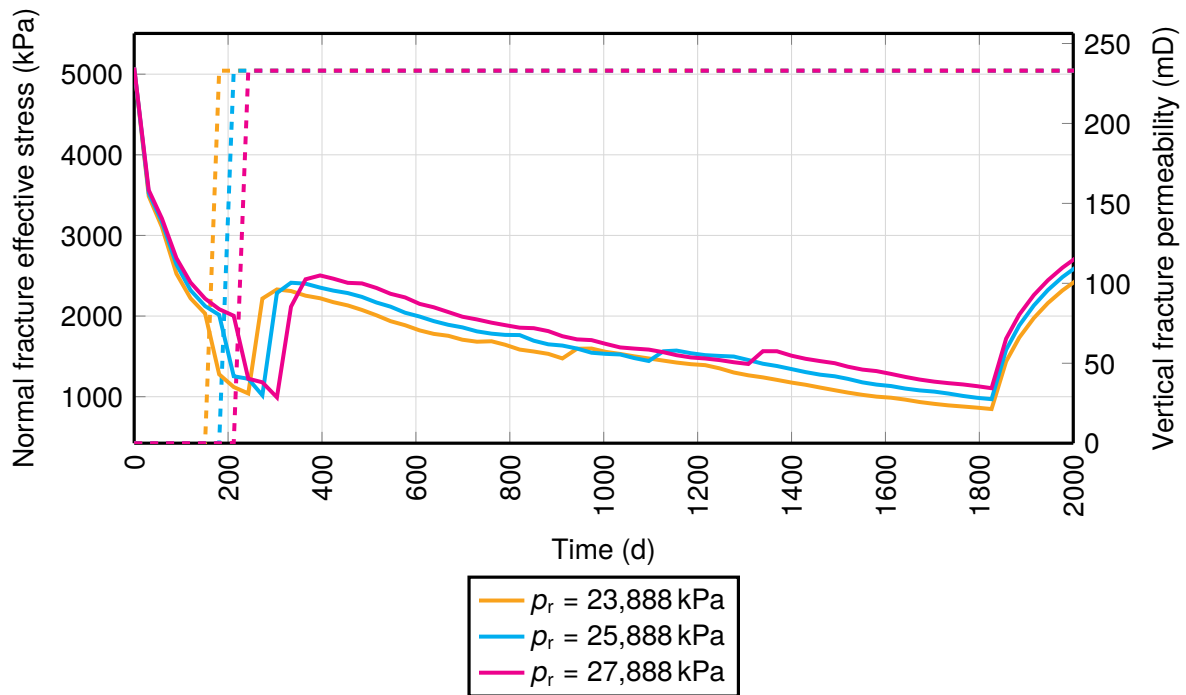


**Figure 6.30** – Fracture normal effective stress (solid) and fracture permeability (dashed) over time at the bottom center of the caprock.

## 6.2 Caprock properties

### 6.2.1 Matrix permeability

Caprock horizontal matrix permeability values ranging from  $10^{-7}$  to  $10^{-2}$  mD are tested, while the anisotropy ratio is kept the same (0.25). Horizontal fracture permeability is left unchanged at  $10^{-7}$  mD.

At the overpressure values encountered in the simulation, the caprock starts becoming permeable to water above  $10^{-4}$  mD. As shown in fig. 6.31, the pressure curve starts to deviate from the original case ( $10^{-7}$  mD) as the caprock becomes permeable; this is because some of the built-up pressure is partially relieved by formation fluid seeping out of the reservoir and into the upper aquifer. Immediately prior to gas breakthrough, the total water flux along the layer overlaying the caprock is around 0.71/d at  $10^{-4}$  mD, while it is 436 l/d at  $10^{-3}$  mD.

## 6 Sensitivity analysis

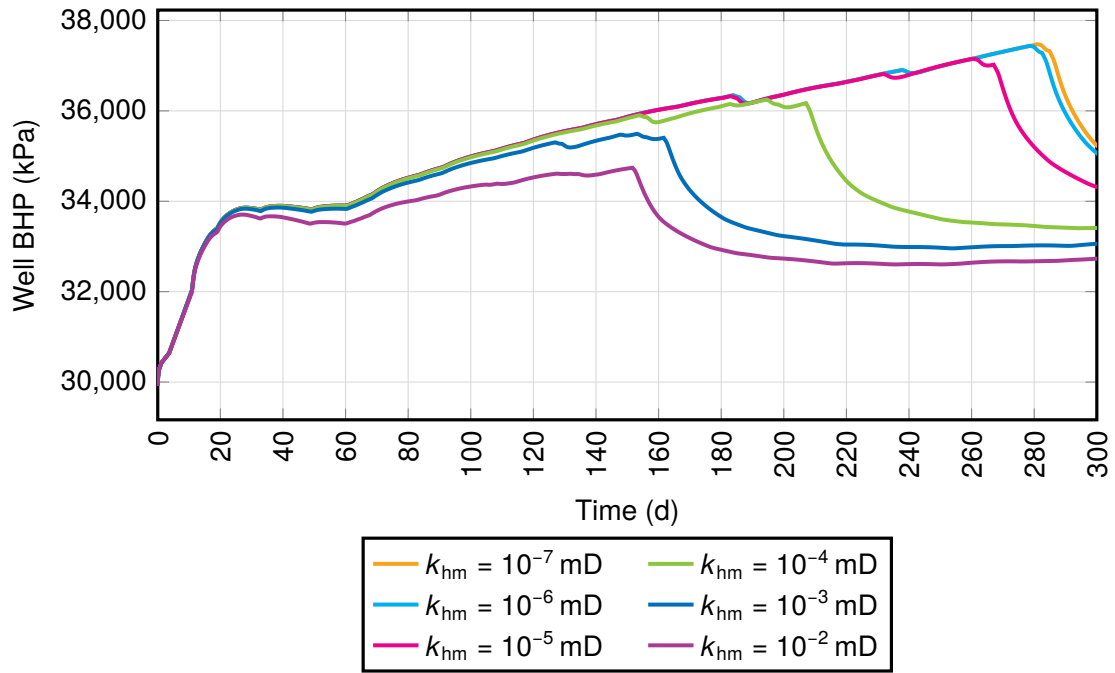


**Figure 6.31** – Well BHP with time.

Because of the higher pressure, the peak vertical displacement is highest in the caprock with lowest permeability. Nevertheless, fracture opening and propagation happens earlier in the more permeable caprock, as shown in fig. 6.32. Indeed,  $\sigma'_h$  in the caprock increases with decreasing matrix permeability, pushing the stress state away from failure conditions.

Finally, note that the lower pressure at increased permeabilities also translates as a lower density of the injected fluid. Consequently, buoyancy effects are enhanced and the plume reaches the underside of the caprock faster.

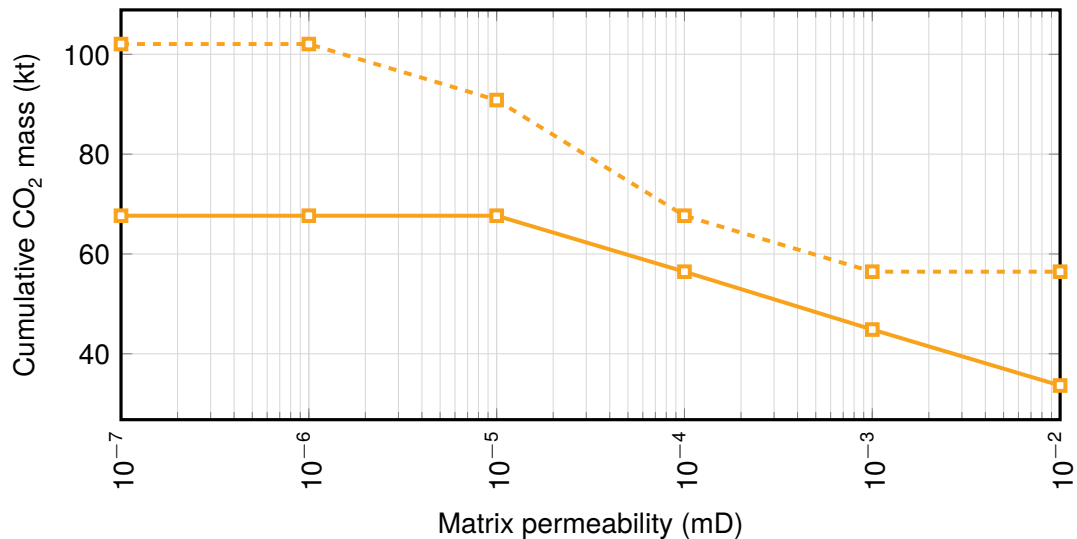


**Figure 6.32** – Cumulative injected mass at first crack (solid) and gas breakthrough (dashed) as a function of caprock matrix permeability.

### 6.2.2 Fracture permeability

The investigated values range from  $10^{-7}$  to  $10^{-2}$  mD. Caprock horizontal matrix permeability is  $10^{-7}$  mD for all runs, and the vertical-to-horizontal anisotropy ratio is 0.25 as in the original case.

As for the case of caprock matrix permeability, the caprock becomes permeable to water for values of  $k_{hf}$  above  $10^{-4}$  mD, which shows as a decreased slope of the BHP curve (fig. 6.33) compared to the original case ( $10^{-7}$  mD).

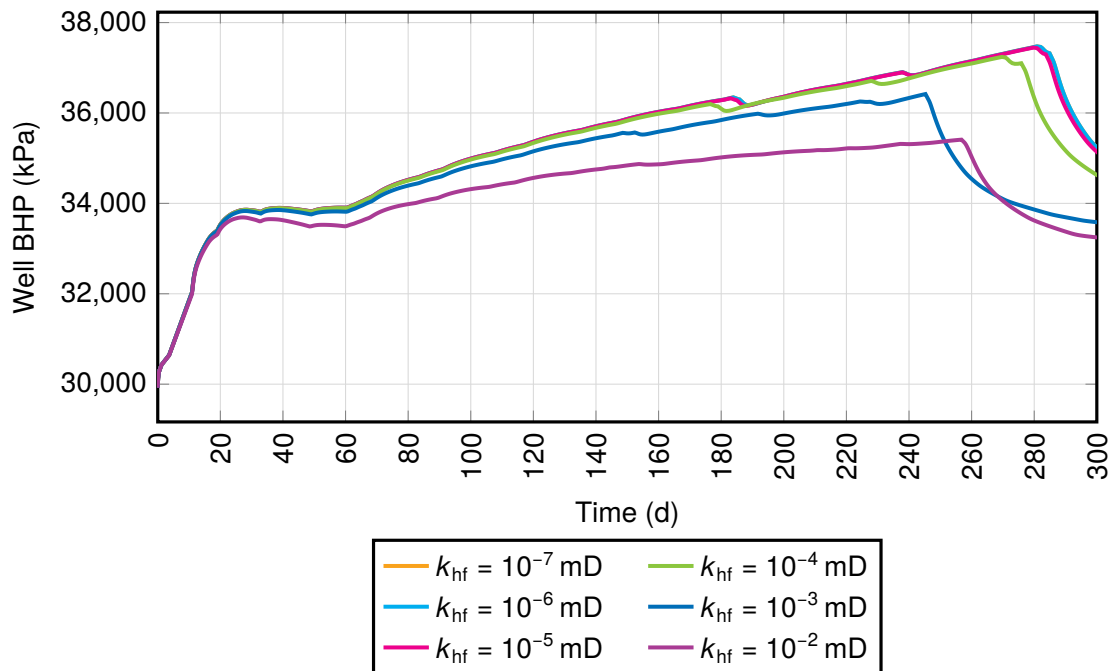
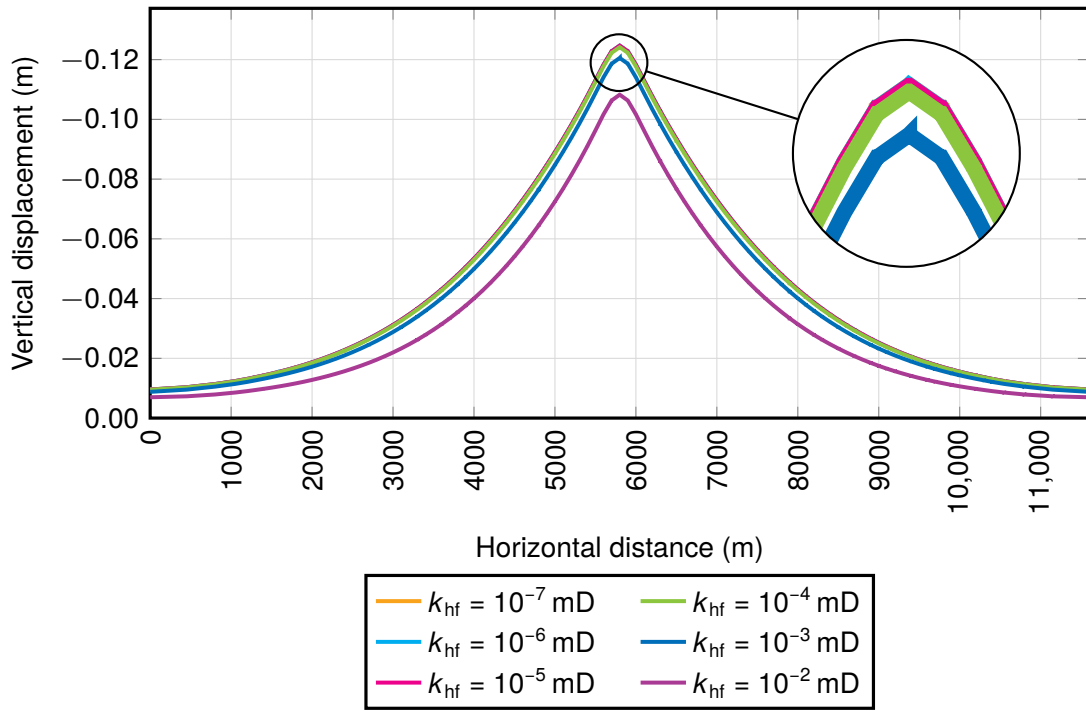


Figure 6.33 – Well BHP with time.

Because of the lower pressure in the reservoir at  $k_{hf} > 10^{-4}$  mD, the peak vertical displacement starts decreasing accordingly (fig. 6.34). For values lower than  $10^{-4}$  mD (tighter rocks), the displacement behavior becomes essentially the same across all runs.



**Figure 6.34** – Vertical displacement profile along the caprock top after 4 months of injection (pre-failure).

The effect of fracture permeability on the injected mass at failure shows a similar trend as that of matrix permeability (fig. 6.35, shown in light color), but the time for the fracture to propagate through the caprock remains consistently higher.

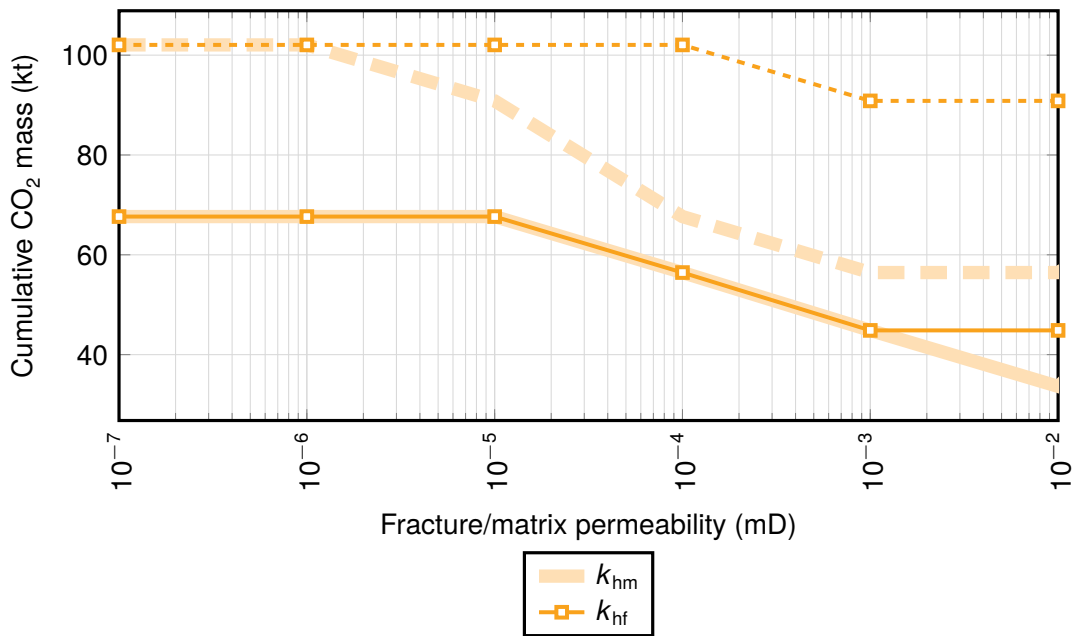
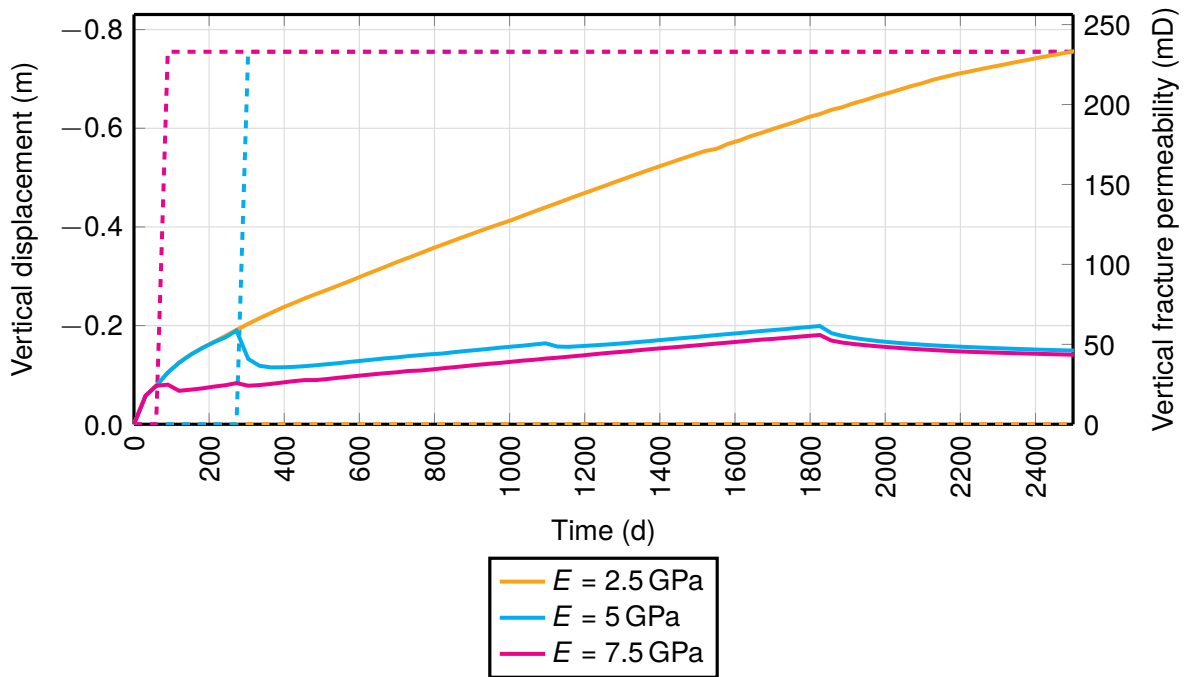


**Figure 6.35** – Cumulative injected mass at first crack (solid) and gas breakthrough (dashed) as a function of caprock fracture and matrix permeability.

### 6.2.3 Young modulus

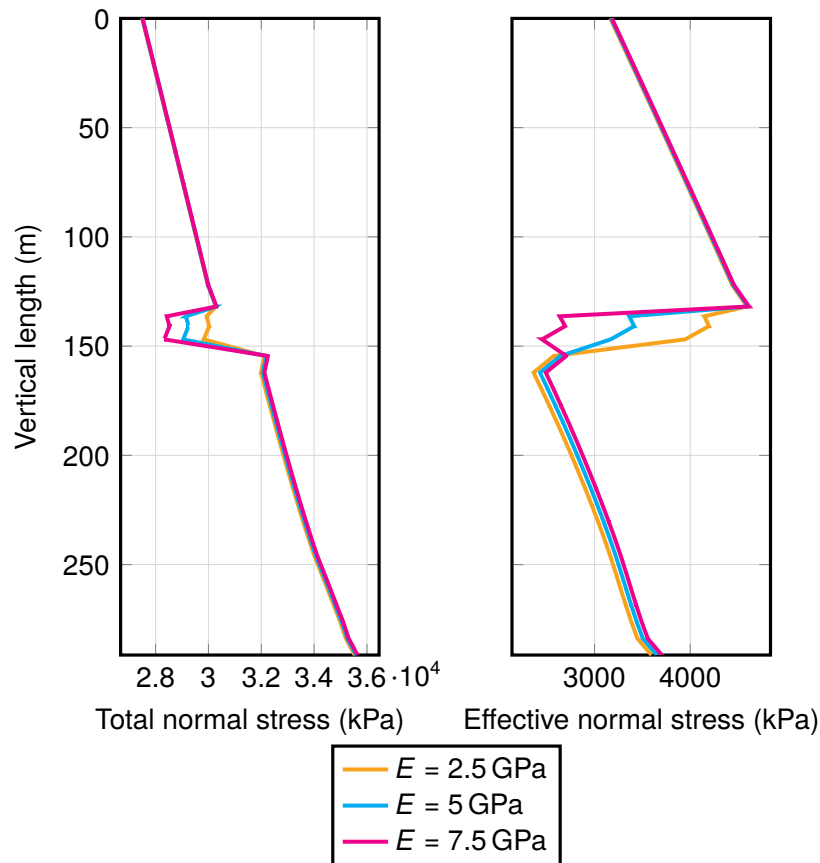
The Young modulus of the caprock is changed from the original 5 GPa to 2.5 and 7.5 GPa respectively.

Figure 6.36 shows how all runs share the same displacement curve pre-failure. However, the rock with a lower Young modulus (ductile) can sustain a much higher peak displacement before failure. Furthermore, the crack propagates slower in the more ductile caprock. In fact, in the 2.5 GPa scenario, the fracture that opens at the bottom of the caprock does not propagate across it, and no gas leaks to the upper aquifer. This is a result of the higher effective normal stresses in the caprock at lower values of  $E$  (fig. 6.37), thanks to which the caprock can sustain a higher amount of unloading before cracking.



**Figure 6.36** – Peak vertical displacement (solid) and fracture permeability (dashed) over time at the top center of the caprock.

## 6 Sensitivity analysis



**Figure 6.37** – Horizontal stresses along the wellbore after 2 months of injection (pre-failure).

The higher the Young modulus, the lower the mass that can be injected before a crack opens (fig. 6.38). Notice how the crack opens immediately at the start of injection and instantly propagates across the caprock when  $E \geq 12.5$  GPa. This shows the importance of caprock ductility for geological sequestration.

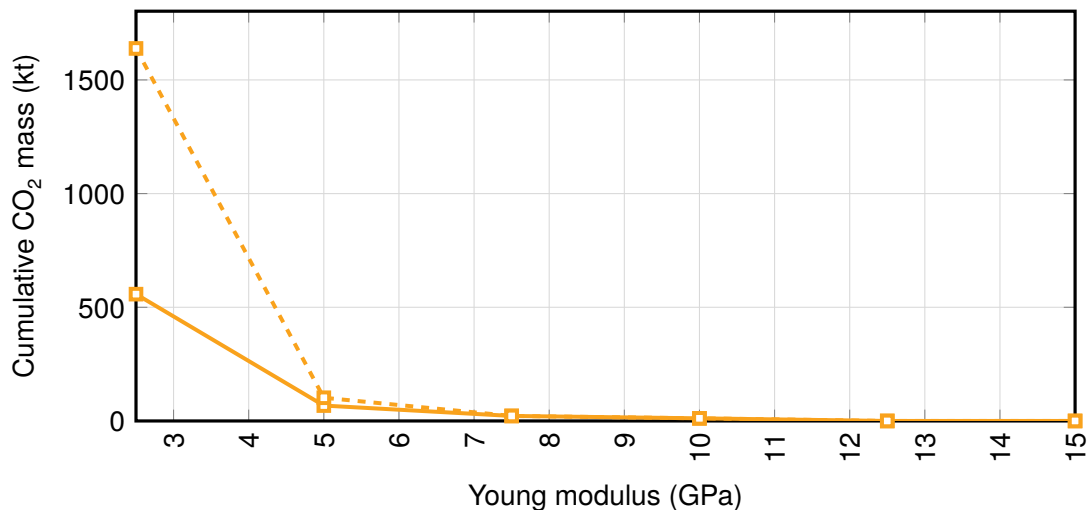


**Figure 6.38** – Cumulative injected mass at first crack (solid) and gas breakthrough (dashed) as a function of caprock Young modulus.

### 6.2.4 Poisson ratio

Different values of Poisson ratio in the caprock are compared: 0.2, 0.25, 0.3 and 0.35.

The Poisson ratio of the caprock has a negative correlation with time to failure, where an increase in  $\nu$  leads to an earlier failure (fig. 6.39). This is caused by a decrease of effective normal stress in the caprock, which brings the state of stress closer to the failure threshold.

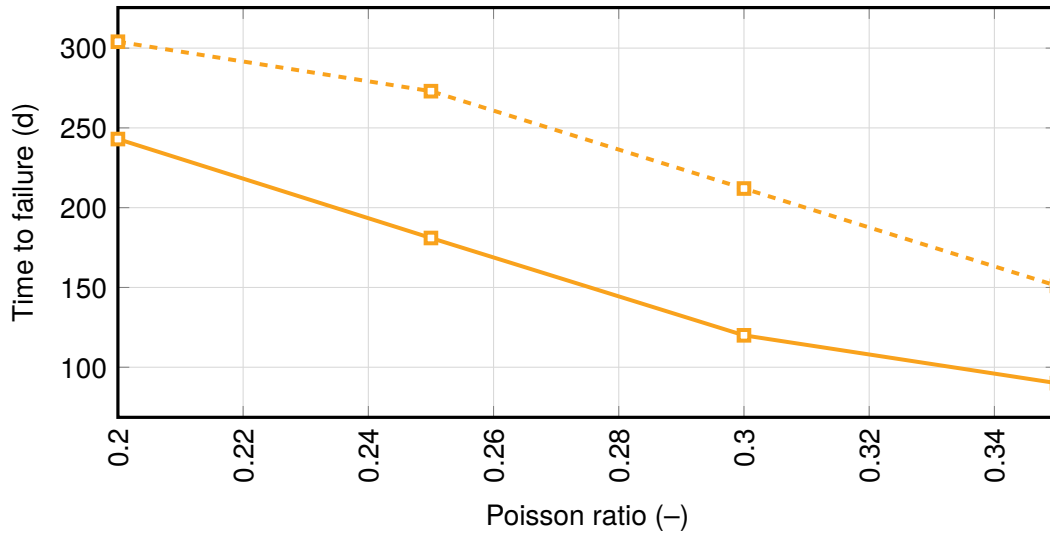


**Figure 6.39** – Time to first crack (solid) and gas breakthrough (dashed) as a function of caprock Poisson ratio.

### 6.2.5 Thickness

The original caprock thickness of 13.5 m (divided in three layers of equal thickness) is compared to a 6 m and a 21 m thick caprock. The grid top is modified so as to always keep the underside of the caprock at the same depth (2429 m), and hence the same density of the injected fluid.

The increase in thickness translates the normal fracture effective stress curve to the right without affecting its shape, thereby delaying the opening of fractures (fig. 6.40). Between the 6 m run and the 21 m run, first crack opening is separated by five months. Indeed, the thicker caprock can sustain a higher pressure increase before rupture, and consequently a higher peak vertical displacement (fig. 6.41). Note that the slope of the vertical displacement curve pre-failure is identical in all cases; consequently, the pre-failure displacement profile is the same for all runs.

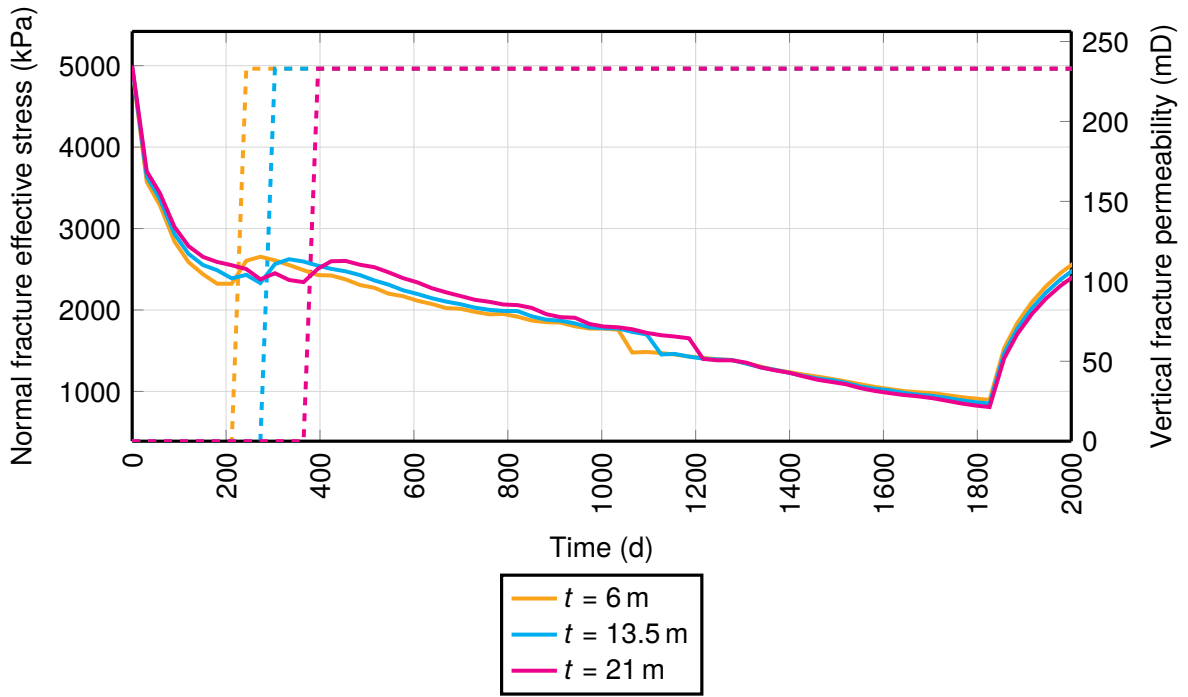


**Figure 6.40** – Fracture normal effective stress (solid) and fracture permeability (dashed) over time at the bottom center of the caprock.

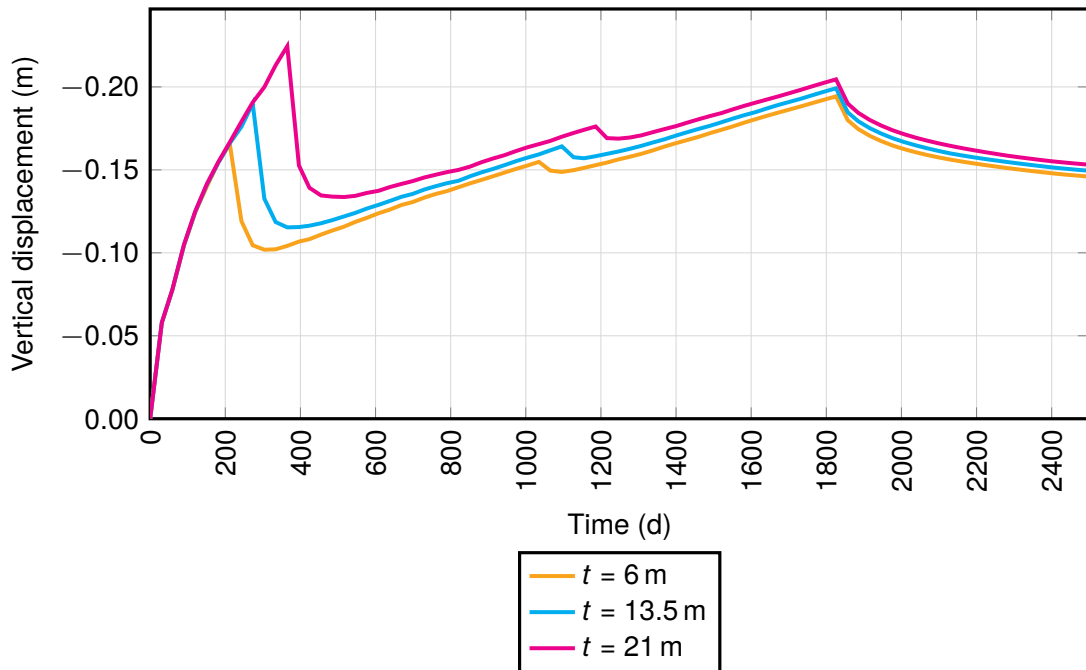


**Figure 6.41** – Peak vertical displacement at the top center of the caprock over time.

### 6.2.6 Fracture spacing

Different values of fracture spacing are investigated, and the spacing value is kept the same in all directions (I – J – K).

Changing the fracture spacing has no effect on the time for the first fracture to open, nor on the system behavior prior to first crack. However, with a denser fracture network, fracture propagation across the caprock is faster. Note that the injected mass at gas breakthrough, and hence the velocity of propagation of the fracture through the caprock, saturates beyond a certain value, as evidenced by fig. 6.42. Values of spacing below 10 cm and above 2 m have no further effect on fracture propagation.

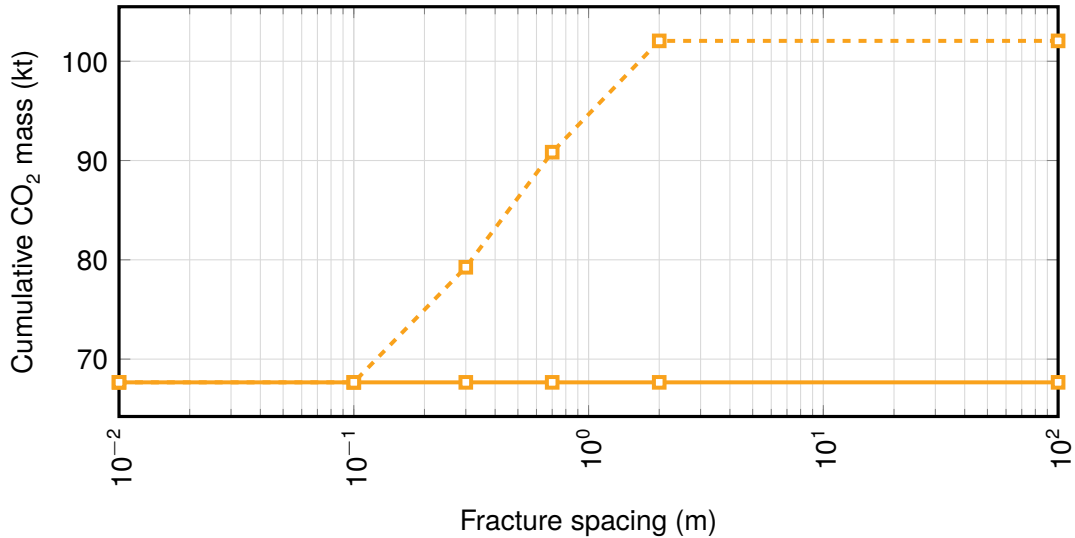


**Figure 6.42** – Cumulative injected mass at first crack (solid) and gas breakthrough (dashed) as a function of fracture spacing.

### 6.2.7 Fracture opening stress

The behavior of the caprock is evaluated for different values of fracture opening stress (1600–2600 kPa in increments of 200 kPa).

Decreasing  $f_{rs}$  delays the opening of fractures, and the well BHP curve is allowed to rise higher without a change in its slope (fig. 6.43). As seen when investigating reservoir matrix permeability, the BHP curve for the 1600 kPa run has a sawtooth profile, where each tooth corresponds to a new block cracking (horizontal propagation of the fracture). From the pressure profiles, it is apparent that the relationship between fracture opening stress and time to gas breakthrough is non-linear (logarithmic). The same logarithmic behavior can be observed when investigating the opening of cracks on the underside of the caprock with respect to time. Consequently, when plotting  $f_{rs}$  against the time to first crack (fig. 6.44) or the total injected mass at first crack (fig. 6.45) on a semi-logarithmic plot, the trend can be fitted by a straight line. Note that the scatter on both plots is the same; this scatter is attributable to the interval at which the solver produces output values, set to one month.

6 Sensitivity analysis

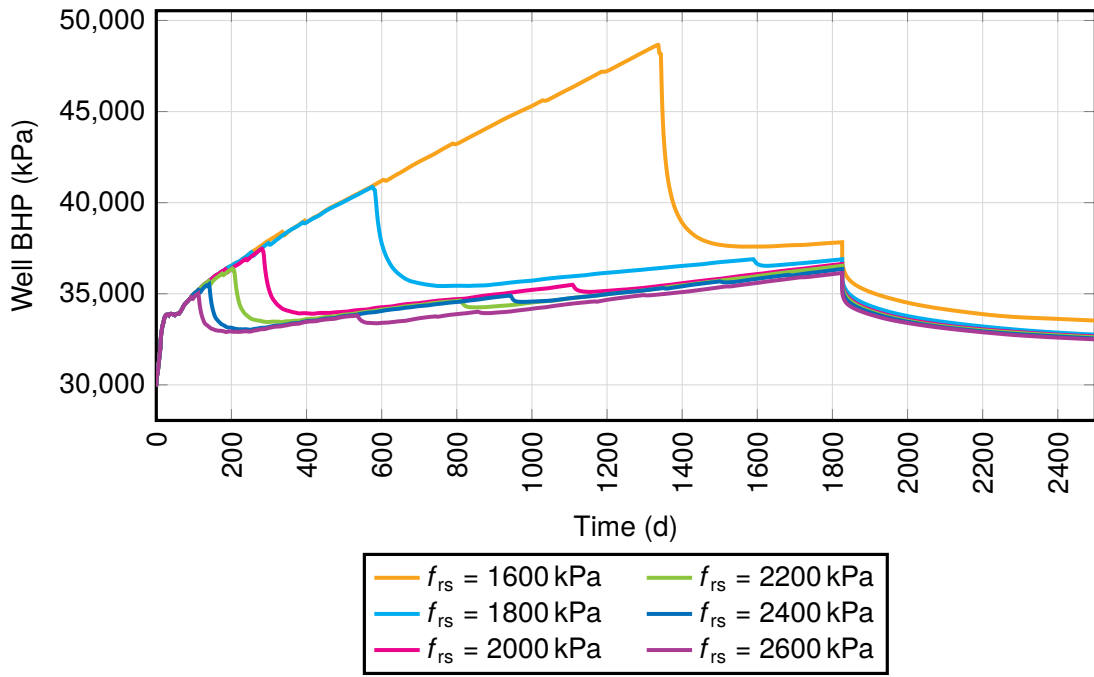


Figure 6.43 – Well BHP with time.

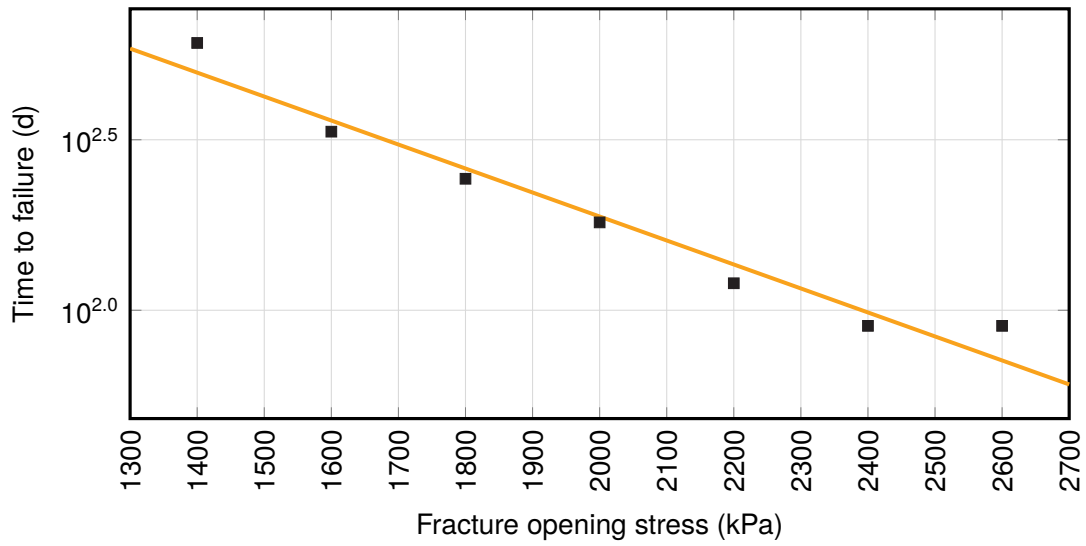
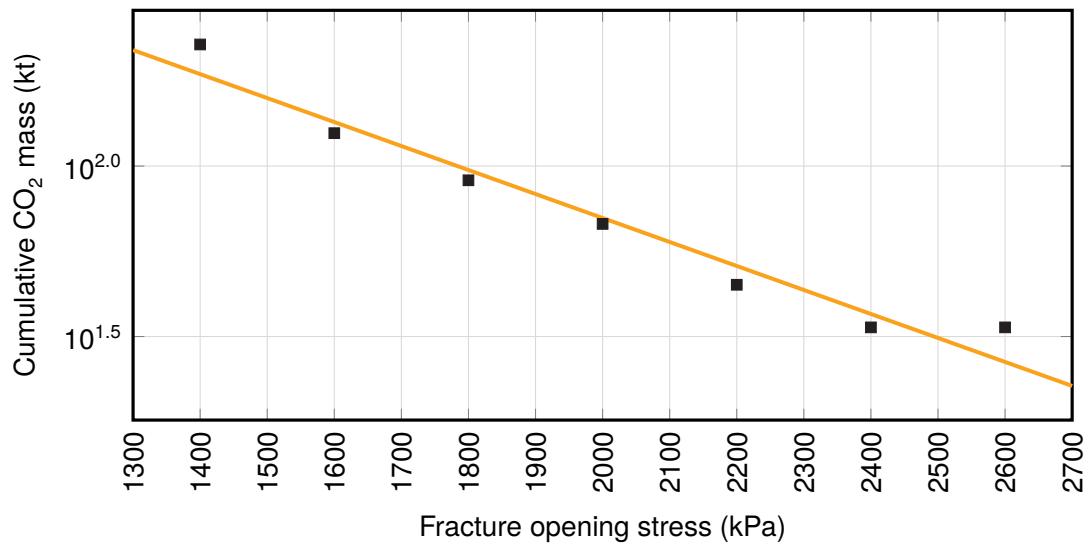


Figure 6.44 – Time to first crack appearance as a function of fracture opening stress.



**Figure 6.45** – Cumulative injected mass at first crack appearance as a function of fracture opening stress.

### 6.2.8 Residual fracture permeability

Residual fracture permeability  $k_{rcf}$  only has an effect on fracture closure, thus post-failure behavior. As seen in fig. 6.46, the fractures on the bottom of the caprock close soon after the CO<sub>2</sub> plume has broken through the caprock and the stress build-up has been released. Because of the continued injection, pore pressure keeps building up (albeit at a slower pace) and fractures fully reopen again, before closing at the end of the injection period.

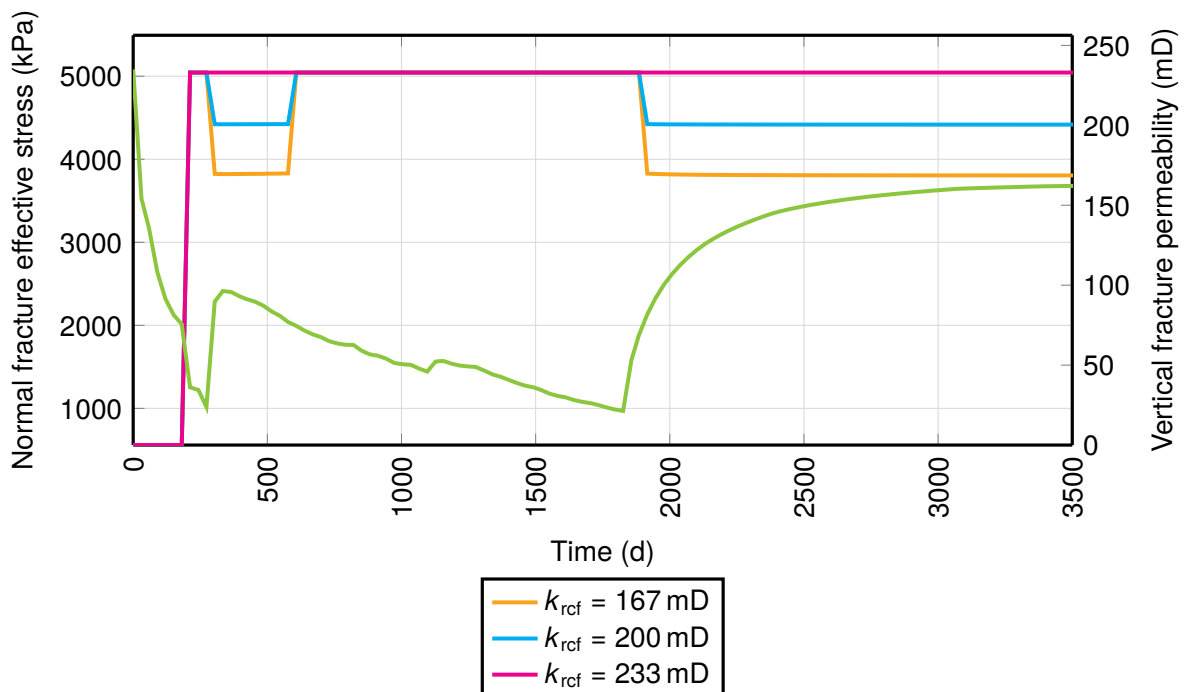


**Figure 6.46** – Fracture permeability (solid) and fracture normal effective stress (green, common for all runs) over time at the bottom center of the caprock.

## 6.3 Simulation options

### 6.3.1 Porosity coupling function

The porosity coupling options GCOUPLING 0, 2 and 3 are compared.

In one-way coupling mode (GCOUPLING 0), reservoir porosity is not a function of deformation, since stresses and strains are not fed back to the fluid-flow simulator. As a result, porosity is purely a function of pressure and temperature. Given that temperature in our model is constant, the porosity curve is perfectly parallel to the pressure curve (fig. 6.47). Note that the porosity increase here is due purely to geomechanical effects and not geochemical effects, which are not considered.

Using GCOUPLING 2 (two-way coupling), porosity is a function of  $\Delta p$ ,  $\Delta T$  and  $d\sigma_m/dp$  according to eq. (4.28) in section 4.3.6. The last term in the equation is null due to reservoir temperature being constant, and since  $d\sigma_m/dp$  is multiplied by bulk compressibility, the influence of mean total stress on the shape of the porosity curve is very small. As a result, the relationship between current porosity and pressure is also linear (fig. 6.48), and the porosity curve in a given block follows that of the pressure.

Finally, with GCOUPLING 3,  $\phi^*$  is a function of  $\Delta p$ ,  $\Delta T$  and  $\Delta\sigma_m$ . Here, the influence of total mean stress is larger, and the porosity curve closely follows that of pressure, but not exactly.

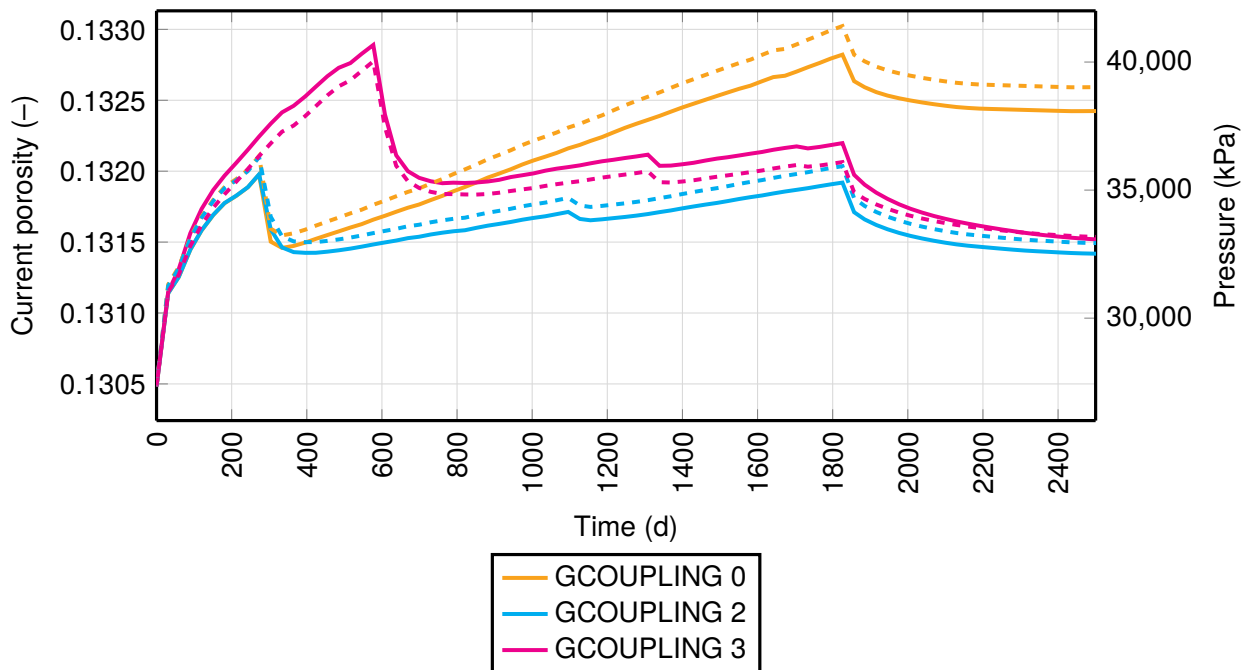


**Figure 6.47** – Evolution of porosity (solid) and pressure (dashed) in the gridblock containing the uppermost perforation.

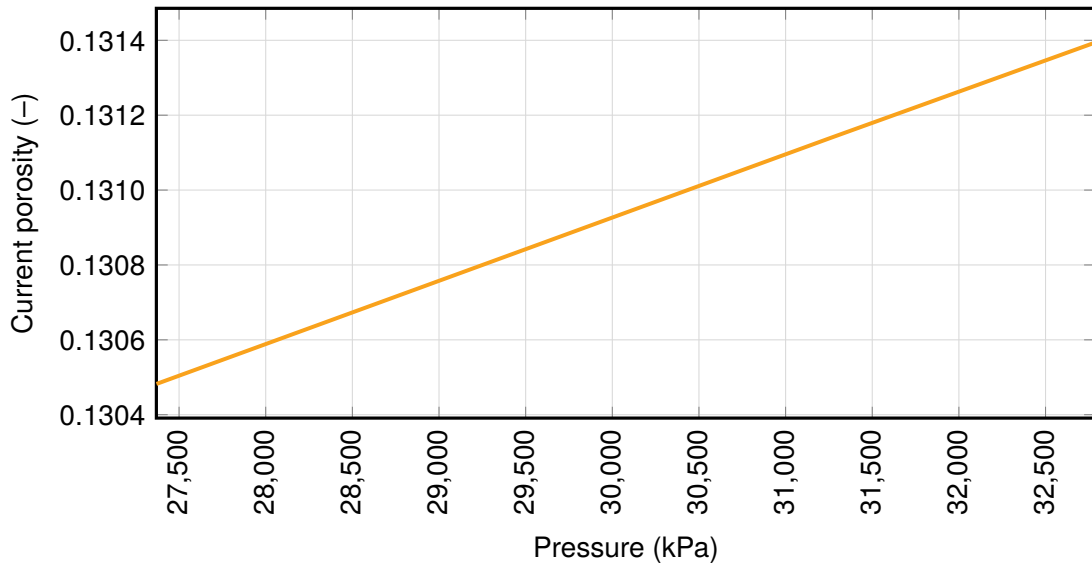


**Figure 6.48** – Current porosity as a function of pressure in the gridblock containing the bottommost perforation.

The choice of the porosity function has a strong influence on the post-peak vertical displacement trend (fig. 6.49), with the non-coupled model exhibiting completely different behavior. While the slope of the displacement curve pre-failure is mostly identical in all cases, the peak displacement that the caprock can sustain before failure is significantly greater for the GCOUPLING 3 run. Note that the fracture permeability curves for the GCOUPLING 0 and 2 cases are the same, as failure occurs at the same timestep.

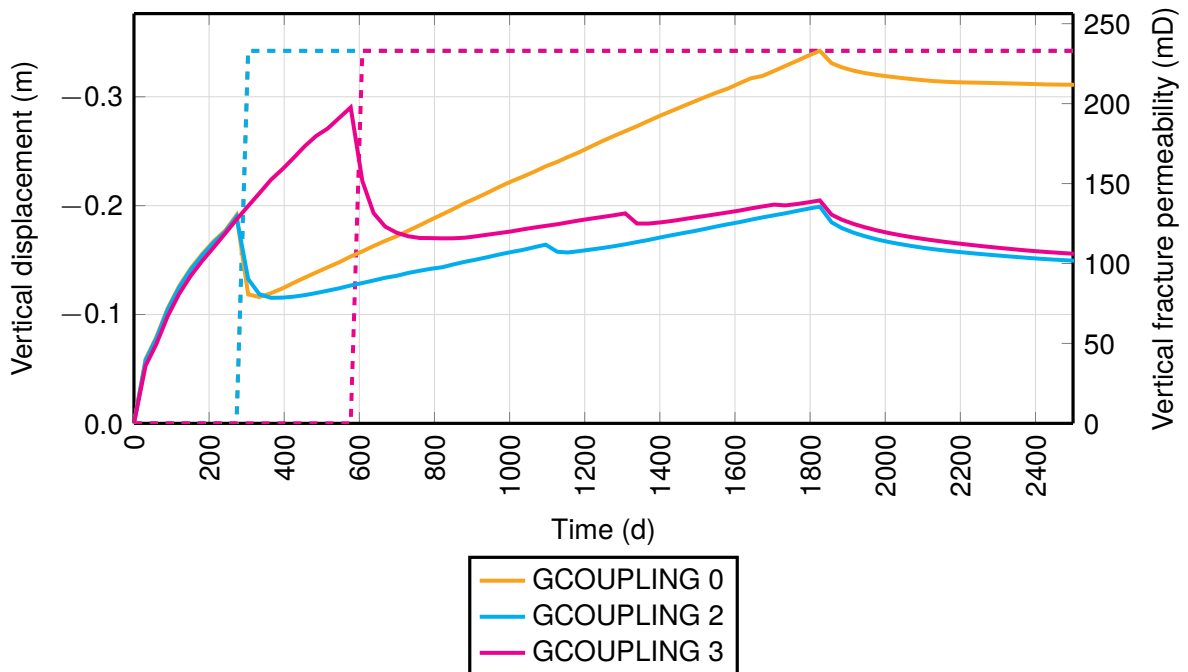


**Figure 6.49** – Fracture permeability (dashed) and peak vertical displacement (solid) over time at the top center of the caprock.

### 6.3.2 Shear failure

In the original scheme, only tensile fracture failure is considered. Here, we specify a threshold value of 500 kPa for shear failure to occur. Once the radius of the Mohr circle exceeds the threshold, fractures in the caprock open due to shear, and fracture permeability changes from the initial fracture permeability to a value computed by

$$k_f = k_{f0} \cdot \exp(-\gamma \cdot \Delta\sigma'_m), \quad (6.2)$$

where  $k_{f0}$  is the initial fracture permeability ( $2.5 \times 10^{-8}$  mD),  $\gamma$  is the permeability modulus ( $10^{-3} \text{ kPa}^{-1}$ ), and  $\Delta\sigma'_m$  is the difference in mean effective stress (kPa).

With the specified threshold, shear failure occurs immediately at the start of the simulation. Results show that the fracture permeability does not change appreciably due to shear failure, increasing from the initial  $2.5 \times 10^{-8}$  mD to a constant value of  $1.4 \times 10^{-7}$  mD over one month. While the caprock remains essentially impermeable, fig. 6.50 shows that the tensile failure threshold of 2000 kPa is reached one month earlier when considering shear failure.

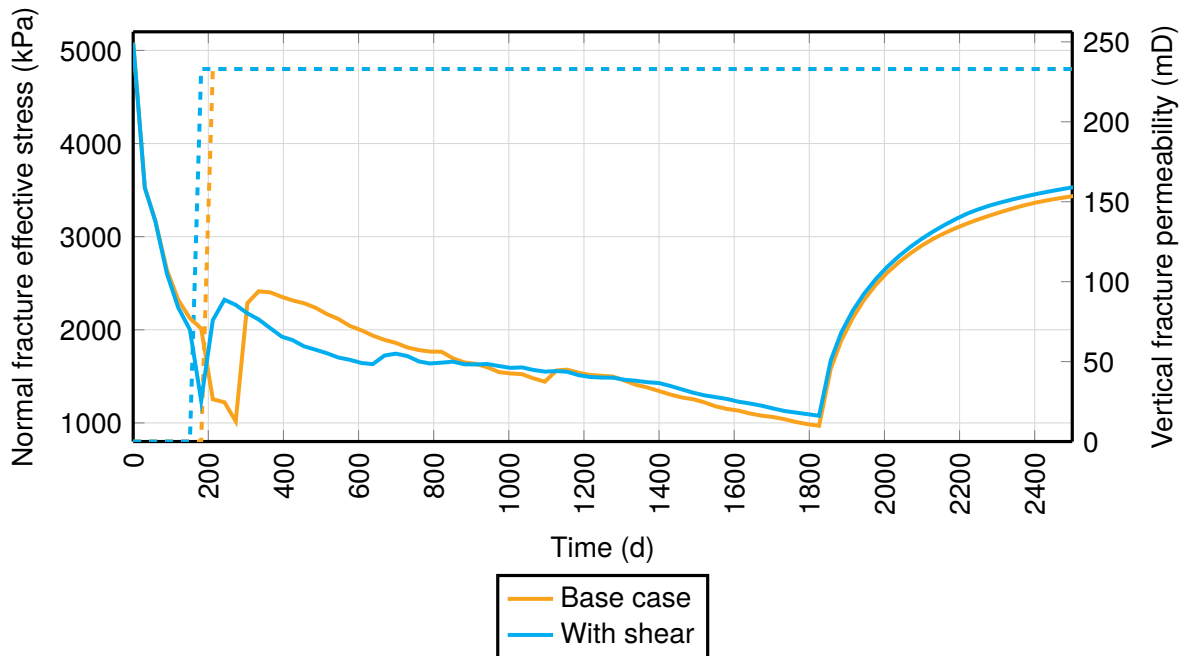


**Figure 6.50** – Fracture normal effective stress (solid) and fracture permeability (dashed) over time at the bottom center of the caprock.

The displacement profile is slightly altered, with a maximum vertical displacement of 14.1 cm for the base case and 13.7 cm for the scenario with shear failure (fig. 6.51).

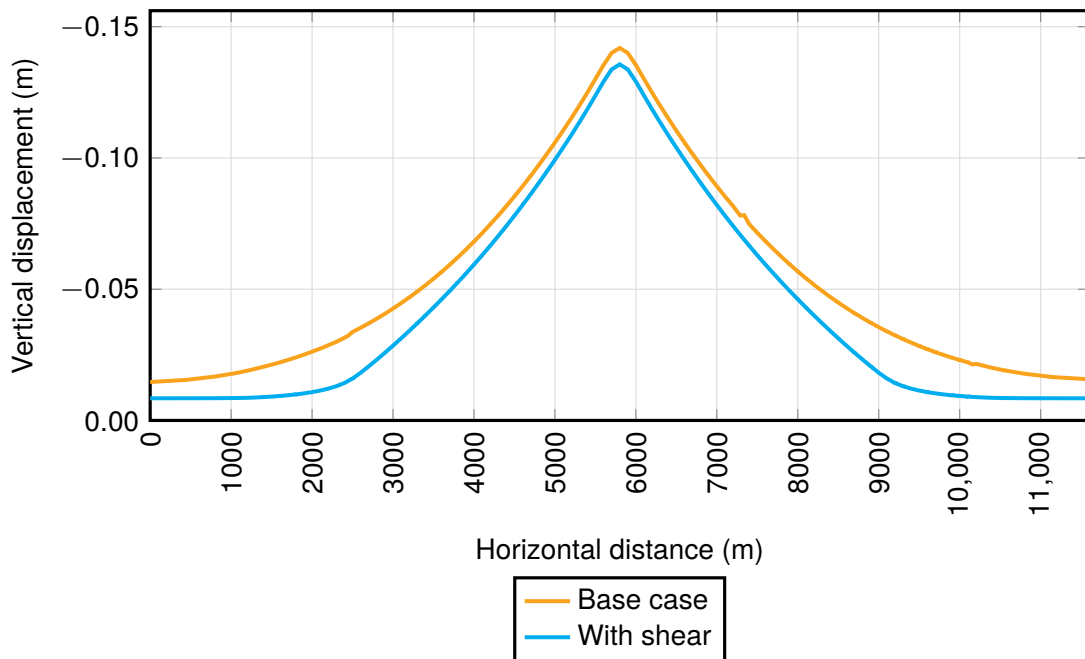


**Figure 6.51** – Vertical displacement profile along the caprock bottom after 5 months of injection (pre-failure).

### 6.3.3 Equation of state

The results of two runs using the Peng-Robinson (base case) and Soave-Redlich-Kwong EoS are compared.

Using the SRK EoS, plume velocity is diminished both horizontally and vertically (fig. 6.52), which results in a thinner and longer plume. Because both sets of EoS calculate different amounts of dissolved  $\text{CO}_2$ , the reservoir pressure is slightly different, and that impacts the effective stress both in the reservoir and the caprock (fig. 6.53). Note that the total stress profile is not significantly impacted.

6 Sensitivity analysis

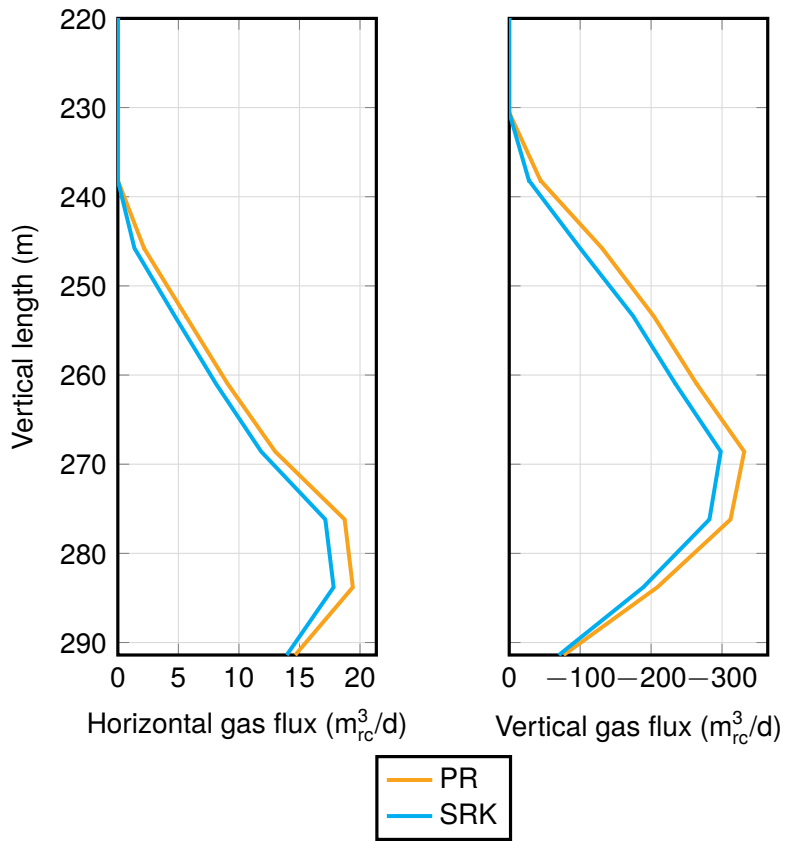
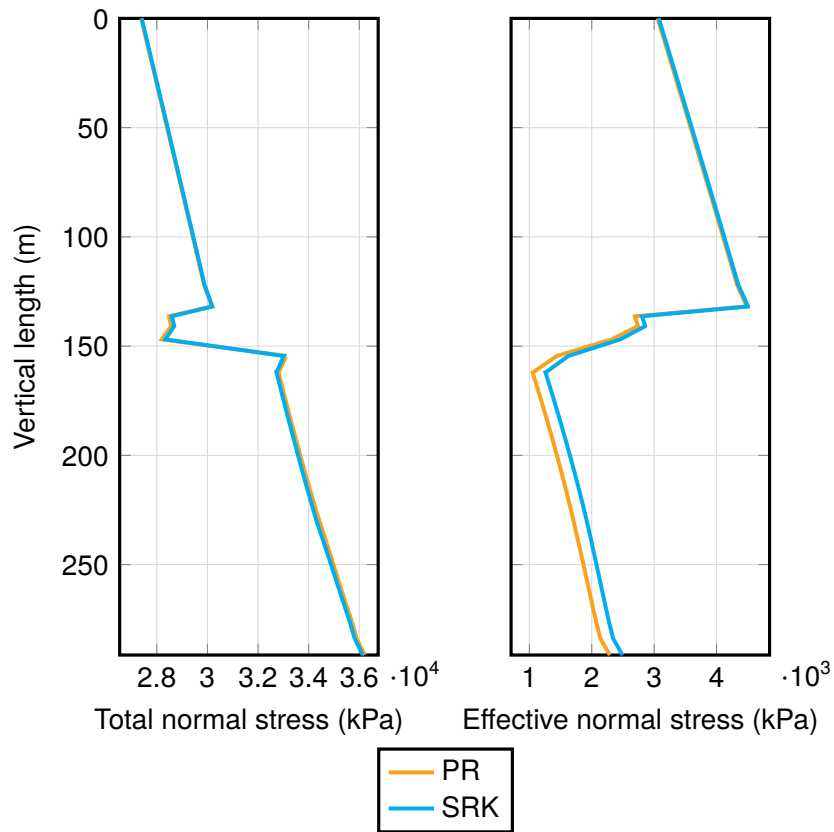


Figure 6.52 – Gas flux along the wellbore after 3 months of injection.

## 6 Sensitivity analysis



**Figure 6.53** – Horizontal stresses along the wellbore after 4 months of injection (pre-failure).

With regard to the SRK run, the higher effective stress delays both the appearance of first crack and gas breakthrough across the caprock, while the lower pressure slightly decreases the slope of the peak displacement curve (fig. 6.54).

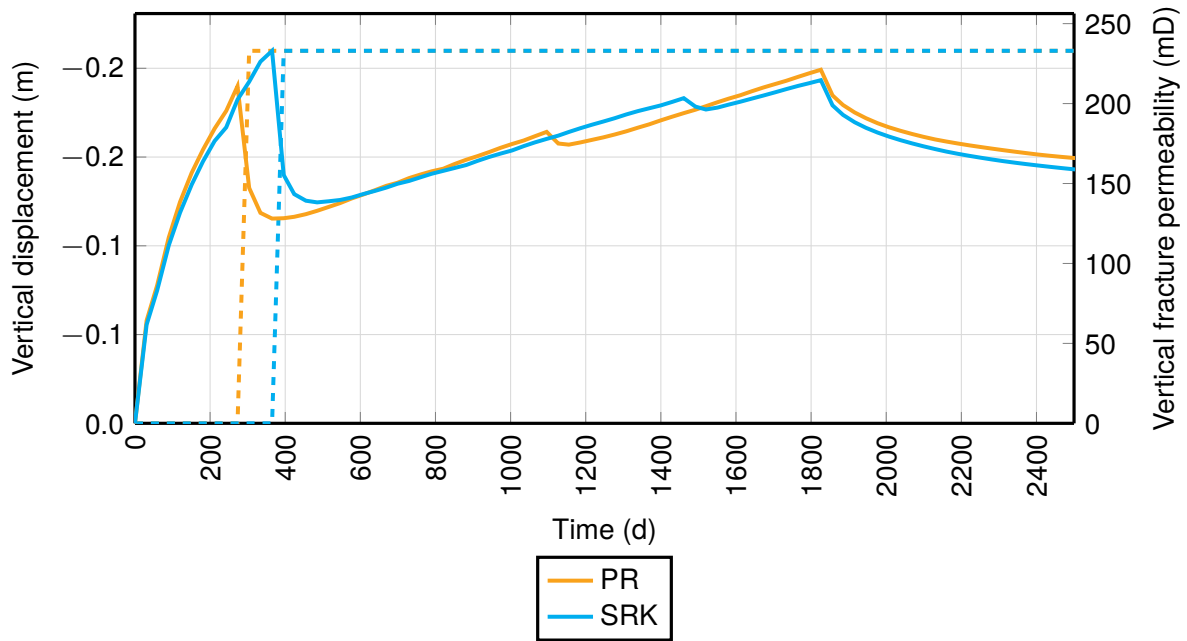


**Figure 6.54** – Peak vertical displacement (solid) and fracture permeability (dashed) over time at the top center of the caprock.

It should be noted that, in general, cubic EoS are not able to accurately model compositional properties of CO<sub>2</sub>-water systems. [127] In particular, vapor-liquid equilibria predictions of SRK EoS are poor. The SPUNG EoS have shown better results than the SRK EoS for modelling CO<sub>2</sub>-water systems, but they still show as much as 20% discrepancy to experimental data when predicting vapor-liquid equilibria. [128]

Multiple authors have attempted to solve this problem, and good results for phase composition and aqueous phase densities of CO<sub>2</sub>-water systems have been obtained by using either:

- the PR EoS with Twu's  $\alpha$  function and Huron-Vidal mixing rules; [129]
- the PR EoS with Huron-Vidal mixing rules and P neloux volume shift; [130]
- the EoS-CG model. [131]

At pipeline and reservoir pressure-temperature conditions, pure CO<sub>2</sub> densities can be well approximated using:

- the PR EoS with the Mathias *et al.* (1989) volume shift; [12]
- the PR EoS with the second Stryjek-Vera modification; [41]
- the Sterner-Pitzer EoS. [12]

There have also been improvements in methods that permit the calculation of mutual dissolution of CO<sub>2</sub> and water using empirical models. [127], [130] Finally, note that the properties of brine differ largely from those of water due to the salt content. In particular, CO<sub>2</sub> solubility is strongly dependent on salinity. EoS do not treat salt as an additional component, but as a variable. [133]

## 6.4 Injection parameters

### 6.4.1 Injection rate

Here, three values of injection rate are considered: 180,000, 200,000 and 220,000 m<sup>3</sup><sub>sc</sub>/d.

Injection rate is one of the few parameters that can be controlled during geological storage. It must be carefully balanced between economical considerations (injecting as quickly as possible) and geomechanical considerations (avoiding reservoir and caprock fracturing).

In order to increase the rate, higher injection pressures are required. Therefore, it is expected that the higher the rate, the higher is the slope of the BHP curve (fig. 6.55). Additionally, the scenario with lower injection rate can sustain a much higher BHP before the caprock fails, with the BHP at failure going from 36,800 kPa in the high rate scenario to 43,400 kPa in the low rate scenario. Due to the higher pressures, the horizontal stress in the caprock decreases (fig. 6.56), and the time to failure decreases as the rate increases; however, the relationship between time to failure and cumulative injected volume is not linear (fig. 6.57). In fact, as suggested by González Martínez de Miguel (2014), injection rate and cumulative injected CO<sub>2</sub> can be fitted to an exponential function (fig. 6.58). The same is true for maximum vertical displacement or time (figs. 6.59 and 6.60). In effect, by slightly lowering the injection rate, the final storage capacity can be increased significantly. However, there is evidently a cost factor that must be taken into account; injecting CO<sub>2</sub> at too low a rate may prove uneconomical.

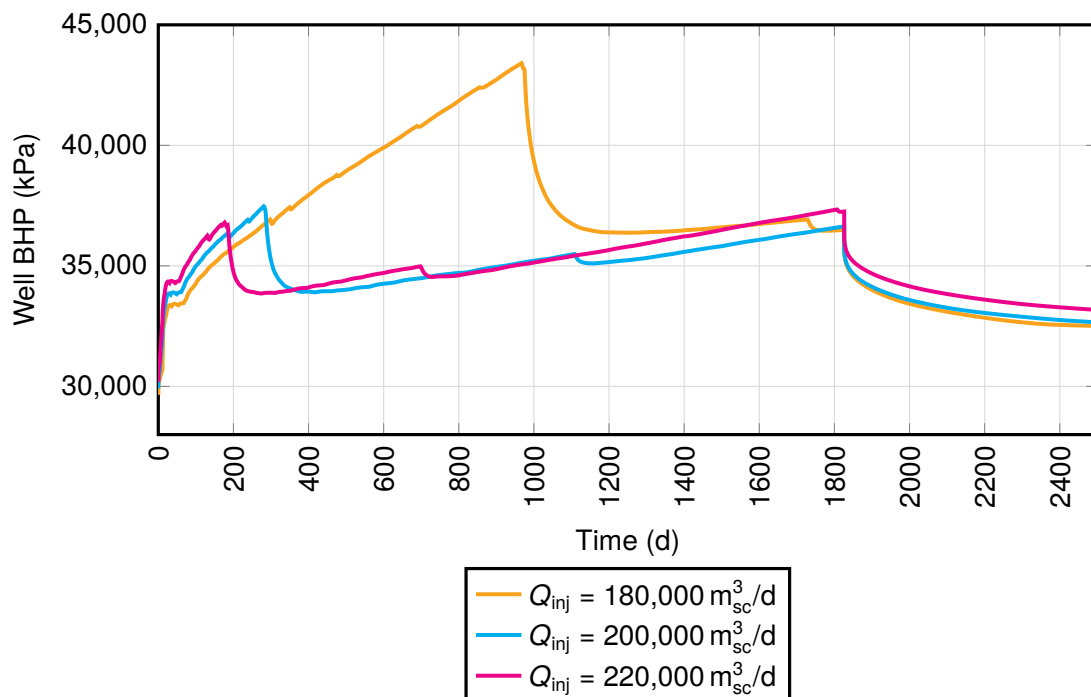


Figure 6.55 – Well BHP with time.

6 Sensitivity analysis

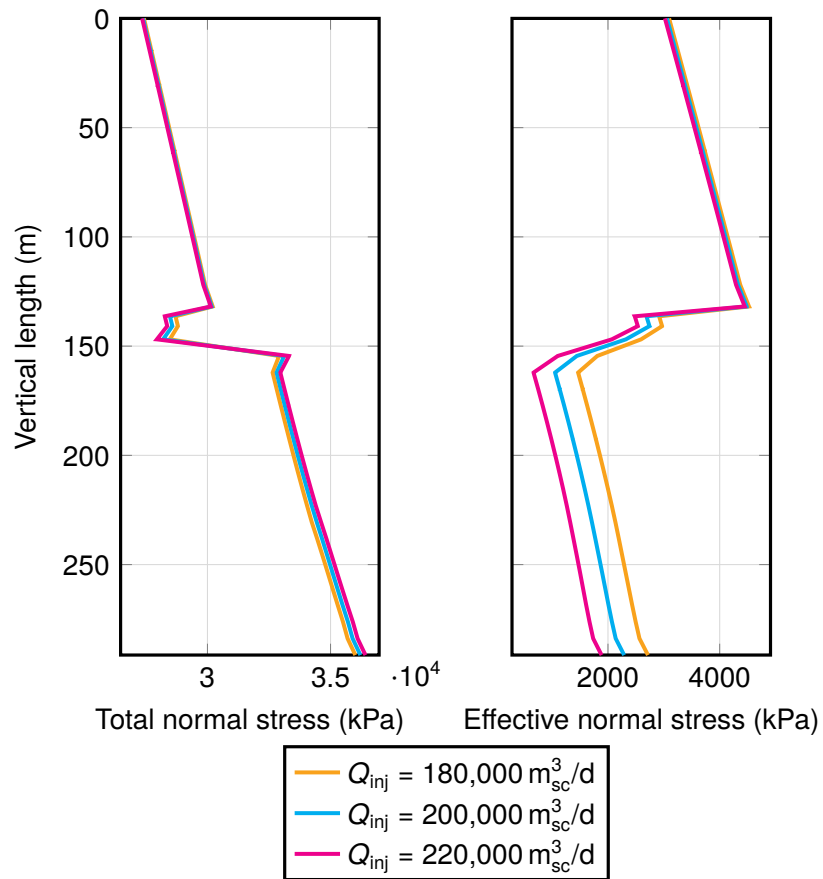
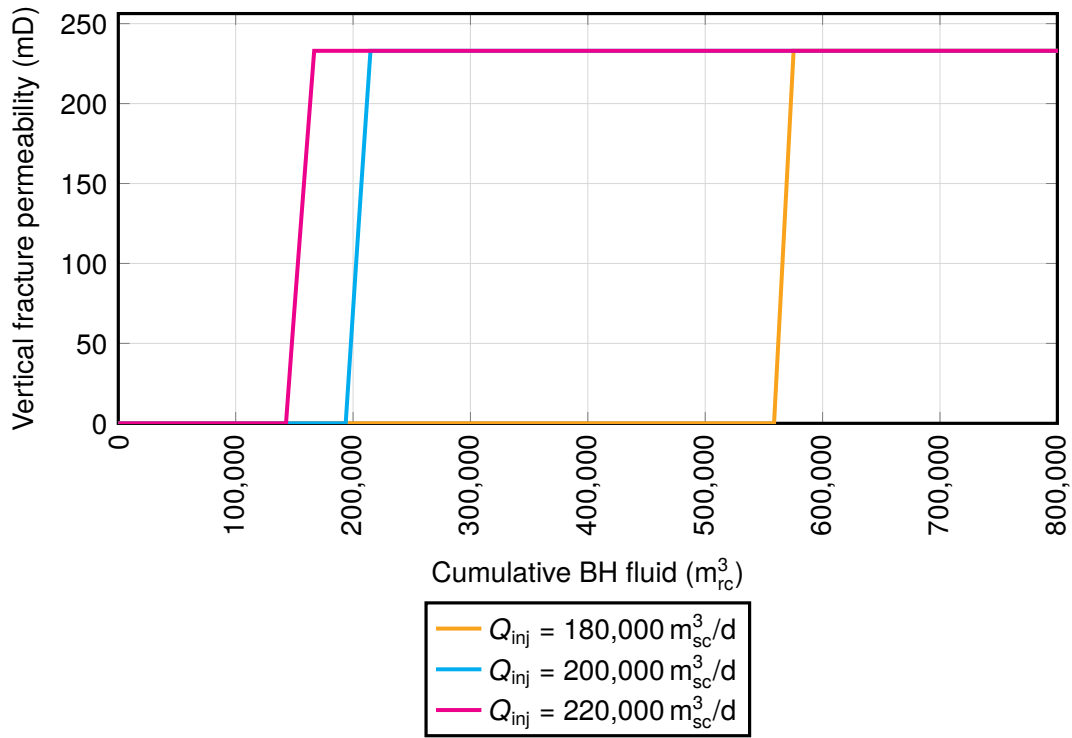
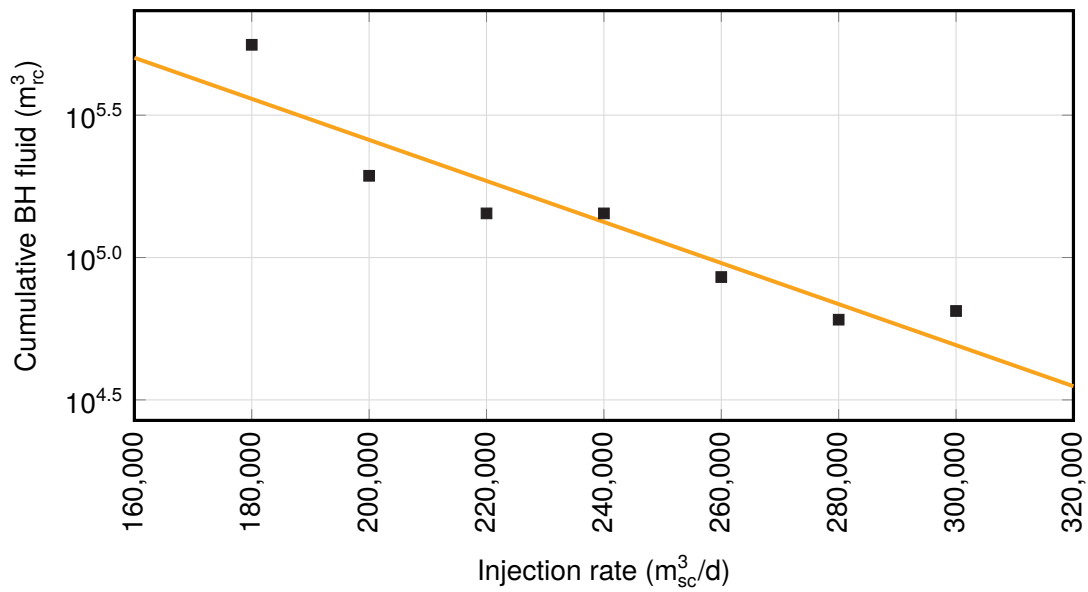


Figure 6.56 – Horizontal stresses along the wellbore after 4 months of injection (pre-failure).

## 6 Sensitivity analysis



**Figure 6.57** – Vertical fracture permeability at the top center of the caprock as a function of cumulative injected volume (RC).



**Figure 6.58** – Cumulative injected volume at CO<sub>2</sub> breakthrough as a function of injection rate.

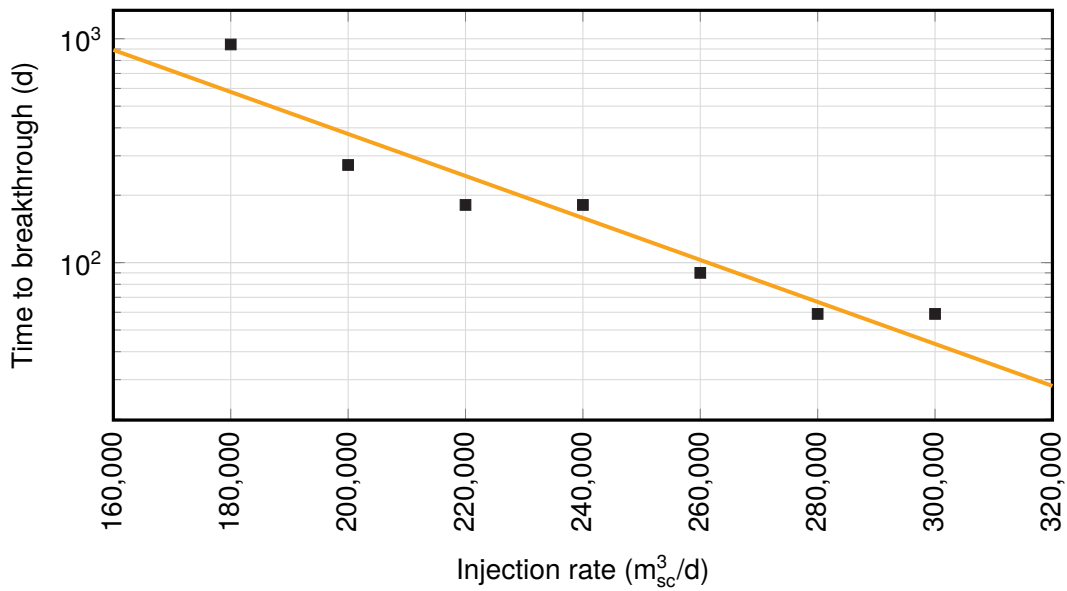


**Figure 6.59** – Time to  $CO_2$  breakthrough across the caprock as a function of injection rate.

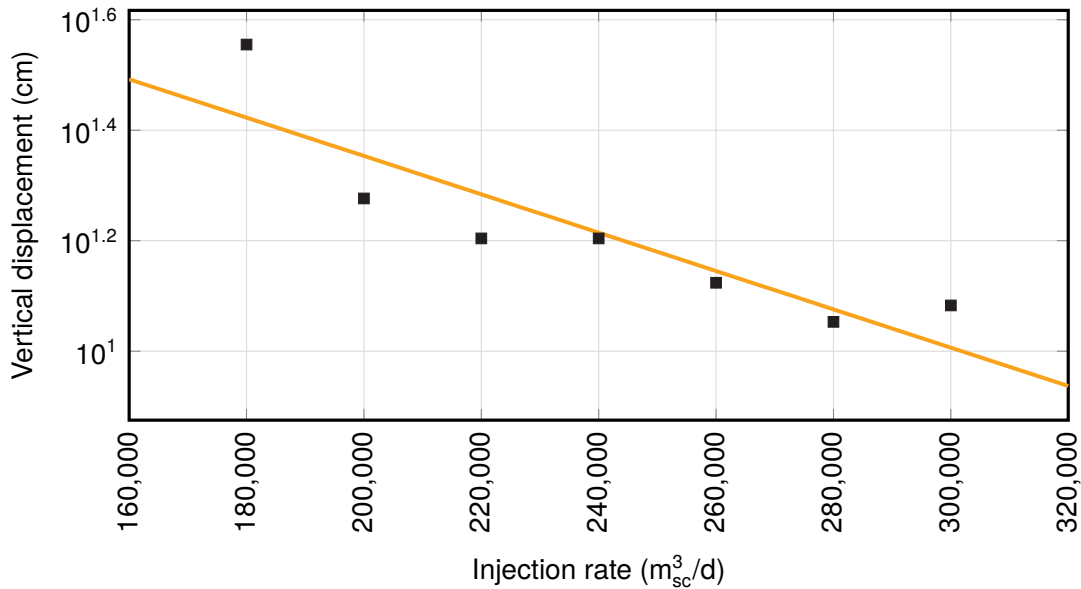


**Figure 6.60** – Vertical displacement (absolute values) in gridblock {51,1,11} at  $CO_2$  breakthrough as a function of injection rate.

Finally, note that in the  $180,000 m^3_{sc}$  scenario, the fracture normal effective stress keeps decreasing after the first layer of the caprock has fractured, even briefly dipping below zero and becoming tensile (fig. 6.61). In this run, there is a long delay between the first crack appearing in the bottommost layer and propagation of the fracture through the caprock (breakthrough). In the high rate scenario, the time between first crack and breakthrough is 61 d; with the intermediate rate, 92 d, and with the low rate, 701 d. During this period, the fracture keeps propagating horizontally, but  $CO_2$  does not migrate to the upper layers and the pressure

build-up is not released. The horizontal propagation of the fracture is evidenced by the multiple small drops on the BHP curve.

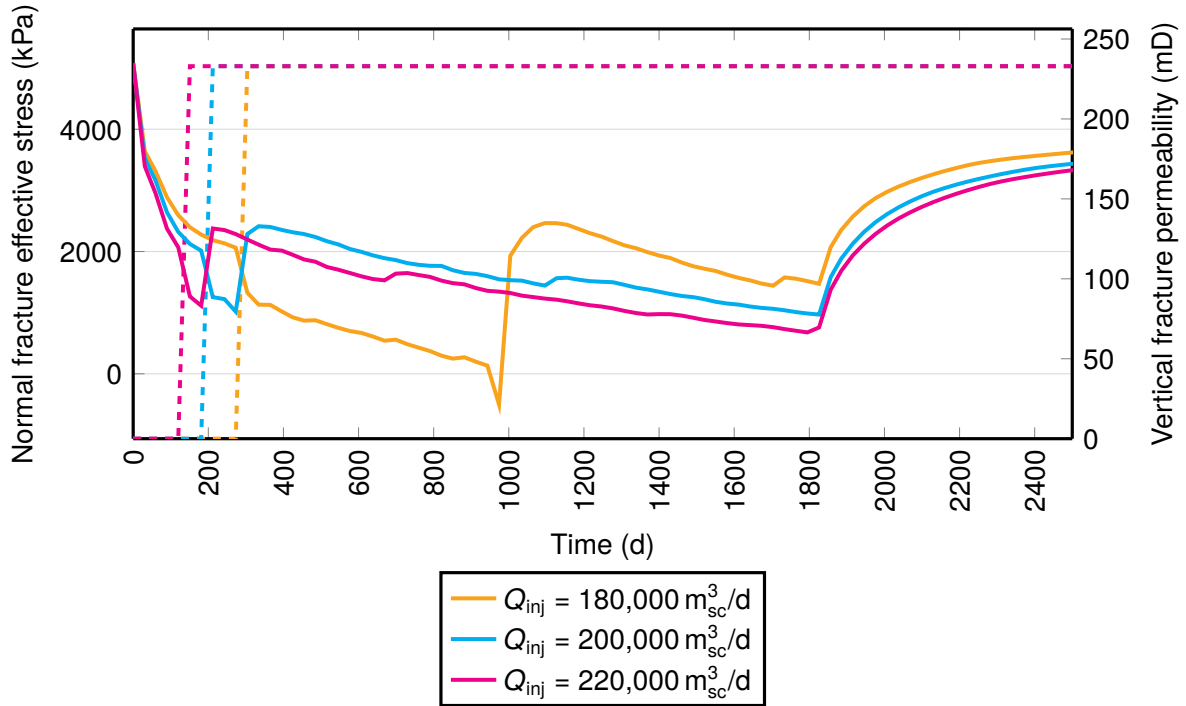


**Figure 6.61** – Fracture normal effective stress (solid) and fracture permeability (dashed) over time at the bottom center of the caprock.

#### 6.4.2 Number of wells

In this run, the original flow rate of  $200,000 \text{ m}^3_{\text{sc}}/\text{d}$  is distributed over two off-centered wells injecting  $100,000 \text{ m}^3_{\text{sc}}/\text{d}$  each, and then over three wells injecting  $66,667 \text{ m}^3_{\text{sc}}/\text{d}$  each. The total rate at the perforations always remains the same.

Figure 6.62 shows the evolution of the normal fracture effective stress with time. The curves refer to gridblock  $\{51,1,13\}$  (above the central injector) for the single and three wells run, and gridblock  $\{31,1,13\}$  for the two wells run (above the first injector). The normal fracture effective stress remains well above the threshold of  $2000 \text{ kPa}$  in both multiple wells cases. As a result, only the base case sees the caprock fail. In the two wells scenario, normal effective stress never goes below  $4000 \text{ kPa}$ , or twice the threshold value. Injection rate for both wells could be safely increased without risking tensile failure in the caprock.

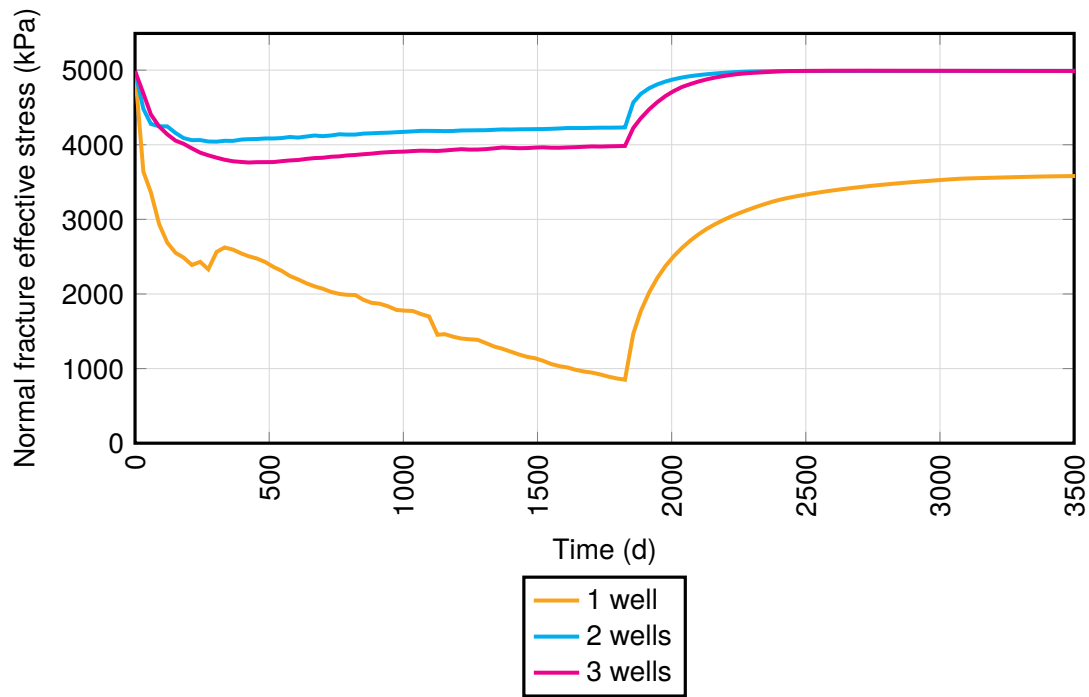


**Figure 6.62** – Normal fracture effective stress with time at the bottom of the caprock.

Arching of the caprock is itself a consequence of the pressure build-up above the injection point. By distributing the rate, this build-up is greatly reduced and the pressure profile below the caprock is much flatter (fig. 6.63). Accordingly, the peak vertical displacement is lowest for the two wells case (fig. 6.64). In the original scenario, the maximum vertical displacement is measured at 17 cm; with 3 wells, it is only 12.1 cm, and a further reduction is achieved with 2 wells to 11.6 cm.

6 Sensitivity analysis

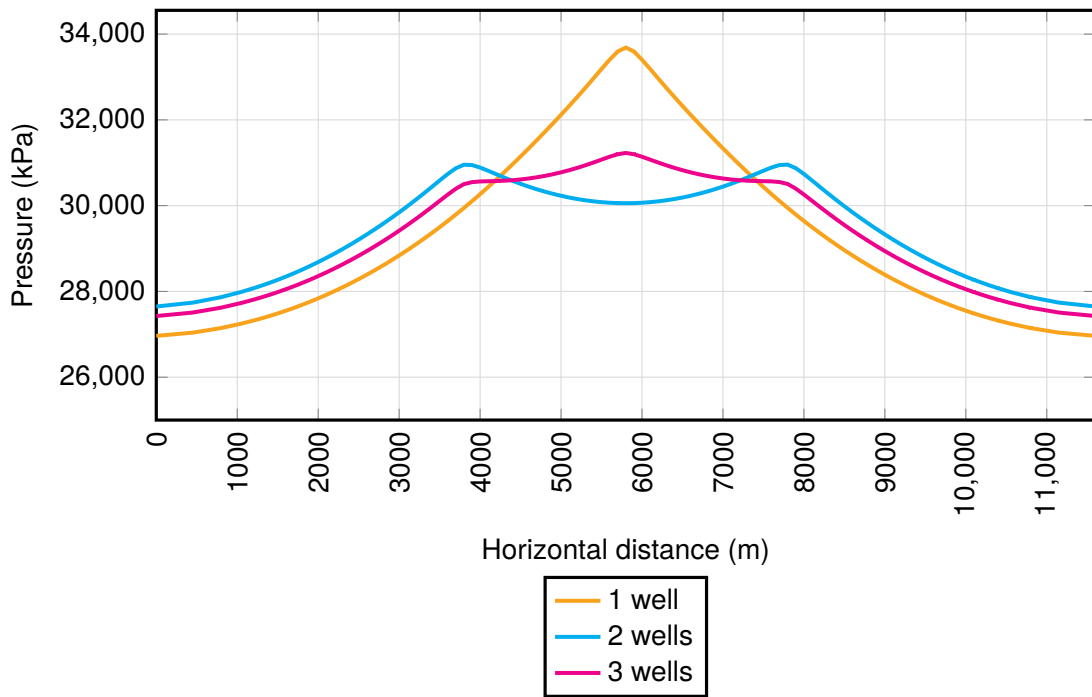


Figure 6.63 – Pressure profile along the bottom of the caprock after 8 months of injection (pre-breakthrough).

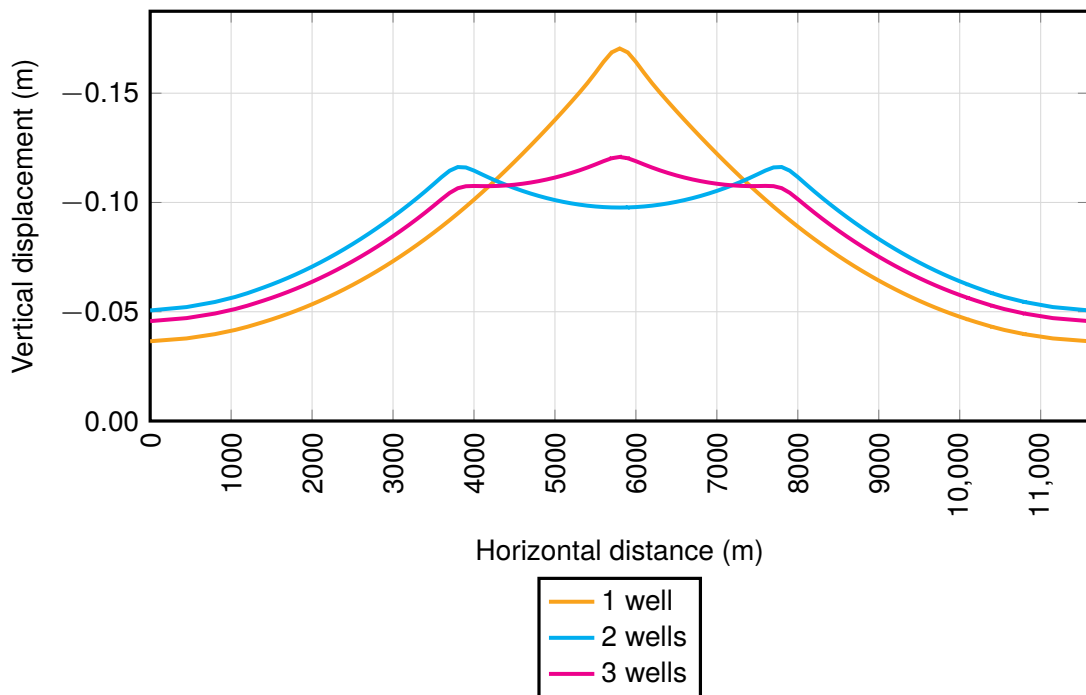


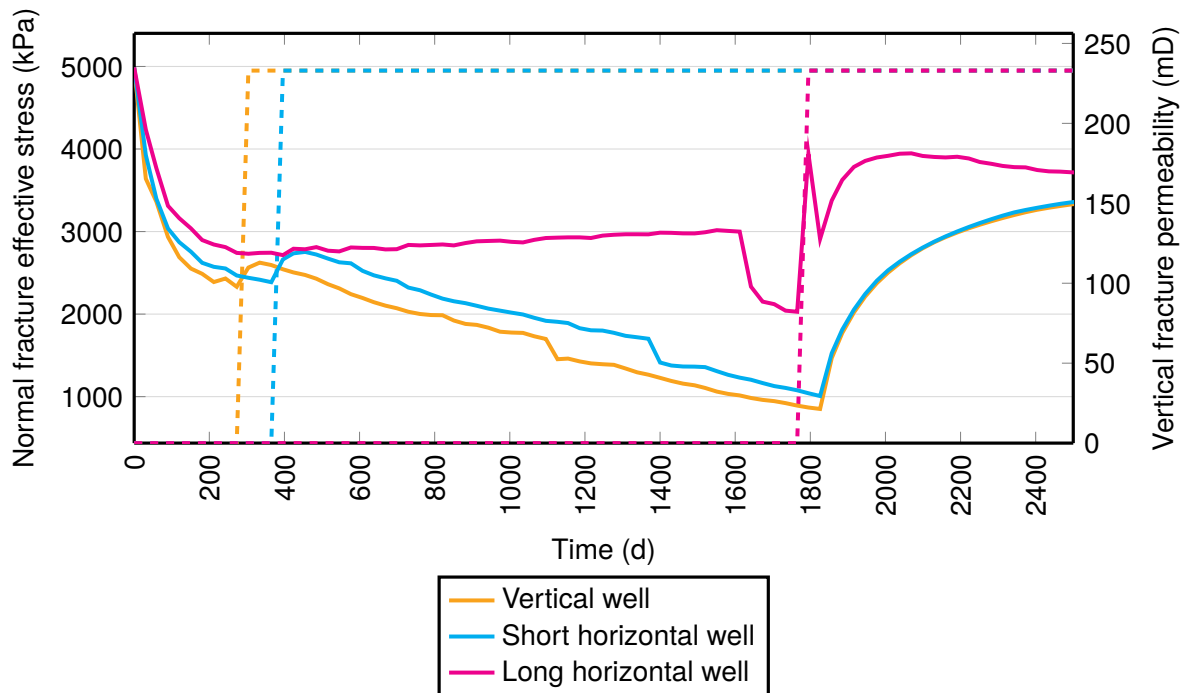
Figure 6.64 – Vertical displacement profile along the bottom of the caprock after 8 months of injection (pre-breakthrough).

### 6.4.3 Well profile

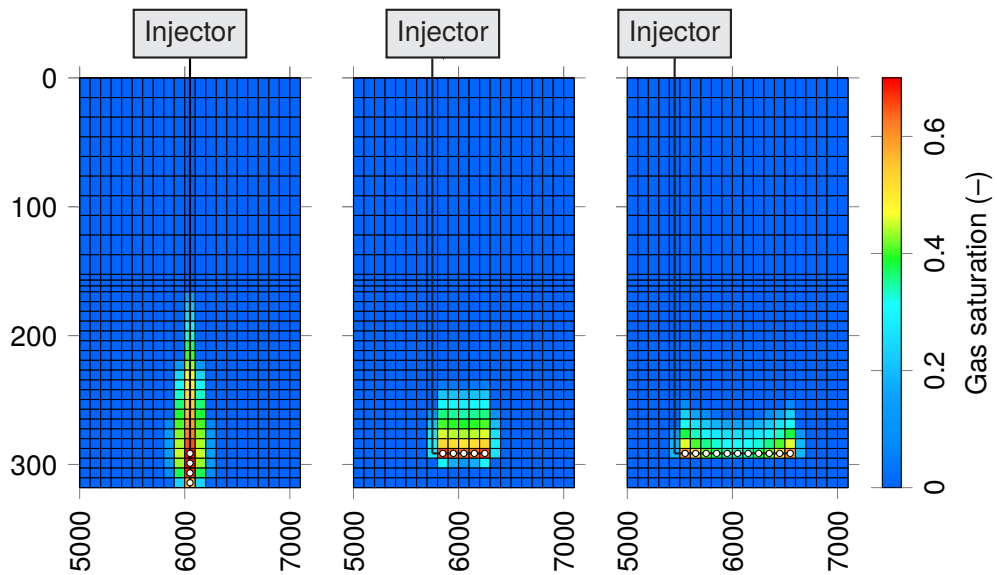
In this section, two different horizontal wells are compared with the original vertical profile. The short well is perforated along 5 gridblocks (400 m), and the long well along 11 gridblocks (1000 m). The perforations are centered in the reservoir (with respect to I), and the well is drilled along layer 30, corresponding to the uppermost perforation in the vertical well case.

Figure 6.65 shows that the time to gas breakthrough is higher for the two horizontal wells; this is due to the larger horizontal extent of the CO<sub>2</sub> plume (fig. 6.66), which causes the pressure build-up to be distributed over a larger area. With a more homogeneous pressure increase, the amount of horizontal stress unloading is lower, and tensile failure happens later. In particular, the long horizontal well can sustain 1492 d of injection more than the vertical well before the caprock is fully breached.

While the pressure build-up is distributed over a larger area, the size of the fractured zone at failure is also linked to the horizontal extent of the CO<sub>2</sub> plume. At failure, the underside of the caprock is fractured along 500 m for the vertical well, 700 m for the short horizontal well and 2700 m for the long horizontal well.



**Figure 6.65** – Fracture normal effective stress (solid) and fracture permeability (dashed) over time at the top center of the caprock.



**Figure 6.66** – Gas saturation after one year of injection: from left to right, vertical well, short horizontal well, and long horizontal well.

Furthermore, the diminished stress concentration at the center of the caprock translates into a more homogeneous lifting of the caprock, and hence lower peak vertical displacement (fig. 6.67).

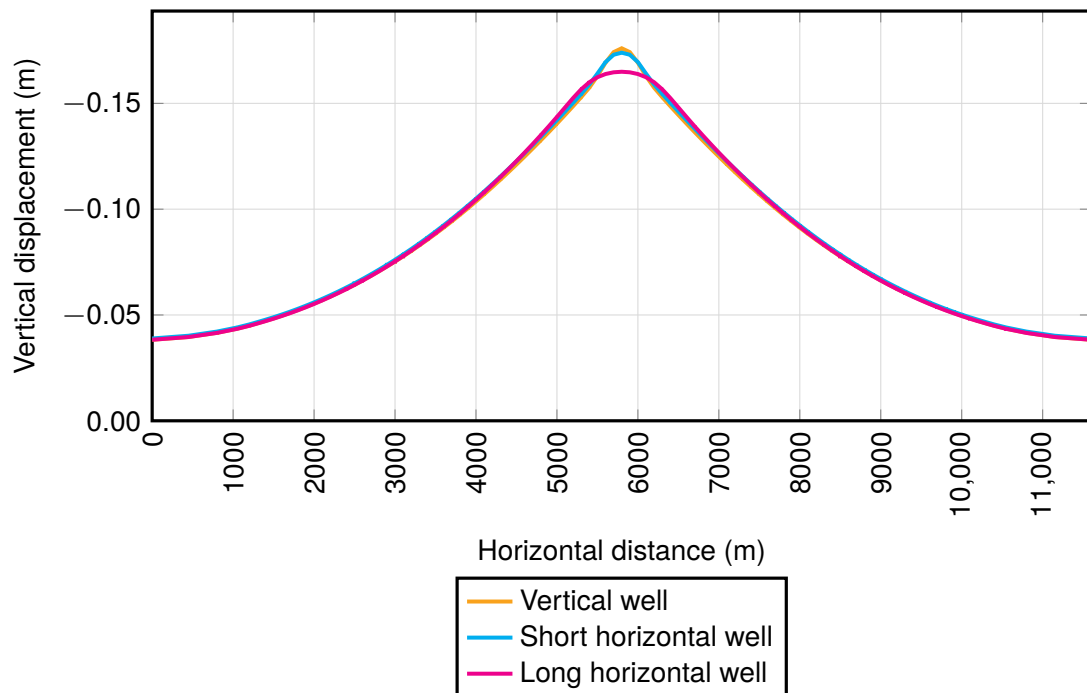


**Figure 6.67** – Vertical displacement profile along the caprock bottom after 8 months of injection (pre-breakthrough).

Note that for the long horizontal well run, the first and last perforations visibly inject a higher quantity of fluid compared to the central perforations. Because the perforations in the center

of the interval have to compete with each other, the pressure increase is higher at that location (fig. 6.68). Consequently, the pressure differential between the wellbore and the reservoir is maximal at the end of the perforated interval; since the resistance to flow is lower, these perforations will inject more fluid.

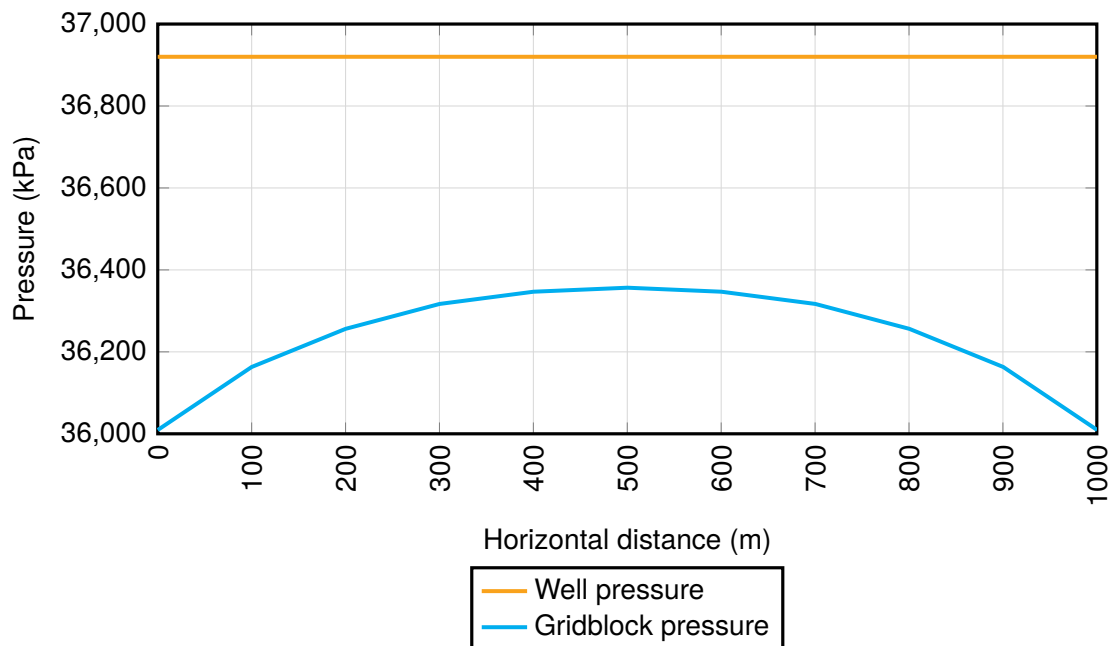


**Figure 6.68** – Pressure profile along the perforated wellbore length after 12 months of injection (long horizontal well).

#### 6.4.4 Perforated interval

The well is perforated from layers 20 to 23, 10 layers above the base case.

Because of the shallower injection point, the required injection pressure is lower, which also lowers the supercritical CO<sub>2</sub> density (fig. 6.69). As the density difference between the resident brine and the injected fluid is increased, buoyant forces will be stronger. However, the actual vertical plume velocity is lower than in the deep interval case, as part of the injection energy is directed downwards, which shows as a positive flux near the bottommost perforation in fig. 6.70 (K is defined positive downwards).

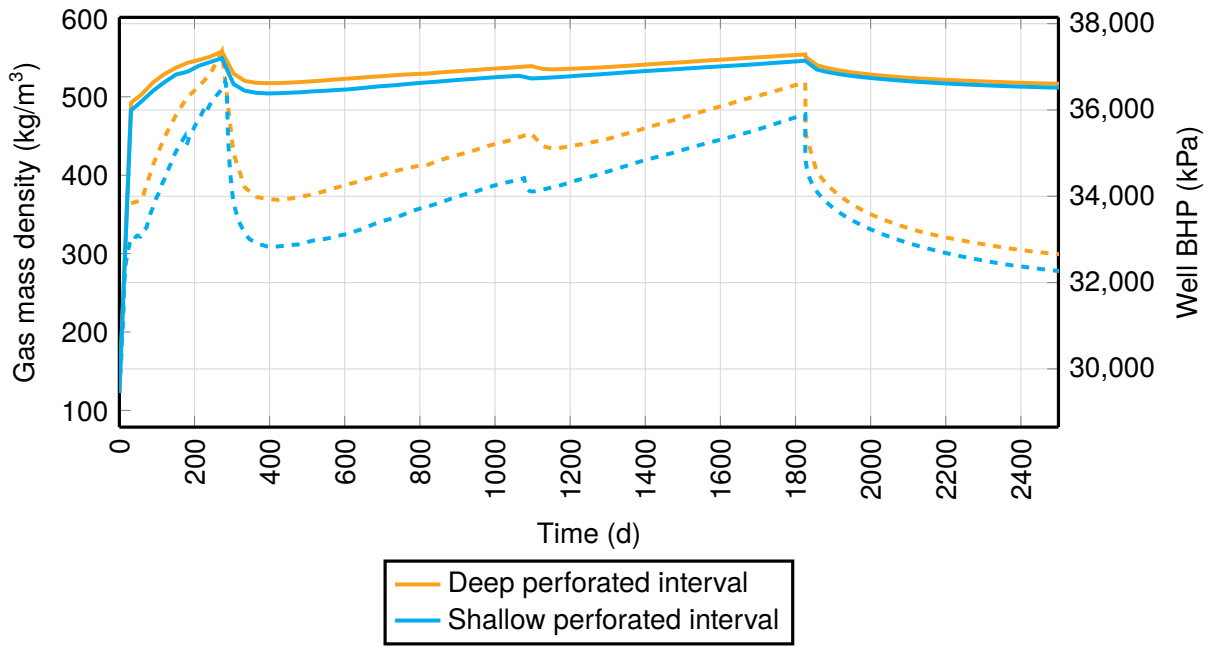


Figure 6.69 – Gas mass density (solid) and well BHP (dashed) at the uppermost perforation.

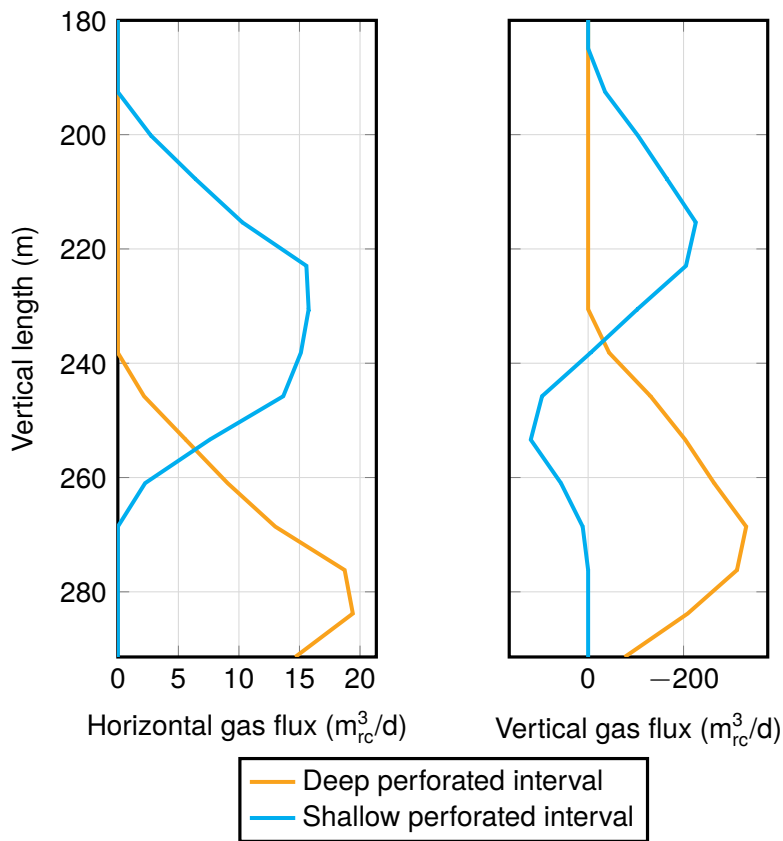
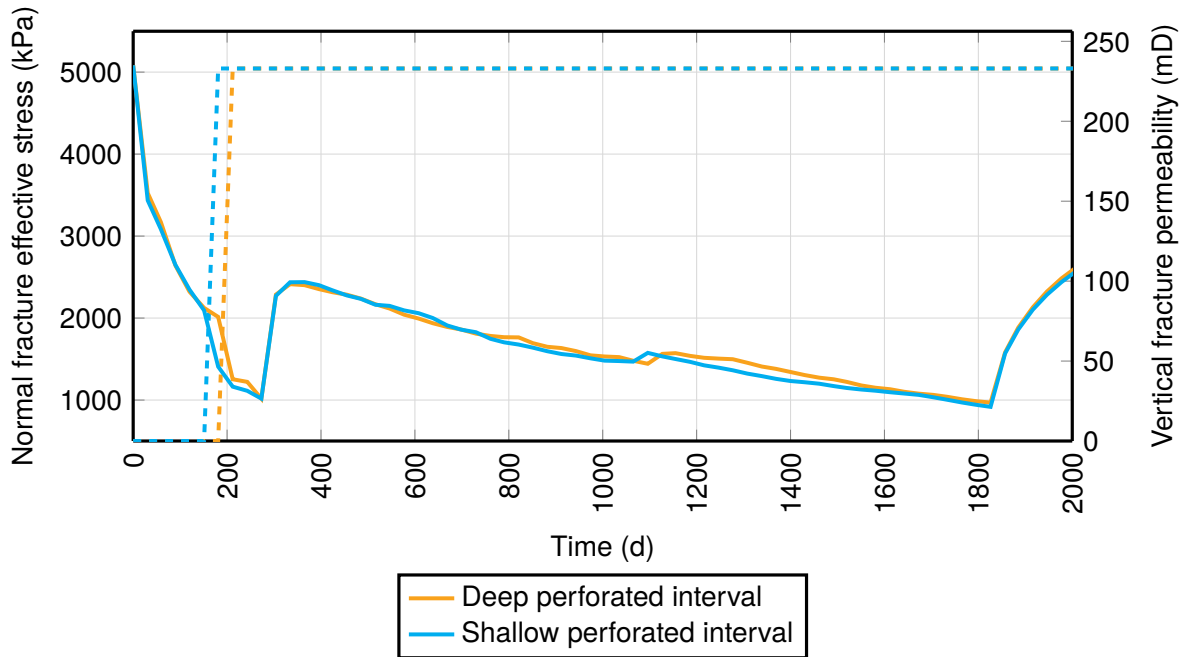


Figure 6.70 – Gas flux along the wellbore after 3 months of injection.

Despite the lower vertical plume velocity, the time taken by the plume to reach the caprock is

shorter in the shallow perforations run, thanks to the much shorter path from the injection point to the caprock. Due to the larger magnitude of the buoyant force, initial crack occurrence is anticipated by 30 days (fig. 6.71).



**Figure 6.71** – Fracture normal effective stress (solid) and fracture permeability (dashed) over time at the bottom center of the caprock.

## 6.5 Summary and discussion

Figure 6.72 summarizes the impact of each investigated parameter on the cumulative injected fluid mass at the onset of fracture failure (in gridblock {51,1,13}), relative to the base case (zero line). Some scenarios have been extended in order to provide a representative range of values.

In regard to reservoir properties, matrix permeability is by far the most impactful parameter; by doubling  $k_{hm}$  from the original 15 mD to 30 mD, an additional 592 kt of supercritical CO<sub>2</sub> can be injected before the first crack appears. For reference, only 68 kt of CO<sub>2</sub> can be injected before fracturing the caprock in the base case. Note that 30 mD is a very low permeability for an aquifer; in real cases, only aquifers with horizontal permeabilities upwards of 500 mD are typically considered for geological sequestration.

The Poisson ratio also has a strong impact on the allowable CO<sub>2</sub> mass to inject, where higher values are better. The anisotropy ratio is the only parameter which has no influence, neither positive nor negative, on crack opening.

The Poisson ratio and Young modulus of the caprock have opposite effect to those of the storage formation, as lower values are better. In particular,  $E$  has a strong influence on the

allowable injected mass. Note that the fracture spacing and residual fracture permeability ( $k_{\text{rcf}}$ ) have no effect on first crack opening.

In short, brittle reservoirs are ideal, given that they deform less, while ductile caprocks are ideal, as they don't fracture as easily.

Simulation options have a small but non-negligible influence on failure behavior, wherein the porosity coupling function is the most important parameter.

Of all the controllable parameters, the number of wells is by far the one that has the greatest influence on the total CO<sub>2</sub> injected mass at failure. The two off-centered wells scenario fails at 751 kt in excess of the base case, while the three wells scenario fails at 671 kt in excess of the base case. Finally, note that the injection rate, which is the only parameter that can be designed, also has a very strong impact; decreasing the rate by 50,000 m<sup>3</sup><sub>sc</sub>/d relative to the base case increases the total storable mass by 223 kt.

Note that of all of the Barton-Bandis model parameters, only fracture opening stress  $f_{\text{rs}}$  has an impact on the time to failure. The other parameters ( $E_0$ ,  $k_{\text{ni}}$ ,  $k_{\text{rcf}}$  and  $k_{\text{ccf}}$ ) solely determine fracture closure behavior.

The numbers provided in fig. 6.72 are obviously case-dependent, so different storages would show different results. However, the impact of each investigated parameter on the cumulative injected fluid mass at the onset of fracture failure is of general validity.

## 6 Sensitivity analysis

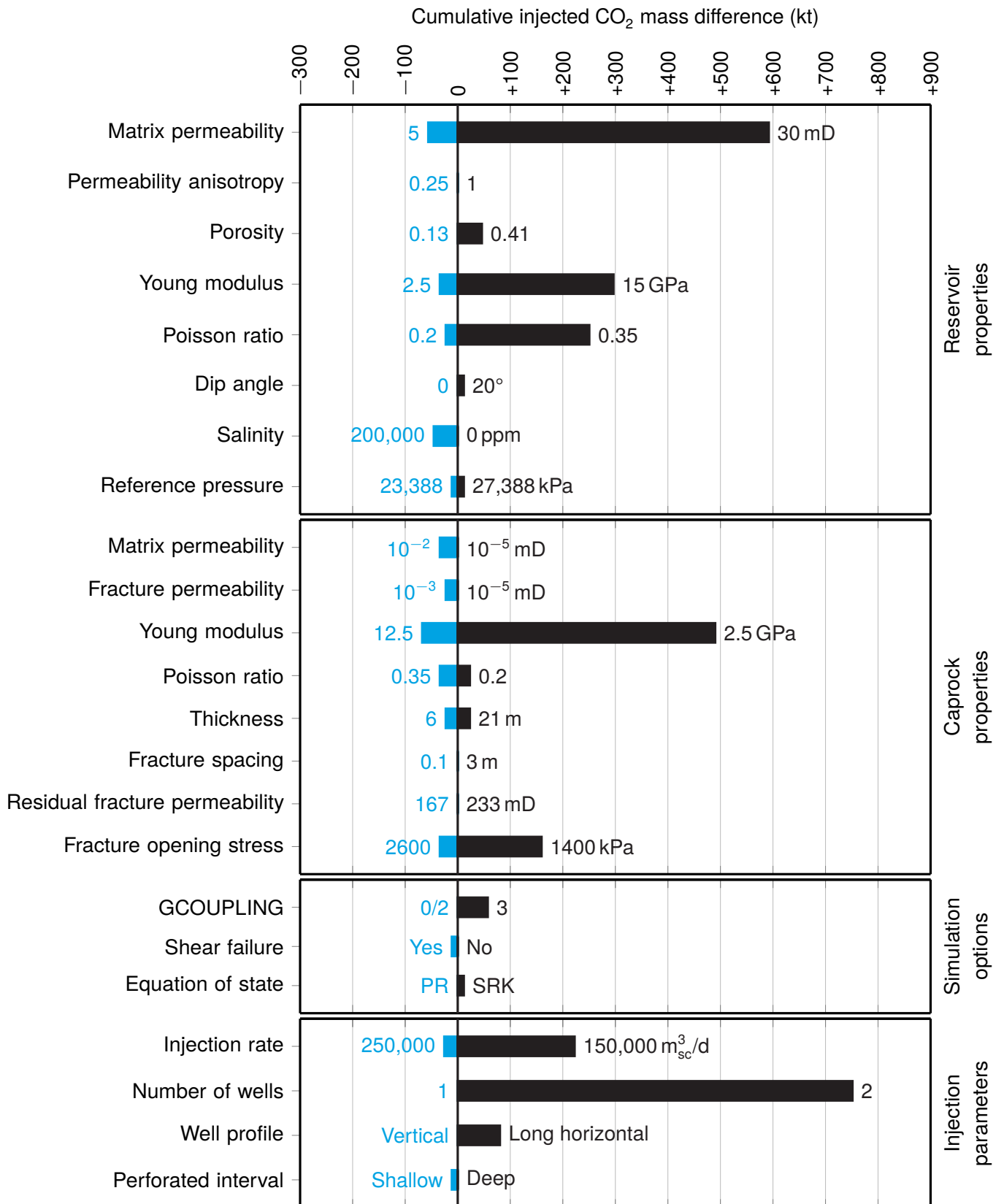


**Figure 6.72** – Effect of investigated parameters on the injected CO<sub>2</sub> mass at the time of first fracture (on the underside of the caprock), relative to base case.

## 7 Conclusions

In this work, tensile failure of the caprock as caused by CO<sub>2</sub> injection has been investigated using CMG GEM. The mechanism of caprock failure according to the model can be summarized as follows.

1. As injection progresses, pore pressure within the aquifer increases; inside the caprock,  $p$  remains the same as no fluid is allowed to enter.
2. Volumetric expansion of the aquifer occurs because of the increase in pore pressure; in turn, because the reservoir is laterally constrained, this causes  $\sigma_h$  to rise.
3. In order for the system to remain in equilibrium with the far-field stresses,  $\sigma_h$  in the caprock decreases by a corresponding amount.
4. Following Terzaghi's law,  $\sigma'_h$  within the caprock decreases, despite no change in pressure, due to the decrease in total stress.
5. Once  $\sigma'_h$  in the caprock has dropped below the rock's tensile strength, fractures starts opening.
6. In time, fractures propagate across the caprock and lead to containment failure.

Injection also causes arching of the caprock over the injection point, which leads to a decrease in horizontal effective stresses at the top of the caprock. However, with the model here considered, this decrease was never sufficient to cause failure by itself. Indeed, the caprock was found to always open first along its bottommost layer, with the fracture then propagating upwards.

Later, a total of 23 parameters have been individually varied in order to study their impact on the behavior of the reservoir-caprock system. The investigated parameters have then been classified based on their measured impact on the cumulative CO<sub>2</sub> mass that can be injected before causing caprock tensile failure.

Findings from the sensitivity analysis have been summarized in a tornado plot, from which it is apparent that ideal reservoirs have a high Young modulus and Poisson ratio, while ideal caprocks have a low Young modulus and Poisson ratio.

In order to avoid caprock tensile failure, the number of wells has been found to be the single most important design parameter; a two-well design drastically increases the injectable CO<sub>2</sub> volume compared to a single-well design. Reservoir matrix permeability is also a crucial parameter, as higher permeabilities allow for easier fluid movement and greatly decrease the pressure build-up at the injector.

In closing, note that this study focused exclusively on tensile failure. However, containment may be breached in many more ways such as fault reactivation, none of which have been investigated here. Furthermore, geochemical interactions have not been considered; a possible axis of further

## *7 Conclusions*

research is then to investigate coupled geochemical and geomechanical interactions. Indeed, geochemical reactions have the potential to weaken the rock, which no doubt will influence failure behavior.

# Bibliography

- [1] M. d. C. Clemente Jul, J. R. Naharro, and L. Pérez del Villar, "Evaluación del desarrollo de las tecnologías de almacenamiento de CO<sub>2</sub>," *Anales de la Real Academia de Doctores de España*, 2011.
- [2] J. E. Mariño-Martínez and L. E. Moreno-Reyes, "Posibilidades de captura y almacenamiento geológico de CO<sub>2</sub> (CCS) en Colombia: Caso Tauramena (Casanare)," *Boletín de Geología*, 2018.
- [3] M. Celia, S. Bachu, J. Nordbotten, and K. Bandilla, "Status of CO<sub>2</sub> storage in deep saline aquifers with emphasis on modeling approaches and practical simulations," *Water Resources Research*, 2015.
- [4] J. Zhan, Z. Niu, M. Li, *et al.*, "Numerical simulation and modeling on CO<sub>2</sub> sequestration coupled with enhanced gas recovery in shale gas reservoirs," *Hindawi*, 2021.
- [5] M. Hefny, C. Qin, M. Saar, and A. Ebigbo, "Synchrotron-based pore-network modeling of two-phase flow in Nubian Sandstone and implications for capillary trapping of carbon dioxide," *International Journal of Greenhouse Gas Control*, 2020.
- [6] C. Ruiz Rivas, "Almacenamiento geológico de CO<sub>2</sub>: Criterios de selección de emplazamientos," Congreso Nacional del Medio Ambiente, 2007.
- [7] E. Kanin, I. Garagash, S. Boronin, *et al.*, "CO<sub>2</sub> storage in deep saline aquifers: Evaluation of geomechanical risks using integrated modeling workflow," 2023.
- [8] Intergovernmental Panel on Climate Change, "Special report on carbon dioxide capture and storage," IPCC, 2005.
- [9] B. Basbug, F. Gumrah, and B. Oz, "Simulating the effects of deep saline aquifer properties for CO<sub>2</sub> sequestration," *Journal of Canadian Petroleum Technology*, 2007.
- [10] T. Vangkilde-Pedersen, K. L. Anthonsen, N. Smith, *et al.*, "Assessing European capacity for geological storage of carbon dioxide: The EU GeoCapacity project," *Energy Procedia*, 2009.
- [11] M. Bentham and G. Kirby, "CO<sub>2</sub> storage in saline aquifers," *Oil & Gas Science and Technology: Revue IFP*, 2005.
- [12] A. Hurtado Bezos, "Metodología para la estimación regional de la capacidad de almacenamiento de CO<sub>2</sub> en formaciones permeables profundas y sus incertidumbres," Ph.D. dissertation, Universidad de León, 2009.
- [13] J. Verdon, J.-M. Kendall, A. Stork, A. Chadwick, D. White, and R. Bissell, "Comparison of geomechanical deformation induced by megatonne-scale CO<sub>2</sub> storage at Sleipner, Weyburn, and In Salah," *Proceedings of the National Academy of Sciences*, 2013.
- [14] S. Ghanbari, Y. Al-Zaabi, G. Pickup, E. Mackay, F. Gozalpour, and A. Todd, "Simulation of CO<sub>2</sub> storage in saline aquifers," *Chemical Engineering Research and Design*, 2006.

- [15] R. Moghadasi, “Residual and critical saturation in geological storage of CO<sub>2</sub>,” Ph.D. dissertation, Uppsala Universitet, 2022.
- [16] L. Nghiem, V. Shrivastava, D. Tran, B. Kohse, M. Hassam, and Y. Chaodong, “Simulation of CO<sub>2</sub> storage in saline aquifers,” in *SPE/EAGE Reservoir Characterization and Simulation Conference*, 2009.
- [17] R. Junin and D. Z. Abang Hasbollah, “CO<sub>2</sub> storage capacity assessment of deep saline aquifers in Malaysia,” in *18<sup>th</sup> International Conference on Oil Reserves and Production*, 2016.
- [18] D. Tran, L. Nghiem, and A. Settari, “New iterative coupling between a reservoir simulator and a geomechanics module,” *SPE Journal*, 2004.
- [19] D. Tran, L. Nghiem, and L. Buchanan, “An overview of iterative coupling between geomechanical deformation and reservoir flow,” in *SPE International Thermal Operations and Heavy Oil Symposium*, 2005.
- [20] F. Delprat-Jannaud, A. Korre, J. Q. Shi, *et al.*, “State-of-the-art review of CO<sub>2</sub> storage site selection and characterisation methods,” CGS Europe, 2013.
- [21] J. Rutqvist, “The geomechanics of CO<sub>2</sub> storage in deep sedimentary formations,” *Geotechnical and Geological Engineering*, 2012.
- [22] A. Badree and D. Alexander, “Fault reactivation and CO<sub>2</sub> migration in carbon storage in a saline aquifer,” *The International Journal of Climate Change: Impacts and Responses*, 2021.
- [23] O. Deweanto Kartikasurja, T. Giok Lin, M. Wakif Sukahar, and B. Viratno, “Study of produced CO<sub>2</sub> storage into aquifer in an offshore field, Malaysia,” in *SPE Asia Pacific Oil & Gas Conference and Exhibition*, 2008.
- [24] A. Chadwick, R. Arts, C. Bernstone, F. May, S. Thibeau, and P. Zweigel, “Best practices for the storage of CO<sub>2</sub> in saline aquifers: Observations and guidelines from the SACS and CO<sub>2</sub>STORE projects,” Global CCS Institute, 2008.
- [25] H. Jung, G. Singh, N. Espinoza, and M. Wheeler, “Quantification of a maximum injection volume of CO<sub>2</sub> to avert geomechanical perturbations using a compositional fluid flow reservoir simulator,” *Advances in Water Resources*, 2018.
- [26] K. Michael, G. Allinson, W. Hou, *et al.*, “Injection strategies for CO<sub>2</sub> storage sites,” IEA GHG, 2010.
- [27] S. Bachu, C. Hawkes, D. Lawton, M. Pooladi-Darvish, and E. Perkins, “CCS site characterisation criteria,” IEA GHG, 2009.
- [28] S. Khan, Y. Khulief, A. Al-Shuhail, S. Bashmal, and N. Iqbal, “The geomechanical and fault activation modeling during CO<sub>2</sub> injection into deep Minjur Reservoir, Eastern Saudi Arabia,” *Sustainability*, 2020.
- [29] M. Delshad, M. Wheeler, and X. Kong, “A critical assessment of CO<sub>2</sub> injection strategies in saline aquifers,” in *SPE Western Regional Meeting*, 2010.
- [30] A. Chadwick and O. Eiken, “Offshore CO<sub>2</sub> storage: Sleipner natural gas field beneath the North Sea,” in *Geological Storage of Carbon Dioxide*. 2013.
- [31] P. Winterfeld and Y.-S. Wu, “Parallel simulation of CO<sub>2</sub> sequestration with rock deformation in saline aquifers,” in *SPE Reservoir Simulation Symposium*, 2011.

- [32] C. Liner, P. Geng, J. Zeng, H. King, and J. Li, "A CO<sub>2</sub> sequestration simulation case study at the Dickman Field, Ness Co., Kansas," in *SPE Annual Technical Conference and Exhibition*, 2011.
- [33] J. Foroozesh, M. Adhil Dier, and M. Gamal Rezk, "A simulation study on CO<sub>2</sub> sequestration in saline aquifers: Trapping mechanisms and risk of CO<sub>2</sub> leakage," in *UTP-UMP-VIT Symposium on Energy Systems*, 2018.
- [34] D. Sopher, C. Juhlin, and M. Erlström, "A probabilistic assessment of the effective CO<sub>2</sub> storage capacity within the Swedish sector of the Baltic Basin," *International Journal of Greenhouse Gas Control*, 2014.
- [35] D. Tran, V. Shrivastava, L. Nghiem, and B. Kohse, "Study of geomechanical effects in deep aquifer CO<sub>2</sub> storage," in *44<sup>th</sup> U.S. Rock Mechanics Symposium*, 2010.
- [36] K. Michael, P. R. Neal, G. Allinson, *et al.*, "Injection strategies for large-scale CO<sub>2</sub> storage sites," *Energy Procedia*, 2011.
- [37] Computer Modelling Group, Ltd. "CO<sub>2</sub> sequestration modelling." (2021), [Online]. Available: <https://vimeo.com/658676763/0b2a8354ce>.
- [38] F. Javadpour and J.-P. Nicot, "Enhanced CO<sub>2</sub> storage and sequestration in deep saline aquifers by nanoparticles: Commingled disposal of depleted uranium and CO<sub>2</sub>," *Transport in Porous Media*, 2011.
- [39] H. Singh, S. Hosseini, and F. Javadpour, "Enhanced CO<sub>2</sub> storage in deep saline aquifers by nanoparticles: Numerical simulation results," in *SPE International Oilfield Nanotechnology Conference*, 2012.
- [40] L. Steel, Q. Liu, E. Mackay, and M. Maroto-Valer, "CO<sub>2</sub> solubility measurements in brine under reservoir conditions," *Greenhouse Gases: Science and Technology*, 2016.
- [41] G. Dawson, H. Sidiq, J. Pearce, *et al.*, "Review of laboratory-scale geochemical and geomechanical experiments simulating geosequestration of CO<sub>2</sub> in sandstone, and associated modelling studies," Australian National Low Emissions Coal Research and Development, 2013.
- [42] J.-P. Nicot, S. Hosseini, and S. Solano, "Are single-phase flow numerical models sufficient to estimate pressure distribution in CO<sub>2</sub> sequestration projects?" *Energy Procedia*, 2011.
- [43] M. Rasmusson, "Residual and solubility trapping during geological CO<sub>2</sub> storage: Numerical and experimental studies," Ph.D. dissertation, Uppsala Universitet, 2018.
- [44] S. Krevor, M. Blunt, S. Benson, *et al.*, "Capillary trapping for geologic carbon dioxide storage: From pore scale physics to field scale implications," *International Journal of Greenhouse Gas Control*, 2015.
- [45] N. Kumar, S. Bryant, and J.-P. Nicot, "Simplified CO<sub>2</sub> plume dynamics for a certification framework for geologic sequestration projects," *Energy Procedia*, 2009.
- [46] A. Vafaie, J. Cama, J. Soler, I. Kivi, and V. Vilarrasa, "Chemo-hydro-mechanical effects of CO<sub>2</sub> injection on reservoir and seal rocks: A review on laboratory experiments," *Renewable and Sustainable Energy Reviews*, 2023.
- [47] A. Kumar, M. Noh, R. Ozah, *et al.*, "Reservoir simulation of CO<sub>2</sub> storage in deep saline aquifers," in *SPE/DOE 14<sup>th</sup> Symposium on Improved Oil Recovery*, 2004.

- [48] V. Vilarrasa, S. Olivella, and J. Carrera, “Geomechanical stability of the caprock during CO<sub>2</sub> sequestration in deep aquifers,” *Energy Procedia*, 2011.
- [49] A. Abdullahi Maalim, H. Ben Mahmud, and M. Seyyedi, “Assessing roles of geochemical reactions on CO<sub>2</sub> plume, injectivity and residual trapping,” *Energy Geoscience*, 2021.
- [50] P. Ranganathan, P. Van Hemert, S. Rudolph, and P. Zitha, “Numerical modeling of CO<sub>2</sub> mineralisation during storage in deep saline aquifers,” *Energy Procedia*, 2011.
- [51] A. Ofori and T. Engler, “Effects of CO<sub>2</sub> sequestration on the petrophysical properties of an aquifer rock,” in *Canadian Unconventional Resources Conference*, 2011.
- [52] K. Kim, V. Vilarrasa, and R. Makhnenko, “CO<sub>2</sub> injection effect on geomechanical and flow properties of calcite-rich reservoirs,” *Fluids*, 2018.
- [53] W. Pin Yong, A. I. Azahree, S. S. Ali, F. J. Azuddin, and S. Amin, “A new modelling approach to simulate CO<sub>2</sub> movement and containment coupled with geochemical reactions and geomechanical effects for an offshore CO<sub>2</sub> storage in Malaysia,” in *81<sup>st</sup> EAGE Conference and Exhibition*, 2019.
- [54] B. Ren, S. Bryant, and L. Lake, “Fast modeling of local capillary trapping during CO<sub>2</sub> injection into a saline aquifer,” in *Carbon Management Technology Conference*, 2015.
- [55] A. Lucier, M. Zoback, N. Gupta, and T. Ramakrishnan, “Geomechanical aspects of CO<sub>2</sub> sequestration in a deep saline reservoir in the Ohio River Valley region,” *Environmental Geosciences*, 2006.
- [56] H. Kiran Nambu, “Modeling of caprock seal failure due to fluid injection,” M.S. thesis, West Virginia University, 2014.
- [57] J. Kaldi, R. Daniel, E. Tenthorey, *et al.*, “Caprock systems for CO<sub>2</sub> geological storage,” IEA GHG, 2011.
- [58] G. Woo Kim, T. Hong Kim, J. Lee, and K. Sang Lee, “Coupled geomechanical-flow assessment of CO<sub>2</sub> leakage through heterogeneous caprock during CCS,” *Advances in Civil Engineering*, 2018.
- [59] D. Rodríguez Zambrano, “Modeling of leakage through fault-zone structures in CO<sub>2</sub> geological storage,” M.S. thesis, Louisiana State University and Agricultural and Mechanical College, 2019.
- [60] L. Nghiem, P. Sammon, J. Grabenstetter, and H. Ohkuma, “Modeling CO<sub>2</sub> storage in aquifers with a fully-coupled geochemical EoS compositional simulator,” in *SPE/DOE 14<sup>th</sup> Symposium on Improved Oil Recovery*, 2004.
- [61] A. Jahandideh, S. Hakim-Elahi, and B. Jafarpour, “Inference of rock flow and mechanical properties from injection-induced microseismic events during geologic CO<sub>2</sub> storage,” *International Journal of Greenhouse Gas Control*, 2021.
- [62] R. Chadwick, G. Williams, J. Williams, and N. D., “Measuring pressure performance of a large saline aquifer during industrial-scale CO<sub>2</sub> injection: The Utsira Sand, Norwegian North Sea,” *International Journal of Greenhouse Gas Control*, 2012.
- [63] C. Khazaei and R. Chalaturnyk, “A reservoir-geomechanical model to study the likelihood of tensile and shear failure in the caprock of Weyburn CCS project with regard to interpretation of microseismic data,” *Geotechnical and Geological Engineering*, 2017.

- [64] V. Vilarrasa, S. Orlando, J. Carrera, and S. Olivella, "Liquid CO<sub>2</sub> injection for geological storage in deep saline aquifers," *International Journal of Greenhouse Gas Control*, 2013.
- [65] G. J. González Martínez de Miguel, "A hydromechanically-based risk framework for CO<sub>2</sub> storage coupled to underground coal gasification," Ph.D. dissertation, University of Newcastle upon Tyne, 2014.
- [66] V. Vilarrasa, "The role of the stress regime on microseismicity induced by overpressure and cooling in geologic carbon storage," *Geofluids*, 2016.
- [67] H. Jung, N. Espinoza, and S. Hosseini, "Wellbore injectivity response to step-rate CO<sub>2</sub> injection: Coupled thermo-poro-elastic analysis in a vertically heterogeneous formation," *International Journal of Greenhouse Gas Control*, 2020.
- [68] A. Haghi and R. Chalaturnyk, "Experimental characterization of hydrodynamic properties of a deformable rock fracture," *Energies*, 2022.
- [69] A. Elyasi, K. Goshtasbi, and H. Hashemolhosseini, "A coupled geomechanical reservoir simulation analysis of CO<sub>2</sub>-EOR: A case study," *Geomechanics and Engineering*, 2016.
- [70] Computer Modelling Group, Ltd. "CMG webinar: The role of coupled geomechanical modelling in reservoir simulation." (2016), [Online]. Available: <https://www.youtube.com/watch?v=FAUjmExmHV0>.
- [71] X. Zhao and B. Jha, "Role of well operations and multiphase geomechanics in controlling fault stability during CO<sub>2</sub> storage and enhanced oil recovery," *Journal of Geophysical Research*, 2019.
- [72] M. Bruno, K. Lao, J. Diessl, *et al.*, "Development of improved caprock integrity analysis and risk assessment techniques," *Energy Procedia*, 2014.
- [73] S. Jia, C. Wen, X. Fu, T. Liu, and Z. Xi, "A caprock evaluation methodology for underground gas storage in a deep depleted gas reservoir: A case study for the X9 lithologic trap of Langgu Sag, Bohai Bay Basin, China," *Energies*, 2022.
- [74] S. Soo Park, J. Park, J. Cho, and K. Sang Lee, "Numerical modeling of the tensile fracture reactivation under the effects of rock geomechanical properties and heterogeneity during CO<sub>2</sub> storage," *Environmental Earth Sciences*, 2016.
- [75] Computer Modelling Group, Ltd. "CMG webinar: Modelling hydraulically fractured wells." (2018), [Online]. Available: <https://www.youtube.com/watch?v=SPFSDen1owg>.
- [76] T. Weldu Teklu, W. Alameri, R. Graves, A. Tutuncu, H. Kazemi, and A. Alsumaiti, "Geomechanics considerations in enhanced oil recovery," in *SPE Canadian Unconventional Resources Conference*, 2012.
- [77] D. Bui, T. Nguyen, T. Nguyen, and H. Yoo, "Formation damage simulation of a multi-fractured horizontal well in a tight gas/shale oil formation," *Journal of Petroleum Exploration and Production Technology*, 2023.
- [78] K. Bisdom, G. Bertotti, and H. Nick, "A different perspective on critically stressed fractures and their impact on fluid flow," in *AAPG 2016 Annual Convention and Exhibition*, 2016.

- [79] S. Raziperchikolaee, Z. Cotter, and N. Gupta, “Assessing mechanical response of CO<sub>2</sub> storage into a depleted carbonate reef using a site-scale geomechanical model calibrated with field tests and InSAR monitoring data,” *Journal of Natural Gas Science and Engineering*, 2021.
- [80] H. Li, L.-N. Zheng, S. Lee, and R. Chalaturnyk, “Application of programmatic gridding technique to advanced reservoir geomechanics modeling,” in *49<sup>th</sup> U.S. Rock Mechanics Symposium*, 2015.
- [81] S. Oduwole, L. Zerpa, M. Pohl, J. Behura, and M. Prasad, “Reservoir analysis of a CO<sub>2</sub> sequestration site: Experiment-guided field scale modeling,” in *First International Meeting for Applied Geoscience & Energy*, 2021.
- [82] S. Bandis, A. Lumsden, and N. Barton, “Fundamentals of rock joint deformation,” *International Journal of Rock Mechanics and Mining Sciences & Geomechanics Abstracts*, 1983.
- [83] A. Kubeyev, N. Forbes Inskip, T. Philips, *et al.*, “Digital image-based stress-permeability relationships of rough fractures using numerical contact mechanics and Stokes equation,” *Transport in Porous Media*, 2022.
- [84] S. Heru Prasetyo, M. Gutiérrez, and N. Barton, “Nonlinear shear behavior of rock joints using a linearized implementation of the Barton-Bandis model,” *Journal of Rock Mechanics and Geotechnical Engineering*, 2017.
- [85] L. Guimarães, “Constitutive laws: Behavior of fractures,” in *Introduction to Reservoir Geomechanics*, 2017.
- [86] S. Pulchan, D. Alexander, and D. Boodlal, “Investigating the effects of fault reactivation and CO<sub>2</sub> migration during combined CO<sub>2</sub>-EOR and sequestration within a mature oil reservoir,” *Journal of Petroleum Exploration and Production Technology*, 2020.
- [87] Q. Lei and N. Barton, “On the selection of joint constitutive models for geomechanics simulation of fractured rocks,” *Computers and Geotechnics*, 2022.
- [88] W. Li, L. Frash, N. Welch, W. Carey, M. Meng, and M. Wigand, “Stress-dependent fracture permeability measurements and implications for shale gas production,” *Fuel*, 2021.
- [89] H. Deng, “Modeling stimulated rock volumes using DPDK approach coupled with rock mechanics,” Ph.D. dissertation, University of Calgary, 2016.
- [90] N. Barton, S. Bandis, and K. Bakhtar, “Strength, deformation and conductivity coupling of rock joints,” *International Journal of Rock Mechanics and Mining Sciences & Geomechanics Abstracts*, 1985.
- [91] K. Bisdom, G. Bertotti, and H. Nick, “The impact of different aperture distribution models and critical stress criteria on equivalent permeability in fractured rocks,” *Journal of Geophysical Research: Solid Earth*, 2016.
- [92] K. Bisdom, G. Bertotti, and H. Nick, “The impact of in-situ stress and outcrop-based fracture geometry on hydraulic aperture and upscaled permeability in fractured reservoirs,” *Tectonophysics*, 2016.
- [93] A. Lavrov, “Fracture permeability under normal stress: A fully computational approach,” *Journal of Petroleum Exploration and Production Technology*, 2016.

- [94] N. Barton and V. Choubey, “The shear strength of rock joints in theory and practice,” *Rock Mechanics and Rock Engineering*, 1977.
- [95] N. Barton and S. Bandis, “Characterisation and modelling of the shear strength, stiffness and hydraulic behaviour of rock joints for engineering purposes,” in *Rock Mechanics and Engineering*. 2017.
- [96] N. Barton, “Review of a new shear-strength criterion for rock joints,” *Engineering Geology*, 1973.
- [97] C. Haw Lee and I. Farmer, “A simple method of estimating rock mass porosity and permeability,” *International Journal of Mining and Geological Engineering*, 1990.
- [98] N. Barton, “Modelling rock joint behavior from in situ block tests: Implications for nuclear waste repository design,” Terra Tek, Inc., 1982.
- [99] N. Barton, C. Wang, and R. Yong, “Advances in joint roughness coefficient (JRC) and its engineering applications,” *Journal of Rock Mechanics and Geotechnical Engineering*, 2023.
- [100] N. Barton, A. Makurat, M. Christianson, and S. Bandis, “Modelling rock mass conductivity changes in disturbed zones,” in *The 28<sup>th</sup> U.S. Symposium on Rock Mechanics*, 1987.
- [101] N. Barton, “Suggested methods for the quantitative description of discontinuities in rock masses,” *International Journal of Rock Mechanics and Mining Sciences & Geomechanics Abstracts*, 1978.
- [102] N. Barton, “Non-linear behaviour for naturally fractured carbonates and frac-stimulated gas-shales,” *First Break*, 2014.
- [103] Z. Chen, S. Narayan, Z. Yang, and S. Rahman, “An experimental investigation of hydraulic behavior of fractures and joints in granitic rock,” *International Journal of Rock Mechanics and Mining Sciences*, 2000.
- [104] N. Verma, F. Al-Medhadi, J. Franquet, R. Maddock, D. Natarajan, and E. Al-Mayyas, “Critically-stressed fracture analysis in naturally fractured carbonate reservoir: A case study in West Kuwait,” in *SPE Middle East Oil and Gas Show and Conference*, 2007.
- [105] S. Azizmohammadi and M. Sedaghat, “The impact of stress orientation and fracture roughness on the scale dependency of permeability in naturally fractured rocks,” *Advances in Water Resources*, 2020.
- [106] H. Class, A. Ebigbo, R. Helmig, *et al.*, “A benchmark study on problems related to CO<sub>2</sub> storage in geologic formations,” *Computational Geosciences*, 2009.
- [107] J. Kim, “Sequential methods for coupled geomechanics and multiphase flow,” Ph.D. dissertation, Stanford University, 2010.
- [108] Computer Modelling Group, Ltd., *GEM 2021.10 manual*, 2021.
- [109] S. Echavarría-Montaña, S. Velásquez, N. Bueno, J. D. Valencia, H. A. Solano, and J. M. Mejía, “Semi-implicit finite volume procedure for compositional subsurface flow simulation in highly anisotropic porous media,” *Fluids*, 2021.
- [110] M. Haddad and K. Sepehrnoori, “Development and validation of an explicitly coupled geomechanics module for a compositional reservoir simulator,” *Journal of Petroleum Science and Engineering*, 2017.

- [111] D. Tran, L. Nghiem, and L. Buchanan, "Aspects of coupling between petroleum reservoir flow and geomechanics," in *43<sup>rd</sup> U.S. Rock Mechanics Symposium*, 2009.
- [112] V. Shrivastava, D. Tran, L. Nghiem, and B. Kohse, "Use of improved gridding technique in coupled geomechanics and compositional reservoir flow simulation," in *SPE Middle East Oil & Gas Show and Conference*, 2011.
- [113] D. Tran, V. Shrivastava, L. Nghiem, and B. Kohse, "Geomechanical risk mitigation for CO<sub>2</sub> sequestration in saline aquifers," in *SPE Annual Technical Conference and Exhibition*, 2009.
- [114] H. Liu, Z. Chen, L. Shen, X. Guo, and D. Ji, "Well modelling methods in thermal reservoir simulation," *Oil & Gas Science and Technology: Revue IFP*, 2020.
- [115] F. Dumkwu, A. Islam, and E. Carlson, "Review of well models and assessment of their impacts on numerical reservoir simulation performance," *Journal of Petroleum Science and Engineering*, 2012.
- [116] H. Kukha Hawez, R. Sanaee, and N. Haque Faisal, "A critical review on coupled geomechanics and fluid flow in naturally fractured reservoirs," *Journal of Natural Gas Science and Engineering*, 2021.
- [117] D. Tran, L. Buchanan, and L. Nghiem, "Improved gridding technique for coupling geomechanics to reservoir flow," *SPE Journal*, 2009.
- [118] G. Giani, S. Orsatti, C. Peter, and V. Rocca, "A coupled fluid flow-geomechanical approach for subsidence numerical simulation," *Energies*, 2018.
- [119] D. Tran, L. Nghiem, and L. Buchanan, "Improved iterative coupling of geomechanics with reservoir simulation," in *SPE Reservoir Simulation Symposium*, 2005.
- [120] P. Li and R. Chalaturnyk, "Geomechanical model of oil sands," in *SPE International Thermal Operations and Heavy Oil Symposium*, 2005.
- [121] A. Touhidi-Baghini, "Absolute permeability of McMurray formation oil sands at low confining stresses," Ph.D. dissertation, University of Alberta, 1998.
- [122] J. Curnow and A. Tutuncu, "A coupled geomechanics and fluid flow modeling study for hydraulic fracture design and production optimization in an Eagle Ford shale oil reservoir," in *SPE Hydraulic Fracturing Technology Conference*, 2016.
- [123] M. Ibrahim Mohamed, T. Thaker, M. Ibrahim, and E. Ozkan, "Developing methodology for DFIT design and pressure interpretation by coupled reservoir geomechanics flow simulation," in *SPE Hydraulic Fracturing Technology Conference and Exhibition*, 2020.
- [124] H. Fan, M. Kouma, and N. Sibaweihi, "Investigation and optimization of infill well spacing using geomechanical and simulation studies on shale gas reservoir to maximize performance and financial return," *International Journal of Oil, Gas and Coal Engineering*, 2022.
- [125] M. Tingay, R. Hillis, C. Morley, R. King, R. Swarbrick, and A. Razak Damit, "Present-day stress and neotectonics of Brunei: Implications for petroleum exploration and production," *AAPG Bulletin*, 2009.
- [126] N. Kumar, S. Bryant, and J.-P. Nicot, "Simplified models for plume dynamics: Simulation studies for geological CO<sub>2</sub> storage certification framework," in *Sixth Annual Conference on Carbon Capture and Sequestration*, 2007.

## Bibliography

- [127] V. Núñez López, “Fundamentos del modelado de flujo de CO<sub>2</sub> en el subsuelo,” in *Global CCS Institute Webinar*, 2013.
- [128] M. Ibrahim, G. Skaugen, and I. Ertesvåg, “Modelling CO<sub>2</sub>-water thermodynamics using SPUNG equation of state (EoS) concept with various reference fluids,” *Energy Procedia*, 2014.
- [129] Z. Cui and H. Li, “Towards accurate density and interfacial tension modeling for carbon dioxide/water mixtures,” *Petroleum Science*, 2021.
- [130] L. Larroudé Olivieri Setaro, “Simulação da injeção alternada de CO<sub>2</sub> e salmoura em reservatórios de petróleo: Efeito da densidade das fases no fator de recuperação de óleo,” M.S. thesis, Universidade Federal da Bahia, 2022.
- [131] A. Aasen, M. Hammer, G. Skaugen, J. Jakobsen, and Ø. Wilhelmsen, “Thermodynamic models to accurately describe the PVTxy-behavior of water/carbon dioxide mixtures,” *Fluid Phase Equilibria*, 2017.
- [132] P. Mathias, T. Naheiri, and E. Oh, “A density correction for the Peng-Robinson equation of state,” *Fluid Phase Equilibria*, 1989.
- [133] Z. Hongjun, L. Xinwei, C. Yanfang, and Z. Xiaoliang, “Sensitivity analysis of CO<sub>2</sub> sequestration in saline aquifers,” *Petroleum Science*, 2010.